

**AN INVESTIGATION INTO HYDROPHOBIC
MICRO-TEXTURED SURFACES ON HEAT TRANSFER AND
SURFACE WETTING PHENOMENON DURING VAPOR
CONDENSATION**

A Dissertation

By

Thamer Khalif Salem

Advisor: Prof. Dr. Mehmet Arık, (Özyeğin University)

Co-advisor: Asst. Prof. Dr. Mete Budaklı, (Turkish-German University)

Submitted to the

Graduate School of Sciences and Engineering
in Partial Fulfillment of the Requirements for
the Degree of

Doctor of Philosophy

in the

Department of Mechanical Engineering

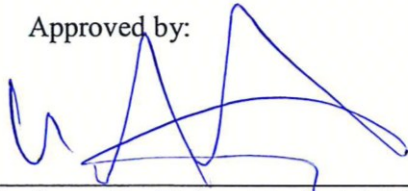
Özyeğin University

December 2018

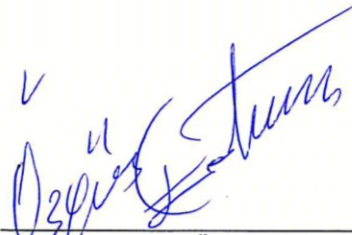
Copyright © 2018 by Thamer Khalif Salem

**AN INVESTIGATION INTO HYDROPHOBIC
MICRO-TEXTURED SURFACES ON HEAT TRANSFER AND
SURFACE WETTING PHENOMENON DURING VAPOR
CONDENSATION**

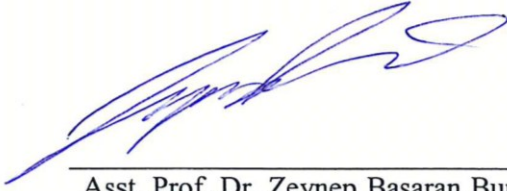
Approved by:



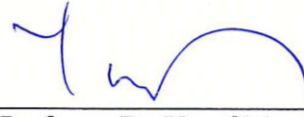
Professor Dr. Mehmet Arık, Advisor,
Department of Mechanical Engineering
Özyeğin University



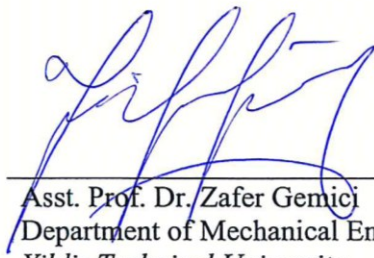
Asst. Prof. Dr. Özgür Ertunç,
Department of Mechanical Engineering
Özyeğin University



Asst. Prof. Dr. Zeynep Başaran Bundur
Department of Civil Engineering
Özyeğin University



Professor Dr. Yusuf Menceloğlu,
Department of Engineering and
Natural Sciences
Sabancı University



Asst. Prof. Dr. Zafer Gemicı
Department of Mechanical Engineering
Yildiz Technical University

Date Approved: 28 December 2018

To ...

My father may Allah have mercy on him,

*My mother who always encouraged me and she pray for me during this
studying trip,*

My wife,

My kids (Mohammed, Aya, Khalid, Zinah and Waleed),

My Brothers and sister who supported me during this studying journey,

*My best friends who encouraged me especially (Asst. Prof. Saad Sami
Farhan, Mete Muslu, Prof. Dr. Tahseen Ahmad Tahseen and Dr. Enes
Tamdoğan)*

ABSTRACT

Efficiency and performance of a system that involves condensation process have been one of the primary considerations over the last decades for a number of applications including thermal management systems such as vapor compression (refrigeration) cycle, electronic cooling etc. In fact, predicting the performance of a system is essential to assess and enhance system components such as condensers and evaporators. Thus, the primary objective of this study is to investigate the condensation phenomena using various characteristics of surface topographies and surface wetting at different saturation pressures ranging from 1.02 Bar to 1.25 Bar. For this purpose, a number of tasks were completed to provide an in depth understanding. The first task focused on analyzing the performance of a heat pipe at various orientations of a condenser (-90° to $+90^\circ$). In addition, the condenser part of a heat pipe was considered as a vertical plate with different surface topographies such as unstructured, square groove and V-groove. Then, heat flux and heat transfer coefficients were calculated as a second task based on the experiments carried out over untreated surfaces. In addition, some specifications of surface topographies including surface energy and droplet contact angle were examined while two treated cases before and after coating by Ultra-ever-dry chemical were studied. Another task was accomplished by comparing experimental results of a set of studies by other authors with analytical results of the current study for each sample before coating at a constant vapor pressure of 1.02 Bar. In the final task, IPTES silane coating was applied at various vapor pressures to observe the condensation process on a vertical surface with different topographies and wettings (hydrophobic surface). Today's conventional thermal management systems working by means of conduction and convection which are not sufficient when a high amount of waste heat is generated.

Tightly packaged double-sided PCBs and high power LEDs can be considered as examples of such thermal problems as they produce undesired local heat that may lead to device failures. To ensure the system reliability, more effective new cooling techniques need to be developed. Thus, a special study with a heat-pipe-embedded PCB was performed. Moreover, a series of numerical models were developed to determine the local temperature distribution and validate analytical and experimental results. The results show that spreading resistance is significantly lowered due to the effective heat spreading when heat pipe is flattened and embedded inside the plates with known conductivities. Thermal resistances at each case were also compared with the conventional cooling of a PCB made up of polymer or aluminum. The proposed cooling method shows a reduction in the overall resistance by approximately 50%. Furthermore, novel surface characteristics were studied as another task during the condensation experiments. Hydrophobic surfaces are some of those novel surfaces that are widely used to increase liquid repellence typically by controlling liquid-solid contact angle. These micro-nano-textured surfaces are fabricated by using advanced manufacturing technologies and methods including etching, electrospinning, and chemical vapor deposition. While these fabricated surfaces can be used for a variety of purposes, such as protecting a material from external effects and avoiding deposition, they are also considered to improve heat transfer mechanisms. Thus, a set of experimental and analytical studies was conducted to investigate the influence of micro-nano-textured surfaces on liquid wetting phenomena.

Since the liquid-wall interaction is a key parameter for droplet formation, the effect of liquid wetting phenomena on heat transfer performance of a heat pipe condenser was also investigated as another interest of this study. For this purpose, copper samples with

different surface topographies at micro-scale were subjected to a chemical treatment process by using dip-coating and spray-coating techniques. Before and after coating with Ultra-ever-dry, measurements were performed with deionized water in order to determine the difference in droplet contact angle at the surfaces to be used. In the analytical study, capillary Laplace equation with available analytical correlations from the literature was used to predict the contact angles and surface energies. Results clearly show that the coated square-grooved surface has a larger average contact angle than the v-grooved surface by 4.6 %. The influence of super-hydrophobic surface on the condensation heat transfer rate compared to the untreated surfaces was also investigated and explained in this task. Thus, experimental investigations on liquid transport and heat transfer during water vapor condensation on subcooled, nano-coated microstructured copper substrates were performed in a generic setup. Two types of surfaces were used, an unstructured sample as a reference surface and a sample with longitudinally oriented micro-structures of square geometry. The first set of experiments was performed with micro-structured surfaces without coating of nano particles while other measurements were carried out after spray-coating the micro-structures with nano particles using a commercially available mixture (Ultra-ever-dry). Finally, the effect of a different surface topography was studied by comparing surface temperature, heat flux and HTC. In general, it is found that HTC drops for all surfaces as temperature difference ($T_{v, ch} - T_s$) increases. It is also realized that micro-grooves on the surfaces do not result in a significant enhancement of HTC and heat flux which show a similar behavior with the unstructured surface. Specifically, the coated surfaces show lower HTC values compared to the uncoated samples. Another task focused on understanding the fundamentals of condensation phenomenon during dropwise and filmwise modes on

micro-structured surfaces and validating the experimental results in the condensation process at 1.02 Bar. Analytical calculations and experiments for condensation were carried out at vertically aligned copper substrates. An experimental setup was used to observe the impact of three different surface topographies on the condensation process under various operation parameters such as saturation pressure of vapor and inlet temperature of cooling liquid. Experimental heat transfer coefficients measured at an unstructured surface was found to be higher than those of the surface embossed with V-grooves and square-grooves by 30 % and 7.2 % respectively. Moreover, the impact of vapor pressure inside a vapor chamber on condensation at various surface topographies and wetting (hydrophobicity) conditions was studied. The hydrophobic surface was prepared in a dip coating process by applying perfluoro-silane coating since it causes a strong promotion of DWC as the droplet contact angle is increased. The effects of the vapor pressure on DFWC on both untreated and treated surfaces that include the unstructured and micro-structured surfaces were performed at various Re numbers. Experimental results show that an increase in the droplet contact angle with coating is achieved for all surfaces. As a result, after the coating is applied, the largest droplet contact angle is obtained ($130.9^\circ \pm 2.0^\circ$) for the microstructure square groove surface when compared to other samples. In conclusion, thermal resistance of the embedded heat pipe is found to be lower than the conventional heat pipe's thermal resistance and the change in the effective thermal conductivity of the embedded heat pipe with respect to the angle of the heat pipe inclination was investigated. As the angle of inclination is changed from -90° to 90° , the effective thermal conductivity increases by 68.7% at the maximum heat flux of 76 W/cm^2 . Furthermore, applicability of ultra-ever dry coating in condensation tests was questioned. It was determined that Ultra-ever dry coating is not a

suitable coating technique for the condensation tests because this type of coating cannot be applied in high temperature gradients although it provides a large contact angle more than 165° over super-hydrophobic surface. On the other hand, unstructured surface gives a good enhancement in condensation heat transfer than micro-structures. The condensation heat rate is elevated with the rise in vapor pressure for all surfaces.



ÖZETÇE

Yoğuşma sürecini içeren bir sistemin verimliliği ve performansı, son yıllardaki buhar sıkıştırma (soğutma) döngüsü, elektronik soğutma vb. gibi termal yönetim sistemlerini kapsayan birçok uygulama için en önemli konulardan biri olmuştur. Kondenserler ve evaporatörler gibi sistem bileşenlerini değerlendirmek ve geliştirmek için sistem performansını öngörmek oldukça önemlidir. Bu nedenle, bu çalışmanın temel amacı, 1.02 Bar'dan 1.25 Bar'a kadar değişen farklı doyma basınçlarında, yüzey topografyası ve yüzey ıslatma özelliklerini inceleyerek yoğuşma olaylarını incelemektir. Bu amaçla, derinlemesine bir anlayış oluşturmak üzere bir dizi görev tamamlanmıştır. İlk görev, bir ısı borusunun çeşitli kondenser yönlerindeki (-90° ile $+90^{\circ}$ arası) performansını analiz etmeye odaklanmıştır. Isı borusunun kondenser kısmı, yapısal olmayan, kare oluk ve V-oluk gibi farklı yüzey topografyalarına sahip dikey bir plaka olarak düşünülmüştür. İkinci görev olarak, işlenmemiş yüzeyler üzerinde gerçekleştirilen deneylerdeki ısı akışı ve ısı transfer katsayıları hesaplanmıştır. Yanı sıra, Ultra-ever dry kimyasal madde ile kaplamadan önce ve sonra işlem yapılmış iki durum üzerine çalışılırken, yüzey enerjisi ve damlacık temas açısı dahil olmak üzere yüzey topografyalarının bazı özellikleri incelenmiştir. Bir başka görev olarak, 1.02 Bar'lık sabit buhar basıncında, kaplama yapılmamış her bir numuneye ait mevcut çalışmanın analitik sonuçları ile diğer yazarların deney sonuçlarını karşılaştırmak olmuştur. Son görev olarak ise, çeşitli buhar basınçlarında farklı topografiler ve ıslatmalar (hidrofobik yüzey) ile dikey bir yüzey üzerindeki yoğunlaşma olayını gözlemlemek için IPTES silan kaplama uygulanmıştır.

Günümüzdeki iletim ve konveksiyon yoluyla çalışan geleneksel termal yönetim sistemleri yüksek miktarda atık ısı ürettiklerinde yeterli kalmamaktadır. Sıkıca paketlenmiş çift taraflı PCB'ler ve yüksek güçlü LED'ler, cihaz arızalarına yol

açabilecek, istenmeyen bölgesel ısı üretirken, bu gibi termal sorunların örnekleri olarak düşünülebilir. Sistem güvenilirliğini sağlamak için ise daha etkili yeni soğutma tekniklerinin geliştirilmesi gerekmektedir. Bu sebeple, ısı borusu-gömülü PCB ile özel bir çalışma gerçekleştirilmiştir. Ayrıca, yerel sıcaklık dağılımını belirlemek ve analitik ve deney sonuçlarını doğrulamak için bir dizi sayısal model geliştirilmiştir. Sonuçlar, ısı borusunun düzleştirildiği ve bilinen iletkenliklere sahip plakaların içine gömüldüğü zaman, yayılma direncinin etkili ısı yayılmasına bağlı olarak önemli ölçüde düştüğünü göstermektedir. Her bir duruma özgü termal dirençler de polimer veya alüminyumdan yapılmış bir PCB'nin geleneksel soğutması ile karşılaştırılmıştır. Önerilen soğutma metodu, toplam direncin yaklaşık %50 oranında azaldığını göstermektedir. Ayrıca, yoğunlaşma deneyleri sırasında yeni yüzeylere ait özellikler bir başka görev olarak incelenmiştir. Hidrofobik yüzeyler, sıvı-katı temas açısının kontrol edilmesiyle sıvı geçirmezliğini arttırmak için yaygın olarak kullanılan yeni yüzeylerden bazılarıdır. Bu mikro-nano dokulu yüzeyler, aşındırma, elektrospınleme ve kimyasal buhar biriktirme gibi gelişmiş üretim teknolojileri ve yöntemleri kullanılarak imal edilir. Bu yüzeyler, bir malzemenin dış etkilerden korunması ve birikimden kaçınılması gibi çeşitli amaçlar için kullanılabilirken, aynı zamanda ısı transfer mekanizmalarını geliştirdiği de kabul edilmektedir. Bu sebeple, mikro-nano dokulu yüzeylerin sıvı ıslatma olayı üzerindeki etkisini araştırmak için bir dizi deneysel ve analitik çalışma yapılmıştır. Sıvı-duvar etkileşimi, damlacık oluşumu için anahtar bir parametre olduğundan, sıvı ıslatma olayının bir ısı borusu kondansatörünün ısı transfer performansı üzerindeki etkisi de bu çalışmanın bir başka ilgi alanı olarak incelenmiştir. Bu amaçla, mikro ölçekli farklı yüzey topoğrafyalarına sahip bakır numuneler daldırma ve sprey kaplama teknikleri kullanılarak kimyasal arıtma işlemine tabi tutulmuştur. Ultra-ever dry ile

kaplamadan önce ve sonra, kullanılacak yüzeylerdeki damlacık temas açısındaki farkı belirlemek için iyonsuzlaştırılmış su ile ölçümler yapılmıştır. Analitik çalışmada, temas açıları ve yüzey enerjilerini tahmin etmek için literatürdeki mevcut analitik korelasyonlar ile kapiler Laplace denklemi kullanılmıştır. Sonuçlar, kaplanmış kare oluklu yüzeyin, v-oluklu yüzeye göre %4.6 oranında daha büyük bir ortalama temas açısına sahip olduğunu açıkça göstermektedir. Süper hidrofobik yüzeyin işlenmemiş yüzeylere kıyasla yoğuşma ısı transfer hızı üzerindeki etkisi de araştırılmış ve bu görevde açıklanmıştır. Bu nedenle, su buharı soğutulmuş, nano kaplı mikro yapılı bakır substratlar üzerinde yoğunlaşırken sıvı taşınması ve ısı aktarımı üzerine deneysel araştırmalar genel bir düzenekte gerçekleştirilmiştir. İki tip yüzey kullanılmıştır: referans yüzey olarak yapılandırılmamış bir örnek ve uzunlamasına yönelimli kare geometrilik mikro yapılara sahip bir örnek. İlk deney seti, nano parçacıkların kaplanmadığı mikro-yapılı yüzeyler ile gerçekleştirilirken, diğer ölçümler, mikro-yapıları nano partiküller ile ticari olarak temin edilebilen bir karışım Ultra-ever dry kullanılarak sprey kaplama yapıldıktan sonra gerçekleştirilmiştir. Son olarak, yüzey sıcaklığı, ısı akısı ve ısı transfer katsayısı karşılaştırılarak farklı bir yüzey topografyasının etkisi incelenmiştir. Genel olarak, ısı transferi katsayısının sıcaklık farkı ($T_{v, ch} - T_s$) arttıkça tüm yüzeylerde düştüğü görülmüştür. Ayrıca, yüzeylerdeki mikro olukların ısı transferi katsayısı ve ısı akışında önemli bir artışa neden olmadıkları ve yapısal olmayan yüzeyde benzer bir davranış sergiledikleri anlaşılmaktadır. Spesifik olarak, yüzey kaplamalı numuneler kaplanmamış numunelere kıyasla daha düşük ısı transferi katsayısı değerlerini göstermektedir. Bir başka görevde ise, mikro yapılı yüzeyler üzerinde damlalı ve filmlilik modları sırasında yoğuşma olayının temellerini anlamak ve 1.02 Bar'da farklı topografyalı işlenmemiş yüzeylerdeki yoğuşma

süreçlerinin deneysel doğrulamasına odaklanılmıştır. Yoğuşma için analitik hesaplamalar ve deneyler, dikey olarak hizalanmış bakır substratlarda gerçekleştirilmiştir. Üç farklı yüzey topografyasının, buharın doyma basıncı ve soğutma sıvısının giriş sıcaklığı gibi çeşitli çalışma parametreleri altında yoğuşma işlemi üzerindeki etkisini gözlemek için bir deney düzeneği kullanılmıştır. Yapılandırılmamış bir yüzeyde ölçülen deneysel ısı transfer katsayıları, V-oluklar ve kare oluklara sahip işlenmiş yüzeylerden sırasıyla %30 ve %7.2 oranında daha yüksek bulunmuştur.

Ayrıca, bir buhar odası içindeki buhar basıncının, çeşitli yüzey topografileri ve ıslanma (hidrofobiklik) koşullarında yoğuşma üzerine etkisi incelenmiştir. Hidrofobik yüzey, damlacık temas açısı arttıkça güçlü bir damlalı yoğuşma geçişine neden olduğu için perfluoro-silan kaplama uygulanarak bir daldırmalı kaplama prosesinde hazırlanmıştır. Bu çalışmada, buhar basıncının, hem yapısal olmayan hem de mikro yapıları yüzeyleri içeren işlem görmemiş ve işlenmiş yüzeylerdeki damlacık filmleri yoğuşmaya etkileri çeşitli Reynolds sayılarında gözlemlenmiştir. Tüm yüzeylerdeki deneysel sonuçlar, kaplama sonucu damla temas açısında bir artışın elde edildiğini göstermektedir. Sonuç olarak, kaplama uygulandıktan sonra, diğer örnekler ile karşılaştırıldığında, en büyük damlacık temas açısı ($130.9^{\circ} \pm 2.0^{\circ}$) mikroyapılı kare oluk yüzeyinde elde edilmiştir. Son olarak, gömülü ısı borusunun ısı direncinin, konvansiyonel ısı borusunun termik direncinden daha düşük olduğu görülmüş ve etkin ısı iletkenliğinin gömülü ısı borusunun ısı borusu eğim açısına göre değişimi araştırılmıştır. Eğim açısı -90° den 90° ye değiştirildiğinde, maksimum ısı akışındaki (76 W/cm^2) etkin ısı iletkenliği %68.7 oranında artmaktadır. Ayrıca, yoğuşma testlerinde Ultra-ever dry kaplamanın uygulanabilirliği sorgulanmıştır. Ultra-ever dry kaplamanın, süper-hidrofobik yüzey

üzerinde 165°'den fazla büyük bir temas açısı sağlamasına rağmen yüksek sıcaklık gradyanlarında uygulanamaması sebebiyle yoğuşma testleri için uygun bir kaplama tekniği olmadığı tespit edilmiştir. Diğer taraftan, yapılandırılmamış yüzey yoğuşma ısı transferinde mikro yapılardan daha iyi bir iyileştirme sağlamaktadır. Yoğuşma ısı katsayısı ise tüm yüzeylerde buhar basıncındaki artışla beraber yükselmektedir.



ACKNOWLEDGEMENTS

First, I would like to extend my sincere appreciation for my advisors, Prof. Dr. Mehmet Arık, and Asst. Prof. Dr. Mete Budakli for giving me the opportunity to carry out this study under their supervision and who with their professionalism, they advised me during the whole process of my Ph.D. and offered constructive criticism and help.

I would also like to extend my gratitude to my committee members: Asst. Prof. Dr. Özgür Ertunç, Asst. Prof. Dr. Zeynep Başaran, Asst. Prof. Dr. Zafer Gemici and Asst. Prof. Dr. Bahar Basim for their advice during my research and also to Prof. Dr. Yusuf Menceloğlu for his guidance and hospitality during my short visit at Sabanci University.

Next, I would like to thank my family and my wife for always encouraging me to pursue my interests and for making that pursuit possible. I truly lack words to express how grateful I am for all the sacrifices your made.

I am also grateful to all of my colleagues at EVATEG and ARTgroup. Specially, I appreciate all the technical discussions. I have benefited a great deal from our individual meetings and your technical expertise. I would like to thank Mr. Barca Donmez from Sabanci University for helping me to prepare my samples.

Partial funding for this project was provided by the Turkish Ministry of Science and Technology under the grant number 1464.STZ.2012-2. This work was also supported by the Istanbul Development Agency under the contract number ISTKABIL26 and ISTKATR10/15/YNK/0029 especially for EVATEG infrastructure. I am thankful to FARBA Corporation for their support in building the experimental setup. The Scientific and Technological Research Council of Turkey (TÜBİTAK), co-funded by Marie Curie Actions under FP7 in the framework of the research Grant No. 116C027.

Thank you all.

TABLE OF CONTENTS

ABSTRACT	IV
ÖZETÇE	IX
ACKNOWLEDGEMENTS	XIV
LIST OF TABLES	XIX
LIST OF FIGURES	XXI
NOMENCLATURE	XXIX
1 INTRODUCTION	1
1.1 Motivation	1
1.1.1 Heat Pipe Technology	2
1.1.2 Physics of Surface Wettability	3
1.1.3 Phase Change Heat Transfer -Condensation Phenomena	4
1.2 Description of the Problem	4
1.2.1 Introduction	5
1.2.2 LHP and CHP Limits	6
1.2.3 Condenser Limit	7
1.3 Outline of Thesis	8
2 LITERATURE REVIEW	11
2.1 The Objectives of the Thesis	29
3 HEAT PIPE TECHNOLOGY	30
3.1 Experimental Setup for Heat Pipe Measurements	30
3.1.1 Heat Pipe Embedded Inside a Board	33
3.2 Numerical and Computational Analysis of Heat Pipe	35
3.2.1 Thermal Resistance Network of a Heat Pipe	37

	3.3 Results and Discussions.....	40
4	CONDENSATION EXPERIMENTS	51
	4.1 Basic Concept of Experimental setup.....	51
	4.2 Microstructured Surfaces.....	52
	4.3 Fabrication of Hydrophobic Surfaces	53
	4.3.1 Fabrication of Hydrophobic Coating over Copper Surfaces	54
	4.3.2 Application of Hydrophobic Coating for Unstructured Surfaces	56
	4.3.3 Application of Hydrophobic Coating for Micro-Structured Surfaces	57
	4.4 Fabrication of Superhydrophobic Surfaces	58
	4.4.1 Application of Superhydrophobic Coating for Various Surfaces	59
	4.4.2 Surface Coating Method	60
	4.5 Experimental Details for Surface Energy Analysis	63
	4.5.1 Contact Angle Measurement Procedure	64
	4.6 Experimental Parameters.....	65
	4.7 Heat and Mass Transfer Analysis.....	68
5	THEORETICAL STUDY	73
	5.1 Droplet Contact Angle.....	73
	5.2 Surface Free Energy Analysis.....	75
	5.3 Analytical Calculations of Untreated Condensation Surface.....	76
	5.3.1 Heat Transfer Analysis	76
	5.3.2 Analytical Analysis.....	78
	5.3.3 Experimental Uncertainty	82
	5.3.4 Development of Heat Transfer Correlation	84
	5.3.5 Heat Transfer Parameters of the Condensation	89

5.3.6	Thermocouple Calibration	92
5.4	<i>Computational Analysis of Condensation</i>	93
6	RESULTS AND DISCUSSIONS	97
6.1	<i>Micro-Textured Surfaces and Wetting Phenomena.....</i>	97
6.1.1	Superhydrophobicity over Microstructured Surfaces	97
6.1.2	Influence of Superhydrophobicity over Heat Transfer Parameters	105
6.2	<i>Condensation Heat Transfer and Wettability Characteristics at Uncoated Substrates.....</i>	108
6.2.1	Unstructured Surface	109
6.2.2	Square Grooved Surface	111
6.2.3	V- Grooved Surface	114
6.2.4	Comparison: Unstructured, Square-grooved and V-grooved Surfaces ..	117
6.3	<i>Condensation on Hydrophobic Surfaces.....</i>	120
6.3.1	Unstructured Surfaces.....	122
6.3.2	Square-grooved Surface.....	127
6.3.3	V- Grooved Surface	133
6.3.4	Comparison: Unstructured, Square-grooved and V-grooved Surfaces ..	138
6.4	<i>High-Speed Image Analysis</i>	144
6.4.1	High-Speed Image Analysis for Untreated Surfaces	145
6.4.2	Image Analysis for Unstructured Surface with Different Wettability	146
6.4.3	High Speed Data Analysis with Different Wettability	148
6.5	<i>Comparison with Literature and Developed Correlation.....</i>	149
6.5.1	Unstructured Surface	150
6.5.2	Square-grooved Surface.....	157
6.5.3	V- Grooved Surface	162

7	SUMMARY AND FUTURE WORK.....	167
	<i>7.1 Summary and Conclusions</i>	167
	<i>7.2 Recommendations for Future Work</i>	172
8	REFERENCES	177
	APPENDIX A	190
	A.1 Literture Summary	190
	APPENDIX B	191
	B.1 Optical Window Optimization.....	191
	B.2 Heatsink Design	193
	B.3 Measurement Technique and Instrumentation	194
	APPENDIX C	205
	C.1 Analysis of Uncertainty for independent Parameters.....	205
	C.2 Uncertainty Estimation of Thermocouples	206
	LIST OF PUBLICATIONS	209
	BIBLIOGRAPHY	211

LIST OF TABLES

Table 1-1: The design limitation of mini flat loop heat pipe [4]	6
Table 3-1: Analytical and experimental results for heat pipe performance test	38
Table 4-1: Droplet contact angles prior to and after coating for different velocities	61
Table 4-2: Droplet contact angle before and after coating for various coating layers...	62
Table 4-3: Droplet contact angle at unstructured surfaces after heat treatment	63
Table 4-4: Design of experiments (DOE)	66
Table 5-1: Constants and R^2 values of the developed correlations for the heat flux, HTC, and Nu number for unstructured, square-grooved and V-grooved samples	85
Table 5-2: List of uncertainty values of the condensation heat transfer mechanism at the velocity of chiller range from 100 to 3300 rpm	87
Table 5-3: Experimental uncertainties for all independent and dependent parameters .	88
Table 5-4: Experimental parameters and the boundary conditions of DFWC condensation for untreated surfaces	90
Table 5-5: Comparison between numerical and experimental results of an unstructured surface at a constant liquid flow rate	96
Table A-1: The summary table of literatures review	190
Table B-1: The optical glass transmission	193
Table B-2: The optical glass thickness calculation by EES program	193
Table B-3: The heatsink specification	194
Table B-4: The specification of all measurement devices	202

Table C-1: The instrument error of measurements devices 207

Table C-2: The uncertainty calculation procedure for curving-fitting temperature 208



LIST OF FIGURES

Figure 1-1: Illustration the types of wetting surfaces; A) Superhydrophobic, B) Hydrophobic, C) Hydrophilic, D) Superhydrophilic	4
Figure 1-2: Moore’s law for power consumption of miniaturized electronics with high performance [3].....	5
Figure 1-3: The operating limits of a heat pipe [7].....	7
Figure 1-4: Schematic diagram for the outlined thesis methodology	9
Figure 3-1: Schematic of the test system (a) setup, and (b) thermocouple locations	31
Figure 3-2: Fine porous surface image obtained using a high-resolution microscope ..	33
Figure 3-3: (a) Embedded heat pipes in a polymer and an aluminum plate, (b) Temperature distribution.....	34
Figure 3-4: Schematic view of a heat pipe [63].....	35
Figure 3-5: Computational model of current experimental setup[71].....	39
Figure 3-6: Temperature difference sensitivity of heat pipe to mesh elements.....	40
Figure 3-7: The schematic diagram of the heat pipe with different angle of inclination	41
Figure 3-8: System validation with experimental study from literature for varying orientation angles [13]	42
Figure 3-9: Variation of temperature difference from (a) analytical results and (b) experimental results at different input power with different orientation of heat pipe	43
Figure 3-10: Variation of the total thermal resistance from (a) analytical results and (b) experimental results at different input power with different orientation of heat pipe	45

Figure 3-11: Impact of the pressure difference over temperature difference (a) analytical results and (b) experimental results at different orientations.....	46
Figure 3-12: Teflon plate with a single heat pipe at the same heat removal condition (a) IR image and (b) Temperature contours obtained in MATLAB.....	48
Figure 3-13: Aluminum based substrate with a single heat pipe at the same heat removal condition (a) IR image and (b) Temperature contours obtained in MATLAB.	49
Figure 3-14: Comparison of heat pipe embedded and unembedded cases in a plate (a) Timewise variation and (b) IR images	50
Figure 4-1: Schematic diagram of the axial grooves on the inner wall of heat pipe [75]	52
Figure 4-2: Longitudinal square-grooved surface: a) top view b) 4X view c) cross-sectional view	52
Figure 4-3: Longitudinal v-grooved surface: a) top view b) 4X view c) cross-sectional view.....	53
Figure 4-4: Overview of the chemical reaction of IPTES+PFA with the addition of Dibutyltin dilaurate (DBDU).	54
Figure 4-5: FT-IR image of IPTES silane	55
Figure 4-6: FT-IR comparison IPTES silane vs. fluorinated silane compound	56
Figure 4-7: Microscopic images of the unstructured surface after coating procedure with IPTES SILANE: a) top view, b) 50x view c) 100x view d) cross-section at the solid-ambient interface	56
Figure 4-8: Microscopic images of the square groove surface after coating procedure with IPTES SILANE: a) top view, b) 50X view c) 100X view d) cross section at the solid-ambient interface	57

Figure 4-9: Microscopic images of the V- grooved surface after coating procedure with IPTES SILANE: a) Top view, b) 50X view c) 100X view d) Cross-section at the solid-ambient interface.....	57
Figure 4-10: Dip coating technique: a) desktop dip coating device (PTL-MMB01) with immersion equipment (1 - 200 mm/min) b) sample holder c) beaker inside dip coating chamber d) Area covered by coating and fixation	59
Figure 4-11: Microscopic images of the unstructured surface after coating procedure with Ultra-Ever Dry: a) top view, b) 50x view c) 100x view d) cross-section at solid-ambient interface.....	60
Figure 4-12: Microscopic images of the square-grooved surface after coating procedure with Ultra-Ever Dry: a) top view, b) 50x view c) 100x view d) cross-section at solid-ambient interface.....	60
Figure 4-13: Microscopic images of the V-grooved surface after coating procedure with Ultra-Ever Dry: a) top view, b) 50x view c) 100x view d) cross-section at solid-ambient interface	60
Figure 4-14: Locations of sessile droplets during contact angle measurements	64
Figure 4-15: Experimental setup [83].....	67
Figure 4-16: a) Position of the embedded thermocouples in copper samples, b) Cross-sectional view of the condensation chamber and the liquid chamber.....	69
Figure 4-17: Deviation of wall temperatures measured inside the uncoated copper block vs. subcooling temperature $T_{v, ch} - T_s$ for planes x_a (a) and x_b (b).....	71
Figure 5-1: Definition of contact angles, apparent or measured contact angle on a rough (Wenzel) surface θ_W , Cassie-Baxter contact angle θ_{CB}	74
Figure 5-2: Droplet contact angle ($\theta_{CL}/2$) on uncoated, polished surface	76
Figure 5-3: Schematic diagram of the analytical approach	78

Figure 5-4: Schematic diagram for the heat transfer analysis of finned copper (unstructured/microstructured) substrates: a) side view, b) view from the back.....	79
Figure 5-5: Schematic diagram for calculating the experimental uncertainties	92
Figure 5-6: The schematic diagram of the heat sink.....	93
Figure 5-7: Mesh structure.....	94
Figure 5-8: Mesh sensitivity analysis	94
Figure 5-9: Temperature distribution over the heat sink for unstructured surfaces	95
Figure 5-10: Velocity distribution inside the cooling chamber	95
Figure 6-1: Liquid droplet profile at different times at the center position of each surface: (a) untreated surface, (b) coated surface	99
Figure 6-2: High-speed image sequences of droplet propagating on the superhydrophobic unstructured surface: a) Center position, b) Edge- 4 position	100
Figure 6-3: Variation of the average droplet contact angle at five positions on the unstructured superhydrophobic surface by ultra-ever dry coating compared with an untreated surface	101
Figure 6-4: Variation of the average droplet contact angle at five positions on the V-grooved superhydrophobic surface by ultra-ever dry coating compared with an untreated surface	101
Figure 6-5: Variation of the average droplet contact angle at five positions on the square grooved superhydrophobic surface by Ultra-Ever Dry coating compared with an untreated surface	102
Figure 6-6: Free surface energy for (A) Cassie-Baxter contact angle theta (B) Wenzel contact angle theta for all samples after coating compared with the results [16].....	104

Figure 6-7: Effect of the Young contact angle on the Cassie-Baxter contact angle for all samples after coating process compared with the results [16].....	105
Figure 6-8: HTC at varying $T_{v, ch} - T_s$ for uncoated/coated UED unstructured and square-grooved surfaces at $p_{v, ch}=1.02$ Bar	106
Figure 6-9: Comparison of surface temperatures for uncoated/coated UED of unstructured and square-grooved surfaces at $p_{v, ch}=1.02$ Bar with varying MI	107
Figure 6-10: Comparison of heat flux for uncoated/coated UED of unstructured and square-grooved surfaces at $p_{v, ch}=1.02$ Bar with a different subcooling temperature....	108
Figure 6-11: Variation of surface temperature with liquid mass flow rate.....	109
Figure 6-12: Effect of subcooling temperature difference on heat flux	110
Figure 6-13: Variation of heat transfer coefficient with temperature difference.....	111
Figure 6-14: Surface temperature at condensation surface at varying mass flow rate of cooling liquid	112
Figure 6-15: Variation of condensation heat flux versus temperature difference	113
Figure 6-16: Effect of the temperature difference on heat transfer coefficient	114
Figure 6-17: Wall temperatures at condensation surface at different mass flow rates of cooling liquid	115
Figure 6-18: Variation of condensation heat flux with subcooling temperature.....	116
Figure 6-19: Heat transfer coefficient versus subcooling temperature ($T_{v, ch}-T_s$)	117
Figure 6-20: Comparison of (a) surface temperatures and (b) heat fluxes of various surfaces	118
Figure 6-21: Comparison HTC of microstructured surfaces with unstructured surface	119

Figure 6-22: Average droplet contact angle at the hydrophobic condensing surface compared to the untreated surface	121
Figure 6-23: Surface temperature at various vapor pressures.....	123
Figure 6-24: Effect of subcooling temperature difference over condensation heat flux at various vapor pressures.....	124
Figure 6-25: Measured Heat transfer coefficient versus subcooling temperature difference for different vapor pressures.....	126
Figure 6-26: Heat transfer coefficient at various heat fluxes for different vapor pressures.....	127
Figure 6-27: Variation of surface temperature at different vapor pressures.....	128
Figure 6-28: Heat flux versus subcooling temperature ($T_{v,ch}-T_s$) at various $p_{v,ch}$	130
Figure 6-29: Variation of heat transfer coefficient with subcooling temperature difference at different vapor pressures.....	131
Figure 6-30: Variation of heat transfer coefficient with heat flux for different pressures	133
Figure 6-31: Surface temperature at the condensation surface at various mass flow rates	134
Figure 6-32: Variation of heat flux with the temperature difference at various $p_{v,ch}$..	135
Figure 6-33: Variation of Heat transfer coefficient at different vapor pressures	137
Figure 6-34: Variation of HTC with heat flux for different surfaces and vapor pressure	138
Figure 6-35: Variation of HTC with heat flux at 1.02 Bar	139
Figure 6-36: Heat transfer coefficient versus heat flux at 1.10 Bar	141

Figure 6-37: Variation of condensation heat transfer coefficient with heat fluxes at 1.20 Bar.....	142
Figure 6-38: Variation of HTC with heat flux at 1.25 Bar	144
Figure 6-39: Surface wetting phenomena, dropwise condensation at untreated, unstructured and micro-structured surfaces.....	146
Figure 6-40: Surface wetting phenomena during condensation over uncoated and coated surfaces.....	147
Figure 6-41: Surface wetting phenomena during condensation at the uncoated and coated surfaces.....	149
Figure 6-42: Effect of subcooling temperature over heat flux at different pressures ..	151
Figure 6-43: Variation of condensation heat transfer coefficients with subcooling temperature at various pressures.....	152
Figure 6-44: Variation of heat flux with subcooling temperature difference ($T_{v,ch} - T_s$)	153
Figure 6-45: Effect of subcooling temperature over heat transfer coefficient.....	154
Figure 6-46: Variation of Nu number with temperature difference	155
Figure 6-47: Comparison of the experimental results with analytical results of the unstructured surface, a) heat flux and b) heat transfer coefficient.....	156
Figure 6-48: Heat flux versus subcooling temperature difference of square groove surface.....	157
Figure 6-49: Heat transfer coefficient versus Subcooling temperature difference of square groove surface	158
Figure 6-50: Nu number versus subcooling temperature difference of square groove surface.....	159

Figure 6-51: Comparison of experimental results with analytical results of square groove surface, a) heat flux and b) heat transfer coefficient	161
Figure 6-52: Heat flux versus subcooling temperature difference of V-grooved.....	162
Figure 6-53: Effect of subcooling temperature over Heat transfer coefficient of the V-groove surface.....	164
Figure 6-54: Nu number versus temperature difference of V- groove surface.....	165
Figure 6-55: The experimental results versus the analytical results over V- groove surface, a) heat flux and b) heat transfer coefficient.....	166
Figure B-1: Shows the schematic diagram of a circular optical window with two types design are (a) Clamped, St_{max} at edge and (a) Unclamped, St_{max} at center.....	192
Figure B-2: High-speed camera with lamps lights during the condensation test	196
Figure B-3: IR camera during the embedded heat pipe test	197
Figure B-4: The correlation test of pressure transmitter.....	198
Figure B-5: Correlation for the rotameter.....	199
Figure B-6: Calibration test for thermocouples	200
Figure B-7: Show the correlation equation of boiler thermocouple related to the chiller set point temperature.....	200
Figure B-8: Show the correlation equation of chiller flow rate in mm vs chiller pump speed in rpm.....	201
Figure B-9: Show the circuit diagram components of the water level sensor	202
Figure B-10: Shows the photograph of condensation experimental setup with all measurment tools	204

NOMENCLATURE

A	Area, [m ²]
CA	Contact angle, [°]
\overline{CA}	Average contact angle, [°]
CHF	Critical heat flux, [W/m ²]
C _p	Specific heat of water, [kJ/kg-K]
C ₁ , C ₂ , C ₃	Correlation coefficients, [-]
d	diameter, [m]
DR	Droplet radius, [m]
EI	Elastic limits, [Pa]
Fa	Applied force, [N]
g	Gravitational constant (m/s ²)
G	Gibbs free energy, [J]
G ^o	Reference-free energy of the system assuming that the surface and bulk properties of the material are identical, [J]
h	heat transfer coefficient, [W/m ² -K]
\bar{h}	Local Heat transfer coefficient, [W/m ² -K]
H	Droplet height, [m]
HF	Surface heat flux, [kW/m ²]
h _{fg}	latent heat vaporization, [J/kg]
HTC	Heat transfer coefficient, [W/m ² -K]
I	Current, [mA]
k	Permeability, [-]
K	Thermal conductivity, [W/m-K]
Kc	Empirical constant
L	Length, [m]
m _{w,i}	Molar mass of particular component, [g/mol]
\dot{M}	Mass flow rate, (kg/s)
\dot{M}_{out}	Outlet Mass flow rate of liquid-vapour mixture, [g/s]
n _{fin}	Fins number, [-]
p	Absolute pressure, [Bar]
P	Perimeter, [m]
Q	Flow rate, [cm ³ /min]
\dot{Q}	heat transfer rate, [W]
\dot{q}	Heat flux [kW/m ²]
r	radius, [m]
R	Thermal resistance, [°C/W]
r _n	radius of the nucleation (2.54×10 ⁻⁵ - 2.54×10 ⁻⁷), [m]
rr	Roughness ratio, [-]
RU	relative uncertainty, [%]
s	Entropy, [J/K]
SF	Safety Factor
S _{opt}	Optimum fin spacing, [m]
St	Stress, [Pa]
t	Thickness, [m]
T	Absolute temperature, [°C, K]

\bar{T}	Average temperature at the base of the heat sink, [$^{\circ}\text{C}$]
$T_{w,i=1-6}$	Temperatures at the base of the heatsink, [$^{\circ}\text{C}$]
u	Velocity, [m/s]
U	Absolute uncertainty
V	Voltage, [volt]
W	Width, [m]
\bar{x}	average of measuring values
x_1, x_2, \dots, x_n	independent variables
x, y, z	Coordinate axis, [-]
x, x_a, x_b	Distance in x-direction, The planes for detecting the deviations of wall temperatures and the base of heat sink

Dimensionless Groups

f	friction factor, [-]
Nu	Nusselt number, [-]
Pr	Prandtl number, [-]
Ra	Rayleigh number, [-]
Re	Reynolds number, [-]

Greek Symbols

α	Diffusivity, [m^2/s]
β	Heatsink coefficient, [-]
γ	Surface tension, [N/m^2]
Δ	Difference, change in
ε	Emissivity of the surface, [-]
ϵ	Porosity, [-]
θ	Contact angle, [$^{\circ}$]
μ	Dynamic viscosity, [$\text{kg}/\text{m s}$]
ν	Kinematic viscosity, (m^2/s)
ρ	Density, [kg/m^3]
σ	Stefan Boltzmann constant, [N/m]
σ_x	Standard deviations
$\sigma_{\bar{x}}$	Mean standard deviations
\emptyset	Surface angle, (rad)
ψ	Axial angle, [$^{\circ}$]

Subscripts

a	Adiabatic
ad	Advancing
amb	Ambient
Ana	Analytical
avg	Average
$base$	Base of copper block
bo	Boiling
c	Condenser
cap	Capillary
CB	Cassie-Baxter
cc	Current correlation
ch	Chamber

CL	Capillary Laplace
cond	Condensation
corr	Correlation
conv	Convection
cr	Cross section area
cu	Copper
DSS	Data sheet supplier
e	Evaporator
eff	Effective
elec	Electric
en	Entrainment
Exp	Experimental
h	hydrostatic
Hp, hp	Heat pipe
Hy	Hysteresis
i	inner
in	Inlet
int	Interfacial
l	Liquid
lv	Liquid-vapor interface
m	Apparent
max	Maximum
o, out	Outside, Outlet
por	Porous structure
r	Receding
rad	Radiation
s	Surface
sat	Saturation
si	Sintered porous
sl	Solid–liquid interface
So	Sonic
Std	Standard
sub	Subcooling
Surr	surrounding
sv	Solid – vapor interface
T, Temp	Temperature
un	Unfinned surface
v	vapor
W	Wenzel
wi	Wick
Y	Young’s

Abbreviations

abs	Absolute
AFM	Atomic force microscopy
B	Bias error
CaF ₂	Calcium Fluoride
CCD	Charged Coupled Device

ccm	Cubic centimeter per minute (cm ³ /min)
CHP	Conventional heat pipe
CPL	Capillary pumped loops
DAQ	Data acquisition
DFWC	Dropwise-filmwise condensation
DLC	Diamond-like carbon
DOE	Design of experiments
DWC	Dropwise condensation
EDM	Electrical discharge machining or drilling method
EES	Engineering equation solver
FOV	Field of view
EPDM	Ethylene propylene rubber or Diene Monomer
FWC	Film-wise condensation,
HPS	High power supply
HSC	High-speed camera
HY	Hydrophobic
LED	Light emitting diodes
LHP	Loop heat pipe
LPS	Low power supply
M _v	Measured value
n	numbers of measuring values
PCB	printed circuit board
PLD	Pulsed laser deposition
PTFE	Polytethefluoroethylene
P _T	Precision error of temperature
P _x	Precision error
RS	Results
Ref.	Referances
rpm	Revolution per minute
RSS	root-sum-squares
SAM	Self-assembled monolayers
SiO ₂	Silicon oxide
TiO ₂	Titanium dioxide
UED	Ultra Ever Dry, commercially available coating material
ZnO	Zinc oxide

CHAPTER I

INTRODUCTION

1.1 Motivation

Electronics require new thermal management solutions due to technology progression and continuously increasing heat dissipation. Moreover, the cooling becomes more difficult due to the increasing complexity of electronics. While, such needs were giving directions for the current study, the cooling capabilities of heat pipes with different surface structures on the condenser part were the fundamental aim of this thesis. Therefore, to gain a more detailed understanding of the aimed topics a set of mathematical modeling and experimental tests were applied. It is preferred to understand the methods that will be used to solve high power problem:

- HP is a passive system that means it doesn't need extra power even for working with small designs. A HP is also capable of removing undesired high chip thermal powers with high efficiency.
- Effect of the saturation vapor pressure on the condensation heat transfer coefficient by using deionized water.
- Effect of the micro-nanostructured surface on dropwise condensation compared with the unstructured surface. Also, the challenging idea of this study by using liquid coating such as polymer and ultra ever dry is to decrease surface wettability for having hydrophobic and super hydrophobic surfaces. Finally, the hydrophobicity phenomenon is very important to decrease the test surface size with increasing the surface area of heat transfer.
- Determining of the dominant heat transfer mechanisms such as heat transfer coefficient (HTC) and critical heat flux (CHF).

- Developing a new prediction capability through analytical correlation and providing insights through the visualization study.

In addition, condensation phenomena play an important role in engineering and heat transfer process. Drop-film wise condensation DFWC with different wettability surface can be encountered in many technical applications including condenser section, such as power plants, refrigeration, and electronics cooling and heat pipe cycles. A distinction has to be made between drop-wise and film-wise condensation on the vertical plate which is solely driven down due to the gravity effect. Generally, this drop-film wise condensation occurred at saturation conditions existing at the effective surface area. However, they can also condense in unsaturated conditions. The heat transfer depends on the vapor temperature and pressure in the vapor chamber and the condensation surface temperature. To obtain optimal heat transfer rates such as heat transfer coefficient and heat flux, the vapor temperature and the inlet temperature of the cooling liquid has been kept constant at moderate conditions. Thus, high heat transfer rates can be achieved by using drop-film wise condensation with different wall temperatures. This can be additionally supported by the effect of a wetting surface.

1.1.1 Heat Pipe Technology

The dramatic energy consumption has caused many global problems and energy crisis at different places of the world. Important part of the solution for the energy crisis depends on boosting efficiency. Light emitting diodes (LEDs), as an example, are an energy efficient lighting technology that has been invented in early 1970s at General Electric Research Laboratories [1]. On the other hand, solid state lightings in general and LEDs in particular have been proven to improve lighting efficacy in a number of lighting applications such as automotive, indoor and outdoor. Since output light is only

a percentage of the input power to an LED (the rest of power is converted to heat), heat generated in a chip is growing abruptly, leading to high junction temperatures on the chip. The elevated junction temperature requires novel thermal management systems, since high junction temperature leads to lower light extraction, shorter lifetimes and to device destruction. To prevent the junction from overheating and to raise LED rated power, thermal engineers are exploring different techniques to reduce the thermal resistance between the junction and the PCB. Heat pipes are one of the promising thermal management technologies, which have been used for decades in various technical applications. Moreover, heat pipes are potentially useful for avoiding the hot spots on the electronic package by distributing the heat locally generated over the board since it increases the axial heat transfer significantly. Moreover, heat pipes work passively (without any pumping power) using the principle of phase change from liquid to vapor to remove high heat loads, which makes it appropriate for the usage in high-power lighting applications. While heat pipes are so functional for many applications, they are still limited by the condensation heat transfer. Therefore, further research has to be performed to improve effective heat transfer coefficients of heat pipes.

1.1.2 Physics of Surface Wettability

Recent developments of industrial devices have shown that the interaction between a liquid and a wall plays an important role in terms of preventing metal surfaces from corrosion, icing or poor thermal performance [2]. Especially for thermal management, where the formation of liquid droplets is desirable, one of the most important challenging factors for better thermal performance is the controlled surface wettability phenomena. While this phenomenon can be used to evaluate the desired surface properties, it can usually be determined by calculating the surface forces such as

adhesive and cohesive by a liquid droplet residing on the solid surface to demonstrate the wettability easily (see Figure 1-1).

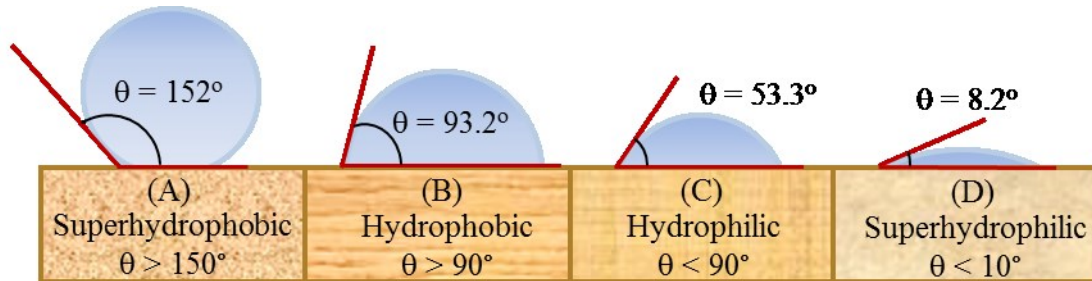


Figure 1-1: Illustration the types of wetting surfaces; A) Superhydrophobic, B) Hydrophobic, C) Hydrophilic, D) Superhydrophilic

1.1.3 Phase Change Heat Transfer -Condensation Phenomena

Developing electronic systems incorporating miniaturized components with increased performance capability causes increase in waste heat dissipation. Thus, system reliability, which depends heavily on components' temperature becomes crucial. Thermal management of electronics becomes a major challenge while guaranteeing a proper and secure operation of systems. Conventional thermal management systems, working with the principles of conduction and convection, cannot meet high waste heat generation requirements. Therefore, new cooling techniques have to be developed in order to ensure system reliability.

1.2 Description of the Problem

Technology has no limits and the speed of technologic innovations has increased dramatically during the last couple of decades. While it is exciting how incredible developments occur in many different fields, these developments also bring out many problems with them and it is again science and scientists that need to resolve all these

issues. Like any other technology, electronic chips have covered a distance with the advancement of the information age. Our age brought shrinkage to all electronic devices and increment to their performances which forces us to build devices and processors in micro scale and gets challenging day by day. It is clear that this high amount of heat must be removed from the system in the condenser region and many different methods of cooling have been innovated through many years (see Figure 1-2) [3]. Finally, a novel way of cooling is used to achieve the higher performances with increasing the convective coefficients of the system that is called dropwise condensation with different wettability phenomena over nano-textured surfaces.

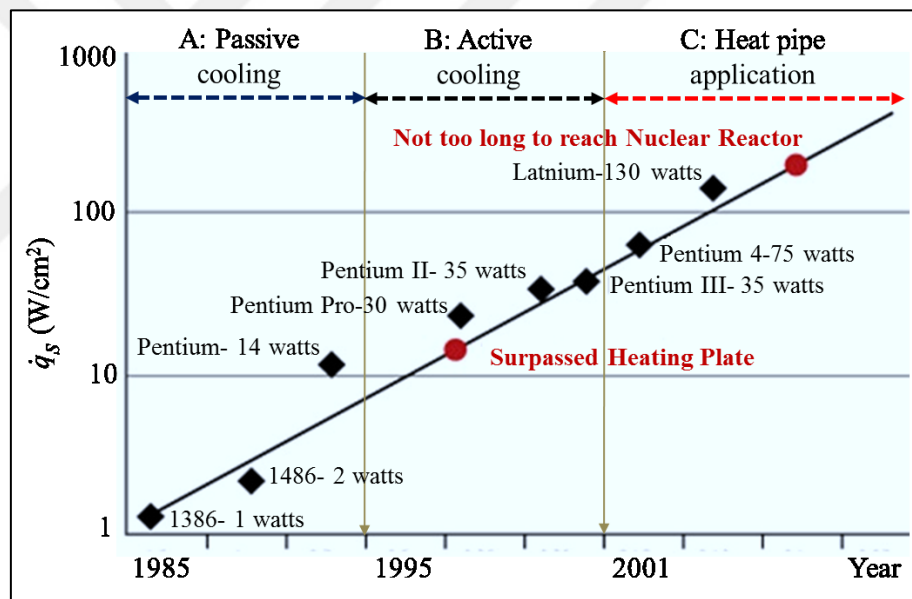


Figure 1-2: Moore's law for power consumption of miniaturized electronics with high performance [3]

1.2.1 Introduction

The electronic components require new thermal management solutions due to the technology advancement and continuously increasing the heat dissipated from the electronic chips (see **Figure 1-2**) [3]. Moreover, electronic systems are becoming more

complex, which makes the case of cooling more difficult. Then, miniature flat loop heat pipe (MFLHP) is a passive device which doesn't need any extra power for working with small design and the phase change phenomena such as (evaporation and condensation process) can be shown as one possible technology. Moreover, working limitations of a heat pipe are the heat transport less than 120 W and the dimensions limit should be less than 500 mm (see Table 1-1).

Table 1-1: The design limitation of mini flat loop heat pipe [4]

Miniature flat loop heat pipe	MFLHP
Capillary evaporator length active zone, [mm]	10-50
Evaporator diameter, [mm]	< 8
Evaporator thickness, [mm]	< 6
Liquid, vapor line diameter, [mm]	< 3
Total length heat transport, [mm]	< 500
heat load, [Watt]	5-120

1.2.2 LHP and CHP Limits

A loop heat pipe is subjected to several limitations related to physical phenomena involved during its operation, as well as to its operating specifications. These limitations have magnitudes and characteristics different from those of conventional heat pipes. There are several parameters that affect LHP and sometimes CHP such as capillary limit, sonic limit, entrainment limit, boiling limit and condenser limit. In general, more concern is given for increasing the heat pipe performance by increasing the evaporation and condensation efficiency such as droplet formation on the condensation chamber [5]. In the current research we are focusing on the condenser limit to extend the heat transfer performance beyond current levels.

1.2.3 Condenser Limit

The condensation heat transfer is maintained by natural convection inside a water tank, which absorbs the heat dissipation from a heat pipe. At steady state, the heat rejection rate in the condenser must be equal to the heat addition rate in the evaporator. Typically, the condenser coupling is either by convection and/or radiation. The main parameters that have impact on the condenser part are the condenser surface area, emissivity and operating temperature. In this case, the heat transfer from condenser, assuming a constant condenser temperature, is determined from [6].

$$\dot{Q}_c = \dot{Q}_{conv} + \dot{Q}_{rad} = hA(T_c - T_{amb}) + \epsilon A_s \sigma (T_c^4 - T_{surr}^4) \quad (1-1)$$

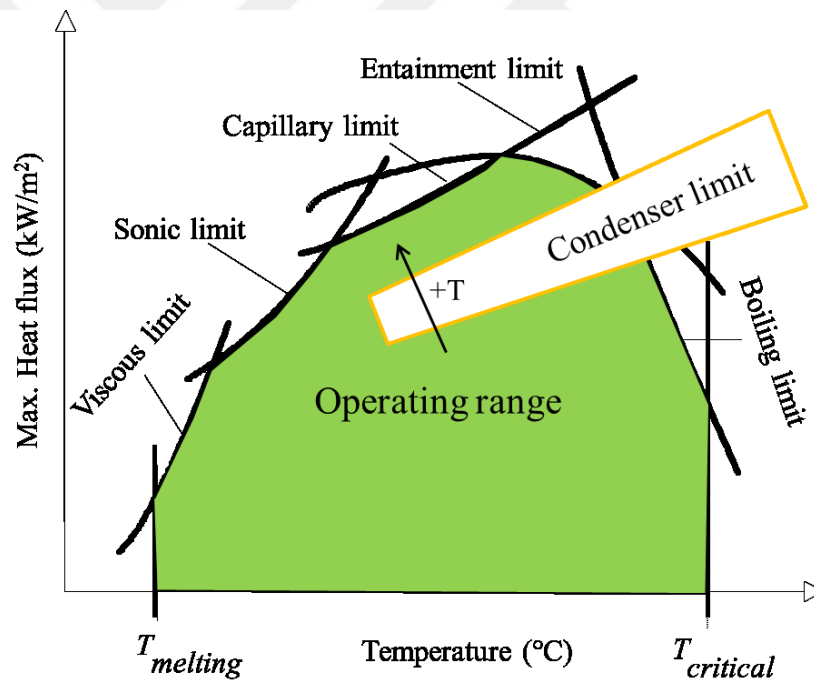


Figure 1-3: The operating limits of a heat pipe [7]

The main problem of the condenser is the condensation type especially the liquid film condensation that led more restriction in heat transfer with the increase in thermal

resistance between vapor and wall surface. The limiting of the condenser section (see Figure 1-3) can be solved by rising the condensation heat transfer coefficient.

The solution of this problem can be done in two steps. While the first step is performed by increasing the heat transfer surface area by using microstructured surface, the second step is achieved by decreasing the surface wetting (hydrophobicity phenomena) due to texturing that led to less thermal resistance to condensation heat transfer.

1.3 Outline of Thesis

The greatest advantage of the proposed idea in the current study is that the heat pipe technology removes the exceeded heat effectively and naturally. Moreover, the performance of this technology is limited due to condensation heat transfer coefficient. To augment heat transfer at various operating vapor pressure, with increasing the condensation surface area by using different microstructured grooved surfaces are studied. Furthermore, the experimental study is extended to show the effect of active surface coating for changing the surface wettability to have hydrophobic and super-hydrophobic surfaces by using IPTES silane and Ultra-ever-dry liquids respectively. The methodology of the thesis is displayed as a schematic diagram (see Figure 1-4), which demonstrates the outline of the current thesis with all tasks calculations during the main topic of condensation phenomena.

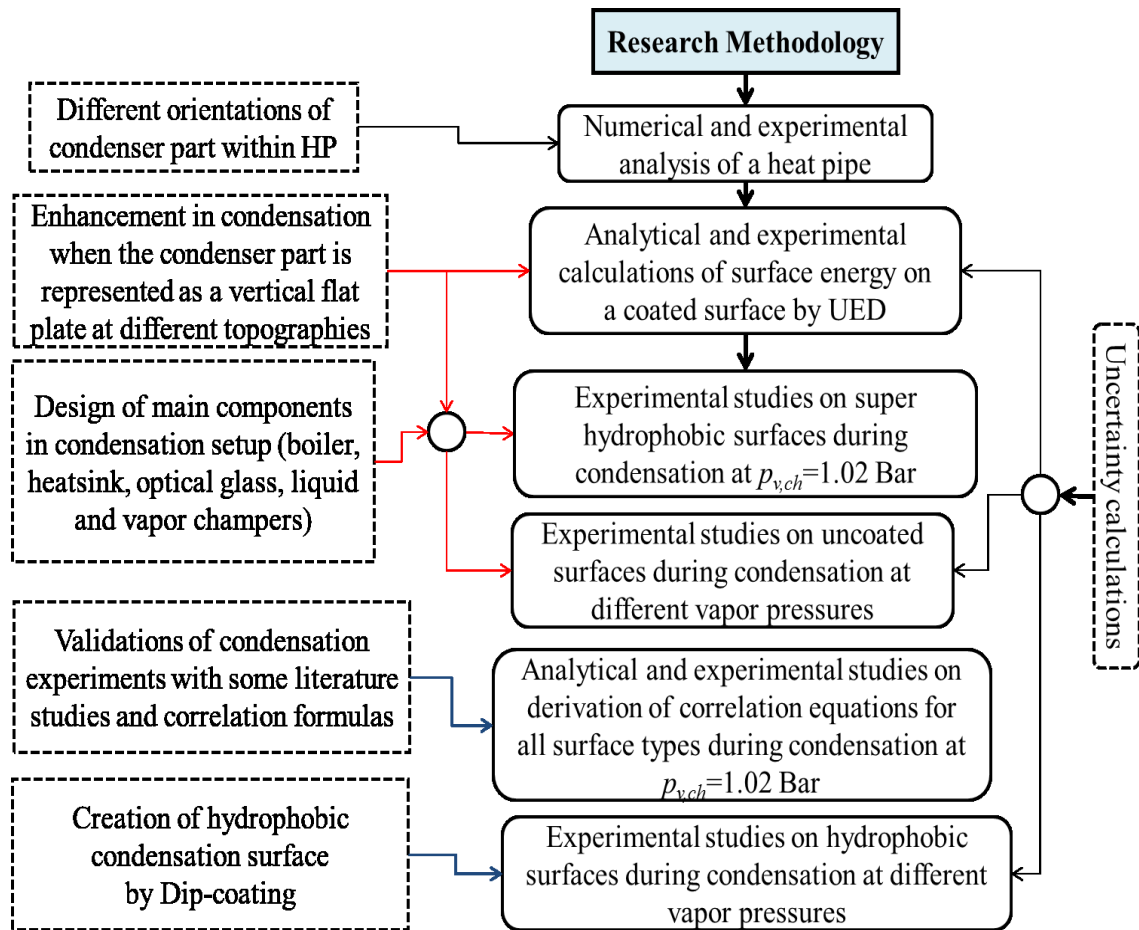


Figure 1-4: Schematic diagram for the outlined thesis methodology

The first chapter of thesis, Chapter 1, starts with some specific studies on industrial applications of condensation process. The required conditions for condensation process and the effect of various parameters on condensation phenomena are briefly described in two-phase flow over the vertical plate composed of different surface structures in the condenser part of the heat pipe. Chapter 2 presents the literature review of the current thermal management technologies, their progress over the years and the scope of these approaches in dropwise condensation at different topography and wetting surfaces. To address and enhance one of the effective thermal solutions, Chapter 3 was dedicated to theoretical and experimental studies of conventional and embedded heat pipe systems. The results of these heat pipe systems at different orientations are given and discussed.

In Chapter 4, general methodology of the experimental study is further expanded. Experimental parameters and the measurement technique are explained in detail. Related manufacturing processes for the fabrication of hydrophobic and superhydrophobic surfaces with surface coating are discussed. In addition, experimental studies are realized for droplet contact angle measurements at different topographies and wetting surfaces during the drop-film wise condensation over the vertical plate.

The following chapter, Chapter 5, contains theoretical studies such as numerical and computational analysis of the condensation surface, correlation derivations of heat transfer coefficients using surface energy analysis of the condensation surface. Data analysis of the condensation heat transfer is also conducted in this chapter for the uncertainty analysis. In addition, Chapter 6 investigates the influence of hydrophobicity phenomena on surface energy and the condensation heat transfer mechanism at different saturation pressures. Results are validated by comparing literature with in-house developed correlations. These results are discussed by considering the impact of the surface topographies and wettings on the condensation process at different saturation pressures. The analysis of the hydrodynamic phenomena during the condensation process over the active surface is also explained in this chapter. In the final chapter, Chapter 7, the summary, conclusions and future work are presented to the reader's attention. APPENDIX A, APPENDIX B, and APPENDIX C are also added at the end of the thesis to present the summary table of literature review, optical glass and heat sink models, measurement instrumentation and the uncertainty analysis of independent parameters and thermocouples.

CHAPTER II

LITERATURE REVIEW

A candidate cooling technology for electronics can be obtained by reducing the size while raising the heat flux. The resulting heat generation with smaller electronic packages has caused to decrease the reliability of the passive cooling system and this necessitates the development of new technologies with higher performance for effective removal of the produced heat [8]. While the convection heat transfer is one of the heat transfer mechanism that can be experienced over a heat sink and a heat pipe [9], heat transfer by phase change as in heat pipes is more efficient mechanism for heat dissipation. Moreover, for having a heat pipe with a high effective thermal conductivity, the condenser part has been chosen for enhancing the condensation heat transfer coefficient in the current study. This enhancement is achieved by using two approaches, which are microstructured surfaces to increase the condensation surface and surface wetting to increase the droplet contact angle that can lead to an increase in the heat transfer coefficient.

Heat pipe technology - There are a number of studies in the literature that show the performance of heat pipes. While Pounds et. al [1] has shown a heat pipe embedded in a metal core printed circuit as capable of high heat flux applications in their conceptual study, an experimental study about micro heat pipes at different orientation was done by Moon et al. [10]. In this study, micro heat pipes with polygonal cross-section were manufactured and tested for operating characteristics and heat transfer limits. Micro heat pipes had a triangular and rectangular cross section with curved sides. In the experiments, a vacuum chamber was used and the test was performed for operating temperatures of 60°C to 90°C. It was found that the heat transfer limit of a triangular

micro heat pipe was 1.6 times larger than the rectangular heat pipe. Moreover, Kucuk [11] studied an analytical 1-D heat-pipe model which was compared with a computer code to analyze parameters effecting on the heat transfer performance of a heat pipe. Water, Ammonia and Mercury are investigated as working fluids for different operating temperatures. Results showed maximum heat transfer capacities for all three heat pipe working fluids. Also, water as a working fluid provides the maximum heat transfer capacity for the temperature range of 280 K – 373 K. Therefore, water observed as the best working fluid than Ammonia and Mercury under the room temperature applications. In another study, heat-pipe-embedded plates which are made of aluminum silicon carbide were studied by Weyant et al. [12]. They made a comparison using different plate material such as AlSiC, copper and Aluminum. The experimental results showed that embedding heat pipes into AlSiC plates reduced the temperature gradient more than 50% in comparison to plain AlSiC plate, with improving the effective thermal conductivity in the range of 417 W/m-K to 492 W/m-K. A performance comparison of heat-pipes in different inclination angles is presented by Loh et al. [13]. An experimental setup was prepared and three heat-pipe wick structures (sintered powder metal, grooves and mesh) for various inclination angles (-90° to $+90^\circ$) were examined. The study has reported that heat source orientation and gravity had less effect on sintered metal powder heat pipes due to the fact that the sintered powder metal wick had the strongest capillary action compared to groove or mesh wick structures. The experimental results showed that the heat pipe with groove had better thermal performance than mesh and sintered powder metal with the different orientations from $+90^\circ$ to 0° due to that the gravity becomes more effective to the horizontal orientation (0°). On the other hand, the sintered wick structure gave the highest performance than the other wicks at the heat pipe orientated from 0° to -90° when the evaporator part at

the top location. It was also shown that by increasing tilt angle of the evaporator, from horizontal to the vertical position ($+90^\circ$), the thermal performance of all heat pipes decreased.

Surface wettability - There is a significant number of experimental and numerical publications reported in the past decades that are concentrating on the manufacturing methods, chemical durability, mechanical and thermal resistivity of hydrophobic and hydrophilic surfaces.

The hydrophilic effects over a non-uniform condenser surface was studied by Pulipaka [14], who has focused on the effects of hydrophilicity on droplet condensation and the growth rate of the droplets. This study shows that the droplet growth rate and droplet condensation on the hydrophobic surface is lower than at a hydrophilic surface. Finally, when the droplet contact angle decreases, it has decreased the initiation nucleation time. Wettability of nanostructured surfaces was studied by Duta et al. [15]. A pulsed laser deposition process has been used to change the wettability of nanostructured surfaces by changing the hydrophilic surface to hydrophobic surface. In addition, they developed correlations for three major conditions of droplet-surface interaction such as Young, Cassie, and Wenzel for wetting phenomena. For the experimental part materials such as ZnO, SiO₂, TiO₂, and DLC were used as nanostructures to achieve hydrophobic or hydrophilic surfaces behavior. The experimental results showed more improvement on the wettability of nanostructured surfaces, especially by using PLD method that can give some advantages such as thermal evaporation, enhanced the chemical vapor deposition and more helpful of improved the characteristics of a number of applications. On the other hand, super-hydrophobic and amphiphilic nanostructured surfaces were also used to investigate the condensation phenomena that was studied experimentally and theoretically by Anderson [16] who has used a new experimental technique to

manufacture nanostructured amphiphilic surfaces combining hydrophilic and hydrophobic properties. In this study, the super-hydrophobic surface is determined by two parameters, which are the droplet contact area and low surface energy. An analytical study was done by using the free surface energy model that can be validated by predicting the droplet contact angles for each method of Wenzel and Cassie-Baxter model. Consequently, theoretical results showed when a nanowire length increases from 200 to 250 nm, it caused an increase on the surface roughness from 2.7 to 3.16 and again Wenzel angle from 146.5° to 167.3° , while the Cassie Baxter angle remained constant (157.7°).

Moreover, Wenzel [17] enhanced the surface wettability by forming roughness on the surface of samples. He found that the droplet contact angle thus the wetting properties are directly proportional to the surface roughness.

Furthermore, Lichao and Thomas identified that it was not possible to determine the contact angle at the three-phase contact line when the sample surface had some spots, after they investigated the Wenzel's and Cassie's states [18]. Later, a set of experiments has been completed by Nosonovsky who has modified the Wenzel and Cassie equation for the usage on rough super-hydrophobic surfaces [19]. Although there are a large number of studies presented in the literature, there is still a gap on knowledge about developing fine-tuned thermal management surfaces with smart intermolecular properties that are enhancing the liquid repellence (hydrophobicity) at the existing surfaces.

The superhydrophobic phenomenon achieved by Frank et al. [20] on nano and microstructured surfaces by using a way that protuberances inside the air below the droplet liquid. The microstructure surface was coated chemically by using SU-8 with a silicon layer thickness of 70 nm. Then, they have manufactured three distinct square

arrays of micropillars epoxy that based by SU-8 with different geometry as pillar diameter and spacing. In their study, they have focused and measured the apparent contact angle θ_m on the title structure surface as 9° . The main reason for the superhydrophobic phenomenon, the contact line should overcome the trapped air between the grooves compared to a smooth surface. Microscopic videos of droplet liquid were captured by using the confocal microscope on the micro pillars structure. They also measured the apparent advancing contact angle θ_{ad} on the front side as 180° and the apparent receding contact angle θ_r on the rear side of the sample. The receded contact angle has shown much more effect on the superhydrophobic surface than advancing contact angle. The droplet contact angle measured by using a sessile drop method at droplet volume range (3–5 μL), the rolling velocity was 1mm/s and the upper limit of apparent advancing contact angle was 180° . Finally, the superhydrophobic surface is achieved at the liquid droplet diameter larger than the spacing between protrusions. Moreover, the superhydrophobic surface has been occurred when the apparent advancing contact angle is higher than 150° and the hysteresis is less than 10° .

The basic knowledge of chemistry on natural phenomena and practical applications of transparent superhydrophobic glass slides have been investigated by Jessica [21]. The chemistry processes were done to obtain different hydrophobicities of the glass slides by using two organosilanes that are methyl trichlorosilane, and octadecyl trichlorosilane. The modification process was also used to get three glass slide one is hydrophilic surface and two slides are hydrophobic and superhydrophobic with different heat treatment temperatures (20 $^\circ\text{C}$ and 4 $^\circ\text{C}$ respectively). The main challenge of this study when increasing glass surface roughness can be enhanced by the hydrophobicity but decreasing the transparency due to light scattering. The results showed the contact angle value for three glass slides as $19^\circ \pm 3^\circ$, $112^\circ \pm 2^\circ$, and $152^\circ \pm 3^\circ$ at the droplet liquid

volume as 1-5 μL . Moreover, temperature reaction effects on the droplet contact angle were $152^\circ \pm 3^\circ$ at 4°C and $156^\circ \pm 2^\circ$ at 20°C . Finally, the highest transmissivity for each glass slides was the superhydrophobic glass that prepared at 4°C compared the other glass slides at the film coating layer less than 100 nm.

Besides conventional techniques, two-phase capillary thermal control devices, such as heat pipes (HP), capillary pumped loops (CPL), and loop heat pipes (LHP) has shown notable application potential [22]. LHPs have proven to be very promising due to their ability to operate against gravity. They show high operational reliability and robustness such that the specific demand of areas such as aerospace technology can be satisfied ([23], [24], [25], [26], and [27]). Furthermore, they have flexible transport lines and can manage large heat transfer rates compared to conventional heat pipes [28].

There are different heat transfer mechanisms one of which is the condensation heat transfer. This phenomenon occurred when the material state changes from vapor to the liquid phase with a large value of heat transfer coefficient and classified into two types as filmwise and dropwise condensation. To transfer high rates of waste heat, heat pipes work with the principle of phase-change from liquid to vapor in the evaporator and from vapor to liquid in the condenser. The process represents a two-phase flow regime in which the heat transfer mechanisms are closely related depending on the thermo-hydrodynamic transport mechanisms. Both heat transfer and hydrodynamics mechanisms are again partially governed by the surface's materials and their microscopic topography existing at the inner surfaces of the evaporator and the condenser. As already classified, the surface condensation can be categorized into two groups, as dropwise and film condensation. Thin film condensation has a larger thermal resistance compared to dropwise condensation, which occurs on surfaces exhibiting poor wettability [29]. The relationship between the condensation rate and the contact

angle is reported to be directly proportional, which means that the poor wettability can lead to an increase in heat transfer coefficient during condensation [2]. Thus, researchers have especially emphasized the optimization potential of the condenser [30]. To achieve high hydrophobicity, special surface treatments such as teflon coating or sand blasting can be considered. Micro-nano-structures as selectively distributed obstacles at the condensation surface can also be used to microscopically manipulate the wetting behaviour of condensation of vapour. This can lead to an intensification of the condensation process through increase of the three-phase contact line inside the condenser ([31], [32], [33] and [34]). With this approach, two essential physical effects can be used to intensify the condensation process. The first effect is expected to increase the number of active nucleation sites. This will help to intensify and initiate early dropwise condensation of vapor and hence contribute to performance increase ([35] [36]). The second effect is the reduction of hydrodynamic drag at the wall-liquid interface. This reduced friction stimulates the motion of condensate droplets and promotes their accumulation to form a thin liquid condensate film. As a result, an improvement of heat transfer coefficient in the condenser can be anticipated. This value can be at the order of 3-4 times of non-treated surfaces.

Condensation over micro-structured surfaces - The microstructured surface is fabricated by using new techniques to manufacture some novel surfaces for increasing the condensation surface area. In addition, the wetting surfaces as hydrophobic and superhydrophobic are created by surface coating to decrease the surface energy. The droplet contact angle was also higher than 90° that it is again used to improve the condensation heat transfer mechanism.

Filmwise condensation on a hydrophobic surface is studied in DelCol et al. [37]. Smoothly condensing surfaces with low contact angle can be optimal to contribute

dropwise condensation at high heat fluxes by avoiding the flooding mechanism which would occur on a superhydrophobic surface while at lower heat flux hydrophobic and rough surfaces have a better performance. The difference between a surface and saturation temperature gets higher and higher when the condensate film thickness increases due to the rising thermal resistance between saturated vapor and the condensation surface. To enhance the condensation heat flux, two parameters, which are steam mass velocity and temperature difference between saturation and wall temperature, play a critical role. Dropwise condensation on some part of the heat transfer area doesn't have a considerable impact on condensation heat transfer over hydrophobic surfaces. The condensation heat transfer coefficient (HTC) on the hydrophobic surface decreases by increasing the subcooling temperature due to the increasing liquid film thickness. The results showed that the HTC on the hydrophobic surface was higher by 10-45% than the hydrophilic surface.

The dropwise condensation on superhydrophobic surfaces is also investigated Chen et al. [38]. Dropwise condensation is more effective on heat transfer magnitude as compared to filmwise condensation. Two mentioned methods, Cassie state and Wenzel states, are used to measure the droplet contact angle and the surface energy on the perylene-coated two-tier textures. Condensate drops are collected into a few large drops after a few cycles of horizontal oscillation which leads to completely be dry the hexadecane thiol-coated two-tier surface. The results showed that dropwise condensation can be achieved with short carbon nanotubes deposited on micromachined pillars on a biomimetic two-tier. In general, the superhydrophobic surfaces don't only affect the two phases of heat transfer mechanism but the engineering part of solid superhydrophobic materials.

The condensation phenomena and wetting behavior on the microstructured

surfaces are also studied by Zhong et al. [39]. Surfaces had a significant contribution as much as the chemical properties of surfaces for achieving super-hydrophobicity. Superhydrophobic surfaces are created corresponding to two underlying principles are the surface roughness and the surface energy. The surface tension is a dominant force to create a new condensation on the top surface fall into the grooves compared to the gravity. Condensation is observed obviously everywhere on the surface when its size smaller than the dimension of microstructures. The results showed that the droplets are collected on the posts in a thin film form or fall into the grooves, which could play a significant role for macro-scale condensate drainage and frost formation.

Condensation phenomena with different surface energy and drops size are also studied by Macner et al. [40]. Terrestrial heat transfer is increased by changing the drop size population and employing a surface energy gradient that affects the drop size population. The drop coalescence in the central hydrophobic region has enhanced the coverage until they are large enough to drip off the surface while the number of drops is decreasing. Chemical treatments are done to increase the heat transfer for condensing surfaces without transitioning to filmwise condensation. Moreover, the results showed that the gradient surfaces are benefited by terrestrial-based technologies because the critical length scale required for movement of drops considerably reduced. In addition, the optimum size of drops formation is greater than 80 μm that are observed after the dropwise condensation process is started.

On the other hand, the droplet condensation on various micro-structured surfaces is presented in Sharma [41]. The experiments showed how the droplet formation occurs during the condensation test on the superhydrophobic hierarchical surface on which the material is aluminum. Results showed two types of hierarchical superhydrophobic surfaces on which the microstructure surface consisting of irregular re-entrant micro-

cavities and an overlaying nanostructure channel with a height of 300 nm. They also showed the growth rate of a liquid droplet on the nanostructure surface is faster than hierarchical microstructure surface by at least 4 times, due to the increasing the surface area of heat transfer that reduces the heat transfer resistance by the vapor trapped inside the microgroove of the structured surface.

Nanograssed micropyramidal architectures for continuous dropwise condensation is given in Chen et al. [42]. Droplet condensation can occur successfully if the surface enables both efficient droplet nucleation and droplet departure. The hierarchical nano-grassed micro-pyramid structure was used as a modern surface to generate the superhydrophobicity by increasing the wettable nucleation sites. Results showed enhancement of heat transfer rate during dropwise condensation by using a micro-pyramid surface compared to a superhydrophobic surface with nanostructures alone. Moreover, the drop number density and the droplet departure volume of micro-pyramid surface was higher than superhydrophobic surface by 65% and 450% respectively.

On the other hand, condensation heat transfer on superhydrophobic surfaces is studied by Miljkovic et al. [43]. The metal oxides were used to create a superhydrophobic surface by increasing the thermal conductivity and decreasing the droplet adhesion due to low surface energy with the stable droplet jumping from the surface. There were some limitations on the metal oxide during condensation process which is flooding applications with low supersaturation. The experimental results showed that the jumping condensation phenomenon is enhanced by 30% of the heat transfer rate in pure vapor environments, and also with the presence of non-condensable gases.

A theoretical study on the condensation heat transfer in microchannels is also studied by Wang and Rose [44]. The theoretical model is developed related to many parameters such as surface tension, surface curvature, gravity, streamwise shear stress and pressure

gradient. Results showed on a certain length of the channel that the heat transfer coefficient is independent on the gravity and vapor shear stress under the same boundary conditions such as the vapor temperature and wall temperature. Moreover, the results showed the heat flux remained constant at constant subcooling temperature by using different working fluids, channel geometries and mass flow rates of vapor.

Finally, an analytical and experimental study of the surface wettability with different topography surface is investigated by Seemann et al. [45]. Two types of micro-structured silicon surfaces that are rectangular and V-channels are used with different wetting surfaces, which were analyzed by using atomic force microscopy AFM. However, the completed theoretical model highly depends on two parameters such as groove geometry and the droplet contact angle. In addition, the theoretical calculations are done by using the classical Laplace equation with different groove aspect ratios from 0.04 to 0.60.

Condensation at various process parameters - Dropwise condensation testing inside a vapor chamber of electronics cooling is studied by Bonner [46]. A self-assembled monolayers (SAM) method is utilized to improve the dropwise condensation on the horizontal unstructured coated surface by decreasing the thermal resistance that associated with the condensation. The case of wettability phenomena was the hydrophobic surface when the contact angle increased to 110° after coated the condensation surface in the vapor chamber. The experimental setup tested to predict dropwise and filmwise condensations on the hydrophobic surfaces at various heat fluxes from 2 to 25 W/cm^2 , with keeping the saturation vapor temperature constant 70°C . The results showed that the heat transfer coefficient of dropwise is higher than filmwise condensation by four times.

The dropwise condensation process in a cylindrical condenser studied by Neumann et al. [47], with different hysteresis contact angles θ_{Hy} . The chemical materials are Palmitic and Stearic acids are used to coat the condenser surface with different surface characteristics of condensation. Experimental results showed an increase in the coefficient of heat transfer HTC in the condenser with decreasing θ_H , and the largest values of HTC were obtained higher than $34 \text{ W/cm}^2\text{-K}$. Finally, the hysteresis contact angle was a significant reason that strongly affected on the heat transfer mechanism in dropwise condensation.

On the other hand, the surface condensation with graded hydrophobicity was conducted with one-dimensional surface gradients by Richard [48]. The gradient of surface wettability caused a variation in the droplet contact angle on condensation surface that it can be moved on the surface without the gravity but with low hysteresis contact angle. An experimental setup (thermosyphoning) is fabricated to measure the heat transfer coefficient on the hydrophobic surface at a constant saturation temperature ($100 \text{ }^\circ\text{C}$) for different heat flux values between 7.75 W/cm^2 - 31 W/cm^2 . In addition, experimental results are recorded for three surface types which are filmwise, dropwise and gradient with different orientations. The condensation on the gradient surface led to an increase of heat transfer coefficient by 35% compared to the conventional dropwise condensation surface in the vertical orientation. Finally, the surface gradient added some additional force to move the droplet in addition to gravity, as a result of the increase on the wettability performance.

An experimental study of dropwise (DWC) and filmwise condensation (FWC) on the vertical titanium plate were also investigated by Baojin et al. [49]. The experiments are done by using three different types of titanium surfaces with different droplet contact angle and surface tension. The first surface is untreated that is tested to predict DWC

and FWC at $\theta = 86^\circ$ and $\gamma = 32.9$. The second surface is hydrophilic that is tested to get FWC at $\theta = 60.9^\circ$ and $\gamma = 48$. The third surface is a hydrophobic surface that is tested to predict DWC at $\theta = 100.41^\circ$ and $\gamma = 29$. At the same temperature difference and constant saturation temperature as 100°C , the experimental results showed the highest values of heat flux and heat transfer coefficient were in the hydrophobic surfaces than untreated and hydrophilic surfaces, while lower values of HF and HTC were in the hydrophilic surface. Also, the comparison between the mathematical model of dropwise region and the experimental results gave a good agreement especially at the temperature difference is higher than 10 K for each surface.

A new technique of nanostructured copper surface to create superhydrophobic condensation and the behavior of condensation droplets is presented in Ryan et al. [50]. A self-assembled monolayer method is utilized to improve the dropwise condensation on the hydrophobic nanostructured surface with the height and width dimensions are $1\mu\text{m}$ and 300 nm respectively. Experimental results showed an enhancement of average contact angle from $92.8^\circ \pm 1.8^\circ$ on the smooth surface to $153.3^\circ \pm 2.6^\circ$ on the nanostructure surface with hysteresis is 15° . The experimental parameters before starting the tests were done at the surface temperature (10°C), while the flow rate of water was 2.5 l/min and the steam pressure in the vapor chamber was 1.55 kPa . A high speed camera (Phantom v7.1) is used to record the nucleation and growth of droplet condensation on the surface at a resolution is 800×600 and pixel size of $22\mu\text{m}$. Finally, they found the nanostructured surfaces may work as a superhydrophobic surface when the length of droplet contact line less than $5\mu\text{m}$. Consequently, the nanostructured surface can be more advantageous than the polished hydrophobic surface in condensation field.

In another experimental study on the condensation heat transfer was carried out on a pure and a modified copper substrate by Huang and Leu [51]. Superhydrophobicity has been obtained through immersing a substrate in a hydrogen peroxide dilution and subsequent processing by spin-coating using fluoro silane polymer (EGC-1720). The effective surface area of condensation was about 34.0 mm x 69.0 mm. Water contact angles at the pure and treated surface were measured as $106.17^{\circ} \pm 1.58^{\circ}$ and $153.43^{\circ} \pm 5.13^{\circ}$ keeping droplet diameter constant at 4 μm . Experimental results show that the condensation heat transfer performance on the superhydrophobic copper surface was higher compared to the pure copper surface for the cooling liquid flow rate spectrum 20 – 2000 cm^3/min . Then, the average convection heat transfer coefficients of the dropwise condensation (DWC) on vertical surfaces were 1.7 to 2.1 times greater than those of filmwise condensation (FWC). In addition, the heat flux of the modified surface by spin coating was higher than pure surface by two times. Finally, maximum heat flux and heat transfer coefficient difference between two types of the copper surface was 234 kW/m^2 and 13.7 $\text{kW}/\text{m}^2\text{-K}$ at the same temperature difference is 16.8 K. Dropwise condensation of steam on a polytetrafluoroethylene (PTFE) coated plate is studied by Ma et al. [52]. The main parts of the experimental setup are the boiler that can generate the steam at atmospheric pressure by using two heaters 15 kW and 3 kW, and the second part is heatsink to increase the cooling heat transfer surface. Experimental results of DWC showed the heat transfer coefficient and heat flux increased by 30 and 47 times respectively compared to the Nusselt correlation formula of FWC at the same temperature difference between the steam and the condensation surface. The maximum fluctuation of surface temperature after coating the condensation copper surface by ultra polymer film is approximately 0.8 $^{\circ}\text{C}$. In addition, the results showed the rate of heat transfer in dropwise condensation increased with increasing the

steam temperature at atmospheric pressure. Finally, the low surface energy of coating material caused an increase in heat flux of DWC with a uniformly distributing of the small drops on the condensation surface.

The heat transfer of the laminar film condensation on a non-isothermal vertical plate is given in Shu [53]. The analytical approach is studied to solve non-uniformly distributed condensation surface temperature related to Prandtl numbers and condensation rates. In addition, the theoretical analysis is validated by using some important formulas and the correlations equations with different Prandtl numbers. There, the comparisons between theoretical and experimental results are shown in a good agreement.

Hu and Tang [54], investigated a new theoretical model of the dropwise condensation heat transfer on a horizontal tube. The theoretical model is analyzed by considering some parameters such as thermal resistance and the effect of convection heat transfer inside the droplet liquid. An analytical calculation was also done to calculate the overall heat flux with varying inclination from 0° to 90° and different contact angles from 90° to 150° on the horizontal tube surface at constant vapor pressure (1 bar). Analytical results showed the droplet size decrease due to the increase on the droplet contact angle and thus the heat transfer coefficient can be increased the condensation. In addition, the results illustrated the heat flux of DWC increases by 147% and 669% when the droplet contact angle was 90° and 150° respectively compared to the filmwise condensation at constant subcooling temperature and saturation pressure. Lastly, the validation of DWC heat transfer is done by comparing the analytical and experimental results that gave an acceptable agreement at low subcooling temperature and maximum contact angle range not more than 150° .

Fayazbakhsh and Bahrami [55] studied an analytical model of foggy condensation of water over the cold flat surface with different orientations (30° to 90°). The

condensation process is analyzed analytically by considering some parameters such as natural convection heat transfer to the ambient air and the heat transfer through the solid surface of the vertical plate. The first program name is dew formation model that is used to predict the droplet geometry. Then, the real value of droplet contact angle is calculated related to parameters such as wall temperature, liquid properties and advancing contact angle of condensation phenomena. In addition, the main analytical model is combined with the dew formation model for solving the heat and mass transfer equations due to complex condensation process. Analytical results showed the mass flow rate of the condensation liquid increases with decreasing the inclination angle of the flat plate due to the increase on the evaporation latent heat.

The complex geometry of the wetting surface is studied by Herminghaus et al. [56]. The basic fluid mechanisms included the statics and dynamics of wetting on different topography surface such as rectangular and triangular grooves. The impact dynamics of the liquid droplet showed unstable shape in the wedge position of the micro-structured surfaces. The theoretical results showed the effect of the topography surfaces on the hydrodynamic drop inside the groove that because of the contact line pinning and the contact angle hysteresis. Micro-structured surfaces offered a rich spectrum of wetting phenomena that may affect the heat transfer mechanism. Finally, the triangular groove is more effective on the hydrodynamic phenomena than rectangle groove because there is not any resistances of the droplet liquid motion from the groove crest to inside the groove.

Budakli et al. [57], investigated an experimental study of the drop-film wise condensation on coated surfaces. Heat transfer parameters are measured during condensation of saturated vapor on unstructured and micro-structured copper surfaces. The tests are done with and without coating by using chemical slurry (Ultra Ever Dry).

The experimental condensation process is presented due to the effect of different surface topography on the subcooling temperature, heat flux and heat transfer coefficient (HTC). The experimental results showed that the HTC decreased with increasing temperature difference between the wall temperature and vapor chamber temperature at fixed saturation vapor temperature. Finally, the micro-structured square groove showed a minor influence on heat transfer coefficients compared with the unstructured surface due to thin liquid films, which covers the surface inside the grooves.

Viorel [58] developed a numerical model for studying the vapor condensation phenomena with the heat transfer mechanism on the flat surfaces inside buildings. The goal of this study is to simplify hypotheses of the condensation phenomena to solving mass transfer problems. A theoretical study is associated with some parameters such as humidity, airflow and heat transfer that based on computational fluid dynamics method. The theoretical model demonstrated the mass transfer method depends on two parameters are surface wettability and topography.

On the other hand, Cavalli [59], investigated a numerical model to study the wetting phenomena on the micro-structured surfaces by using various fluids. The wetting surface types such as superhydrophobic and the oleophobic surface is analyzed by using different numerical techniques, which is used in several applications by enhancing the condensation phenomena. A superhydrophobic surface can expel the droplet due to a conversion of the low surface energy to the kinetic energy with a high contact angle of the droplet. In addition, the trapezoid micro-structured surface is modeled to enhance the wetting properties of the superhydrophobic surface and the heat transfer mechanism. Moreover, Garvin [60], investigated an experimental study of microstructure hybrid surfaces that affects on the wetting phenomena. A theoretical model is based on low

surface energy and due to increasing the droplet contact angle on the micro-structured surface. The results showed the increasing heat flux with different topography and hybrid surfaces that gave a good stability of the dropwise condensation.

The influence of porous coating on the condensation heat transfer mechanism for each type of dropwise and filmwise is studied by Zheng et al. [61]. The tests for the condensation process are made on the unstructured copper surface with different wetting surfaces, which is done by using Self-Assembled Monolayer (SAM) to create a hydrophobic surface by using sintered copper powder and H_2O_2 to create hydrophilicity. An advanced cooling technology of the power plant is practiced during the condensation process at difference vapor temperature ranges from 35 °C to 60 °C with increasing the input power of the boiler from 50 W to 250 W. Experimental results showed enhancement in the condensation heat transfer for the coated surface compared to the uncoated surface for each type of condensation phenomena with the average value of heat transfer coefficient was $\sim 7 \text{ kW/m}^2\text{-K}$ for the untreated base surface. Also, the SAM coating of the copper powder showed the largest value of the droplet contact angle and HTC were 110° and $\sim 50 \text{ kW/m}^2\text{-K}$ respectively compared the other surfaces with the active condensation surface area was 7.5 cm^2 . While the film-wise condensation is created by H_2O_2 treatment that gave the highest value of HTC was $\sim 21 \text{ kW/m}^2\text{-K}$ compared to the base surface. Consequently, the heat transfer coefficient for hydrophobic dropwise condensation by SAE coating and hydrophilic film-wise condensation by H_2O_2 that is enhanced by 5 times and 2 times respectively compared to the untreated base surface. Hence, the summary table about other people's research are explained in APPENDIX A (see Table A-1).

2.1 The Objectives of the Thesis

In the current study, advanced condensation surfaces have been first studied with a commercially available heat-pipe. It has been studied under various orientations and validated with the results from the previous studies on the literature. A flattened heat-pipe has been embedded inside two different PCBs made of polymer and aluminum. Under the flattened heat pipe, the dissipation performance as well as temperature uniformity is experimentally compared with the first measurements. Computational models were developed and analyzed in ANSYS Icepak for a better understanding of the heat spreading behavior.

Later attention has been turned into investigating the influence of the microstructured surfaces topography on the efficiency, heat transport capability and the hydrodynamic process. Moreover, the hydrophobicity phenomena effect on condenser part of the Heat pipe by coating applications is also in the scope of the thesis. A novel approach has been developed for extending the limits of the condensation process beside of thermal performance enhancements. Then, the hydrophobic phenomenon is studied to make a dropwise condensation by increasing the exposed surface area to the vapor temperature with increasing the heat transfer coefficient.

CHAPTER III

HEAT PIPE TECHNOLOGY

In this chapter commercial heat pipe technology has been studied in a practical application to understand the limits and needs for technology development. Both experimental and computational studies have been performed.

3.1 Experimental Setup for Heat Pipe Measurements

An experimental setup has also been developed and manufactured for the heat pipe measurements. The system has been designed to investigate the influencing parameters such as evaporator heat flux and the inclination angle on the heat pipe performance for different designs by using temperature maps while validating the results obtained by numerical and analytical studies as well. Heat pipes have been tested with the experimental setup illustrated in Figure 3-1 (a). While a maximum heat flux of 76 W/cm^2 has been applied at the evaporator, forced convection liquid cooling has been provided at the condenser. A number of commercially available heat pipes have been evaluated experimentally. In addition, the experiments have been tested by cooling the condenser section with forced convection liquid cooling while keeping the distance between the evaporator and the condenser insulated with an insulation glass. The heat-load was applied by several cartridge heaters in the experimental study. These heaters were embedded symmetrically inside a small Aluminum cylinder along with heat pipe's evaporator with 6 mm in diameter, 150 mm in length which was positioned at center, placed inside the insulation cube while interfaces were filled by the thermal grease (RTV gasket). The measurements were recorded by seven T-type thermocouples that were connected to the external data acquisition device of AGILENT 34972A model. In order to measure the temperatures on the heat pipe, small grooves were opened on the

surface in which the thermocouples were placed and fixed. Placing of the thermocouples is as follows: two (T_1 – T_2) on evaporator wall (with 2.54 cm spacing), two (T_3 – T_4) on adiabatic pipe wall, two (T_5 – T_6) on the condenser wall (with 2.54 cm spacing), and two (T_7 – T_8) on the insulation surface to calculate heat loss as seen in Figure 3-1 (b).

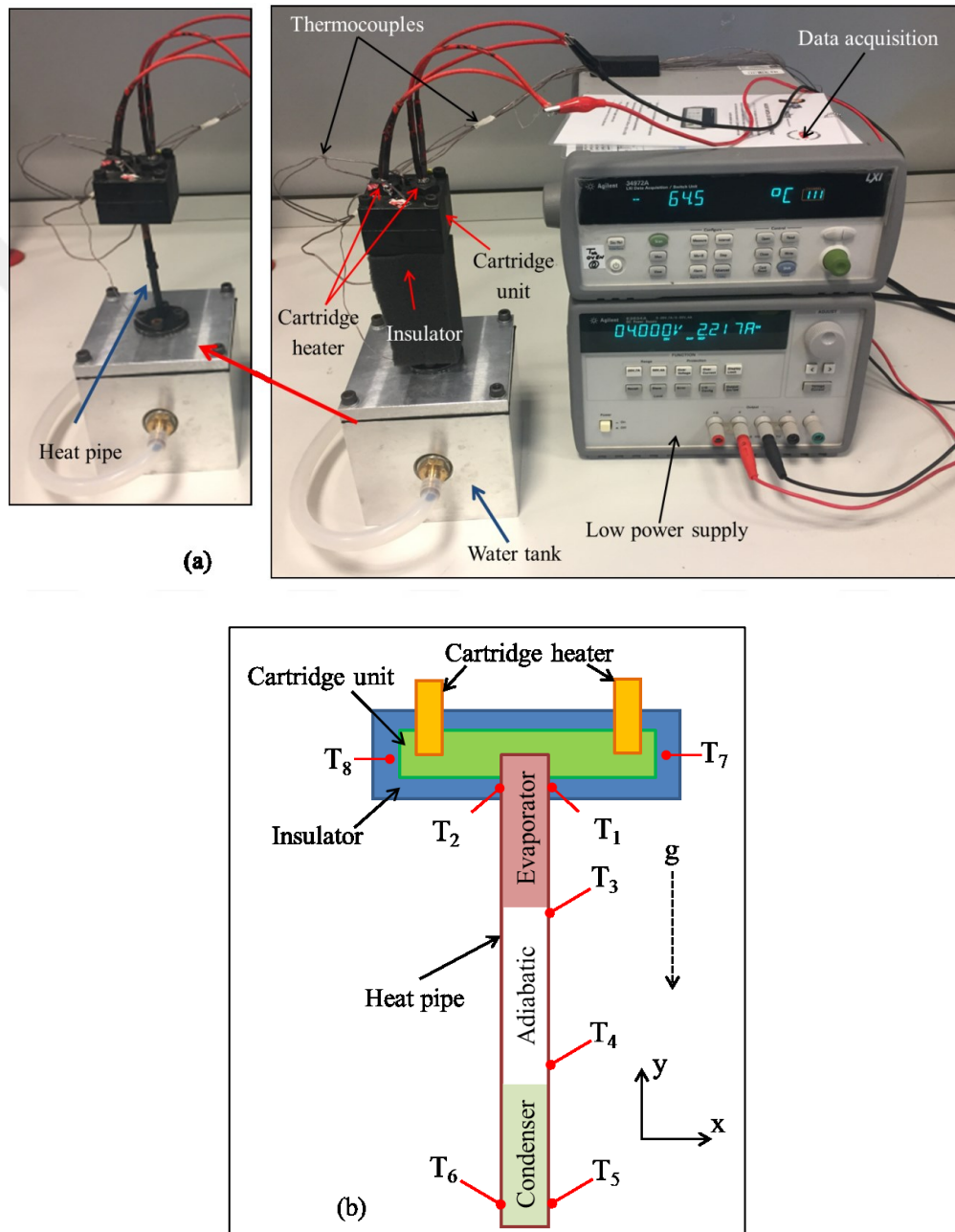


Figure 3-1: Schematic of the test system (a) setup, and (b) thermocouple locations

Heat losses from the heat pipe were calculated by following these Equations from 3-1 to 3-4. The rate of natural-convection heat transfer at a uniform temperature of T_s from solid surface to the fluid is given by Newton's law of cooling [62]:

$$\dot{Q}_{\text{conv}} = hA_s(T_s - T_{\text{amb}}) \quad (3-1)$$

The radiation heat transfer due to the surface temperature T_s that is surrounded by surfaces at T_{surr} is given by the radiation formula:

$$\dot{Q}_{\text{rad}} = \varepsilon\sigma A_s(T_s^4 - T_{\text{surr}}^4) \quad (3-2)$$

Thus, the total heat transfer rate is the sum of both heat transfer rates:

$$\dot{Q}_{\text{total}} = \dot{Q}_{\text{conv}} + \dot{Q}_{\text{rad}} \quad (3-3)$$

$$\dot{Q}_{\text{loss}} = \dot{Q}_{\text{elec}} - \dot{Q}_{\text{total}} \quad (3-4)$$

Then, the heat loss is defined experimentally as the difference between electrical power input and total rate of heat transfer. Moreover, each experiment is repeated at least three times and average values are reported for higher accuracy.

While, experimental boundary conditions are already listed (in **Table 3-1**), the inner wick-structure of copper rod's porous diameter is measured as $d_{\text{por}} = 64.8 \mu\text{m}$ under the microscope as given in Figure 3-2 since the porous structure is one of the most important affecting parameters.

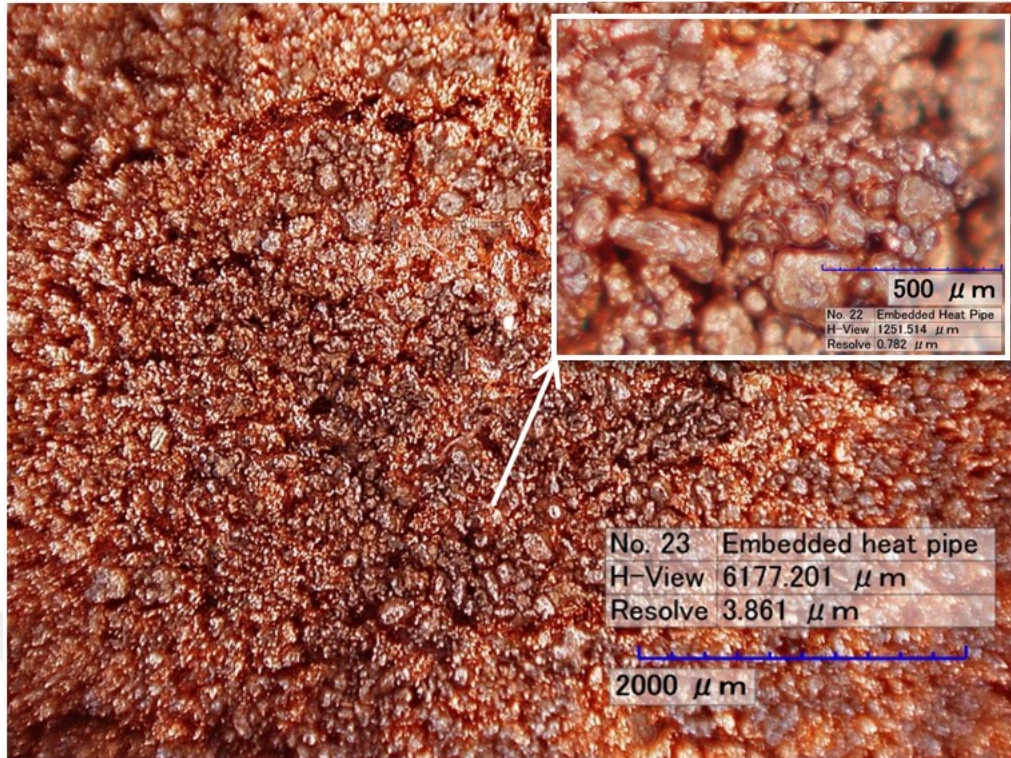


Figure 3-2: Fine porous surface image obtained using a high-resolution microscope

3.1.1 Heat Pipe Embedded Inside a Board

After the plain heat pipe orientation evaluation has been applied, the same heat pipes that were tested previously have been flattened and then embedded inside two plates with different thermal conductivities (aluminum plate with 210 W/m-K and polymer plate with 0.25 W/m-K). They have been embedded by applying a gradual compression force towards the groove of the same cross-sectional perimeter of the heat-pipe as seen in Figure 3-3. Moreover, high temperature contours can be easily seen around the heater compared to the aluminum plate due to the high conductivity of an aluminum substrate. The distinctive temperature contours are very clear in the polymer plate since the conductivity of polymer is less than 0.5 W/m-K. In addition, temperature contours have been explained for each plate (see Figure 3-12 and Figure 3-13). Analytical,

computational and experimental evaluations are repeated for heat pipe embedded cases as well. Accordingly, the results are compared with each other.

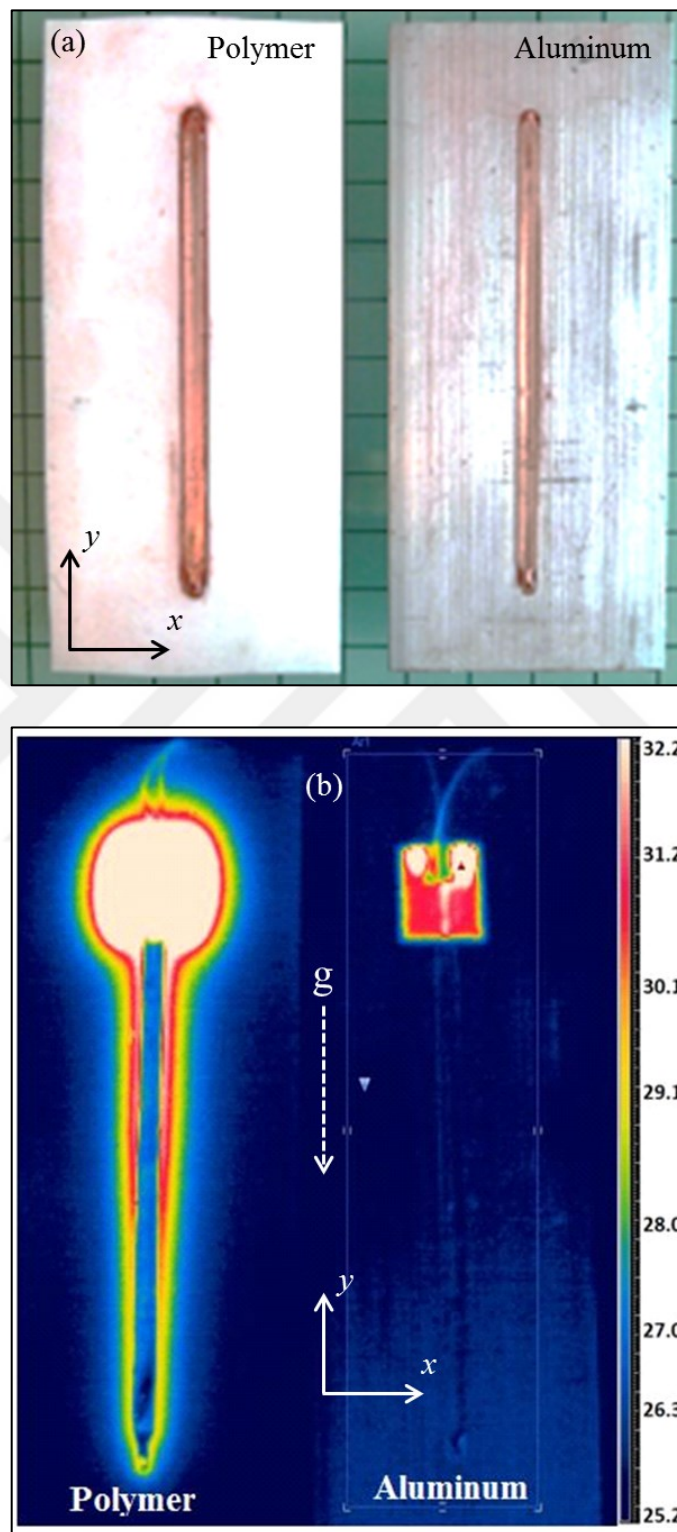


Figure 3-3: (a) Embedded heat pipes in a polymer and an aluminum plate,
(b) Temperature distribution

3.2 Numerical and Computational Analysis of Heat Pipe

The heat pipe constrains are function of many parameters including heat rate to be removed, operating temperature, wettability in the evaporator and condenser, and the inclination angle. The latter is one of the most significant factors affecting a heat pipe operation according to physical phenomena such as the effect of gravity acceleration and buoyancy force of the working fluid occurring in a heat-pipe as shown in Figure 3-4 [63]. In terms of numerical analysis, the maximum capillary pumping pressure, as shown in Eq.3-5, must be greater than the sum of pressure drop in the liquid and vapor, and the pressure drop caused by gravitational forces [64].

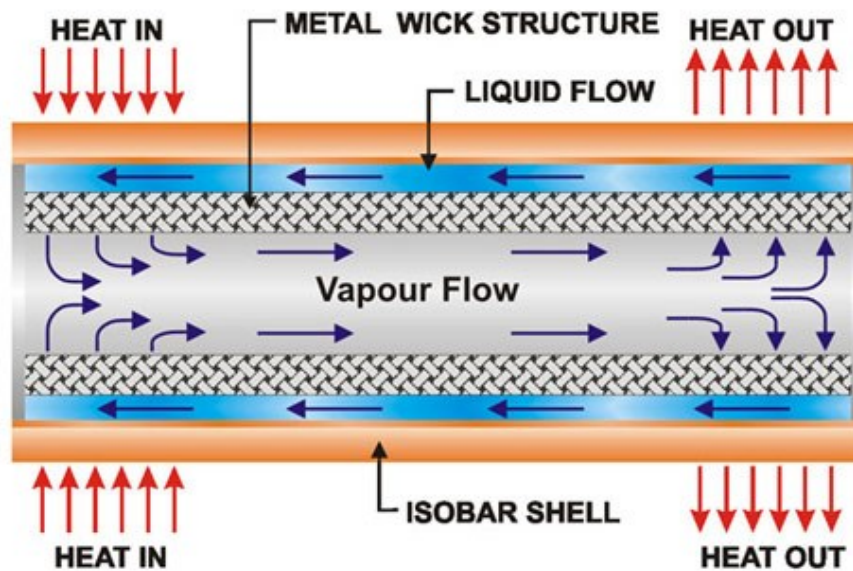


Figure 3-4: Schematic view of a heat pipe [63]

$$\Delta p_{\text{cap,max}} \geq \Delta p_l + \Delta p_v + \Delta p_{\text{normal}} + \Delta p_{\text{axial}} \quad (3-5)$$

where: $\Delta p_{\text{cap,max}} = \frac{2\gamma}{r_{c,e}}$ $r_{c,e} = 0.21d_{wi}$

However, the vapor pressure drop Δp_v is given as in Eq.3-6 [65]:

$$\Delta p_v = \rho u^2 + \frac{8\mu_v \dot{M} L_e}{\rho \pi r_v^4} [L_{\text{eff}}] \quad (3-6)$$

Where: $L_{\text{eff}} = \frac{L_e + L_c}{2} + L_a$ and $u = \dot{M} / \rho_v A_{s,e}$.

The boiling limit is the main influential factor on the heat flow within the heat pipe as given in Eq.3-7 due to the rising temperature difference between the evaporator and condenser parts. In addition, the heat transfer limit based on the entrainment limit is given in the Eq. 3-8 [66].

$$\dot{Q}_{\text{bo}} = \frac{2\pi L_e K_{\text{eff},wi} T_v}{h_{fg} \rho_v \ln \frac{r_i}{r_v}} \left(\frac{2\gamma}{r_n} - \Delta p_{\text{cap,axm}} \right) \quad (3-7)$$

$$\dot{Q}_{\text{en,max}} = A_v h_{fg} \sqrt{\left(\frac{\rho_v \gamma}{2r_{c,e}} \right)} \quad (3-8)$$

Through rearranging and substituting for the mass flow rate (\dot{M}) of working fluid that is spinning inside the heat pipe and for the maximum rate of heat transport in the heat pipe, one can obtain the following relationships [67]:

$$\dot{M} = \frac{\rho_l K A_{wi}}{\mu_l L_{\text{eff}}} \left[\frac{2\gamma_l}{r_c} \cos \phi - \rho_l g L_{\text{eff}} \sin \psi \right] \quad (3-9)$$

$$\dot{Q}_{\text{max}} = \dot{M} h_{fg} \quad (3-10)$$

The porosity and the permeability of sintered porous wick metal can be calculated by using the following equations respectively [68]:

$$\epsilon = \frac{\pi}{6 [1-(r_{c,si})^2]^{2/3}} \left\{ 1-(r_{c,si})^2 \left[2-\sqrt{1-(r_{c,si})^2} \right] \right\} \quad (3-11)$$

$$k = \frac{r_{si}^2 \epsilon^3}{37.5 (1-\epsilon)^2} \quad (3-12)$$

The effective thermal conductivity of sintered porous wick can be calculated by [69],

$$K_{eff,wi} = \frac{K_e [2K_{si} + K_e + 2\epsilon(K_{si} - K_e)]}{2K_{si} + K_e + \epsilon(K_{si} + K_e)} \quad (3-13)$$

3.2.1 Thermal Resistance Network of a Heat Pipe

For a cylindrical heat-pipe with a wick structure, radial conduction resistance at evaporator and condenser parts are given by [64]:

$$R_{hp,e} = \frac{\ln d_{o,i}}{2\pi L_e K_{cu,wall}} \quad (3-14)$$

$$R_{hp,c} = \frac{\ln d_{o,i}}{2\pi L_c K_{cu,wall}} \quad (3-15)$$

$$R_{wi,e} = \frac{\ln d_{i,v}}{2\pi L_e K_{eff,wi}} \quad (3-16)$$

$$R_{wi,c} = \frac{\ln d_{i,v}}{2\pi L_c K_{eff,wi}} \quad (3-17)$$

However, the resistance for the convection inside the heat pipe is ignored since it is too low in comparison to conduction resistances. Hence, the overall thermal resistance (R_{total}) and total thermal conductivity of heat pipe ($K_{eff,hp}$) can be calculated with:

$$R_{total}=R_{hp,e}+R_{wi,e}+R_{wi,c}+R_{hp,c} \quad (3-18)$$

$$K_{eff, hp}=\frac{L_{eff}}{R_{total} A_{eff}} \quad (3-19)$$

Correlation of natural convection from a heated or cooled cylinder that is horizontally aligned with respect to gravity includes Rayleigh number and average Nu number which are commonly based on the diameter of the cylinder [62]. However, Ra number and average Nu number should be affected much from the length of the vertical cylinder rather than its diameter, since boundary layer develops through the length [70]. The set of equations has been formulated and solved by using Engineering Equation Solver (EES). After different parametric studies that have been conducted, the results of these studies are given in **Table 3-1**.

Table 3-1: Analytical and experimental results for heat pipe performance test

		Experimental results				Analytical results			
\dot{Q}_i	φ	ΔT	Δp	R_{total}	$K_{eff, hp}$	ΔT	Δp	R_{total}	$K_{eff, hp}$
W	Degree	°C	Pa	°C/W	W/m °C	°C	Pa	°C/W	W/m °C
2.4	-90	5.1	1469.0	2.20	16311	3.6	1100.0	1.51	23435
	90	3.0	717.3	1.30	27728	2.9	910.9	1.23	28740
3.7	-90	7.1	2737.0	1.90	18257	5.5	2133.0	1.51	23441
	90	4.6	1329.0	1.30	28179	4.5	1780.0	1.23	28748
5.4	-90	9.3	4495.0	1.70	20422	8.1	4275.0	1.51	23449
	90	6.0	2257.0	1.10	31654	6.6	3597.0	1.23	28756
7.3	-90	11.7	8057.0	1.60	22134	11.0	8276.0	1.51	23466
	90	7.6	3576.0	1.00	34074	9.0	7022.0	1.23	28768
9.5	-90	14.0	11106.0	1.50	24010	14.3	12857.0	1.51	23488
	90	8.1	4074.0	0.90	41498	11.7	11012.0	1.23	28776

Furthermore, the geometry of heat pipe setup has been modeled in ANSYS (Icepak) commercial simulation software as seen in Figure 3-5. It consists of the same components of the conventional heat pipe as in the experimental setup that will be presented later (see Figure 3-1 (a)), such as a cartridge heater, cartridge unit, insulations, and water tank. However, the mesh sensitivity study is crucial for the accuracy of the simulation. Thus a set of models have been simulated by increasing the number of elements between 16,000 to 128,000. Accordingly, the model with 128,000 numbers of elements has been selected due to the repeating results for the chosen positions at condenser and evaporator parts by increasing the number of elements (see Figure 3-6).

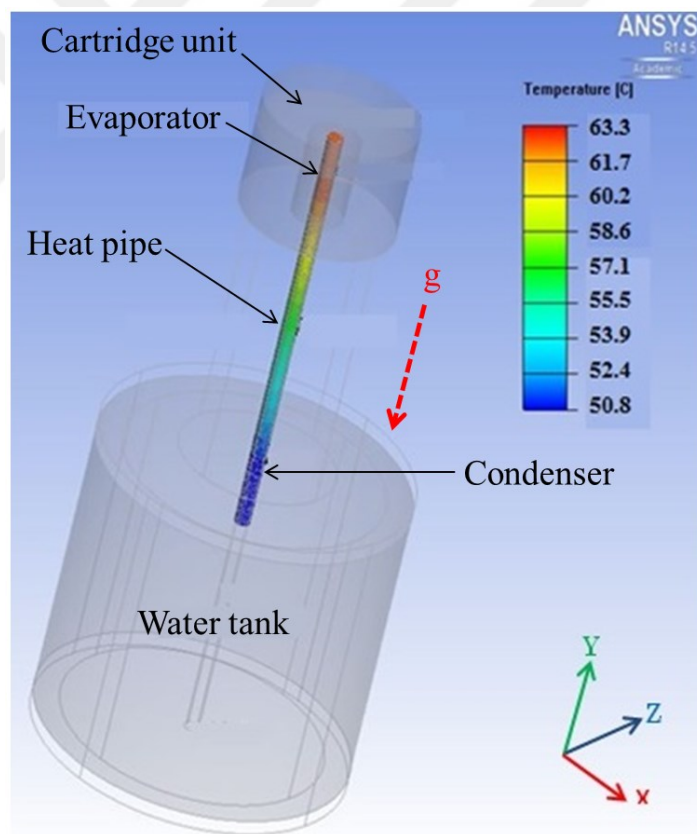


Figure 3-5: Computational model of current experimental setup[71]

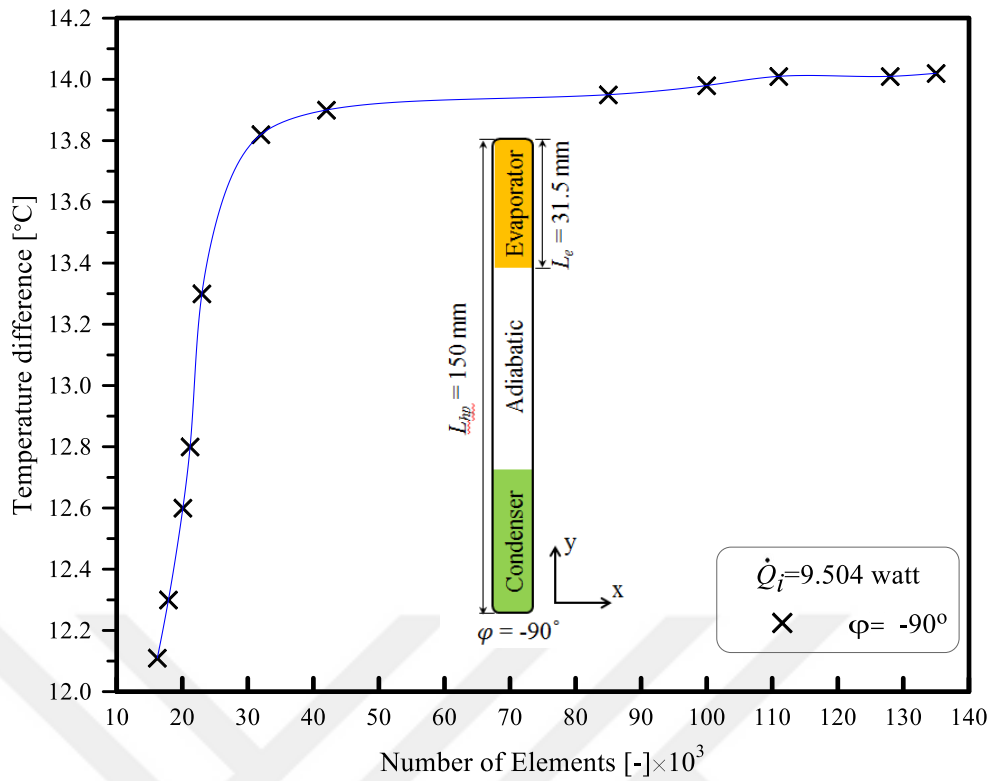


Figure 3-6: Temperature difference sensitivity of heat pipe to mesh elements

3.3 Results and Discussions

Conventional heat pipe technology is a type of thermal cooling system that is used to transport the heat from the hot region (evaporator) to cold region (condenser) without consuming any extra energy. A commercially available heat pipe is first tested before embedding into the substrate plate and results are validated with the previous similar studies from literature [13]. After embedding the heat pipes into two PCB prototypes with different materials (teflon and aluminum), the thermal resistances for various cases are utilized to calculate the effective thermal conductivity at various heat loads again by experimental and numerical models.

First, the orientation effect (from -90° to $+90^{\circ}$) on the performance of a heat pipe was investigated (see Figure 3-7). The temperature difference between condenser and evaporator, thermal resistance and effective conductivity under different heat loads and

orientations are plotted in Figure 3-8, Figure 3-9 and Figure 3-10. Figure 3-8 has shown comparable results with the literature [13] one of which has 200 mm length of heat pipe (copper, water) at 6 mm in diameter. Figure 3-8 is being demonstrated to show the validity of the experimental test and make a comparison with the published work by Loh et al. [13]. The results indicate that our test setup and measurement procedure are predicting a similar performance as the one that was tested and published in the literature [13].

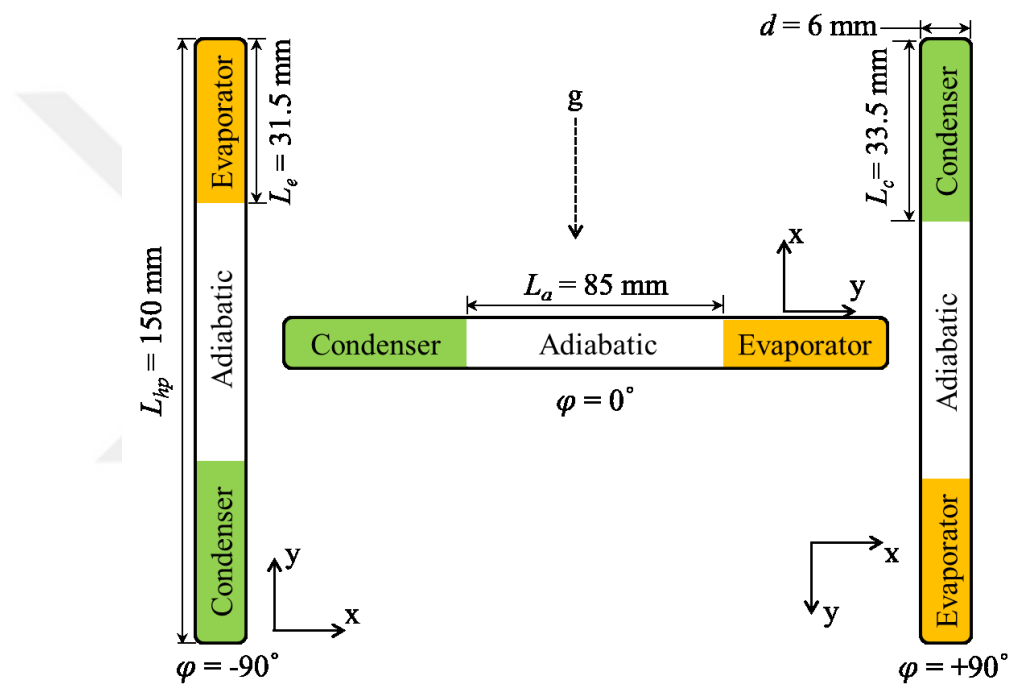


Figure 3-7: The schematic diagram of the heat pipe with different angle of inclination

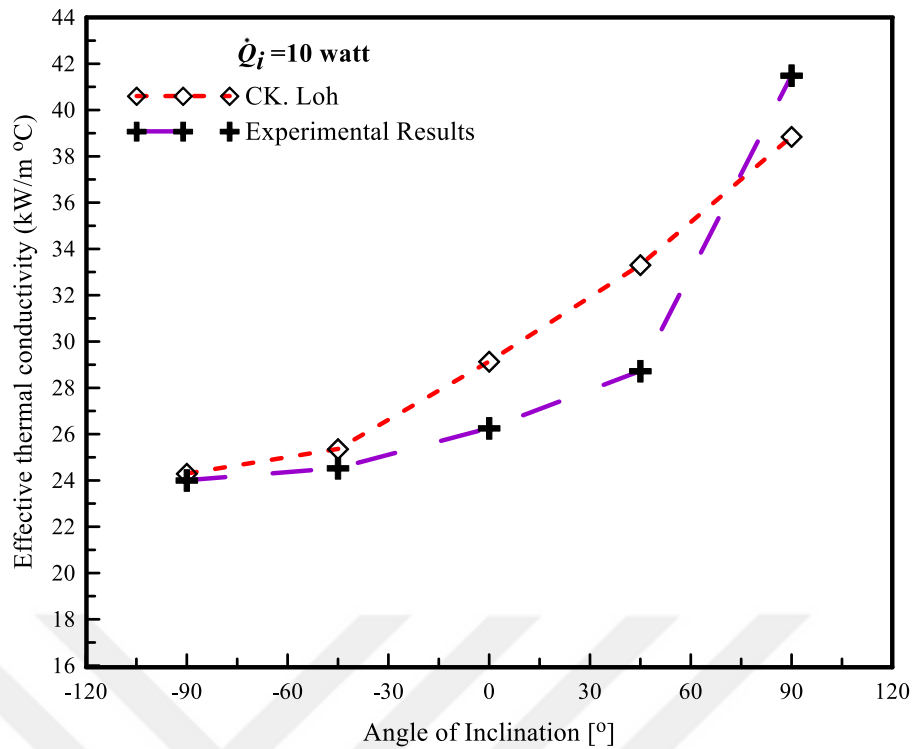


Figure 3-8: System validation with experimental study from literature for varying orientation angles [13]

The increase in temperature difference at high heat load is due to the rise in the amount of evaporated fluid which is required to provide a higher pressure difference to drive the vapor from evaporator to condenser. Since saturation temperature depends on saturation pressure one can predict that the temperature difference will increase as in Figure 3-9.

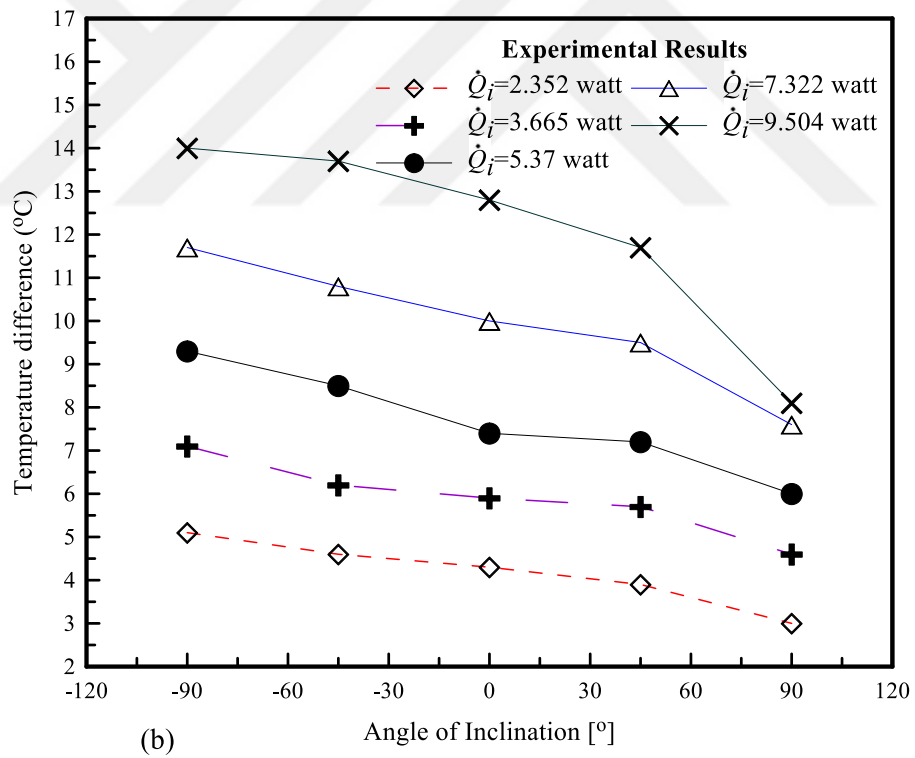
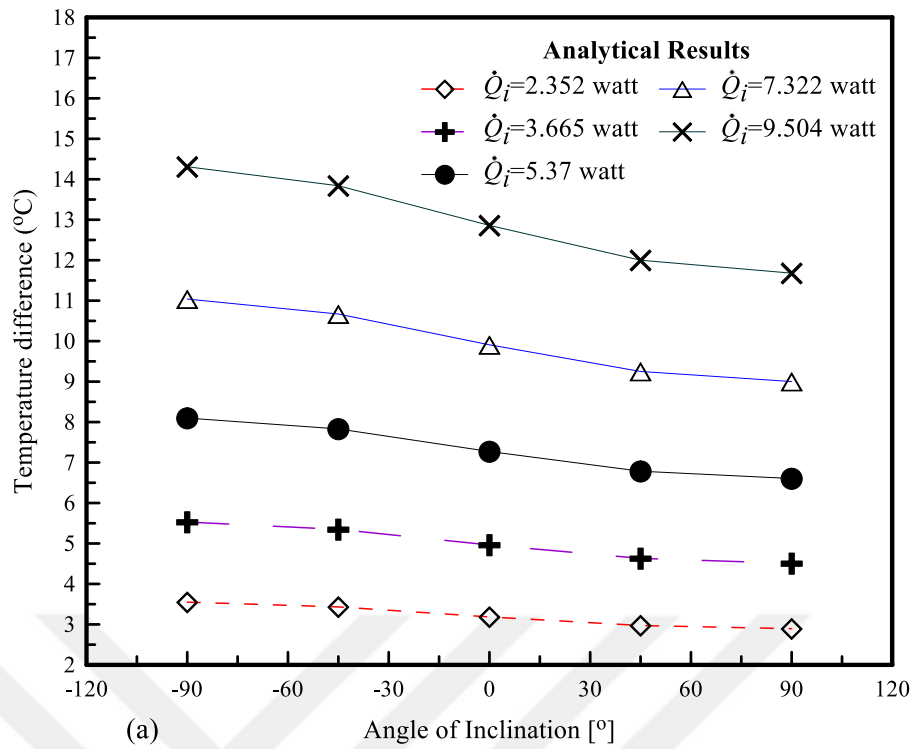
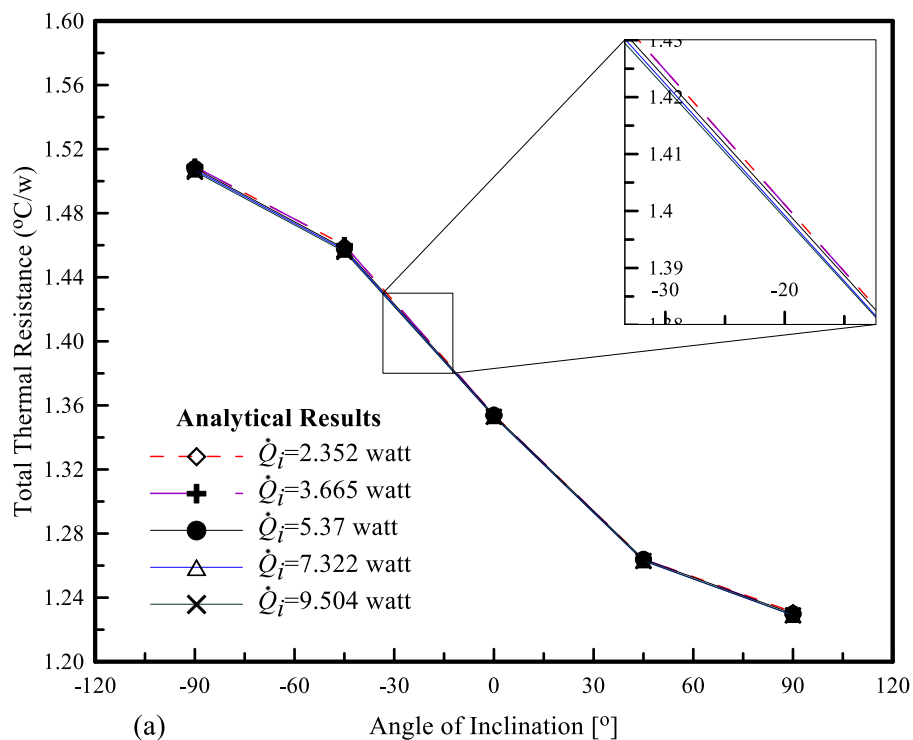


Figure 3-9: Variation of temperature difference from (a) analytical results and (b) experimental results at different input power with different orientation of heat pipe

Figure 3-10 (a) and (b) show the variation in total thermal resistance with the orientation of heat-pipe at different input-power loads for the analytical and experimental results respectively. As shown in Figure 3-10, the thermal resistance decreases as the angle of orientation increases. Figure 3-10 (a) indicates that the thermal resistance does not change with input-power load as expected for an ideal case where thermal resistance does not change with input-power (implicitly with temperature). However, Figure 3-10 (b) demonstrates that heat load affects the thermal resistance, which is due to the fact that convection inside the heat pipe and outside the heat pipe depends on surface temperature which is affected by input power values. Moreover, in the analytical model shown in Figure 3-10 (a), the convection resistance inside the heat pipe was ignored since it is too less in comparison to other resistances related to conduction. However, in the experimental measurements, one can easily see that the effect of increasing power leads to the higher convection inside the heat pipe and decrease in the thermal resistance as seen in Figure 3-10 (b).



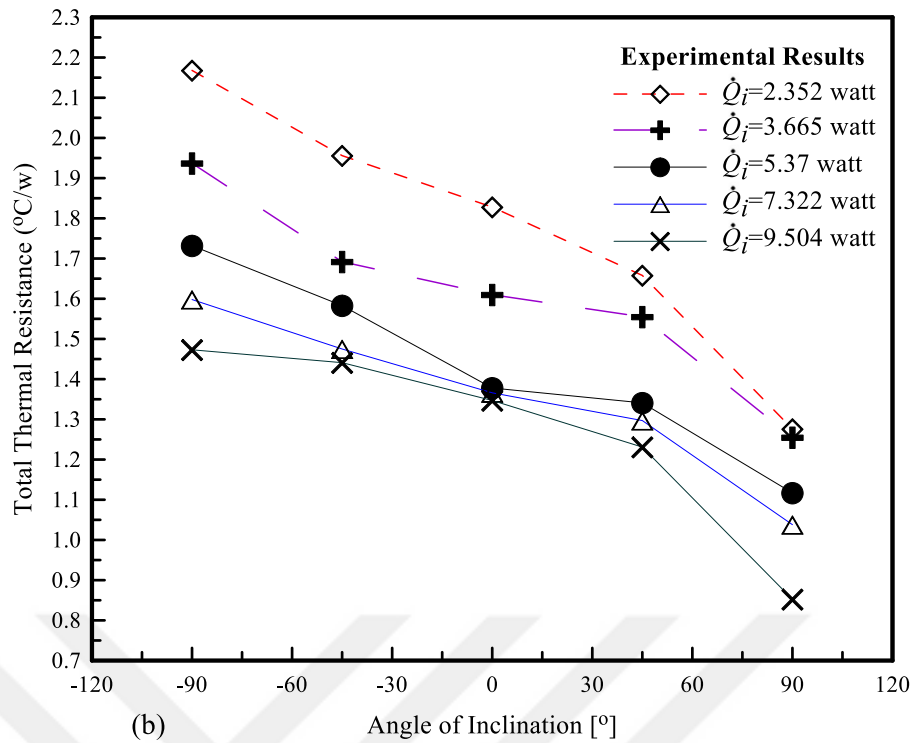


Figure 3-10: Variation of the total thermal resistance from (a) analytical results and (b) experimental results at different input power with different orientation of heat pipe

Furthermore, the explanation can be detailed with the degree of uniformity in the wick structure or the existence of non-condensable gases inside a heat-pipe, thus about the internal conditions of a heat pipe. For this reason, a special relationship between temperature and pressure differences for condenser and evaporator regions of a heat-pipe is presented in Figure 3-11.

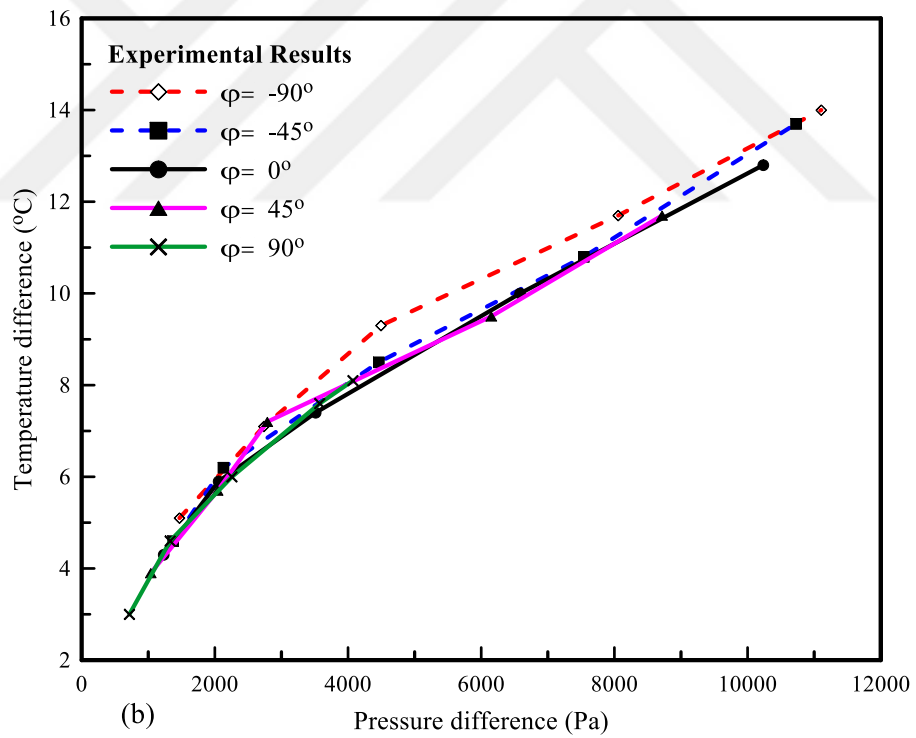
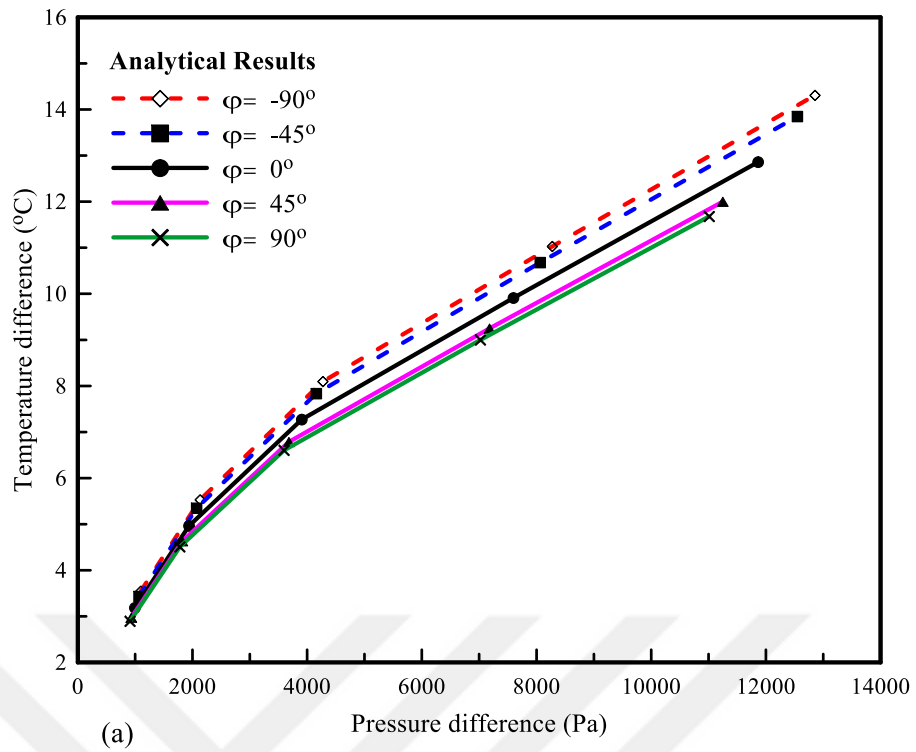


Figure 3-11: Impact of the pressure difference over temperature difference
 (a) analytical results and (b) experimental results at different orientations

The previously tested heat pipes were flattened and embedded inside two different PCB substrates. Similar thermal performance evaluations with experimental and numerical models are repeated for heat pipe embedded cases and the results are compared to each other. The temperature distribution over the heat pipe is measured experimentally by using infrared camera whose specification is previously explained. The temperature contours are developed by using MATLAB software (see Figure 3-12 to Figure 3-14) during the natural convection cooling of the condenser region, with the increase of the heat load of the evaporator. The value of temperature span is $17.8\text{ }^{\circ}\text{C}$ that is measured on the Aluminum plate by using IR camera where the heat pipe performance cannot be observed much as seen in Figure 3-13 (a). While the polymer plate, shown in Figure 3-12 (a), results in a higher range of temperature, in which the significant role of heat spreading is observed. Moreover, the teflon plate is being tested without any embedded heat pipe and a temperature gradient of 8 K is obtained even for a low heat removal condition. In addition, Figure 3-12 (b) has shown a non-uniform temperature distribution, which clearly shows the effect of the heat pipe embedded in teflon plate due to its low thermal conductivity of 0.25 W/m-K . Next, the temperature distribution for a heat pipe embedded aluminum plate is also shown in Figure 3-13. A uniform temperature distribution can be easily seen in the figure since the substrate's thermal conductivity is higher than 205 W/m-K . In addition, this figure showed the temperature gradient on the plate around 3 K . Moreover, Figure 3-14 demonstrates the infrared thermal results for the baseline test with and without a heat-pipe for a teflon substrate. It is shown that heat pipe embedded plate experienced a much lower temperature than the baseline case.

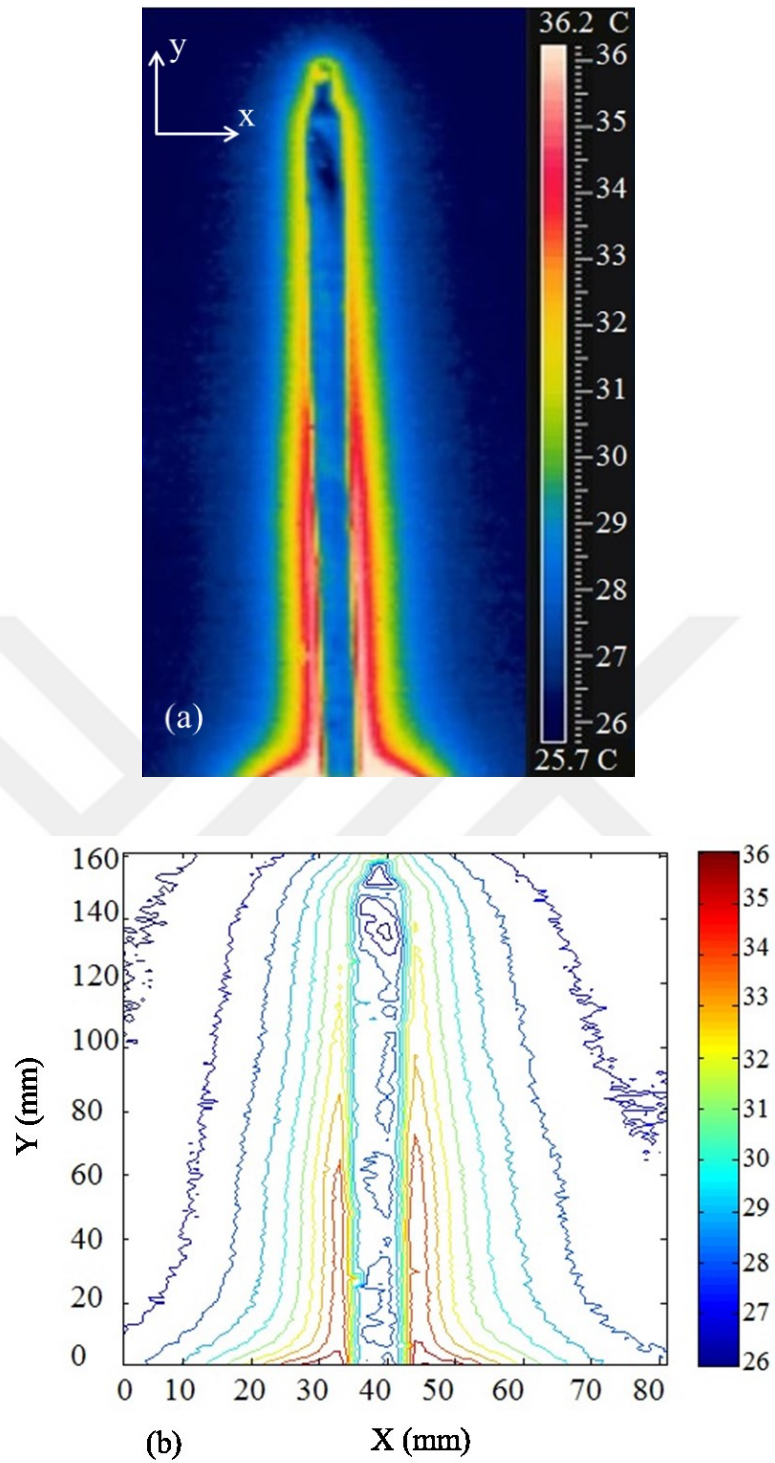


Figure 3-12: Teflon plate with a single heat pipe at the same heat removal condition
 (a) IR image and (b) Temperature contours obtained in MATLAB

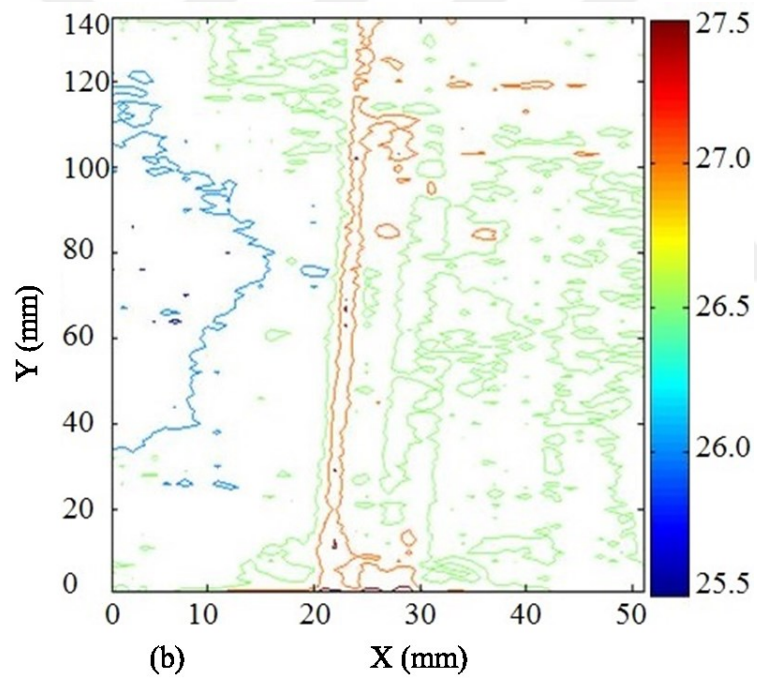
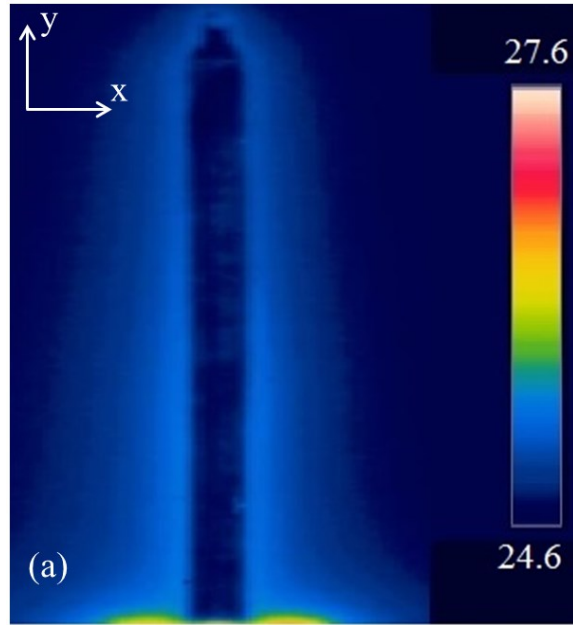


Figure 3-13: Aluminum based substrate with a single heat pipe at the same heat removal condition (a) IR image and (b) Temperature contours obtained in MATLAB

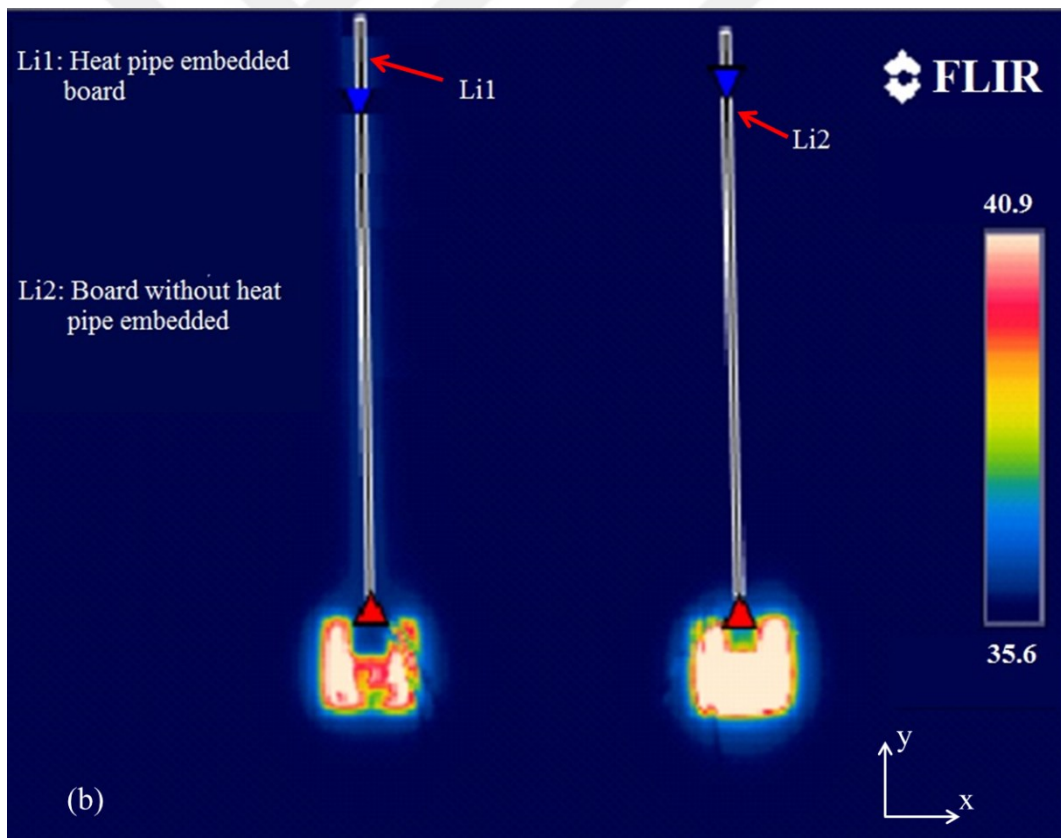
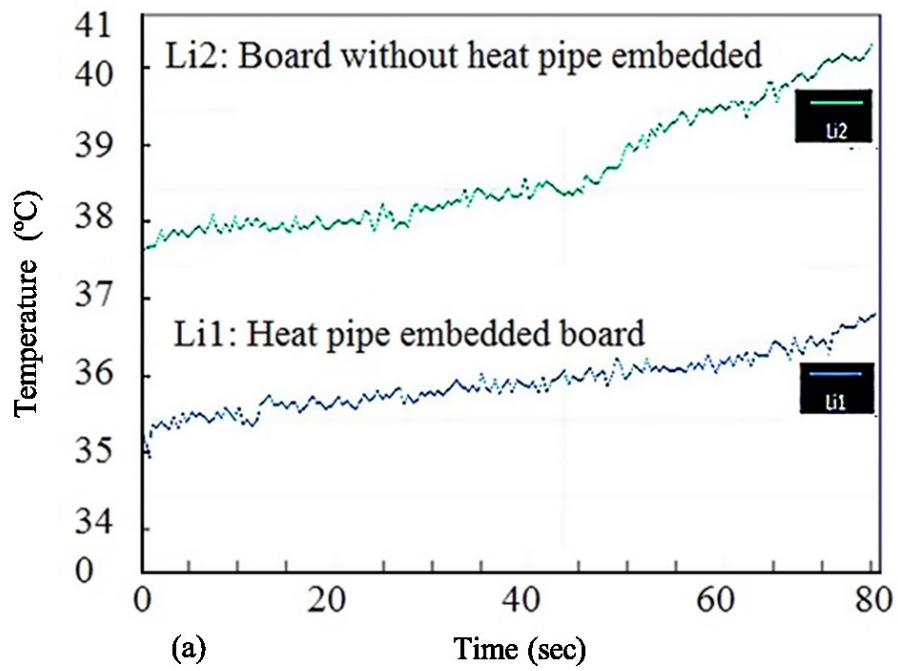


Figure 3-14: Comparison of heat pipe embedded and unembedded cases in a plate
 (a) Timewise variation and (b) IR images

CHAPTER IV

CONDENSATION EXPERIMENTS

In this chapter, various manufacturing techniques have been investigated to enhance the heat transfer characteristics of the condensation surface. These techniques include the fabrication of hydrophobic and super-hydrophobic surfaces. The measurement technique, manufacturing processes and coating method are also explained in detail in the chapter.

4.1 Basic Concept of Experimental setup

Since hydrophobicity is a key parameter for heat transfer systems such as heat exchangers, refrigerators, and industrially used condensers, our major research is focusing on the condensation of vapor in micro-nano-structured surfaces. In the framework of condensation research, investigations on heat transfer performance of the condenser of two commercially available heat pipes are carried out. There are many types of inserts that are used inside the heat pipe such as rectangular, triangular and trapezoidal grooves [72]–[74] or wick structures. The inserts of the heat pipes have been built as longitudinal square-grooves and longitudinal V-grooves compared with the unstructured surfaces (see Figure 4-1). Due to the fact, that the overall condensation-evaporation interaction inside the heat pipe is highly complex, the basic condensation process is investigated on plane copper surfaces with different topographies such as unstructured/smooth, square-grooved and V-grooved surfaces. The groove sizes were chosen to be $500 \times 500 \mu\text{m}$ related to the commercially available heat pipe.

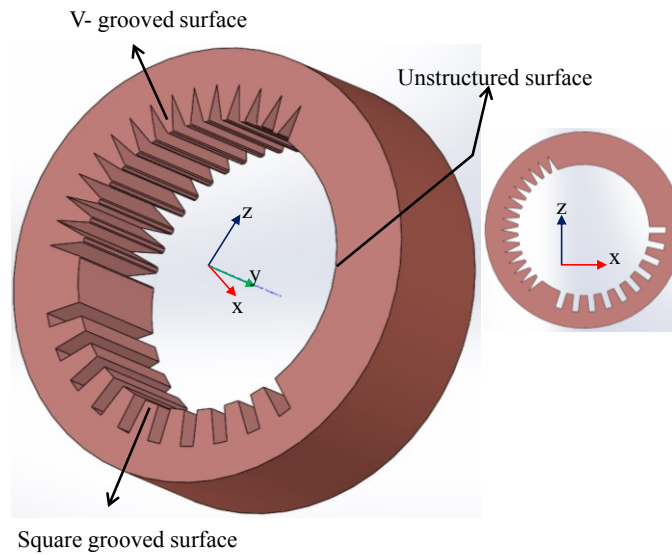


Figure 4-1: Schematic diagram of the axial grooves on the inner wall of heat pipe [75]

4.2 Microstructured Surfaces

Besides an unstructured surface, two surfaces with different structural geometries have been chosen as micro-structuring; longitudinal rectangular grooves and longitudinal V-grooves. The obstacles have been micro-milled onto the surfaces of copper blocks. In Figure 4-2, the longitudinal square grooved surface can be seen. The microscopic images show that a rather distinctive topography could be obtained. However, there are some fine-scaled rough areas which are due to the milling machines tool. Nevertheless, the cross-sectional view shows a reasonable manufactured rectangular shape.

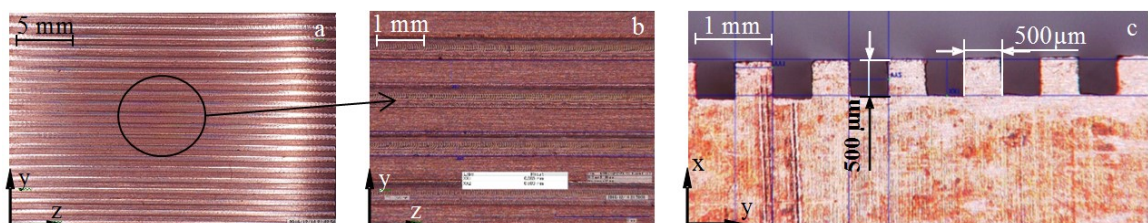


Figure 4-2: Longitudinal square-grooved surface: a) top view b) 4X view c) cross-sectional view

As it can be seen in Figure 4-3, grooves and crests over the longitudinal V-grooved surface cannot be achieved as sharp edges due to manufacturing constraints. The tales and the crests exhibit a radius. This can be attributed to the manufacturing process and the milling tool tip used. It seems that because of the low solidity of copper the milling machine has smeared the edges of the crests. The radius in the tales can be justified by the tip of the milling tool, which in generally must be curved to ensure material removal at this location. By considering the manufacturing capability, the longitudinal rectangular and V-grooved surfaces were reasonably manufactured for further use in the experiments.

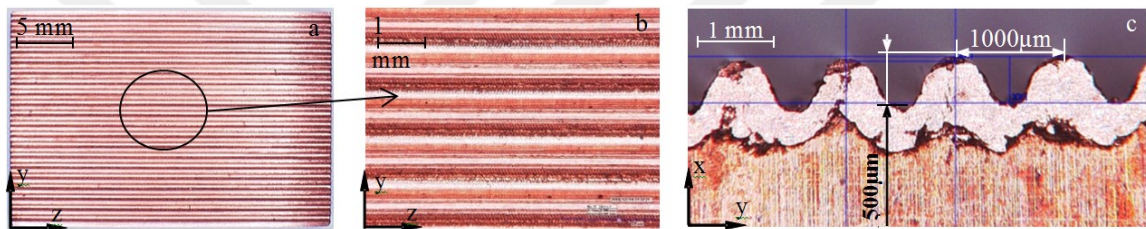


Figure 4-3: Longitudinal v-grooved surface: a) top view b) 4X view c) cross-sectional view

4.3 Fabrication of Hydrophobic Surfaces

This work has been performed jointly with researchers from Sabanci University in Istanbul. Fluorinated silane exhibits optimal properties for composing coatings resulting from hydrolysis and condensation of alkoxy silane groups on surfaces [76]–[78]. The layer can resist temperatures up to 125 °C, which was sufficient in terms of the experimental parameters used in this study. Triethoxy (3-isocyanatopropyl) silane IPTES (IUPAC) and 3-(Triethoxysilyl)propyl isocyanate 95 % ((C₂H₅O)₃Si(CH₂)₃NCO) are manufactured by Sigma Aldrich and reacted with perfluoro alcohol (C₆F₁₃OH), PFA (see Figure 4-4).

Synthesis of fluorinated silane compound is the next step in surface texturing. A molar ratio of 1:1 was considered with a 0.1 mol (24.7 g) of IPTES ($m_{w,IPTES} = 247.36$ g/mol) and 0.1 mol (27.5 g) of PFA ($m_{w,PFA} = 262.87$ g/mol). PFA was first added to flask and stirred at room temperature until it was totally dissolved. Subsequently, Triethoxy (3-isocyanatopropyl) silane was added and stirred very slowly, while the mixture was heated up incrementally to 80 °C. At 80 °C, the mixture was kept at constant stirring intensity for one hour. After this step, 0.6 ml of Dibutyltin dilaurate (DBDU) and 95 % of $((CH_3CH_2CH_2CH_2)_2Sn[OCO(CH_2)_{10}CH_3]_2)$ with a molar mass of $m_{w,DBDU} = 631.56$ g/mol as a catalyst was added into the mixture and stirred under nitrogen for 24 hours. After this process, the solid residue was removed from the flask and stored at room temperature.

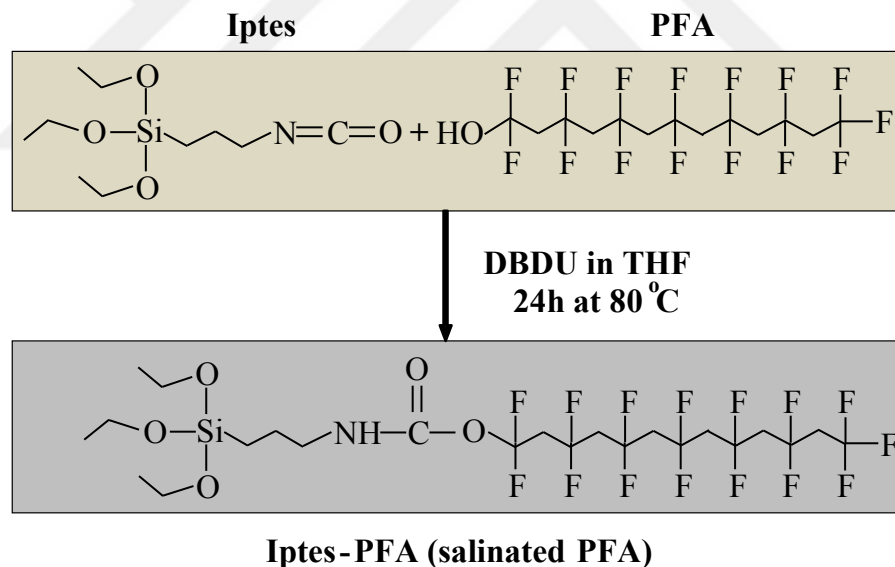


Figure 4-4: Overview of the chemical reaction of IPTES+PFA with the addition of Dibutyltin dilaurate (DBDU).

4.3.1 Fabrication of Hydrophobic Coating over Copper Surfaces

For the coating of the copper substrate, dip-coating method was used. At the stage of coating mixture preparation, IPTES+PFA monomer was mixed as a solution. 2 g of

monomer as 5 % (g of monomer/g of solution mixture) was dissolved in solution prepared by adding 23 ml ratio of 50 % THF (Tetrahydrofuran) and 22 ml ratio of 50 % DMF (Dimethylformaldehyde). The mixture was stirred for one hour. Then, the condensation surfaces of the copper blocks were dipped into the mixture for a minute. This step was repeated approximately 15 times. Then the coated copper blocks were kept in a furnace at 110°C for 24 hours.

Material characterization is the next step to understand the surface behaviour. To ensure chemical reaction between IPTES and PFA, Fourier-transform infrared spectroscopy (The Thermo Scientific™ Nicolet™ iS™10 FT-IR spectrometer) was used (see Figure 4-5). The N=C=O bond stretching is in the range of 2260– 2300 cm^{-1} . The isocyanate functional group disappears as shown in Figure 4-6 after reacting with the hydroxyl group of perfluoro alcohol and a new peak at 1600 cm^{-1} appears, which is proof of the completion [79]. By using a tensiometer device (Krüss K100MK2 Tensiometer) the surface tension at the surface was determined to be $\gamma = 43.68 \text{ N/m}$.

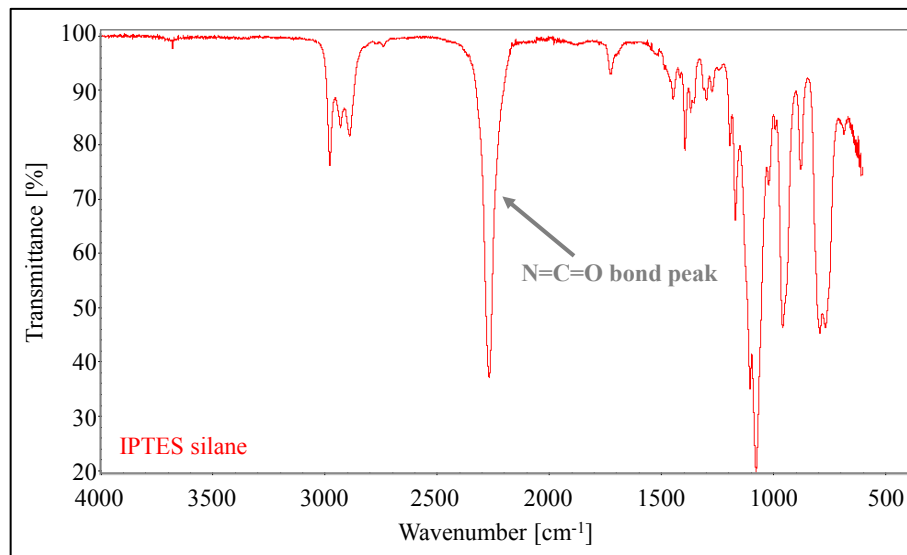


Figure 4-5: FT-IR image of IPTES silane

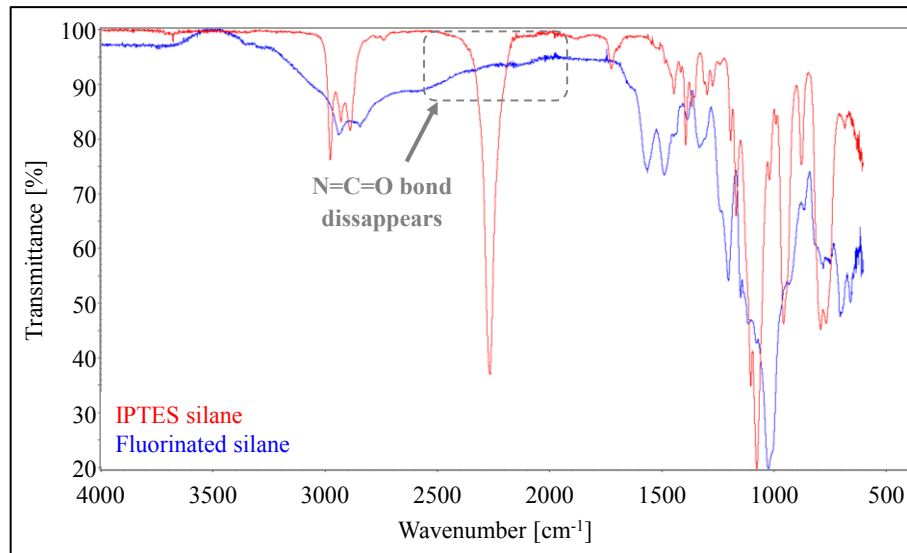


Figure 4-6: FT-IR comparison IPTES silane vs. fluorinated silane compound

4.3.2 Application of Hydrophobic Coating for Unstructured Surfaces

The obstacles have been micro milled onto the surfaces of copper blocks. In Figure 4-7 the longitudinal unstructured surface can be seen. The microscopic images show that a rather distinctive topography could be obtained and can be increased the hydrophobicity of the surface by dip coating process by using APTES SILANE liquid. However, there is some fine-scaled roughness in the first view c) and d) which are due to the coating liquid particle. Nevertheless, the cross-sectional view shows a coating layer thickness is 26 μm . By considering the manufacturing capability, the longitudinal unstructured surface was reasonably manufactured for further use in the experiments.

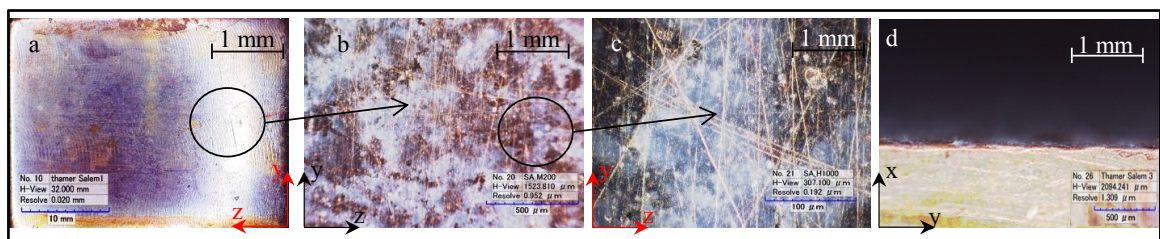


Figure 4-7: Microscopic images of the unstructured surface after coating procedure with IPTES SILANE: a) top view, b) 50x view c) 100x view d) cross-section at the solid-ambient interface

4.3.3 Application of Hydrophobic Coating for Micro-Structured Surfaces

After the dip coating process, the measurements of the droplet contact angles are obtained on the uncoated and coated surface for surfaces. Then the surface topography of the samples has been analyzed by using a high-resolution microscope (Hirox KH-7700). The surface topographies, shown in Figure 4-8 and Figure 4-9 are representing the square-grooved and v-grooved surfaces respectively. Then, the condensation surface topographies are captured after coating that are analyzed by using the microscope for all samples with different resolutions at five positions (see Figure 4-14 in section 4.5.1). The results have shown that a few particles of the coating are distributed semi-uniformly on square and V- grooves. In addition, results also show that the coating layer thickness is 20 μm for square groove (see Figure 4-8d), while the thickness of coating layer for the V-groove is 16 μm (see Figure 4-9d).

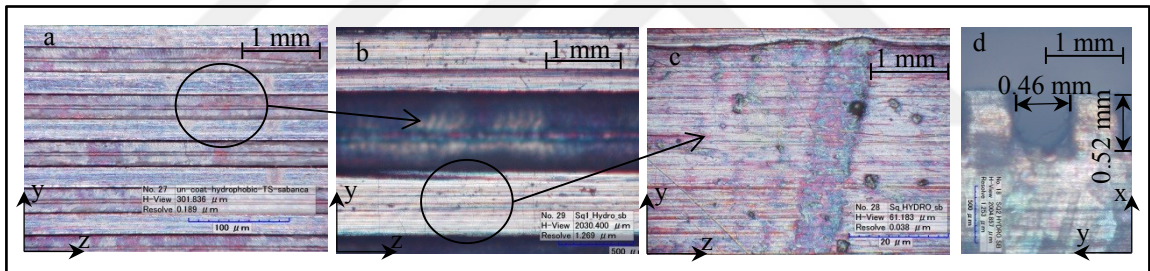


Figure 4-8: Microscopic images of the square groove surface after coating procedure with IPTES SILANE: a) top view, b) 50X view c) 100X view d) cross section at the solid-ambient interface

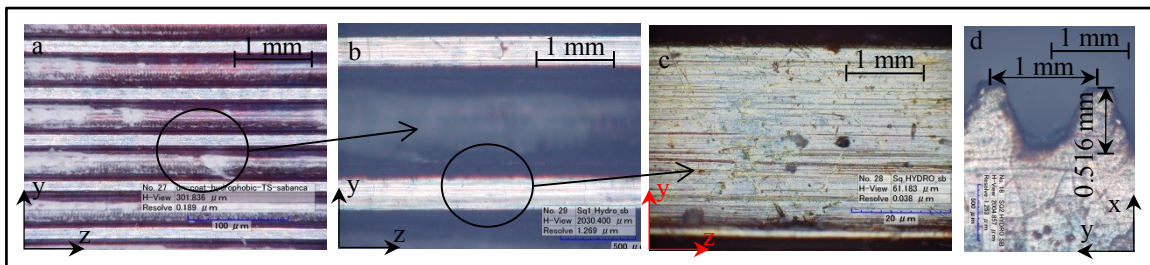


Figure 4-9: Microscopic images of the V- grooved surface after coating procedure with IPTES SILANE: a) Top view, b) 50X view c) 100X view d) Cross-section at the solid-ambient interface

4.4 Fabrication of Superhydrophobic Surfaces

A number of test vehicles are prepared in the current study. 20x30 (mm) copper samples are first cut and cleaned with a three-step alcohol treatment. Then, a commercially available chemical liquid (ultra-ever dry®) has been used to achieve superhydrophobic surface structured copper samples. The coating has been performed in two steps using a bottom coat and a top coat. Thermophysical properties and chemical properties of the coating material can be found in the manufacturers' data sheet [80]. 12 copper test vehicles (4 unstructured, 4 micro-square-grooved, 4 micro-v-grooved) have been prepared. The square-grooved and v-grooved samples are presented in Figure 4-2 and Figure 4-3.

To furnish the samples with a superhydrophobic coating, the dip coating technique has been utilized, which is widely used in industrial coating processes. The sample was fixed in a sample holder moving inside a desktop dip coating device shown in Figure 4-10a and Figure 4-10b, while all samples have been fixed at the shorter edge individually (see Figure 4-10d). After fixing the sample, the liquid mixture for the application of the bottom coat has been filled inside a beaker (see Figure 4-10c) embedded inside a holder aperture and has been mixed for about 5 minutes. Afterwards, the sample has been lowered at a constant velocity such that it was dipped in the liquid mixture. As soon as the surface was covered fully by the mixture, the immersion device has been operated reversely with similar velocity to until the sample was pulled out of the liquid. This procedure has been repeated for other samples and similarly when using the top coating liquid.

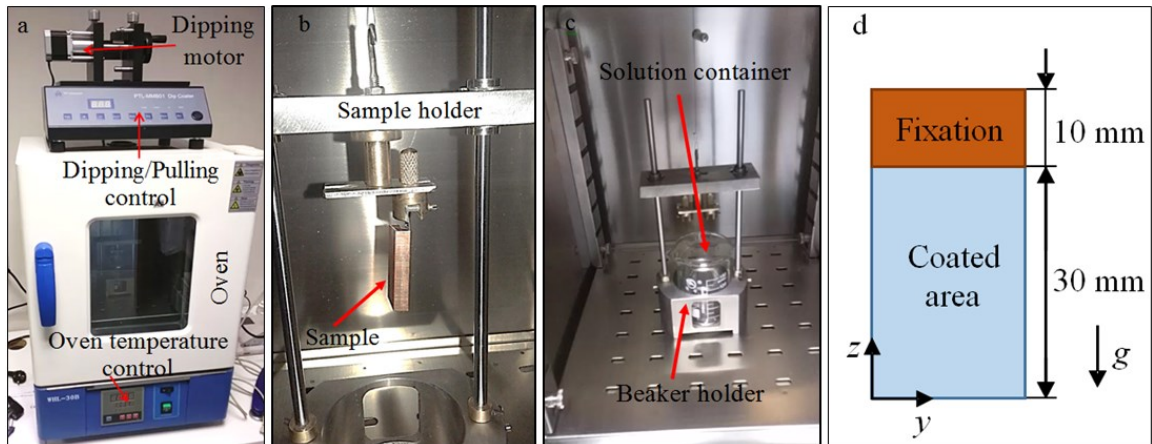


Figure 4-10: Dip coating technique: a) desktop dip coating device (PTL-MMB01) with immersion equipment (1 - 200 mm/min) b) sample holder c) beaker inside dip coating chamber d) Area covered by coating and fixation

4.4.1 Application of Superhydrophobic Coating for Various Surfaces

After the dip coating process and measurements on contact angles, the surface topography of the samples have been analyzed by using a high-resolution microscope (Hirox KH-7700). The surface topographies, shown in Figure 4-11, Figure 4-12 and Figure 4-13, are representing the unstructured surface, square-grooved and v-grooved surfaces respectively. Then, the particles from top coating are analyzed by using the microscope for all samples at five different positions (see Figure 4-14 in section 4.5.1). The results have shown that the particles are distributed semi-uniformly on unstructured and square groove surfaces, except for V-groove surface because the coating particles move inside the groove much intensely. Moreover, the shape of particles is semi-circular with an average diameter of coating particles for all samples is changing between 30 μm to 35 μm . While, the bottom coating covers 100% of the surface for each sample, the top-coating is wrapping around 75% because of using sprayer gone. In addition, results also show that particles are distributed around 50% on the crests of the square groove, while they are distributed only to the 25% of the V-groove surface.

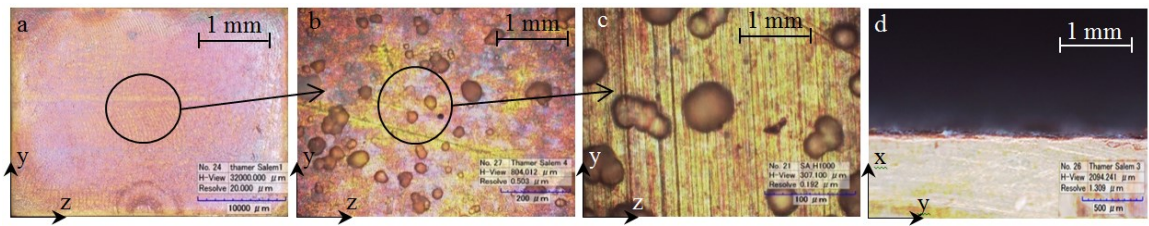


Figure 4-11: Microscopic images of the unstructured surface after coating procedure with Ultra-Ever Dry: a) top view, b) 50x view c) 100x view d) cross-section at solid-ambient interface

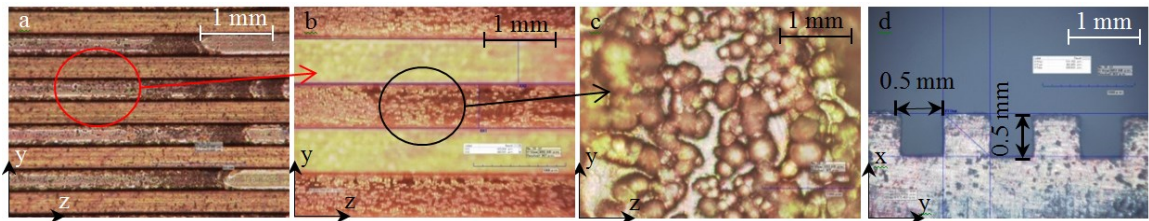


Figure 4-12: Microscopic images of the square-grooved surface after coating procedure with Ultra-Ever Dry: a) top view, b) 50x view c) 100x view d) cross-section at solid-ambient interface

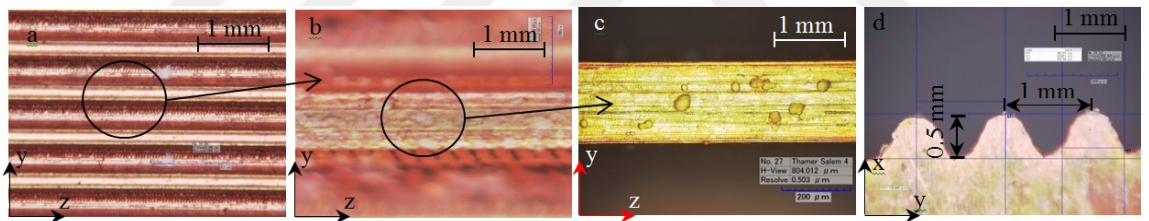


Figure 4-13: Microscopic images of the V-grooved surface after coating procedure with Ultra-Ever Dry: a) top view, b) 50x view c) 100x view d) cross-section at solid-ambient interface

4.4.2 Surface Coating Method

Coating process has been carried out in two parts as bottom coating and top coating (Ultra-Ever Dry®). First, the bottom coating has been organized by dip coating method. Optimum values of contact angle for bottom coating have been determined as 50 mm/min and 3-layers after several experiments. This method has been applied to three different types of samples, which are S-grooved, V-grooved and unstructured surfaces.

Each sample was dipped into a glass beaker of Ultra-Ever Dry and rested about 5 minutes (see section 4.4 Figure 4-10c). Then, the sample was removed from the liquid and left it to dry for one hour in a natural convection condition. Thus, the first layer of bottom coating was completed for each sample after it fully dried. Then, two more steps were followed as same as the first step in order to have three layers. After bottom coating process finished, top coating was applied to each sample again. In contrast to the bottom coating, the top coating process was done with Ultra-Ever Dry (top coating) liquid by using a spray pistol. Liquid was sprayed on each sample one pass from left to right direction, then it was left to dry for 24 hours. The chemicals used for achieving super-hydrophobic behavior on the surfaces had boiling temperatures of 138 °C and 149 °C at room ambient respectively. The optimum coating can be defined with respect to coating properties such as surface tension, density, adhesion etc with an increase in resistance of the temperature gradient to achieve high droplet contact angle. To find an optimum coating, several tests have been performed in order to ascertain the effect of immersion/pull velocity, the influence of the number of coating layer and the temperature effect. The first dip coating test was done by varying the pull speed from 50 to 200 mm/min for a single layer of coating (see **Table 4-1**) only on four unstructured samples in order to represent the reference test.

Table 4-1: Droplet contact angles prior to and after coating for different velocities

Sample	Immersion/pull velocity	CA prior coating	CA after coating
1	50	80.9°	164.9°
2	100	82.9°	163.6°
3	150	87.5°	152.9°
4	200	81.8°	150.5°

As a result, the lowest velocity of 50 mm/min has given the highest droplet contact angle, pointing out that higher immersion/pull velocities do not lead to any increase in CA. The reason might be a larger contact time between the surface and the liquid mixture, attaching the copper material adhesively.

Once the effect of immersion/pull velocity for coating was determined, a second experiment was accomplished for varying numbers of coating layers from 1 to 5 at a constant immersion/pull velocity. Using 50 mm/min as the immersion/pull velocity, five unstructured samples have been coated. The details of the coating layers for each sample are presented in **Table 4-2**, which shows the largest value of contact angle at three pass coating. The thickness of the coating layer has been determined with an optical microscope as approximately 24 μm .

Table 4-2: Droplet contact angle before and after coating for various coating layers

Sample	CA before coating	Uncertainty	Layers	CA after coating	Uncertainty
1	79.5°	0.4°	5	161.8°	0.9°
2	81.6°	0.8°	4	158.3°	0.4°
3	86.3°	0.3°	3	162.3°	0.9°
4	84.1°	0.2°	2	148.2°	0.5°
5	85.1°	0.2°	1	86.6°	0.1°

Finally, the effect of temperature has been investigated by means of an oven at temperatures between 25 °C and 95 °C for the duration of 1 to 3 hours for each of samples after coating with ultra-ever dry. The heat treatment results represented a small change of the contact angle with rising temperature from 25 °C to 95 °C (see **Table 4-3**). The drying time of the coating was about 60 minutes for bottom coating and 24 hours for top coating. As a conclusion, the effect of temperature has been neglected.

Consequently, a pull speed of 50 mm/min and a 3-layer coating has been selected for the coating of unstructured and micro-structured surfaces since it provided the highest droplet contact angle.

Table 4-3: Droplet contact angle at unstructured surfaces after heat treatment

Time (hour)	CA at 25 °C	CA at 95 °C
1	163.6°	161.3°
2	163.6°	162.8°
3	163.6°	165.8°

4.5 Experimental Details for Surface Energy Analysis

The main goal is to observe the enhancement in heat transfer by condensation phenomena. For this purpose, the first task is determined as investigating the effects of different heat flux (19- 76 W/cm²) and heat pipe orientations (from -90° to +90°) on the condensation process. Then, the attention was shifted to the condenser part of the heat pipe for the enhancement of the condensation process by considering two parameters such as surface topographies and wettability. Thus, test samples with different surface topographies have been designed and manufactured. A detailed uncertainty analysis has also been performed at the beginning of our study and key design parameters have been identified and analyzed by using the equations in Section C.1. In addition, droplet contact angle is very critical in the current study for discovering the nature of the surface wettability as hydrophilic or hydrophobic etc. Hence, the droplet contact angle measurements are performed before and after the chemical treatment by using sessile droplets (deionized water) for each of the treated surfaces. The surface treatment is shown in Section 4.4 and the related contact angle measurement procedures are explained in detail.

4.5.1 Contact Angle Measurement Procedure

Prior to coating, each sample has been cleaned by using a liquid acetone bath. Later, actual contact angles have been measured with a Tensiometer (KSV ATTENSION, Theta Lite, Optic Contact Angle Tensiometer) by using DI water. A large number of tests were utilized to adjust the volume of droplet between two boundaries and the field of view of the CCD camera of the Tensiometer device. Consequently, the optimal volume of the droplet is measured as 125 μL , and a non-slipping sessile droplet could be placed on the surfaces as well as within the FOV the shape of the droplet was detected fully. At each sample, a sessile droplet has been placed at five different locations individually while keeping the droplet volume constant (see Figure 4-14).

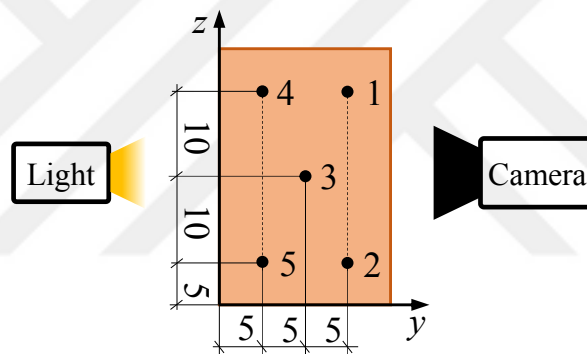


Figure 4-14: Locations of sessile droplets during contact angle measurements

The liquid droplet profile has been captured by using a high-end CCD camera (ThetaLite101 model). The contact angles were determined by using the software provided by the manufacturer of the Tensiometer. For the CA determination, a tangent starting at the location where the solid-liquid-vapor interface coincided has been created as already presented in Figure 5-2, section 5.2. A second line has been identified as a horizontal line indicating substrates' surface. Hence, contact angles have been calculated as the opening between these two lines for a particular droplet [81].

To elucidate the wettability characteristics, contact angles on all three surfaces have been determined using a contact angle measurement device (KSV Attention Theta Lite Optic Contact Angle). Sessile water (de-ionized) droplets with constant volume of 125 μL ($\text{O} = \sim 6.2 \text{ mm}$) were put at five different locations on the surfaces (see Figure 4-14). Subsequently their shapes were recorded within the camera field of view of 5 mm x 10 mm (spatial resolution: 10 $\mu\text{m}/\text{pixel}$). The average CA for each location was calculated based on five droplets placed at each location:

$$\overline{\text{CA}}_n = \frac{\sum_n \text{CA}_n}{n} \quad (4-1)$$

Using the following expression, the average contact angle for the entire surface has been determined;

$$\overline{\text{CA}} = \frac{\overline{\text{CA}}_1 + \overline{\text{CA}}_2 + \overline{\text{CA}}_3 + \overline{\text{CA}}_4 + \overline{\text{CA}}_5}{5} \quad (4-2)$$

4.6 Experimental Parameters

The experimental parameters are listed in Table 4-4. Before starting each experiment, a degassing procedure was performed using a vacuum pump to ensure that non-condensable gases were minimized by sucking the gases inside the system. After that, the vacuum pump was turned off and the saturated vapor was released into the system. For each measurement point, the steady-state condition was ensured through the continuous monitoring of temperature and pressure. As soon as the fluctuations for all measured temperatures and pressures were in the range of $\pm 0.5 \text{ K}$ and $\pm 0.01 \text{ Bar}$, respectively, the measured values were recorded for about 30 seconds. High-speed cameras videos were simultaneously recorded to capture the droplet formation and wetting process on the surface. An uncertainty analysis is performed according to [82]

that resulted in ± 0.3 K and ± 0.1 Bar for temperature and pressure measurements respectively.

The condensation system was run with its maximum efficiency until it reached the steady state condition (30 minutes) for each 33 measurement points of the different mass flow rate of cooling liquid from 4-87 g/s and the temperature of cooling liquid chiller was kept constant. A liquid chiller provides subcooled liquid ($T_{l,in} = 10^{\circ}\text{C}$) which is pumped through an insulated piping to the condensation section. Then, all the tests were tested with different pressures inside the vapor chamber from 1.02-1.25 Bar at the top of the condensation section and streams along a subcooled copper wall.

A total of 184 tests were carried out for each surface with the following variables:

- The vapor pressure inside the vapor chamber varied for a range of 1.02 and 1.25 Bar, and this was done four times.
- The mass flow rate of the cooling liquid was controlled by a Rotameter controller valve, and the chiller pump speed on the water amount passes through the liquid chamber to acquire different values. These values were 33 measurements points at a saturation pressure of 1.02 and 1.10 Bar, and 13 measurements points for each saturation pressure of 1.20 and 1.25 Bar.

Table 4-4: Design of experiments (DOE)

		Uncoated	Coated			
$p_{v,ch}$	Bar	1.02	1.02	1.10	1.20	1.25
$T_{v,ch}$	$^{\circ}\text{C}$	100.2	100.2	102.3	104.8	106.0
\dot{M}_l	g/s	4.5 – 87.3				
$T_{l,in}$	$^{\circ}\text{C}$	10.0				

An experimental setup for the study of heat transfer and hydrodynamics during the condensation has been designed and built as presented in Figure 4-15. The setup

includes a loop for vapor line and a second loop for chilled water line. The working liquid (deionized water) has been stored in an insulated reservoir and has been heated by a heating coil using a high power supply. Concurrently, the pressure and temperature of the liquid/vapor mixture inside the reservoir have been monitored by an in-house developed LabView© program. To reach desired set points, the power input provided by the high power supply that has been controlled by means of a PID system. The generated vapor has been guided through a temperature controlled insulated piping towards the condensation section. The vapor line wall temperature has been controlled by temperature measurements such that a wall temperature did not fall below the vapor saturation temperature at the particular pressure. The saturated vapor enters as a single-phase stream at the top of the condensation section and streams along a subcooled copper wall. There, it partially condenses and exits from the bottom as a liquid-vapor mixture and streams further towards a water-cooled heat exchanger. In addition, more details of experiment setup is explained in APPENDIX B (see **Figure B-10**).

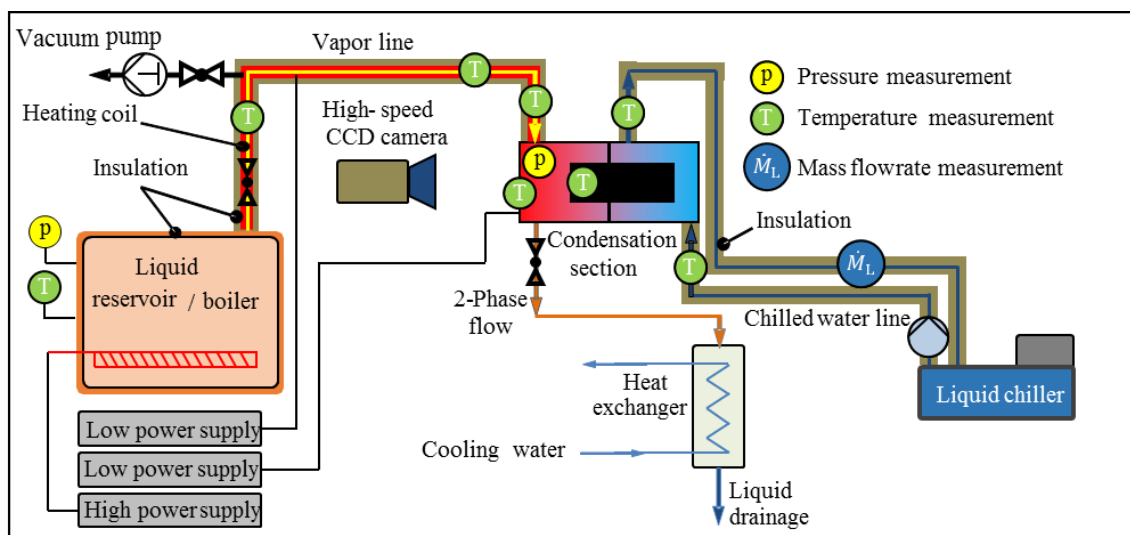


Figure 4-15: Experimental setup [83]

The main part of the condensation section is explained in **Figure 4-16**. The liquid chamber has one inlet and one outlet for the chilled water and temperature measurements. Similarly, the vapor chamber has also two connections for the vapor supply at the top and at the bottom for the two-phase flow exit. Furthermore, the vapor chamber is provided with an optical glass window to observe the condensation process at the copper surface using a CCD high speed camera. The test section has been designed solely for the determination of the effect of different surface properties on the condensation process, rather than investigating the influence of non-condensable gases. In addition, a resistive rope heater with a voltage regulator was wrapped around the exterior of the optical glass and the vapor line to maintain a constant glass temperature and prevent any liquid condensation inside the vapor tube. The resistive heater specifications are given in **Table B-4**.

4.7 Heat and Mass Transfer Analysis

During the condensation tests with different operating vapor pressure and surface topographies, the parameters belonging to following process were measured for the heat transfer analysis. Then, the cooling liquid inlet ($T_{l,in}$) and outlet ($T_{l,out}$) temperatures on the back-side of the heatsink inside the liquid chamber are utilized to determine the heat flux \dot{q}_s (heat capacity law) by measuring the mass flow rate of cooling liquid.

$$\dot{q}_{s,Exp} = \frac{\dot{M}_{l,in} C_{p1} (T_{l,out} - T_{l,in})}{A_{cond}} \quad (4-3)$$

The surface temperature T_s in z- and y- directions on the front-side of heat sink was calculated by using the Fourier law of conduction. It is also used to explain the procedure by calculating the condensation surface temperature in the main part of the condensation section that represents the core of the experimental setup (see

Figure 4-16). In polycarbonate housing the vapor chamber and the liquid chamber are separated with a copper block manufactured as a single body. One side of the block was directed towards the vapor chamber where this side acted as the condensation surface ($y = 20 \text{ mm}$ and $z = 30 \text{ mm}$). Moreover, six calibrated T-type thermocouples, as shown in **Figure 4-16**, were embedded in order to detect the temperature distribution inside the copper block. In the opposite direction, thin fins manufactured at the copper block were exposed to water supplied by a temperature-controlled chiller. The liquid enters to the chamber from the bottom surface and leaves from the top. At the same time, the inlet and outlet temperatures were measured. To avoid any leakages from the liquid and vapor chambers several EPDM sealing parts were used. To observe the condensation process at the copper surface, a glass window made out of calcium fluoride was mounted at the front side of the vapor chamber to allow optical access with a high-speed camera (HSC) for which the field of view had been adjusted to $10 \text{ mm} \times 20 \text{ mm}$ with a spatial resolution of 1024×768 pixels ($20 \mu\text{m}/\text{pixel}$ and fluid motion has been recorded at a frame rate of 800 Hz.

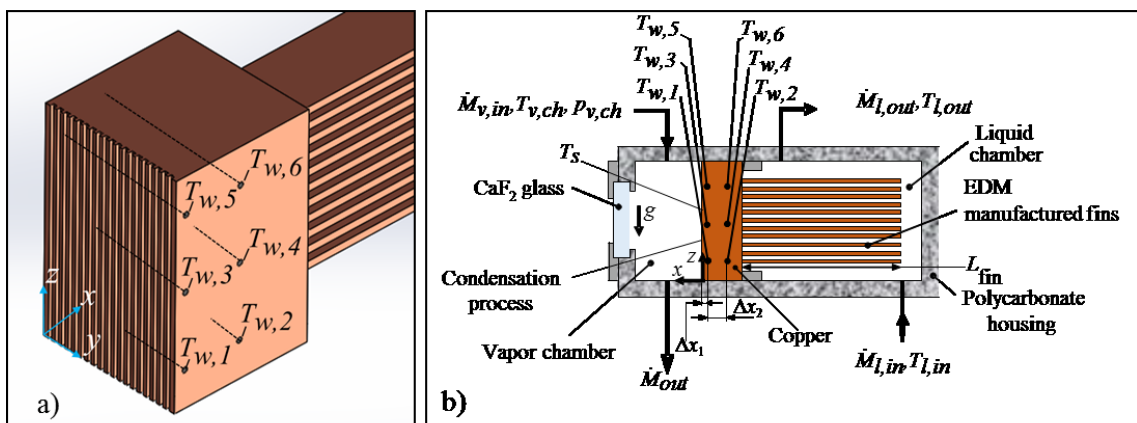


Figure 4-16: a) Position of the embedded thermocouples in copper samples, b) Cross-sectional view of the condensation chamber and the liquid chamber

Then, the condensation surface temperature was calculated based on the following equation:

$$T_{s,Exp} = \dot{q}_{s,Exp} \frac{\Delta x_1}{K_{cu}} + \frac{T_{w,1} + T_{w,3} + T_{w,5}}{3} \quad (4-4)$$

In order to evaluate the homogeneity of the temperature distribution in y- and z- direction inside the copper block, the temperature data are compared by using;

$$\bar{T}(x_a) = \frac{T_{w,1} + T_{w,3} + T_{w,5}}{3} \quad (4-5)$$

$$\bar{T}(x_b) = \frac{T_{w,2} + T_{w,4} + T_{w,6}}{3} \quad (4-6)$$

Average temperatures based on the thermocouple readings positioned at the planes x_a and x_b . shown in Figure 4-17. However, the detected deviations of wall temperatures at the planes x_a and x_b are also displayed as dimensionless values. In both cases, the trend is quite similar, however the deviation at plane x_a indicates slightly larger differences in the range $T_{v,ch} - T_s = 20 - 60$ K. This might be due to the heat conduction in y and z directions, since the side walls of the copper block were in contact with the polycarbonate housing via a narrow area which is quite close to the measurement plane x_a . Nevertheless, the deviations for temperature measurements in the planes x_a and x_b are less than 2.5 % of the corresponding mean wall temperatures $\bar{T}(x_a)$ and $\bar{T}(x_b)$, respectively, which are in an acceptable range.

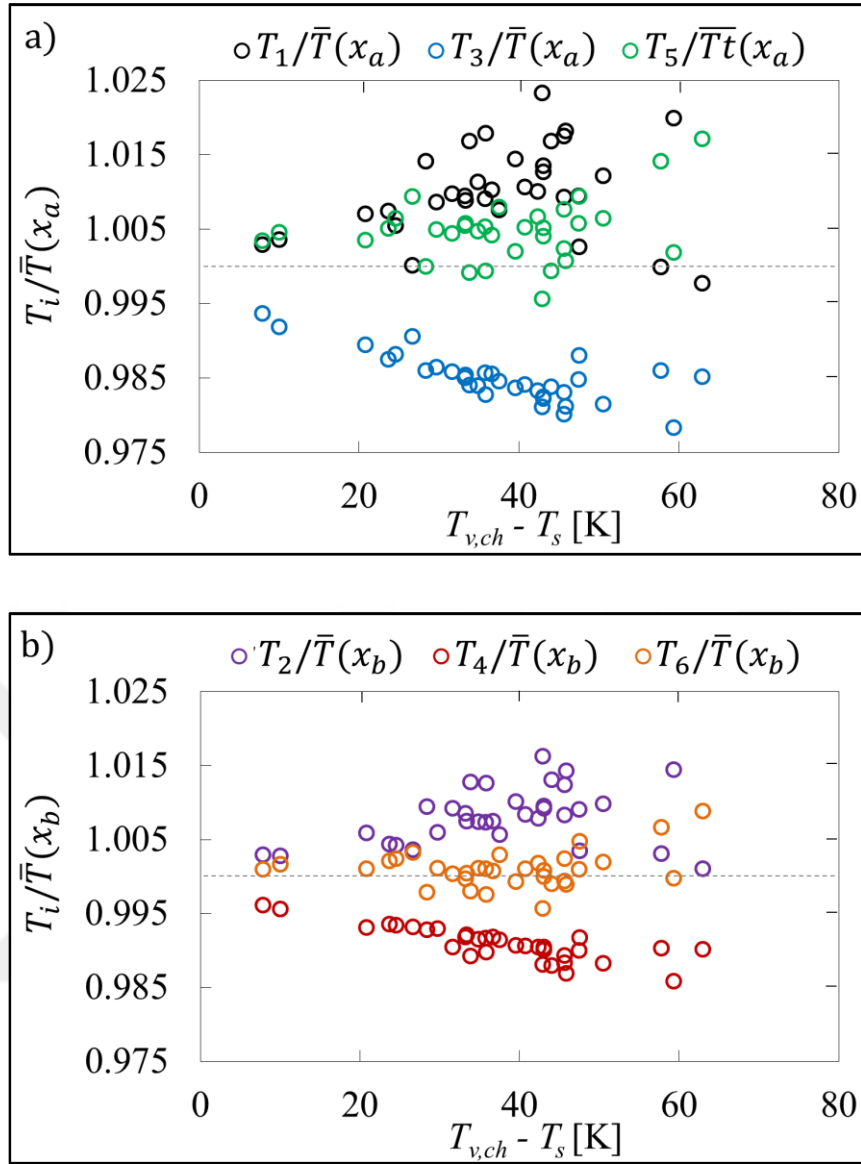


Figure 4-17: Deviation of wall temperatures measured inside the uncoated copper block vs. subcooling temperature $T_{v,ch} - T_s$ for planes x_a (a) and x_b (b)

While the mass flow rate is determined through the reading of a mass flow meter, the condensation heat transfer coefficient HTC was calculated from Newton law of cooling;

$$HTC_{Exp} = \frac{\dot{q}_{s,Exp}}{\Delta T_{sub}} \quad (4-7)$$

Where $\Delta T_{sub} = T_{v,ch} - T_s$. As a referencing parameter for high-speed images, the single-phase flow of cooling liquid inside the liquid chamber between the fins was determined by;

$$Re_1 = \frac{u_1 W_{fin}}{\nu_1} \quad (4-8)$$

While, the inlet velocity of cooling liquid was determined with;

$$u_1 = \frac{\dot{M}_1}{\rho_1 A_{1,in}} \quad (4-9)$$

The liquid density and liquid dynamic viscosity were taken at mean liquid temperature ($T_{l,mean} = (T_{l,in} + T_{l,out})/2$) that is measured in the cooling liquid line. Nu number of condensation is also calculated by this formula;

$$Nu_{Exp} = \frac{HTC_{Exp} L_{cond}}{K_{l,sat}} \quad (4-10)$$

However, the heat and mass transfer analysis for changing the liquid phase to the vapor inside the boiler has not been determined. Only the convective heat transfer between the copper fin and cooling liquid inside the liquid chamber; and also between the condensation surface and the vapor inside the vapor chamber have been analyzed by using the measured data. By considering the measurement data, new correlations for the convective heat transfer in Drop-filmwise condensation (DFWC) have been developed for all surface topographies. Moreover, the approach to develop correlations is elucidated in section 5.3.1. An analytical model has been developed by using EES program for the liquid film condensation and their prediction will be compared with the experimental data in Chapter 6. Moreover, the experimental results for all heat transfer parameters such as heat flux, HTC and Nu number have been compared with different correlation formula and with others authors' studies (see Section 6.5). Hereby, it was intended to enhance the condensation heat transfer on the active surface by increasing the droplet nucleation for different surface topographies and wetting surfaces to differentiate the effect of the hydrodynamic development of condensation for all surfaces.

CHAPTER V

THEORETICAL STUDY

Wetting phenomena over the condensation surface is also studied in this chapter. Firstly, capillary Laplace equation and thermodynamic model were utilized to analyze the droplet contact angle and condensation surface energy. Secondly, the experimental condensation results were validated by applying two correlations found in literature. In addition, uncertainty analysis of the experimental study was performed for various mass flow rates of cooling liquid at 1.02 Bar. The classification of wetting phenomena as hydrophobic and hydrophilic surfaces is explained in sections 5.1 and 5.2 respectively by considering two important parameters such as droplet contact angle and surface free energy.

5.1 Droplet Contact Angle

The wettability for a surface where deionized water is used can be easily determined by measuring the contact angle of the liquid droplet. While the measured contact angle at an ideal surface (surface roughness = 0 μm) can be named as Young contact angle (see Eq. 5-1) which describes the balance at the three-phase contact line represented by the coincidence of solid, liquid and vapor phases. The actual contact angle on a real surface (surface roughness > 0 μm) is defined as the opening between the tangent at the liquid-vapor interface and the actual local surface of the solid (see Figure 5-1).

$$\theta_Y = \cos^{-1}((\gamma_{sv} - \gamma_{sl}) / \gamma_{lv}) \quad (5-1)$$

The apparent contact angle is measured on a rough surface between the liquid-vapor and the liquid-solid interface line that appears clearly at the solid surface [84]. The apparent

contact angle ($\theta_W = \theta_m$) can be calculated according to Wenzel equation (see Eq. 5-2) [17] in which the roughness ratio is defined as ($rr = 1$ for a smooth surface, $rr > 1$ for a rough one) [84].

$$\theta_W = \cos^{-1}(rr \cos \theta_Y) \quad (5-2)$$

$$rr = \text{actual surface area} / (\text{projected solid-liquid surface area}) \quad (5-3)$$

On the other hand, Cassie et al. [85] studied the wettability of porous surfaces by developing a new model to analyze the apparent contact angle of the liquid droplet on a rough surface. Their model considers two mechanisms, the trapped air underneath the droplet and the interface energies, the energy of the solid-liquid interface and the one of liquid-air interface beneath the droplet. For this approach, the Cassie-Baxter contact angle θ_{CB} has to be calculated as a function of Young contact angle θ_Y and an area fraction f factor as:

$$\theta_{CB} = \cos^{-1}[f \cos \theta_Y + f - 1] \quad (5-4)$$

where:

$$f = (\text{unit cell shaded area} / \text{unit cell total area}) \quad (5-5)$$

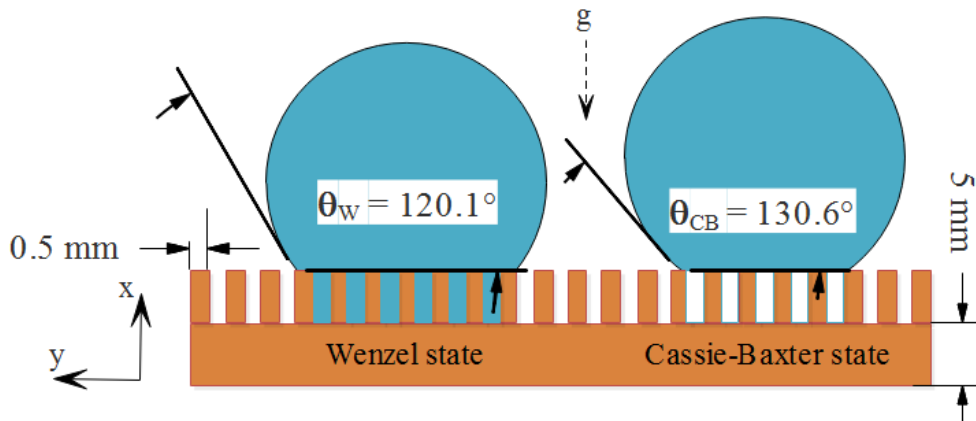


Figure 5-1: Definition of contact angles, apparent or measured contact angle on a rough (Wenzel) surface (θ_W), Cassie-Baxter contact angle (θ_{CB})

5.2 Surface Free Energy Analysis

Surface free energy of wetting has been analyzed on the rough hydrophobic surface by using a thermodynamic model for each of Wenzel and Cassie-Baxter states as a function of Young contact angle. Moreover, the contact angle for each wetting state with the lowest surface energy is relative to the equilibrium contact angle model. These two universal models (Wenzel and Cassie-Baxter) are used to know the wetting modes such as hydrophobic and hydrophilic only to the local minimum surface energy [16]. The total free surface energy can be calculated by [86]:

$$G=G^0+A_{\text{int}}\gamma \quad (5-6)$$

The total change in free surface energy between the initial state; when the liquid droplet does not touch the surface, and the final state; when the droplet touches the surface as a function of the droplet contact angle, can be represented as a result of interfacial energy for three different interfaces solely:

$$\Delta G=\Delta \int_{\text{sl}} \gamma_{\text{sl}} dA_{\text{sl}}+\Delta \int_{\text{sv}} \gamma_{\text{sv}} dA_{\text{sv}}+\Delta \int_{\text{lv}} \gamma_{\text{lv}} dA_{\text{lv}} < 0 \quad (5-7)$$

By simplifying Eq. 5-7, the change in free surface energy for each state can be found through the following equations [16]:

$$\Delta G_{\text{W}}=(\gamma_{\text{sl}}-\gamma_{\text{sv}})\Delta A_{\text{sl,W}}+\gamma_{\text{lv}} \Delta A_{\text{lv,W}} \quad (5-8)$$

$$\Delta G_{\text{CB}}=(\gamma_{\text{sl}}-\gamma_{\text{sv}})\Delta A_{\text{sl,CB}}+\gamma_{\text{lv}} \Delta A_{\text{lv,CB}} \quad (5-9)$$

Generally, there are two significant forces, interfacial and gravitational force that can directly affect the shape and hence the wetting characteristics of the liquid droplet. The

gravitational force is responsible for the extension and flattening of a sessile droplet, while the counteractive surface tension causes a decrease of the area wetted by the droplet by pulling the liquid mass to become a sphere. Moreover, the forces equilibrium on the liquid droplet can be calculated mathematically by using capillary Laplace equation, which describes the droplet shape to determine the surface tension.

$$\frac{\theta_{CL}}{2} = \tan^{-1}(H/DR) \quad (5-10)$$

The droplet contact angle $\theta_{CL}/2$ can be easily calculated by analyzing the droplet shape by means of the radius and height of droplet (see Figure 5-2) [81].

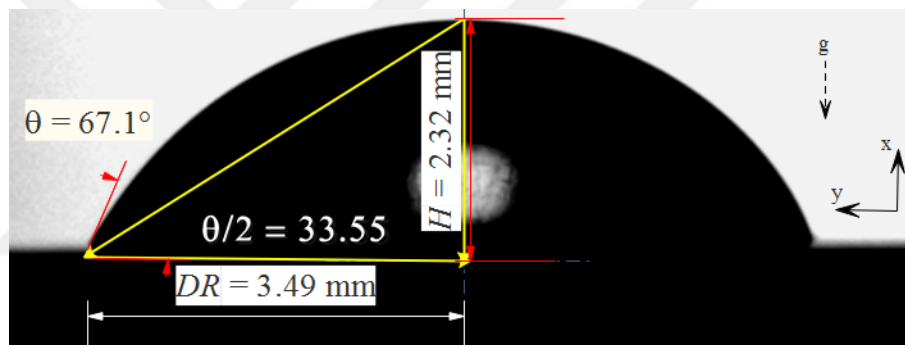


Figure 5-2: Droplet contact angle ($\theta_{CL}/2$) on uncoated, polished surface

5.3 Analytical Calculations of Untreated Condensation Surface

In this section, the experimental results of the condensation test with different surface topographies (unstructured, square groove and V-groove) have been evaluated. The results have been compared analytically by using EES program, and numerically by using Icepak program and by using different correlations.

5.3.1 Heat Transfer Analysis

The Drop-Film-wise condensation (DFWC) on the vertical copper substrate with different surface topographies are analyzed analytically by using two approaches (see

Figure 5-3). The first approach is applied for the current research by using EES program to design the copper block in the first step by detecting the optimum dimensions of Heatsink such as (L_{fin} , t_{fin} , S_{opt} and n_{fin}). The total heat transfer rate from the fins to the cooling liquid inside the liquid chamber is determined by modeling the copper block, which is related to the dimensions of a corresponding heatsink geometry and the experimental input data such as T_s , $T_{v,ch}$, $T_{l,in}$, and $\dot{M}_{l,in}$. As a result, main heat transfer parameters such as HF, HTC, and Nu are calculated analytically as a function of $\dot{Q}_{fin,total}$, subcooling temperature (ΔT_{sub}) and condensation surface area (T_s). Next, the second approach is performed for considering the condensation phenomena on a vertical flat plate that is cooled by using a cold plate according to Nellis and Klein [62]. This second analytical calculation is carried out by using EES program to determine the average heat transfer coefficient (\bar{h}) and after that to find the rest parameters such as heat flux and Nu number. In addition, analytical results from the second approach are used to validate each of the current analytical and experimental results. The experimental results are also validated by using two correlations published in [52] and [87]. The first correlation suggested by Ma et al. [52] takes film-wise condensation on a vertical circular plate into account, while the correlation of Ryan et al. [87] is employed of the condensation phenomena on a horizontal tube as a function of saturation and subcooling temperatures. Additionally, new correlations for each heat transfer parameters such as heat flux, HTC and Nu as a function of input experimental data (T_s , T_{sat} , etc.) are developed in this work by using SPSS program. A schematic diagram including the analytical approach, the method for correlation development, and data comparison is presented in Figure 5-3.

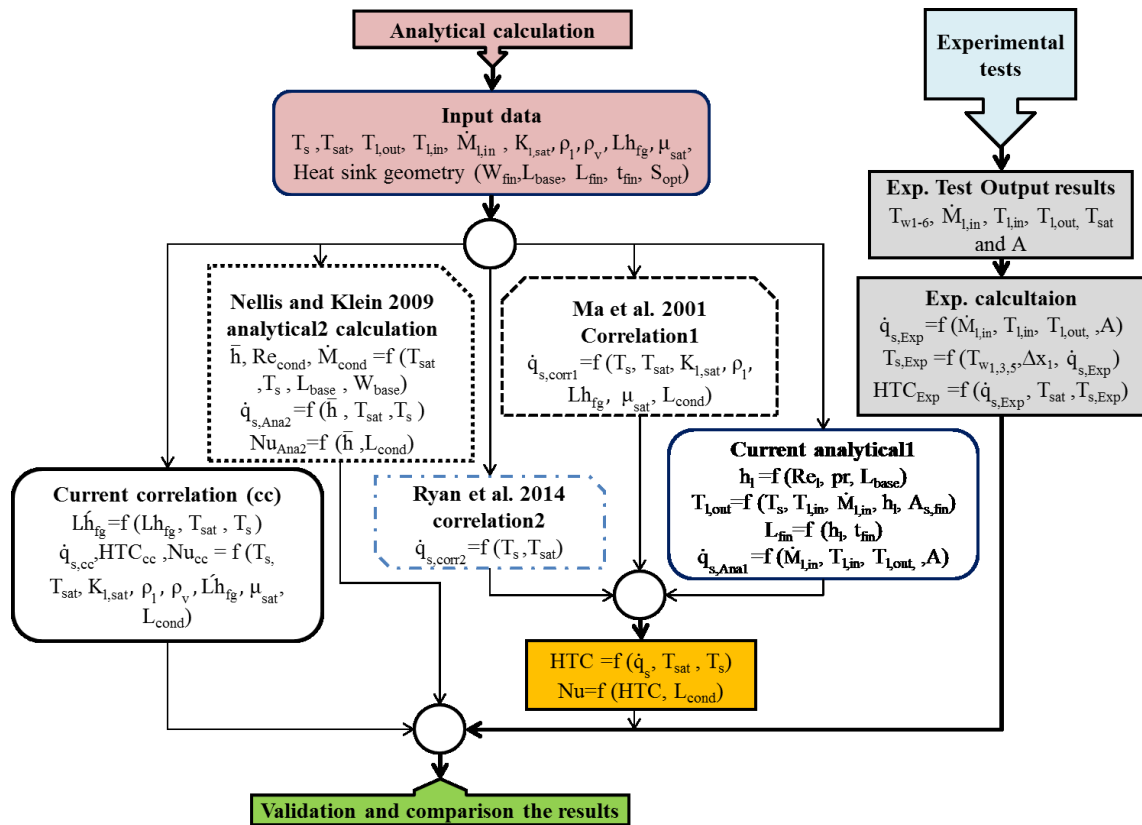


Figure 5-3: Schematic diagram of the analytical approach

5.3.2 Analytical Analysis

The geometric configuration of the substrates used in the experimental study has been based on a finned heat sink design. To determine the geometry necessary for the expected heat transferred from the vapor to the substrate at particular operating parameters, optimal dimensions of fins positioned at the opposed face towards the cooling chamber had to be elucidated. Fins should have enough surface area with a moderate pressure drop and hence they should ensure sufficient heat transfer rate at a preset confined volume. For this purpose, a heat sink model as shown in Figure 5-4 has been used such that heat can be released from the fins to the cooling liquid bulk by forced convection induced through the chiller pump. Furthermore, a microscopic analysis of the droplet-surface interaction dynamics and wettability phenomena has not been included, rather a heat transfer balance calculation procedure has been conducted, since the aim of these calculations was to determine the fin dimensions using a

simplified model and correlations according to literature. The calculations have been performed according to [88]. The surface at the back of the copper substrate has been provided with a multiple-fin array in order to transfer fully the heat flux generated by the phase change of the vapor at the surface A_{cond} at T_s . The sidewalls (A_a) have been considered adiabatic, since in the real configuration in the vicinity of A_a the housing has been designed as polycarbonate material with low thermal conductivity (0.21 W/m-K). The performance of the heat sink is computed by increasing either the surface area of the fins or the heat transfer coefficient between the cooling liquid and the fins' surfaces. The heat transport between the fins and the cooling liquid has been contemplated as forced convection. The calculations on optimum dimensions of the fins have resulted to $L_{fin} = 45$ mm, $t_{fin} = 1$ mm and $n_{fin} = 11$ with a total heat flux dissipation of 100 W/cm² from the copper block to the cooling liquid. Next, analytical calculations have been conducted by using Engineering Equation Solver (EES) as a function of the input experimental data such as (T_s , $T_{v, ch}$, etc) for each sample. Analytically determined heat transfer parameters (HTC, HF, and Nu) have been obtained assuming DFWC occurred at the condensing surface (see Figure 5-4).

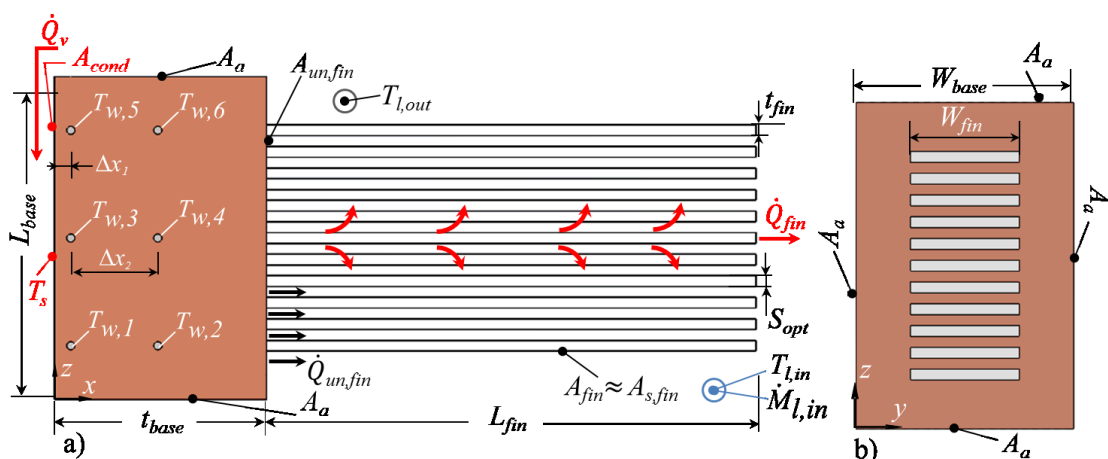


Figure 5-4: Schematic diagram for the heat transfer analysis of finned copper (unstructured/microstructured) substrates: a) side view, b) view from the back

In this case, the maximum heat transfer from the fin can be expressed as [89]:

$$\dot{Q}_{\text{fin,max}} = A_{\text{fin}} h_1 \Delta T_{\text{base}} \quad (5-11)$$

where $\Delta T_{\text{base}} = (T_s - T_{l,\text{in}})$ and $A_{\text{fin}} = 2(W_{\text{fin}} + t_{\text{fin}})L_{\text{fin}}$. Re number for the liquid flowing between the fins is calculated using [88]:

$$\text{Re}_1 = \frac{u_1 W_{\text{fin}}}{\nu_1} \quad (5-12)$$

The average heat transfer coefficient between the fins has been simplified as a function of Re number of the cooling liquid at the back-side of heat sink inside the liquid chamber by using [88]:

$$h_1 = 0.664 \frac{K_1}{W_{\text{base}}} \text{Re}_1^{0.5} \text{Pr}_1^{1/3} \quad (5-13)$$

Total heat transfer rate ($\dot{Q}_{\text{fin,total}}$) of the heat sink has been composed with the following expression [90] and [91]:

$$\dot{Q}_{\text{fin,total}} = n_{\text{fin}} (\dot{Q}_{\text{un,fin}} + \dot{Q}_{\text{fin}}) = h_1 A_{\text{fin,total}} (T_s - T_{l,\text{in}}) \quad (5-14)$$

where $A_{\text{fin,total}} = n_{\text{fin}} (2(W_{\text{fin}} + t_{\text{fin}})L_{\text{fin}}) + (W_{\text{fin}} S_{\text{opt}})$

The heat transfer rate from the unfinned surface of the heatsink has been determined by [92] :

$$\dot{Q}_{\text{un,fin}} = A_{\text{un,fin}} h_1 \Delta T_{\text{base}} \quad (5-15)$$

where: $A_{\text{un,fin}} = (W_{\text{base}} L_{\text{base}}) - n_{\text{fin}} (t_{\text{fin}} W_{\text{fin}})$

Heat transfer rate at the fins have been contemplated assuming very long fins [88]:

$$\dot{Q}_{fin} = [2h_l(W_{fin} + t_{fin})K_{cu} W_{fin} t_{fin}]^{0.5} \Delta T_{base} \tanh(\beta) = \eta_{fin} \dot{Q}_{fin,max} \quad (5-16)$$

while $m = \left(\frac{h_l P}{K_{cu} A_{cr}}\right)^{1/2}$ and $\beta = m W_{fin} = 1.4192 + 1.125 \frac{h_l W_{fin}}{K_{cu}}$, and $P = 2(W_{fin} + L_{fin})$

The fin length at a constant fin thickness can be calculated by using the following equation[88]:

$$L_{fin} = \beta \left[K_{cu} \frac{t_{fin}}{2h_l} \right]^{0.5} \quad (5-17)$$

The optimum number of fins as a function of t_{fin} has been calculated with [88]:

$$n_{fin} = \frac{W_{base}}{S_{opt} + t_{fin}} \quad (5-18)$$

The outlet temperature of the cooling liquid can be calculated by using the energy balance for constant surface temperature (T_s) on the active condensation surface [93]:

$$T_{l,out} = T_s - \left[(T_s - T_{l,in}) \exp\left(\frac{h_l A_{s,fin}}{\dot{M}_{l,in} C_{p_l}}\right) \right] \quad (5-19)$$

where: $A_{s,fin} = 2(W_{fin} S_{opt}) + 2(L_{fin} W_{fin}) \approx A_{fin}$

The amount of heat flux transferred to the cooling liquid (de-ionized water) through forced convection has been determined with [91]:

$$\dot{q}_{s, Anal} = \frac{\dot{M}_{l,in} C_{p_l} (T_{l,out} - T_{l,in})}{A_{cond}} \quad (5-20)$$

while the heat transfer coefficient can be calculated using:

$$HTC_{Anal} = \dot{q}_{s, Anal} / \Delta T_{sub} \quad (5-21)$$

The characteristic length for the nucleation condensation process is determined as [62]:

$$L_{\text{cond}} = \sqrt{\frac{\gamma}{g(\rho_{l,\text{sat}} - \rho_{v,\text{sat}})}} \quad (5-22)$$

Nu number for condensation is calculated with:

$$\text{Nu}_{\text{Anal}} = \frac{\text{HTC}_{\text{Anal}} L_{\text{cond}}}{k_{l,\text{sat}}} \quad (5-23)$$

5.3.3 Experimental Uncertainty

Concerning the uncertainty/repeatability of the experimental results (heat flux, heat transfer coefficient, Nu number) for drop-film wise condensation (DFWC) mode on the vertical aligned copper substrate, the measurements were repeated three times. In addition, three different analytical approaches have been used in order to validate the experimental data as follows.

The first validation was conducted by comparing the data for each sample with the modified Nu correlation for condensation heat transfer at a vertically aligned circular plate (disc) [52]:

$$\dot{q}_{s,\text{corr1}} = 0.83404 \left[\frac{K_{l,\text{sat}}^3 \rho^2 g h_{\text{fg}}}{\mu_{l,\text{sat}} L_{\text{cond}}} \right]^{1/4} \Delta T_{\text{sub}}^{3/4} \quad (5-24)$$

Furthermore, based on the heat transfer calculation approach reported in [62], where FWC at a vertically aligned circular plate cooled by a cold plate has been considered, a second validation of the experimental results have been carried out by comparing the experimental data with the values obtained through the calculation as follows.

Re numbers corresponding to FWC are calculated using the following expressions:

$$\text{Re}_{\text{cond,Ana2}} = \frac{4\dot{M}_{\text{cond}}}{W_{\text{base}} \mu_{1,\text{sat}}} \quad (5-25)$$

where: $\dot{M}_{\text{cond}} = f(T_{\text{sat}}, T_s, L_{\text{base}}, W_{\text{base}}) = \frac{\dot{q}_s A_{\text{cond}}}{h_{\text{fg}}}$

The local condensation heat transfer coefficients \bar{h} are calculated at Re numbers for the range $30 < \text{Re}_{\text{cond,Ana2}} < 1600$:

$$\frac{\bar{h}_{\text{Ana2}}}{k_{1,\text{sat}}} \left[\frac{\mu_{1,\text{sat}}^2}{\rho_{1,\text{sat}} (\rho_{1,\text{sat}} - \rho_{\text{v,sat}}) g} \right]^{1/3} = \frac{\text{Re}_{\text{cond,Ana2}}}{1.08 \text{Re}_{\text{cond,Ana2}}^{1.22} - 5.2} \quad (5-26)$$

The heat flux and Nu number are calculated by using Eqs. 5-27 and 5-28

$$\dot{q}_{s,\text{Ana2}} = \bar{h}_{\text{Ana2}} \Delta T_{\text{sub}} \quad (5-27)$$

$$\text{Nu}_{\text{Ana2}} = \frac{\bar{h}_{\text{Ana2}} L_{\text{cond}}}{k_{1,\text{sat}}} \quad (5-28)$$

The last validation has been done by using a general correlation of the dropwise condensation mode at a horizontal tube, which covers a range of saturation temperature from 48.4 °C to 101.0 °C [87] and which is rather similar to the experimental parameters used in this study:

$$\dot{q}_{s,\text{corr2}} = T_{\text{sat}}^{0.8} [5\Delta T_{\text{sub}} + 0.3\Delta T_{\text{sub}}^2] \quad (5-29)$$

All the calculations made analytically and those done using the correlation are accomplished at the same operating conditions of current experimental results such as

mass flow rate of cooling liquid, inlet temperature of cooling liquid, saturation temperature, and surface temperature (see Table 5-4).

5.3.4 Development of Heat Transfer Correlation

Sets of dependent parameters have been developed for all three surfaces used in this work in order to calculate heat flux, heat transfer coefficient and Nu number. These parameters include Re number of cooling liquid, vapor saturation temperature, and surface temperature, correlations for DFWC at a vertically aligned wall surface. Analytical calculations for the determination of the correlations have been performed by using different values of surface temperature as a function of Re numbers, since the inlet temperature of the cooling liquid and the vapor temperature have been kept constant. For the latter, it is the cooling liquid flowing at the backside of the substrate between the fins. All dependent parameters used to determine the correlations are displayed in Table 5-4 with the average range of Re number ranging between 1825 and 15370.

The analysis is conducted for each sample as a function of Re_l , T_{sat} and T_s for each sample by using the statistical package for the social sciences (SPSS) program. A nonlinear regression technique is used to discover the relation between the dependent parameter and a set of independent parameters such as (T_{w1-6} , $T_{l,in}$, $T_{l,out}$, $\dot{M}_{l,in}$ and $T_{v,ch}$). In addition, it is possible to statistically evaluate the current correlation formula through calculating the coefficient of the determination (R^2), which is a suitable standard of the regression model designed to determine the fit between analytical and experimental results. The correlation constants and R^2 for each sample are shown in **Table 5-1**. The general form of the correlations for heat flux, heat transfer coefficient, and Nu number for all the surfaces can be written as:

$$\dot{q}_{s,cc} = C_1 \left[\frac{K_{l,sat}^3 \rho_l (\rho_l - \rho_v) g \hat{h}_{fg}}{\mu_{l,sat} L_{cond} (\Delta T_{sub})} \right]^{1/4} (\Delta T_{sub}) \quad (5-30)$$

$$HTC_{cc} = C_2 \left[\frac{K_{l,sat}^3 \rho_l (\rho_l - \rho_v) g \hat{h}_{fg}}{\mu_{l,sat} L_{cond} (\Delta T_{sub})} \right]^{1/4} \quad (5-31)$$

$$Nu_{cc} = C_3 \left[\frac{L_{cond}^3 \rho_l (\rho_l - \rho_v) g \hat{h}_{fg}}{\mu_{l,sat} K_{l,sat} (\Delta T_{sub})} \right]^{1/4} \quad (5-32)$$

where the average Re number is ranging in between 1825 and 15370, and the correction term of latent heat vaporization is calculated by [94]:

$$\hat{h}_{fg} = h_{fg} + 0.68 C_{p1} (\Delta T_{sub})$$

Table 5-1: Constants and R^2 values of the developed correlations for the heat flux, HTC, and Nu number for unstructured, square-grooved and V-grooved samples

Parameter	Heat flux (kW/m ²)		HTC (kW/m ² -K)		Nusselt number (-)	
	C ₁	R ² (%)	C ₂	R ² (%)	C ₃	R ² (%)
Unstructured surface	0.401	96.1	0.406	94.7	0.034	94.8
S - groove	0.369	93.2	0.375	91.4	0.031	91.4
V - groove	0.295	95.1	0.298	91.6	0.025	91.6

An approach has been developed to analyze the systematic errors for each parameter such as mass flow rate of cooling liquid, the velocity of Huber chiller, the absolute pressure, the total input power from the low and high power supply. Also, an analytical study was conducted in order to determine the measurement uncertainty for independent and dependent parameters such as the mean temperature of cooling liquid, the subcooling temperature, the condensation heat transfer coefficient and the heat flux. The

specified errors of the manufacturer's devices and also the errors that are determined through the calibration procedure for thermocouples are also presented for each process parameter during the condensation tests. The resulting uncertainty in heat transfer calculations such as heat flux, HTC and surface temperature are presented for different surfaces topographies and wetting phenomena. Finally, the calibration procedure for the Huber chiller, all thermocouples type Pt-100, pressure transmitter and the corresponding uncertainty calculation for the mass flow rate of cooling liquid are demonstrated. At the end, the contribution of each component in the condensation setup to calculate the uncertainty is considered from the calibration certificates of used devices, their reference documents and experiment records.

Error Propagation and Uncertainty Calculation - The analytical calculation of uncertainty in the experimental results is achieved related to many parameters during the condensation test (see Table 4-4). Then, the uncertainty propagation method has been estimated for all parameters by using the Gaussian law, which to describe the errors of experimental results. The result RS is a given function $RS = U(x_1, x_2, x_3, \dots, x_n)$ of the independent variables $x_1, x_2, x_3, \dots, x_n$. Also, the errors of the uncertainties in the independent variables were U_1, U_2, \dots, U_n are used to measure the uncertainty R for each parameter. Then, the absolute and relative uncertainties of the dependent results can be described with the expression [82]:

$$U_{RS} = \left[\left(\frac{\partial U}{\partial x_1} U_1 \right)^2 + \left(\frac{\partial U}{\partial x_2} U_2 \right)^2 + \dots + \left(\frac{\partial U}{\partial x_n} U_n \right)^2 \right]^{1/2} \quad (5-33)$$

$$\frac{U_{RS}}{RS} = \pm \left[\left(\frac{U_{x_1}}{x_1} \right)^2 + \left(\frac{U_{x_2}}{x_2} \right)^2 + \dots + \left(\frac{U_{x_n}}{x_n} \right)^2 \right]^{0.5} \quad (5-34)$$

Table 5-2 shows the uncertainty values for some parameters that have been analyzed in the current study such as measurement values (MV), the data sheet of measurement devices and the analytical uncertainty calculation of heat transfer parameter by using Gaussian method (see Eq. 5-33).

Table 5-2: List of uncertainty values of the condensation heat transfer mechanism at the velocity of chiller range from 100 to 3300 rpm

No	Component	Symbol	Standard uncertainty	Source
1.	Chiller pump speed in rpm	V_{chiller}	± 20.33 rpm	MV
2.	Absolute pressure	$p_{\text{abs.}}$	± 0.01125 Bar	DSS
3.	Voltage of low power supply	V_{LPS}	± 0.001 V	DSS
4.	Voltage of high power supply	V_{HPS}	± 0.015 V	DSS
5.	Current of low power supply	I_{LPS}	± 0.00016 A	DSS
6.	Current of high power supply	I_{HPS}	± 0.00019 A	DSS
7.	Mass flow rate of cooling liquid	\dot{M}_1	$\pm 0.00171 - 0.00971$ kg/s	MV
8.	Current of data acquisition	I_{DAQ}	± 0.03 mA	DSS
9.	Data acquisition	DAQ	± 0.05	DSS
10.	Low power supply	LPS	± 0.03	DSS
11.	High power supply	HPS	± 0.15	DSS

The experimental work includes a wide range of measurements. The errors have come through different measurement operations. The dependent and independent parameters are involved together. Hence the influence of independent parameters' errors on the dependent parameters, which can impact the final practical results of the experimental

work. Therefore, the uncertainty estimation is one of the main matters for safety and veracity of experimental results. It is also general agreement that the experimental results are not acceptable without an uncertainty assessment. Thus, the current uncertainty analysis has been completed by relying on many authors' the procedures and methodologies to find the experimental uncertainties. Issues of experimental uncertainty were dealt with following recommendations of [95] as well as methods of other prominent works in experimental uncertainty [82], [96]–[100]. A few samples of the calculations are displayed here. **Table 5-3** summarizes the range of experimental uncertainty for the untreated unstructured surface at vapor pressure 1.02 Bar and mass flow rate of cooling liquid 2.5 g/s and 78.3 g/s.

Table 5-3: Experimental uncertainties for all independent and dependent parameters

Parameter	Unit	Absolute uncertainty (U_R)	
		$\dot{M}_l=2.5$ g/s	$\dot{M}_l=78.3$ g/s
T_1	°C	± 0.523	± 0.609
T_3	°C	± 0.519	± 0.555
T_5	°C	± 0.543	± 0.575
$T_{v,ch}$	°C	± 0.523	± 0.525
$T_{l,in}$	°C	± 0.550	± 0.552
$T_{l,out}$	°C	± 0.547	± 0.640
T_{avg}	°C	± 0.740	± 0.834
K_{cu}	W/m ² -K	± 3.113	± 8.758
T_{mean}	°C	± 0.846	± 0.777
C_{pl}	kJ/kg-K	± 0.204	± 0.308
\dot{q}_s	W/m ²	± 8811.890	± 22855.000
T_s	°C	± 5.232	± 3.736
HTC	W/m ² -K	± 2767.000	± 609.77

Independent parameters (such as temperature, instruments, calibration formula, etc.) were found, including bias error (B) and accuracy errors (P), using the collect square root (RSS) method,

$$B = [B_1^2 + B_2^2 + B_3^2 + \dots + B_n^2]^{0.5} \quad (5-35)$$

$$P = [P_1^2 + P_2^2 + P_3^2 + \dots + P_n^2]^{0.5} \quad (5-36)$$

Elemental errors were integrated to obtain 95 % uncertainty confidence (U) by using the following relationship:

$$U = [B^2 + P^2]^{0.5} \quad (5-37)$$

Dependent parameters, such as \dot{q}_s , T_s , HTC, etc., are the functions of another measurement for independent variables. The uncertainty of the independent parameters divides them according to their relationship to function. For instance, in the case of the condensation heat flux, surface temperature and heat transfer coefficient are determined as a function of:

$$\dot{q}_s = f(\dot{M}_l, C_{p,l}, T_{l,out}, T_{l,in}) \quad (5-38)$$

$$T_s = f(T_{avg}, \dot{q}_s, K_{cu}) \quad (5-39)$$

$$HTC = f(\dot{q}_s, T_{v,ch}, T_s) \quad (5-40)$$

5.3.5 Heat Transfer Parameters of the Condensation

The major parameters of the dropwise condensation are wall temperature, heat flux, heat transfer coefficient and the subcooling temperature for which the heat capacity law, Newton law of cooling and Fourier law of conduction (see section 4.7) have been used. Moreover, a list of experimental results for the parameters from condensation heat

transfer for different untreated surface topographies are also shown in Table 5-4 at vapor pressure of 1.02 Bar.

Table 5-4: Experimental parameters and the boundary conditions of DFWC condensation for untreated surfaces.

	Unstructured	Square groove	V-groove
$\dot{M}_{l,in}$ [g/s]	4 - 87		
$p_{v,ch}$ [Bar]	1.016-1.030	1.016-1.025	1.011-1.024
$T_{v,ch}$ [°C]	100.10-100.50	100.10-100.33	99.90-100.29
T_s [°C]	37.2 – 92.3	36.3 – 96.1	31.0 – 88.4
$T_{l,in}$ [°C]	9.90-13.20	14.20-10.02	9.80-13.80
Re_l [-]	1829-16177	1792-15440	1854-14493
\dot{q}_s [W/cm ²]	14.40 – 27.30	13.60 – 32.65	10.90 – 33.30

Nine thermocouples (Pt-100) were used to measure the temperature from chosen positions of the main part for the condensation device (see **Figure 4-16a**), while six thermocouples were inserted inside the base of the heat sink (see **Figure 4-16b**) to calculate the condensation surface temperature, heat flux and heat transfer coefficient. All heat transfer parameters T_s , \dot{q}_s and HTC, which couldn't be directly measured, have been calculated as dependent on various experimental parameters such as $T_{v,ch}$, \dot{M}_l , T_{avg} , and etc. For instance, uncertainty calculations for each parameter of the condensation, such as heat flux, surface temperature and heat transfer coefficient, are obtained as:

$$\frac{U_{\dot{q}_s}}{\dot{q}_s} = \pm \left[\left(\frac{U_{\dot{M}_l}}{\dot{M}_l} \right)^2 + \left(\frac{U_{C_{p,l}}}{C_{p,l}} \right)^2 + \left(\frac{U_{T_{l,out}}}{T_{l,out}} \right)^2 + \left(\frac{U_{T_{l,in}}}{T_{l,in}} \right)^2 \right]^{0.5} \quad (5-41)$$

and

$$\frac{U_{T_s}}{T_s} = \pm \left[\left(\frac{U_{T_{avg}}}{T_{avg}} \right)^2 + \left(\frac{U_{\dot{q}_s}}{\dot{q}_s} \right)^2 + \left(\frac{U_{K_{cu}}}{K_{cu}} \right)^2 \right]^{0.5} \quad (5-42)$$

Uncertainty of the condensation heat transfer coefficient is calculated as a function of these parameters such as heat flux, vapour temperature and surface temperature by:

$$\frac{U_{HTC}}{HTC} = \pm \left[\left(\frac{U_{\dot{q}_s}}{\dot{q}_s} \right)^2 + \left(\frac{U_{T_{v,ch}}}{T_{v,ch}} \right)^2 + \left(\frac{U_{T_s}}{T_s} \right)^2 \right]^{0.5} \quad (5-43)$$

The equations above 5-41, 5-42 and 5-43 requires uncertainty components of \dot{M}_l , $C_{p,l}$, T_l , T_{avg} , K_{cu} and $T_{v,ch}$ which are calculated in advance.

In this work, the temperature of the cooling liquid flow at inlet and outlet liquid chamber was measured several times with different mass flow rates of cooling liquid (see Table 4-4) to provide the mean temperature of the cooling liquid, which was assessed as a property of water. The estimate rationale of uncertainty for these properties is written as:

$$C_{p,l} = f(T_{mean}) \quad (5-44)$$

Where $T_{mean} = \frac{T_{l,in} + T_{l,out}}{2}$

$$\frac{U_{C_{p,l}}}{C_{p,l}} = \pm \left[\left(\frac{U_{T_{l,out}}}{T_{l,out}} \right)^2 + \left(\frac{U_{T_{l,in}}}{T_{l,in}} \right)^2 \right]^{0.5} \quad (5-45)$$

The thermal conductivity of heat sink base copper material is calculated by:

$$K_{cu} = f(T_{avg})$$

Where $T_{avg} = \frac{T_1 + T_3 + T_5}{3}$

$$\frac{U_{K_{cu}}}{K_{cu}} = \pm \left[\left(\frac{U_{T_1}}{T_1} \right)^2 + \left(\frac{U_{T_3}}{T_3} \right)^2 + \left(\frac{U_{T_5}}{T_5} \right)^2 \right]^{0.5} \quad (5-46)$$

The main steps of the experimental uncertainty calculations are presented in Figure 5-5.

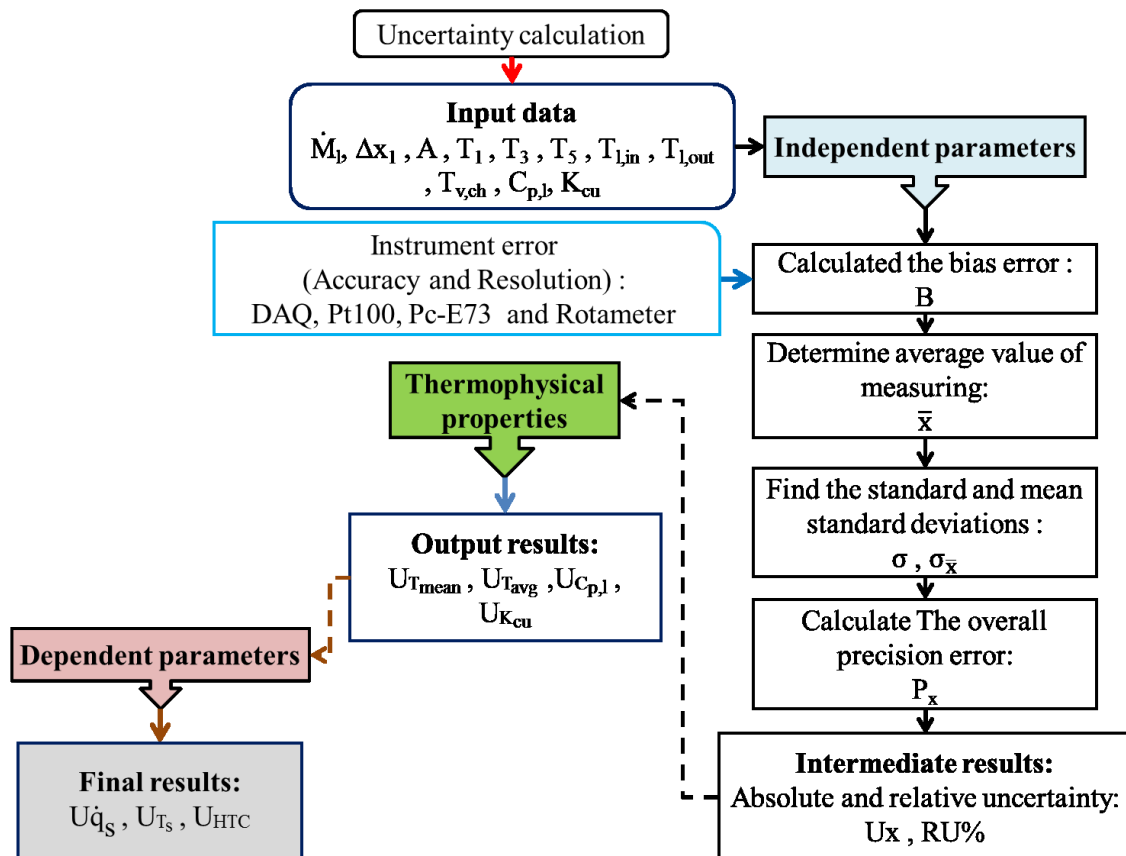


Figure 5-5: Schematic diagram for calculating the experimental uncertainties

5.3.6 Thermocouple Calibration

Before starting each experiment, all thermocouple are calibrated and they are connected to the external devices such as DAQ and LABVIEW program (see section B.3 and Figure B-6). The calibration test is made by coupling them with the reference thermocouple type Pt-100 at the same position inside the water tank of the Huber chiller. The standard uncertainty of each thermocouple that is used during the condensation test is written in **Table 5-3**, while the maximum uncertainty value of all thermocouples was obtained as $\pm 0.10 - 0.35$ K. The details and procedure of finding the uncertainty for experimental parameters were also presented in APPENDIX C sections (C.1 and C.2).

5.4 Computational Analysis of Condensation

Numerical models of the unstructured surface heat sink were developed by using a commercially available ANSYS Icepak software. A passive cooling heat sink with rectangular fins is utilized during the condensation tests, and all the heat sink specifications are written in Section B.2 (see Table B-3). Figure 5-6 represents the front view section of the heat sink with the given dimensions. The boundary conditions were applied as the inlet liquid temperature of 10.47 °C and the active surface temperature of 66.25 °C, while liquid outlet velocity and the mass flow rate were defined as 0.28 m/s and 14 g/s respectively by considering the experimental results.

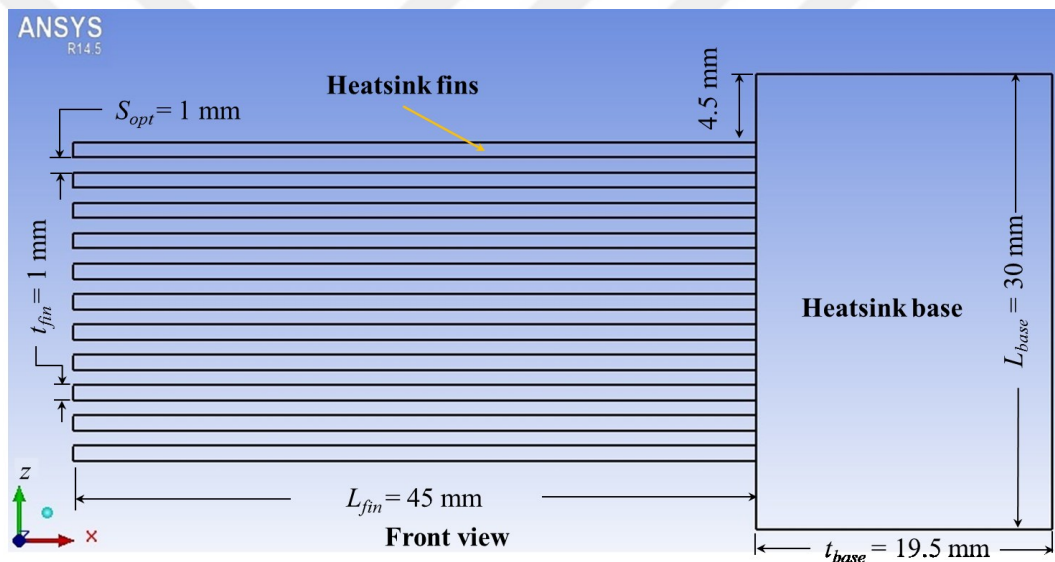


Figure 5-6: The schematic diagram of the heat sink

As a part of the experimental study, one another task was about designing a suitable heat sink that is utilized in the experimental condensation test. Therefore, the thermal performances of the heat sink at different types of the structured surfaces and varying cooling liquid flow rates were evaluated. The physical definition of the model can be stated as laminar flow, steady, three-dimensional multi components liquid and convection heat transfer over the heat sink fins. The mesh generation for the model was

made by using the Mesher-HD option, which denotes the unstructured mesh as shown in Figure 5-7. The mesh independency analysis was carried out in order to ensure the mesh quality. As a result, it was found satisfactory since there is no change in the results with an increase in the number of mesh cells of the heat sink when the element and node numbers exceed 306900 and 319940 respectively (see Figure 5-8).

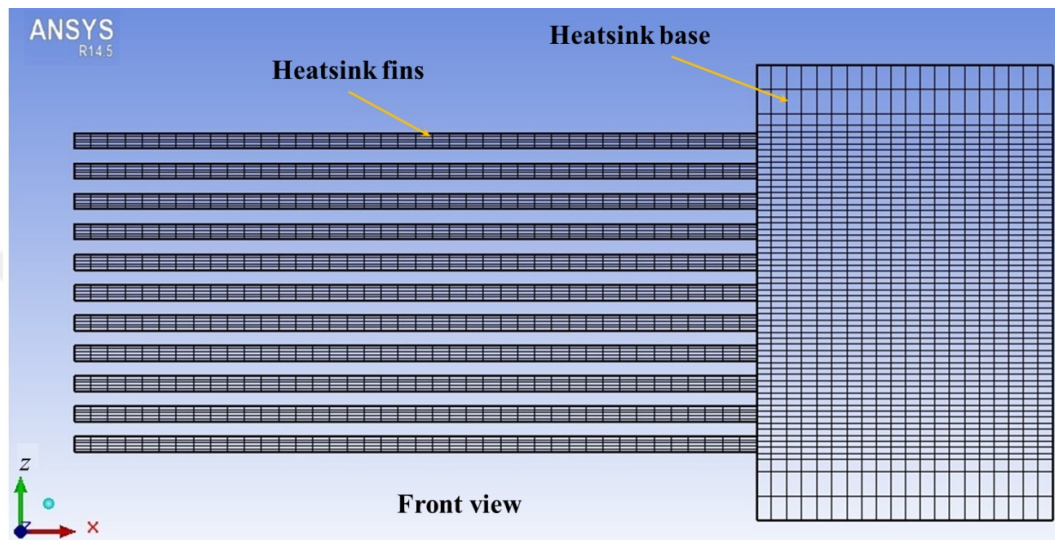


Figure 5-7: Mesh structure

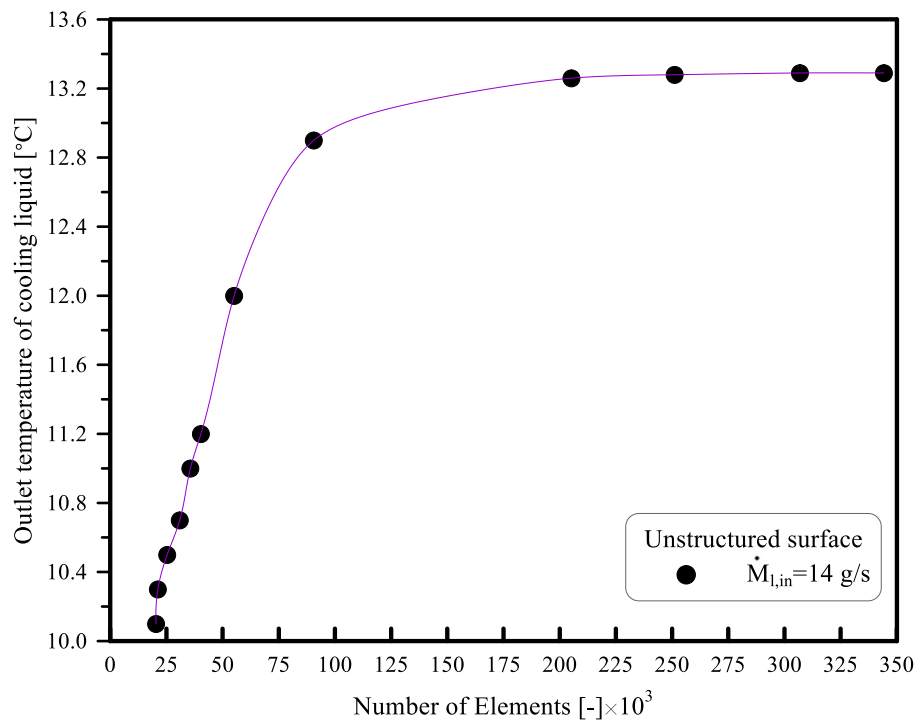


Figure 5-8: Mesh sensitivity analysis

The simulations were run for the unstructured surface at a constant flow rate of 14g/s. The resulting temperature contours at a total heat input of 235.76 W can be seen in Figure 5-9 over the heat sink surface. The numerical results were achieved in a close proximity with the experimental results as seen in Table 5-5 while Figure 5-10 represents the distribution of velocity vectors inside the cooling liquid chamber where the inlet temperature and outlet velocity were defined as 10.47 °C and 0.28 m/s respectively. These boundary conditions were chosen as a comparison case between experimental and numerical results at a constant liquid mass flow rate to determine the relative variation between two cases.

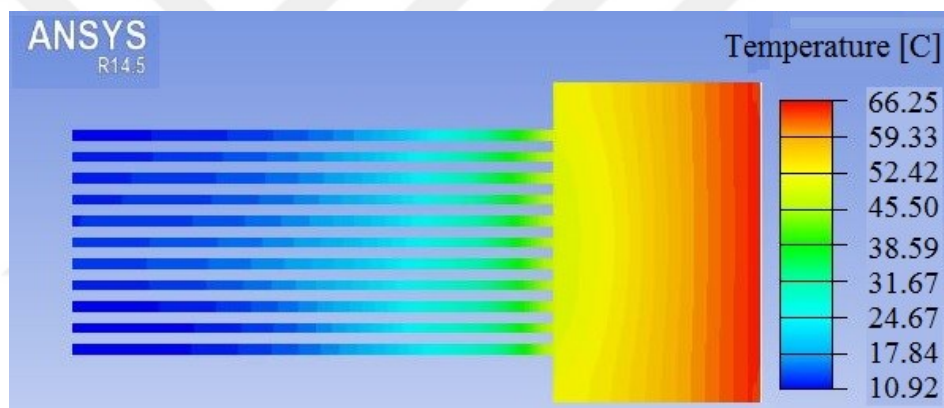


Figure 5-9: Temperature distribution over the heat sink for unstructured surfaces

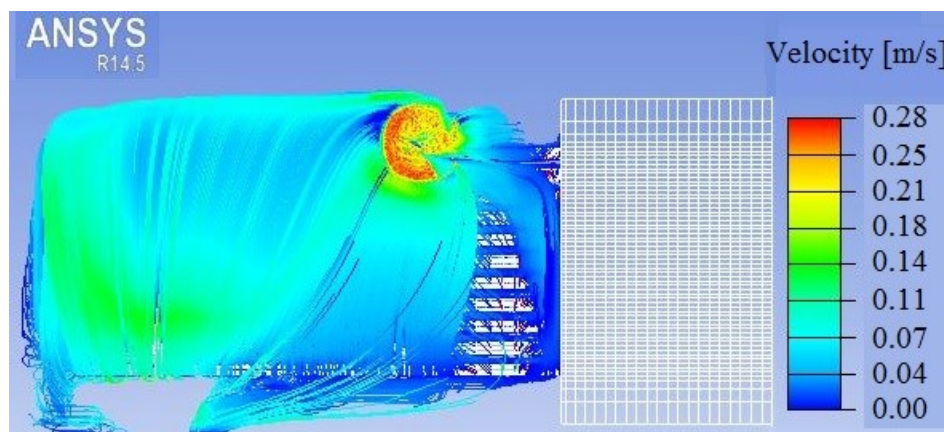


Figure 5-10: Velocity distribution inside the cooling chamber

Table 5-5: Comparison between numerical and experimental results of an unstructured surface at a constant liquid flow rate

$\dot{M}_{l,in} = 14 \text{ g/s}$		Numerically	Experimental	Relative error (%)
Temperature [$^{\circ}\text{C}$]	$T_{W,1}$	64.94	66.28	2.0
	$T_{W,2}$	58.06	63.24	8.2
	$T_{W,3}$	64.90	64.66	0.3
	$T_{W,4}$	57.46	62.18	7.6
	$T_{W,5}$	64.90	66.01	1.7
	$T_{W,6}$	57.74	62.67	7.9
	$T_{l,out}$	13.29	12.34	7.7
Heat loss at the heat sink base (W/m^2)	y-direction	880.10	1038.21	15.2
	z-direction	825.72	994.11	16.9

CHAPTER VI

RESULTS AND DISCUSSIONS

Experimental and analytical results of condensation phenomena at different surface wetting and operating vapor pressure are presented and discussed in this chapter. The primary focus of this study is to investigate the heat transfer performance by considering different parameters such as surface topographies and surface treatments on the condenser part of the heat pipe. Specifically, these parameters include micro-nano-structured surfaces, chemical treatment of the condensation surface (hydrophobicity phenomena) that explained in section 6.1, and operating vapor pressure during the condensation process (see section 6.3) .

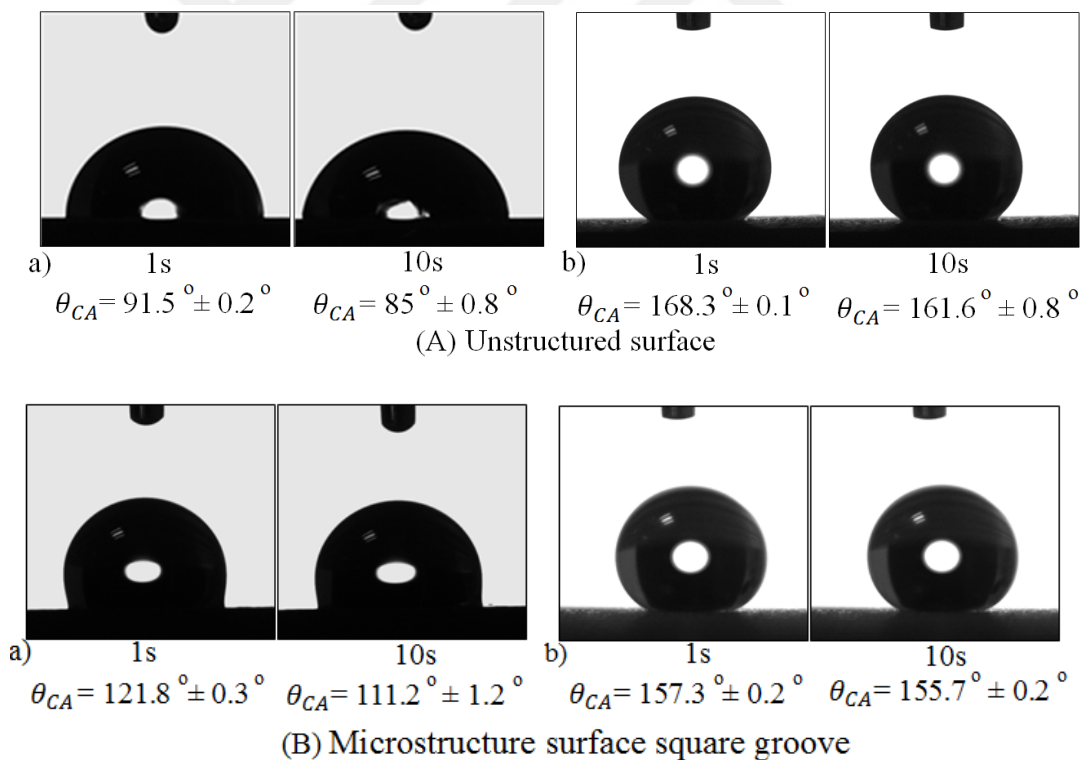
6.1 Micro-Textured Surfaces and Wetting Phenomena

Once the expected optimization is completed with heat pipe technology for the purpose of enhancing the cooling from the condensation part of the heat pipe. Firstly, the condensation surface is prepared as a vertical plate and studied individually. Then, the condenser surface is treated by considering two characteristics: one is the surface topographies to increase the heat transfer surface area of condensation and the other is the surface wetting over the chemically treated condenser surface to provide more hydrophobicity.

6.1.1 Superhydrophobicity over Microstructured Surfaces

A superhydrophobic surface is created experimentally by using a commercially available liquid mixture (Ultra-Ever Dry®) to increase the liquid-repellence of the surface (hydrophobicity) (see section 4.4.1). This method is used to enhance the condensation heat transfer rate by increasing the droplet contact angle more than 150°. This leads to a rise in the exposed surface area to vapor with a lower thermal resistance

of liquid film in condensation. Moreover, water droplet profiles over time on the substrate surface for various wetting properties are also shown in Figure 6-1 (A, B and C) at the central location. Figure 6-1(A) presents the unstructured surface that was considered as a super-hydrophobic surface since the average CA was $162.2^\circ \pm 0.8^\circ$, while Figure 6-1(B) shows the contact angle on super-hydrophobic square groove with $156^\circ \pm 0.15^\circ$. Figure 6-1(C) presents the super-hydrophobic V-groove of $151^\circ \pm 0.2^\circ$. Experimental results showed the highest value of CA of the unstructured surface after coating of the other surfaces due to uniformly distributed TOP coating particles. It is also observed that CA of the micro-structured square groove is higher than V-groove because of the faster moving of water droplet inside the groove which causes a decrease in the value of droplet contact angle.



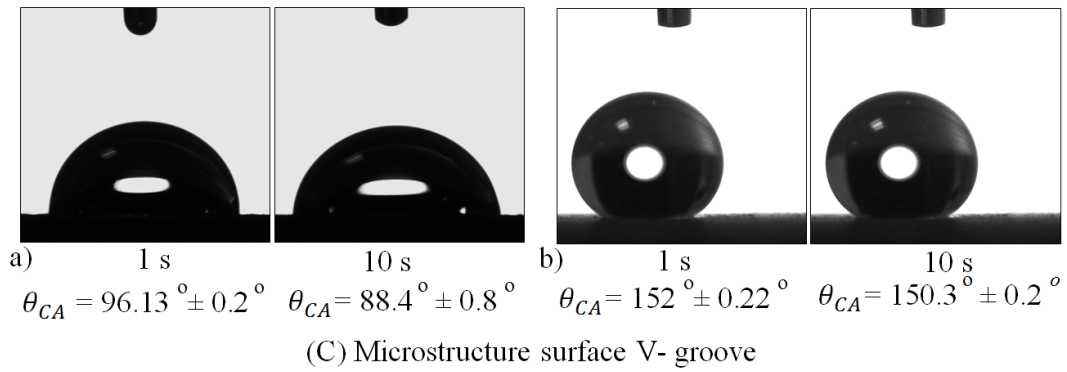
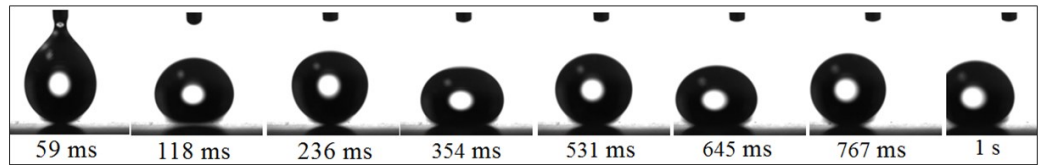
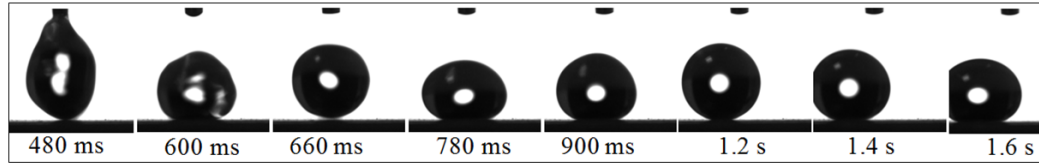


Figure 6-1: Liquid droplet profile at different times at the center position of each surface: (a) untreated surface, (b) coated surface

Figure 6-2 a) and b) show the hydrodynamic phenomena of the sessile droplet on the unstructured superhydrophobic surface for two positions (center and edge 4) at a short timescale (1000 ms). The droplet images are captured by using a high-speed CCD camera of the Tensiometer with a FOV of 5×10 (mm) having a spatial resolution of 512×512 pixel ($10 \mu\text{m}/\text{pixel}$) at a frame rate of 100 fps. Generally, the superhydrophobic surface repels the droplet when it collides with the surface due to the decrease in the surface energy of the active surface. Next, due to the capillary force, the droplet starts jumping and moving outside the surface for each position at 236 ms and 660 ms respectively. Furthermore, the droplet contact angle is measured five times for each position (center and edge-4) to increase the accuracy. The variations at CA values are found to be $162.2^\circ \pm 0.8^\circ$ and $162^\circ \pm 0.6^\circ$ respectively within a 95% confidence level.



a)



b)

Figure 6-2: High-speed image sequences of droplet propagating on the superhydrophobic unstructured surface: a) Center position, b) Edge- 4 position

Surface wettability values for each microstructured surface that was measured experimentally, and calculated theoretically by means of capillary Laplace equation (Eq. 5-10 in section 5.2) given in Figure 6-3, Figure 6-4 and Figure 6-5 respectively and it leads to the development of a new thermodynamic model. It is seen from figures that the chemical modification of the surface by using ultra-ever dry causes a higher contact angle (CA) and super-hydrophobicity in comparison to untreated surfaces. In addition, experimental results of the mean contact angle for each treated surface were $162.3^\circ \pm 0.9^\circ$, $158.4^\circ \pm 0.2^\circ$ and $151.5^\circ \pm 0.3^\circ$ of unstructured, square groove and V-groove surfaces due to the high roughness of the unstructured surface. Comparisons between experimental and analytical results after coating have shown again a good agreement with the maximum variation of 10%.

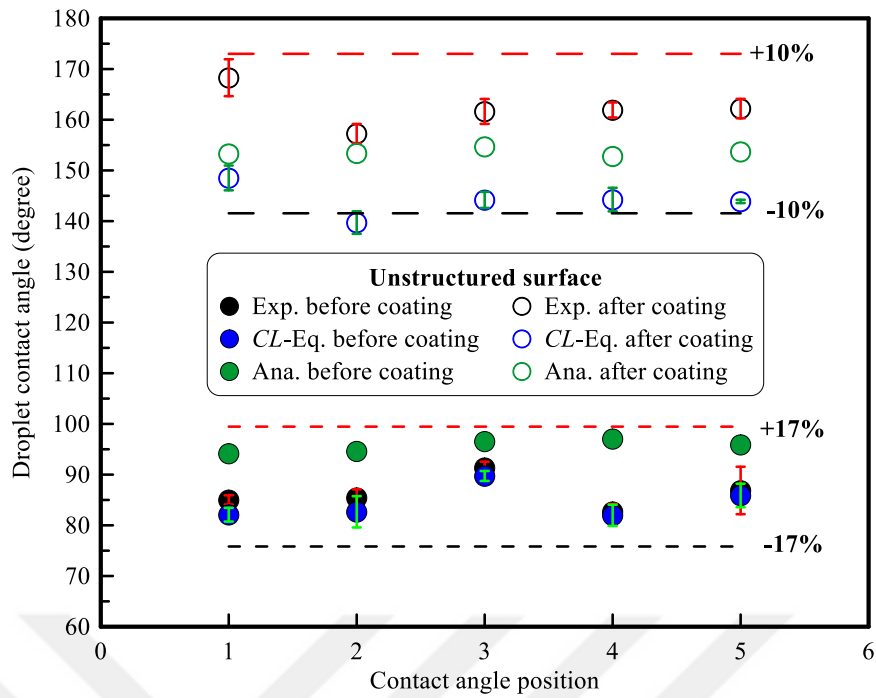


Figure 6-3: Variation of the average droplet contact angle at five positions on the unstructured superhydrophobic surface by ultra-ever dry coating compared with an untreated surface

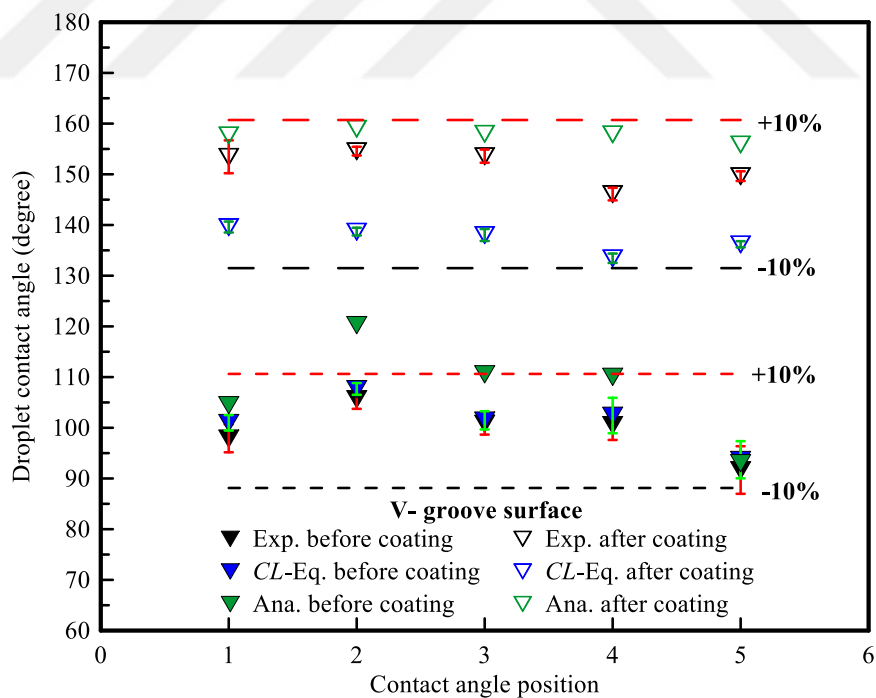


Figure 6-4: Variation of the average droplet contact angle at five positions on the V-grooved superhydrophobic surface by ultra-ever dry coating compared with an untreated surface

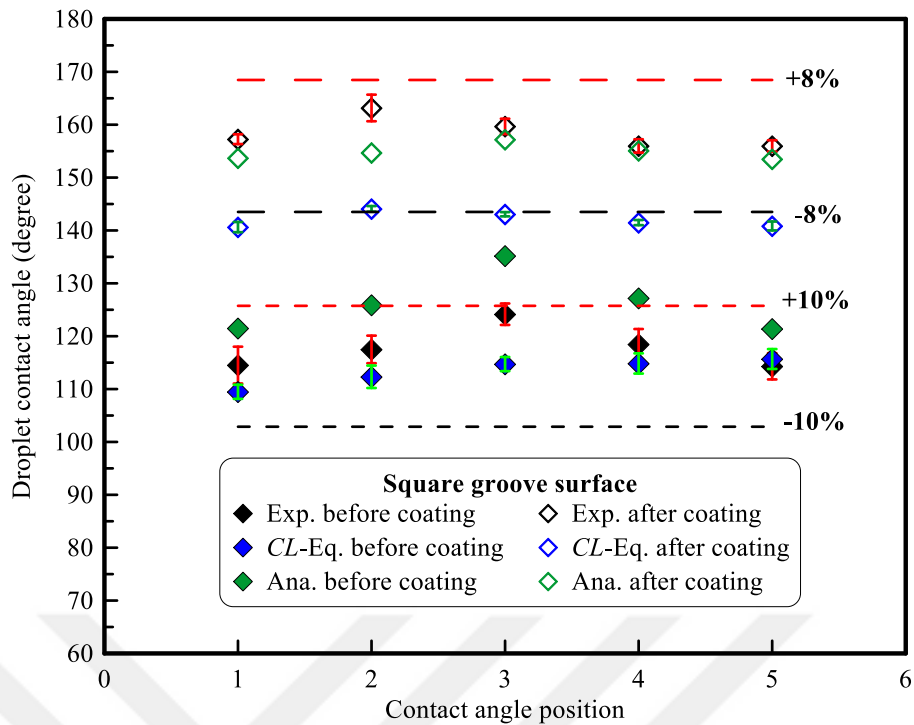
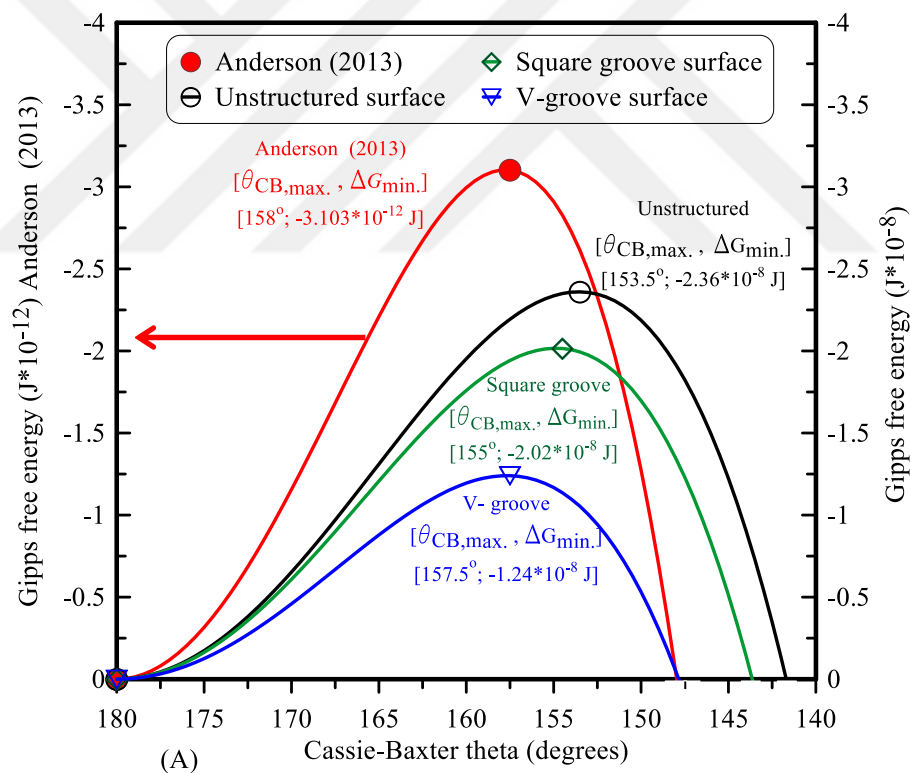


Figure 6-5: Variation of the average droplet contact angle at five positions on the square grooved superhydrophobic surface by Ultra-Ever Dry coating compared with an untreated surface

The change in Gibbs free surface energy of the droplet from the reference state as a function of Young contact angle has been determined by using the analytical model with the supported data of Anderson [16] for three different samples (unstructured, square grooved, and V-grooved micro-structured). In addition, the validation study for all proposed surfaces presents acceptable results compared to Anderson [16]. Corresponding results are also shown in Figure 6-6(A) and (B). Moreover, the determined droplet volumes with the liquid-vapor tension were used as initial conditions for the experimental study to calculate Wenzel and Cassie-Baxter contact angles for each sample after chemical treatment. The analytical results of the thermodynamic model were used to determine the free surface energy with a variation of droplet contact angle. In Figure 6-6(A), the maximum value of Cassie-Baxter contact angle is obtained

for the microstructure V-groove surface after coating as 157.5° with the minimum surface energy of -1.24×10^{-8} J compared to the other surfaces. This might be because of the accumulation of coating particles inside the grooves that can prevent the droplet to sit on the surface crests. In Figure 6-6 (B), microstructured square-grooved surface gave a high value of Wenzel contact angle (118°) with the low surface energy of -5.76×10^{-7} J compared to the other surfaces. This could be explained as the droplet is exposed to more resistance during motion inside the groove and between the coating particles. The Cassie-Baxter state is also unstable because of the surface energy is higher than the Wenzel state. The stable Wenzel state occurs when the droplet is penetrated inside the rough region of the surface.



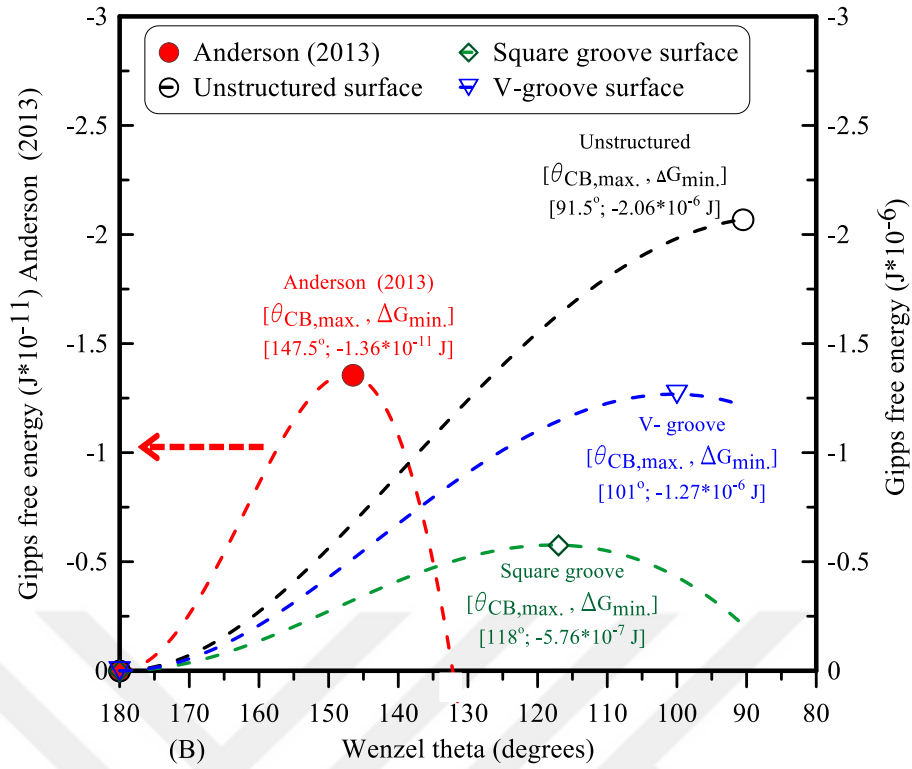


Figure 6-6: Free surface energy for (A) Cassie-Baxter contact angle theta (B) Wenzel contact angle theta for all samples after coating compared with the results [16]

Accordingly, the effect of the intrinsic Young contact angle on the Cassie-Baxter contact angles for each three proposed surfaces is shown in Figure 6-7. When the Young theta increases, the Cassie-Baxter is observed to increase for all surfaces while the V-grooved structured surface has resulted in the highest contact angle compared to others due to the decreasing fraction area. Moreover, it can be seen that the Cassie-Baxter contact angles of microstructured V-grooved and unstructured surfaces are higher than 150° (superhydrophobic surface) with the rise in the Young contact angle. While Cassie-Baxter contact angle of square-grooved surface is higher than 150° at the Young contact angle more than 105° (superhydrophobicity). In addition, the analytical model for all surfaces is validated with the reference Anderson [16] and the results reveal a good agreement.

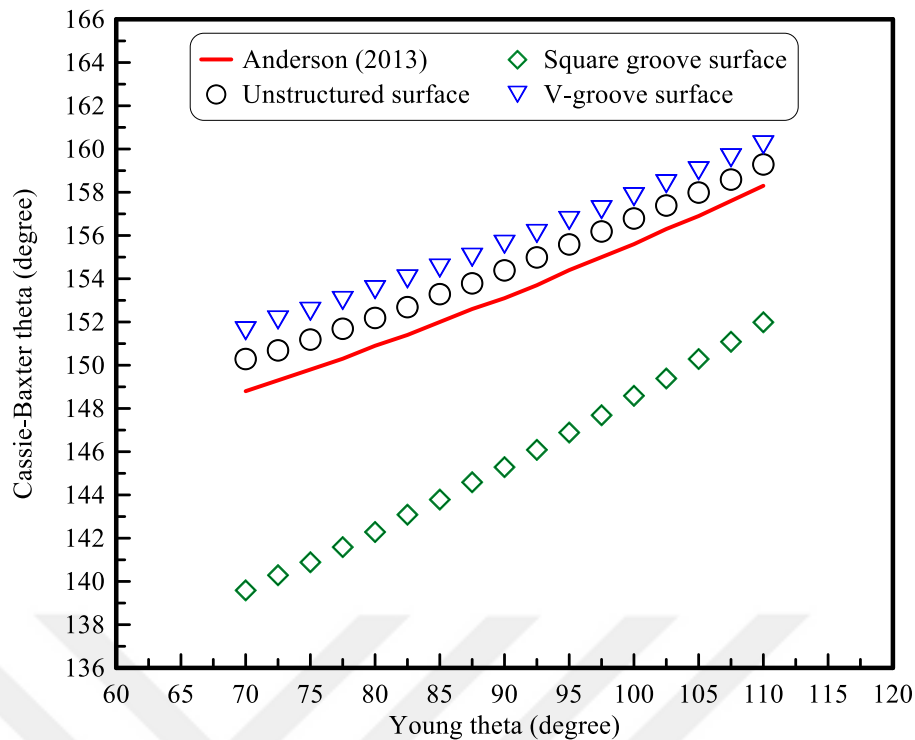


Figure 6-7: Effect of the Young contact angle on the Cassie-Baxter contact angle for all samples after coating process compared with the results [16]

6.1.2 Influence of Superhydrophobicity over Heat Transfer Parameters

The comparison of HTC is illustrated in Figure 6-8. Generally, for all surfaces, HTC is decreasing with the increase in temperature difference ($T_{v, ch} - T_s$). The reason for this could be the decrease in surface temperature that leads to a reduction of heat transfer rates at almost constantly kept heat flux and fixed saturation vapor temperature. Moreover, the effect of micro-grooves on the surfaces does not show a significant enhancement on HTC. Furthermore, the micro-structured square grooved surface has a similar behavior like the unstructured surface solely. By comparing the uncoated and coated heat transfer results, HTC has been expected to be increased in the order of about 3 to 4 times after coating with Ultra-Ever Dry. However, the coated surfaces show lower HTC values compared to the uncoated samples. This can be probably attributed to the coating process, which did not result in homogeneously distributed nano-particles,

leading to an accumulation of coating material and hence to suppression of active nucleate sites.

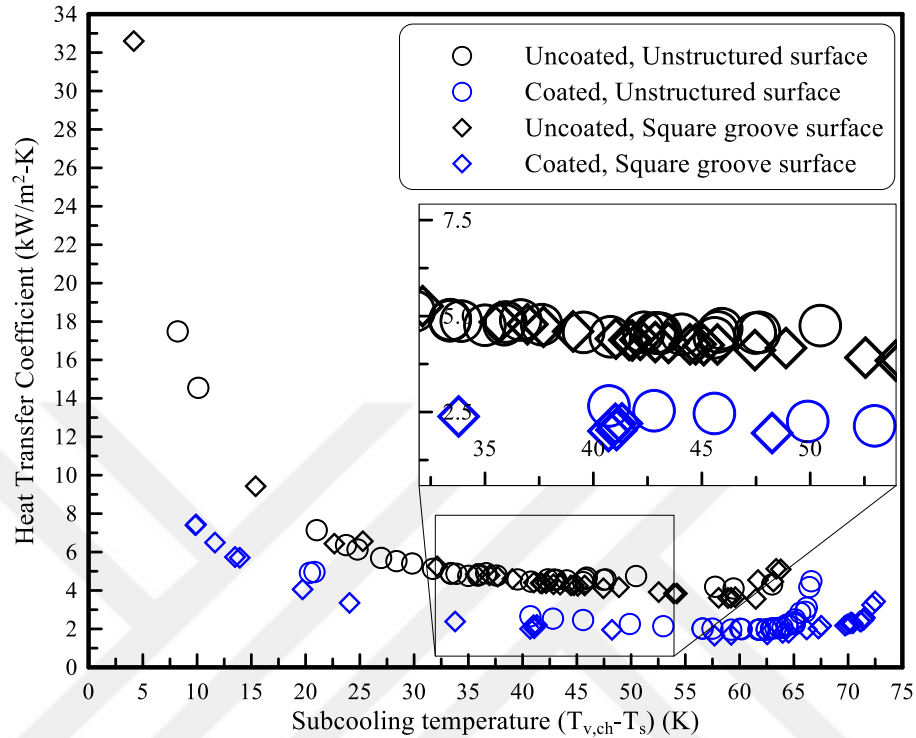


Figure 6-8: HTC at varying $T_{v, ch} - T_s$ for uncoated/coated UED unstructured and square-grooved surfaces at $p_{v, ch}=1.02$ Bar

Figure 6-9 shows the variation of surface temperatures with a different mass flow rate of cooling liquid for uncoated and coated surfaces at constant operating vapor pressure of 1.02 Bar. The surface temperature decreases with the rise in \dot{M}_l for each sample with square groove and unstructured surfaces at different wetting conditions. However, the wall temperature of the coated surface for each sample was observed as lower than the uncoated surfaces, due to the non-homogenous accumulation of coating particles with the thicker liquid film condensation on the active surface. It can be seen at $\dot{M}_l=71.7$ g/s that the highest value of T_s at the uncoated surface was 59.4°C for the unstructured surface, while, the lowest T_s at the coated surface was 28.1°C for the square groove.

This could happen for two reasons: one is due to the DWC occurred on the unstructured surface other than micro-square groove and the second is about the coating material of UED that had a less resistance of the temperature gradient at the surface interface between the cooled back-side of the heatsink and the hot region inside the vapor chamber.

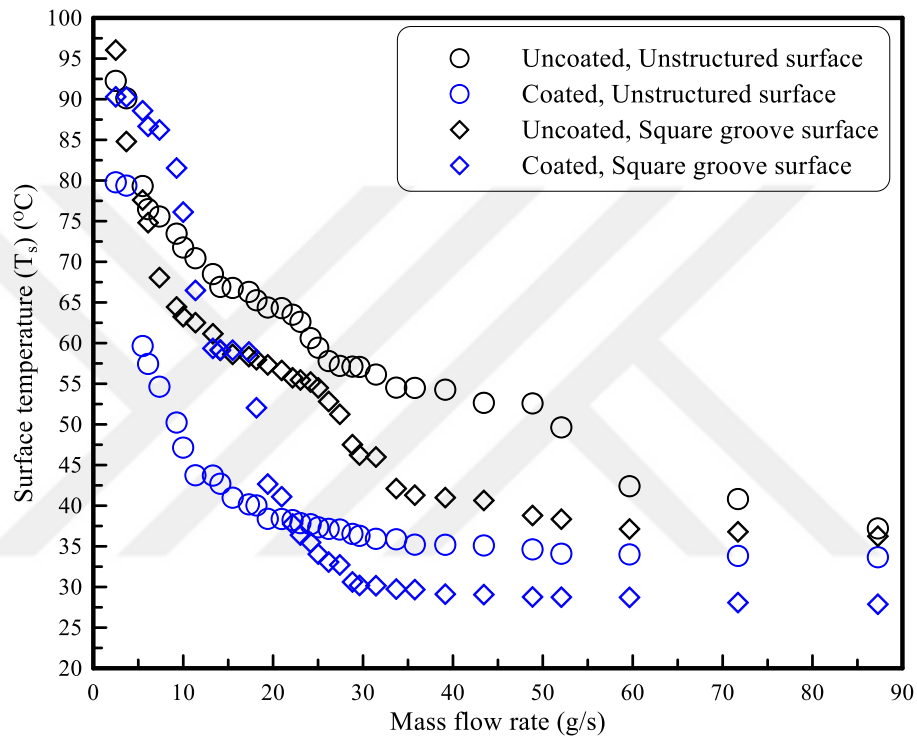


Figure 6-9: Comparison of surface temperatures for uncoated/coated UED of unstructured and square-grooved surfaces at $p_{v, ch}=1.02$ Bar with varying \dot{M}_1

Effect of subcooling temperature over heat transfer is presented in Figure 6-10 for the micro-square groove compared to the unstructured surface with a different wettability at $p_{v, ch} = 1.02$ Bar. As the temperature difference becomes larger between the surface and the vapor chamber temperature, the heat flux is elevated due to the rise in the convective heat transfer rate between the cooling liquid and the copper fins block. In addition, the experimental results indicate that the lowest values of heat flux are

obtained at the superhydrophobic surface for each sample when compared to untreated surface. This is because of the non-homogeneous distribution of the droplets on the condensation surface, which leads to the reduced exposed condensation surface area to the vapor with the lower surface temperature (see Figure 6-9). Also, the heat flux of the unstructured surface is higher than square groove surface for each untreated and treated surface since the strong accumulation of droplets could lead to a drop in the heat transfer rate at different wettability phenomena.

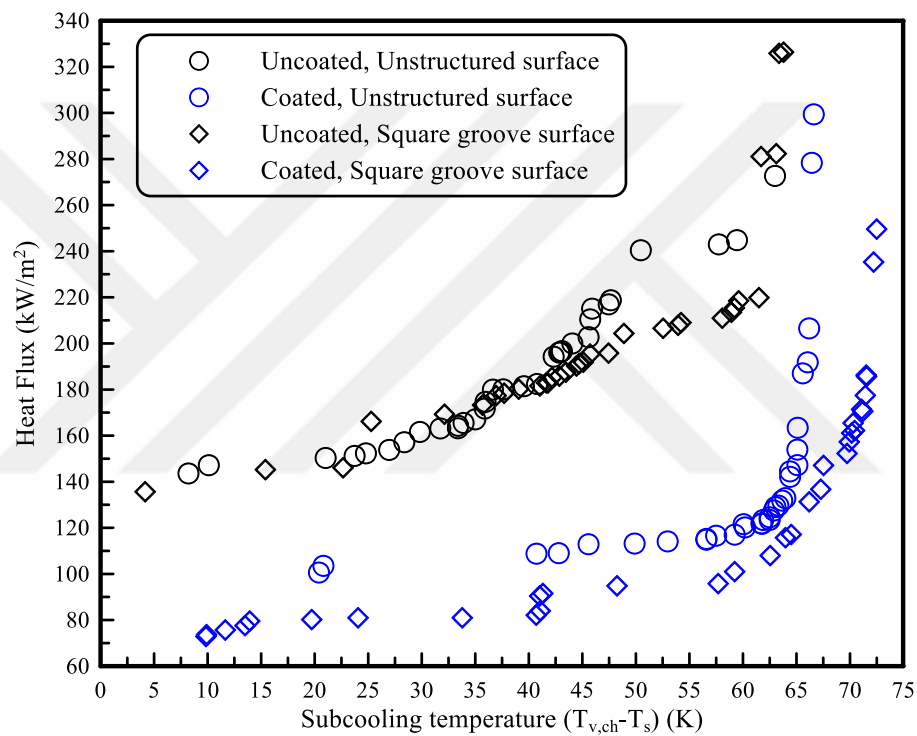


Figure 6-10: Comparison of heat flux for uncoated/coated UED of unstructured and square-grooved surfaces at $p_{v, ch}=1.02$ Bar with a different subcooling temperature

6.2 Condensation Heat Transfer and Wettability Characteristics at Uncoated Substrates

The fourth task of the condensation test was performed by studying the effect of untreated surface topographies on the condensation heat transfer rate at vapor chamber pressure of 1.02 Bar. In addition, the condensation experiments were made by utilizing

the vertical copper plate under the same boundary conditions (see Table 5-4 in section 5.3.5). For more clarification, the specifications of the different surface structures such as square groove and V- groove are explained in (section 4.2).

6.2.1 Unstructured Surface

In Figure 6-11, the wall temperature at varying mass flow rates of cooling liquid is presented. The wall temperature approximately decreases from 92°C to 35°C with the increase of cooling liquid mass flow rate. This can be attributed to the intensification of convective heat transfer between the cooling liquid and the copper fins leading to a stronger heat absorption by the liquid.

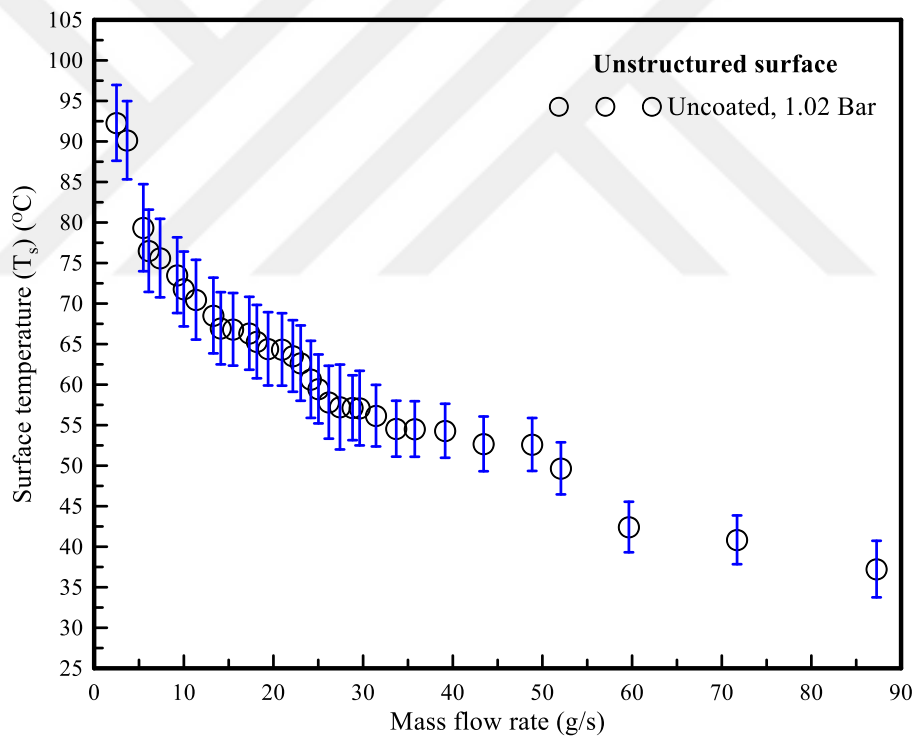


Figure 6-11: Variation of surface temperature with liquid mass flow rate

Since the temperature and pressure inside the vapor chamber were fixed, the surface temperature gets lowered by the intensified cooling performance at the back-side of the

copper block. Thus, the heat flux rises with larger temperature difference between the vapor saturation and surface temperatures (see Figure 6-12).

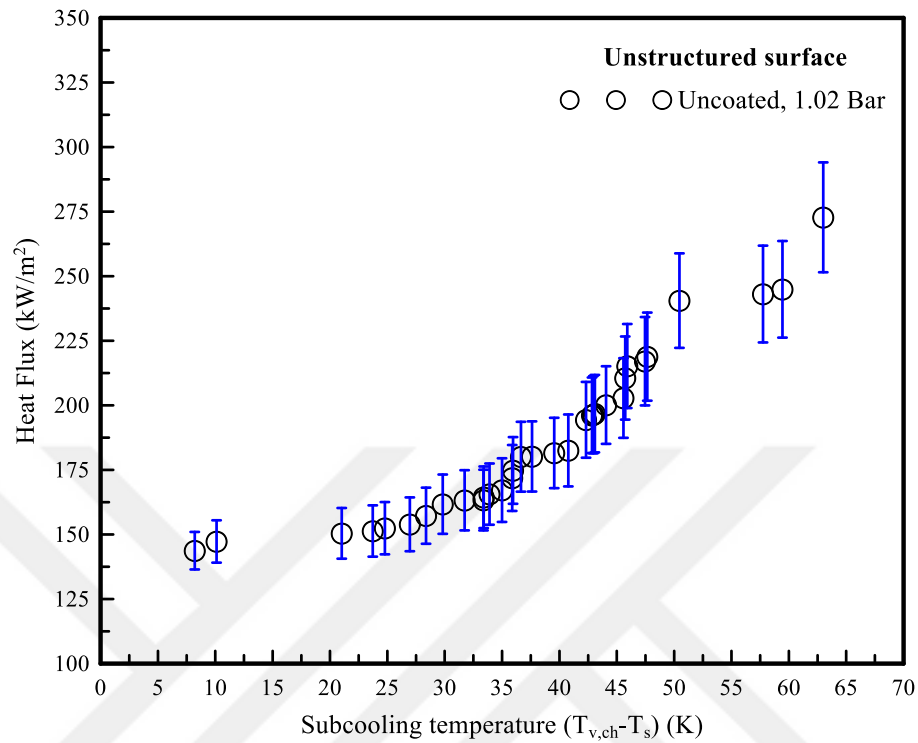


Figure 6-12: Effect of subcooling temperature difference on heat flux

However, for some temperature differences more than one heat flux value has been obtained. This might have occurred due to a measurement error. Figure 6-13 shows the heat transfer coefficients at various temperature differences. Since the vapor and inlet temperature of the cooling liquid have been kept constant, an increase of mass flow rate of cooling liquid will rise the temperature difference between the surface and the vapor.

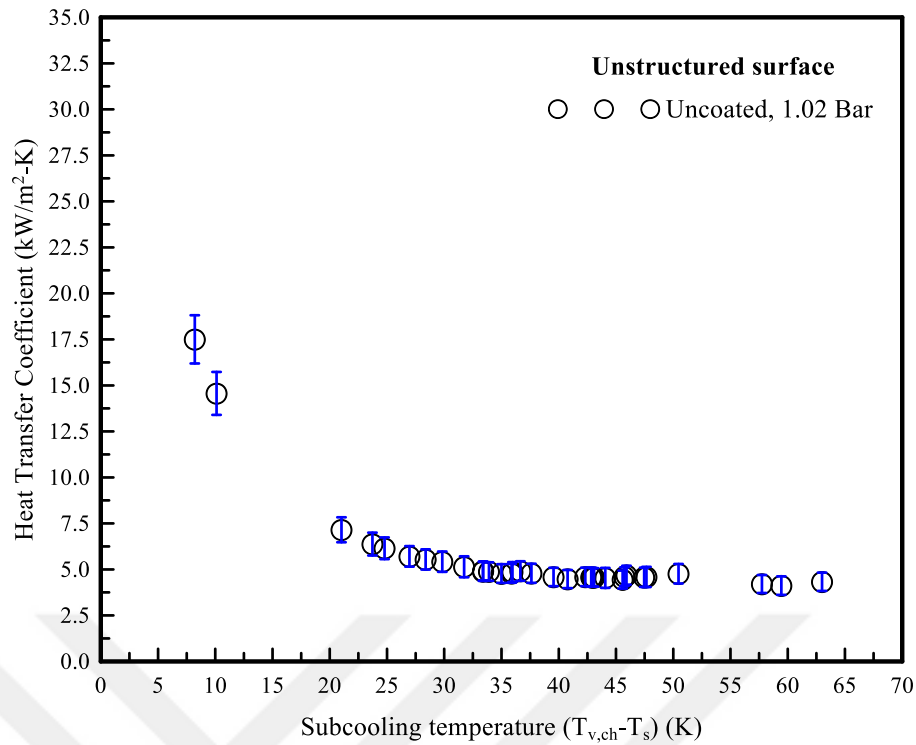


Figure 6-13: Variation of heat transfer coefficient with temperature difference

6.2.2 Square Grooved Surface

In Figure 6-14, wall temperature at different mass flow rates of cooling liquid is illustrated for the measurements using the micro-structured, and square grooved surface. Wall temperature decreases from about 85°C to 35°C with a rise in the mass flow rate of cooling liquid. Again, this is due to a stronger convective heat transfer between the cooling liquid and copper fins that resulted in a high heat transfer rate from the copper block to the liquid.

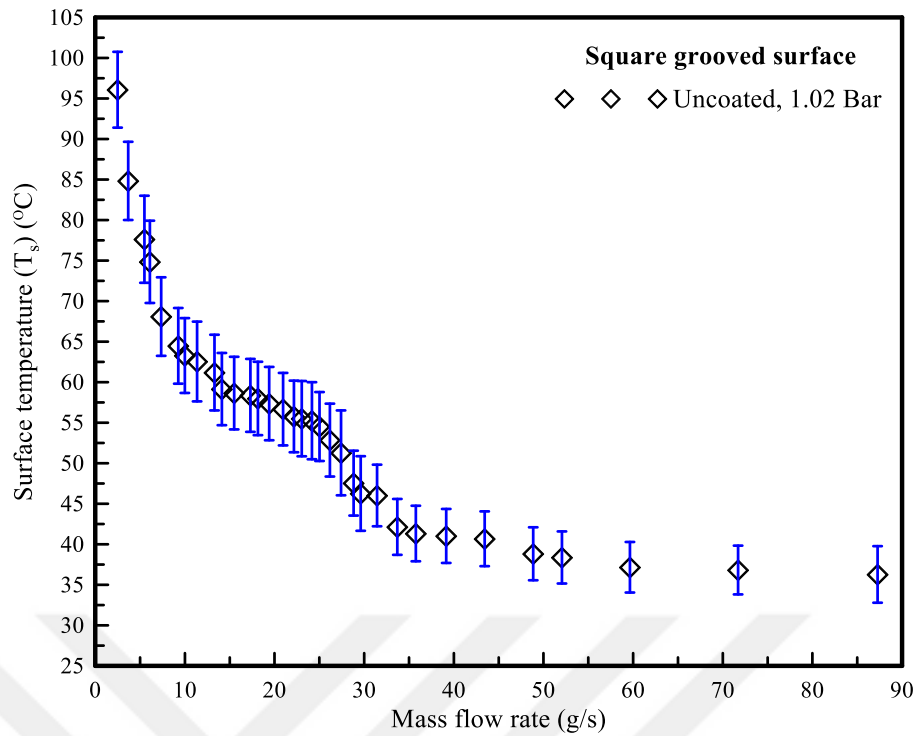


Figure 6-14: Surface temperature at condensation surface at varying mass flow rate of cooling liquid

Figure 6-15 shows the dependency of heat flux with respect to the temperature difference of $T_{v,ch}-T_s$. For large temperature differences, high heat fluxes are obtained. At certain temperature differences, more than one heat flux value has been obtained. Again, this can be attributed to measurement errors resulted from complex condensation physics. The underlying reasons behind the physics problem of this condensation phenomena are related to non-condensable gases, relative humidity, two-phase of vapor condensation that happened at the interface line between the vapor and liquid condensation [101].

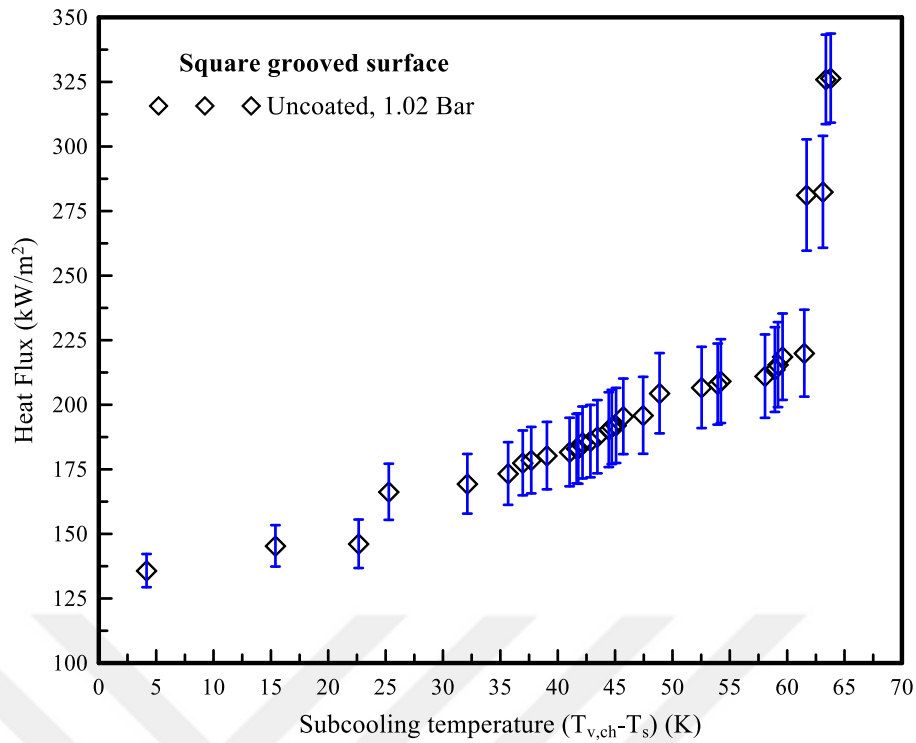


Figure 6-15: Variation of condensation heat flux versus temperature difference

Figure 6-16 shows heat transfer coefficients at various temperature differences. Since the vapor and the inlet temperature of the cooling liquid have been kept constant, the increase of mass flow rate of cooling liquid will raise the temperature difference between the surface and the vapor. Thereby, the rate of convective heat transfer is enhanced by the cooling liquid and it is observed when Newton's law of cooling is applied (see Eq.4-7 in section 4.7).

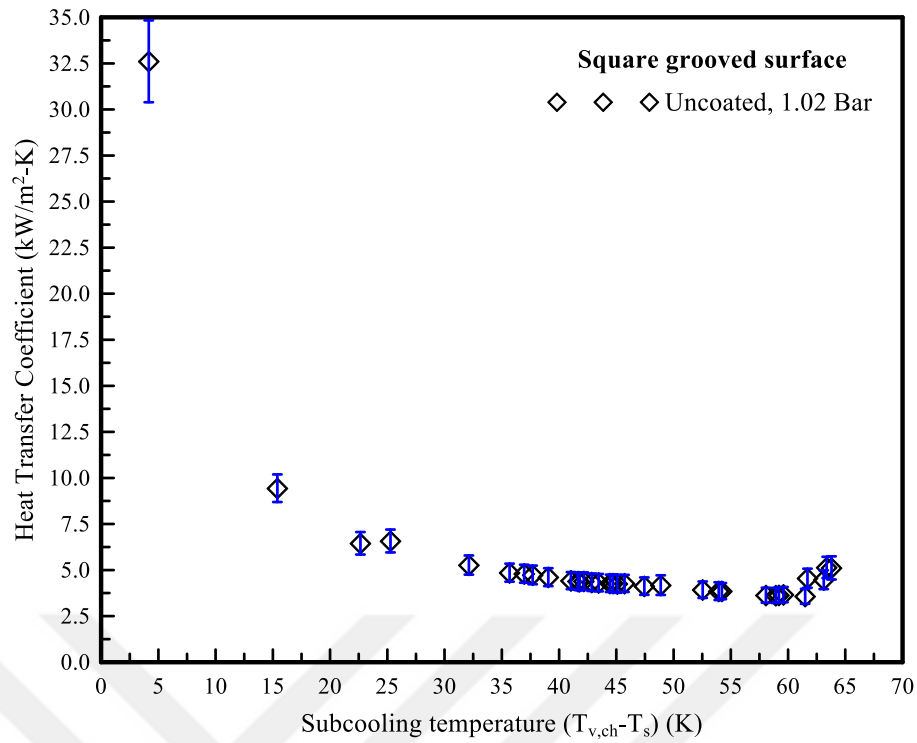


Figure 6-16: Effect of the temperature difference on heat transfer coefficient

6.2.3 V- Grooved Surface

The behavior of the wall temperature at different mass flow rates of cooling liquid is illustrated in Figure 6-17 for the measurements using the micro-structured V-grooved surface. It is seen that the wall temperature decreases from 88°C to 30°C with increasing liquid mass flow rate. Similar to unstructured and square grooved surfaces, this can be referred to the stronger heat transfer existing and growing the temperature difference between the fins surface and the cooling liquid.

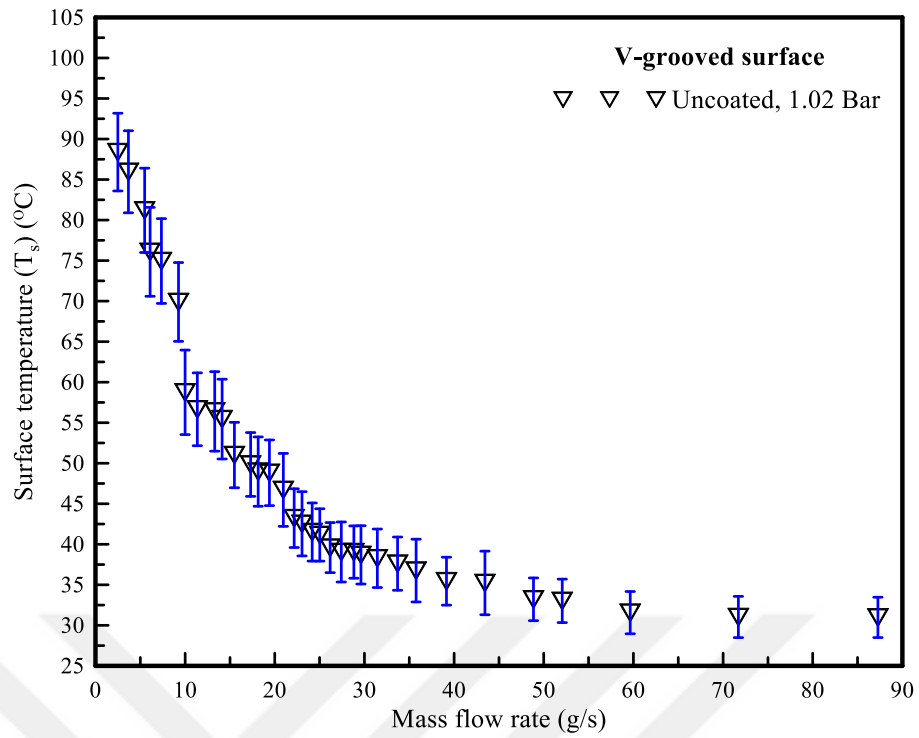


Figure 6-17: Wall temperatures at condensation surface at different mass flow rates of cooling liquid

Moreover, the heat fluxes at various temperature differences are depicted in Figure 6-18. It has been expected that high heat fluxes should arise when increasing the temperature difference. However, similar heat flux values are resulted in different temperature differences.

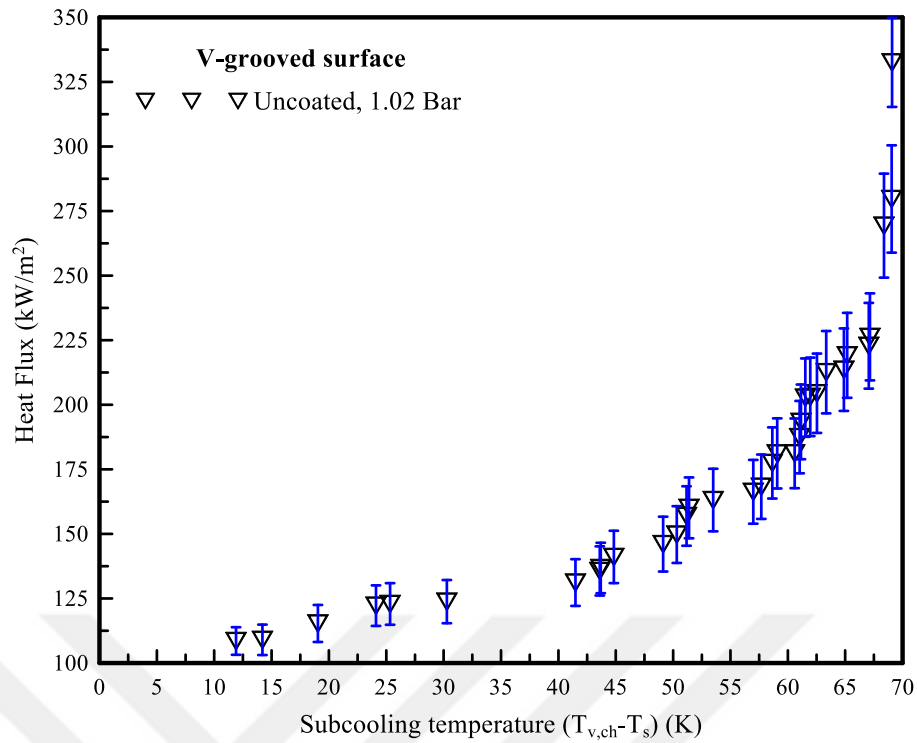


Figure 6-18: Variation of condensation heat flux with subcooling temperature

This unclear behavior requires a detailed investigation, which should be carried out in another phase of this study. Figure 6-19 shows the heat transfer coefficients at various temperature differences. Since the vapor temperature and the inlet temperature of the cooling liquid have been kept constant, the increase of mass flow rate of the liquid will raise the temperature difference between the surface and the vapor. This is because of the improvement in the convective heat transfer by the increment of the temperature difference between the fins surfaces and the cooling liquid in the back side of the heat sink. Consequently, the condensation heat transfer coefficient is enhanced in the front side of heat sink, which is governed by the Newton's law of cooling.

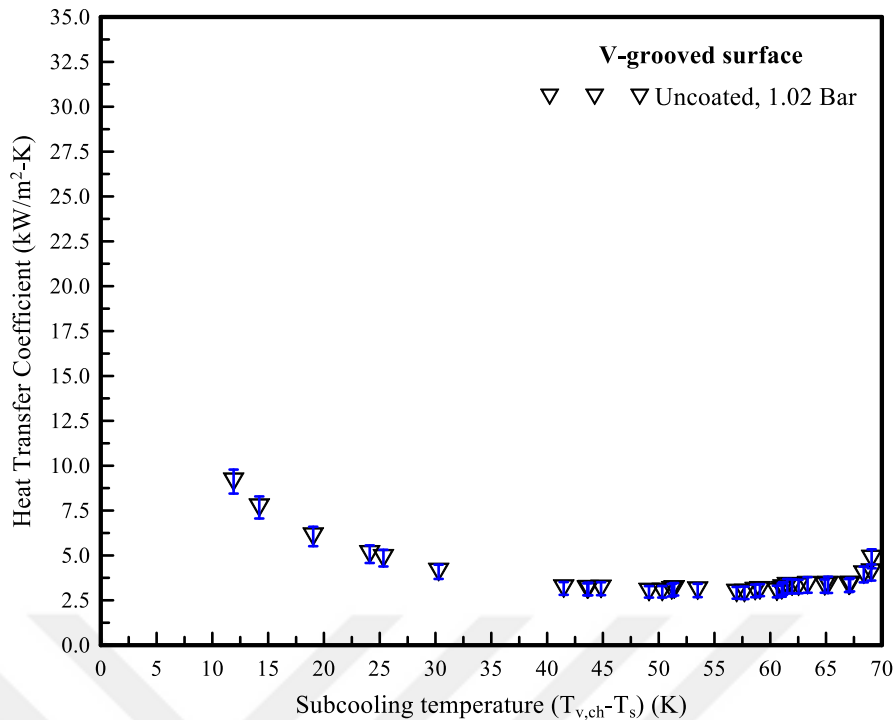


Figure 6-19: Heat transfer coefficient versus subcooling temperature ($T_{v, ch} - T_s$)

6.2.4 Comparison: Unstructured, Square-grooved and V-grooved Surfaces

The comparisons of surface temperatures and heat fluxes are illustrated in Figure 6-20 (a) and (b). Generally, for all copper samples, the surface temperature (wall temperature) decrease with the increase in mass flow rate. The lowest surface temperature values could be reached at the V-grooved surface, while the largest temperatures exist at the unstructured surfaces for comparable mass flow rates.

While heat fluxes show the rather same trend, however high heat fluxes could be obtained at dissimilar temperature differences unexpectedly. Moreover, the maximum heat flux has reached to about 240 kW/m². For temperature differences larger than 50 K, the decrease in heat flux can be seen for all surfaces. This might be explained by the wetting phenomenon occurred at the surfaces. Moreover, the effective accumulation of droplets could lead to temporal decrease in the contact area between the surfaces and vapor phase by reducing the heat transfer rate due to the liquid wetting on the surface.

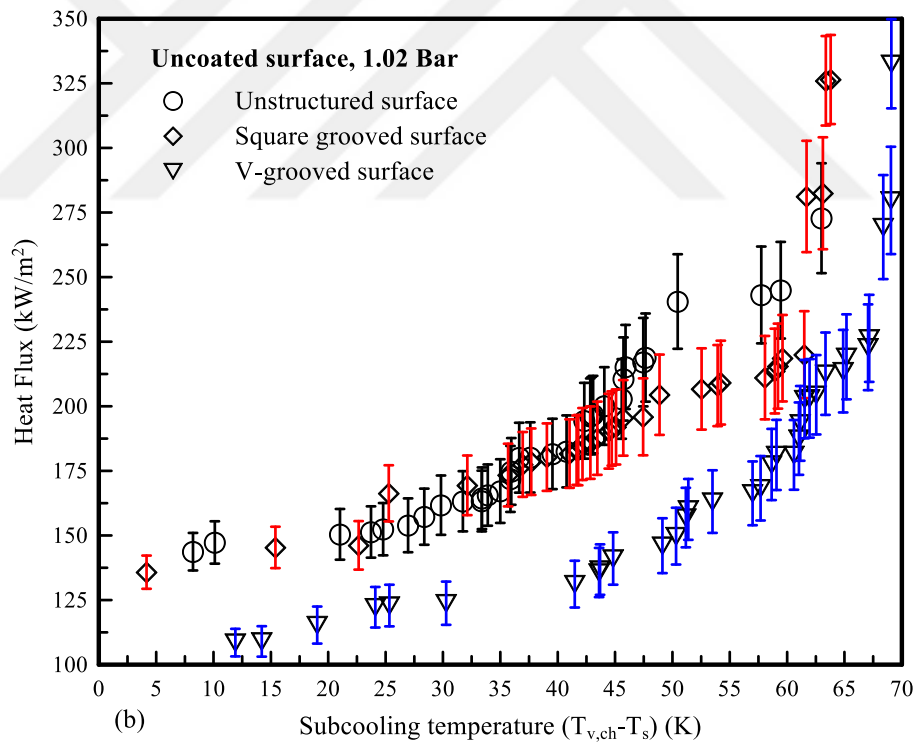
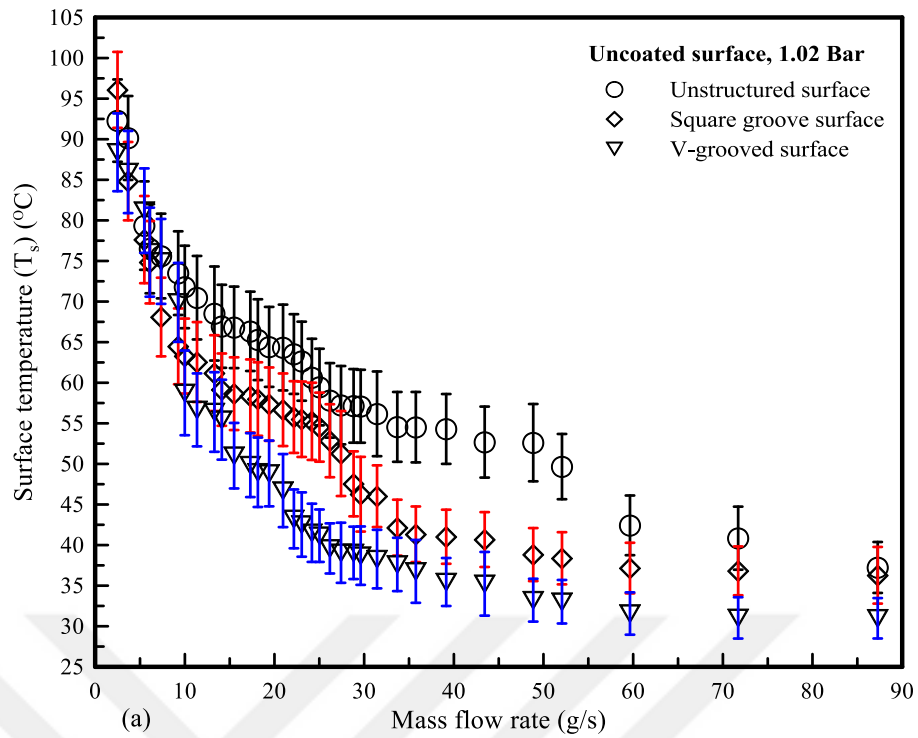


Figure 6-20: Comparison of (a) surface temperatures and (b) heat fluxes of various surfaces

The differences in heat transfer coefficients are observed more clearly when looking at values obtained for the temperature range of 30 K – 65 K (see Figure 6-21) and the HTC for all surfaces reduces with the elevated temperature difference of the vapor and condensation surface. In case of the unstructured surface, the highest heat transfer coefficient has been obtained at temperature differences less than 35 K, while the largest HTC resulted in temperature differences more than 40 K in addition to the decrease with the increasing temperature difference for the micro-structured surfaces. In fact, the micro-structures were expected to improve the heat transfer coefficient because of the increase in the area by about 50%. A larger surface area should provide a higher number of active nucleate sites for droplet condensation. However, for all that, there is no significant advantage in terms of enhancement of HTC when the surface is applied with micro-structures at the particular geometrical dimensions used in the current thesis. The reason for that is the formation of liquid film inside the troughs of the grooves, where actually the onset of dropwise condensation has been anticipated.

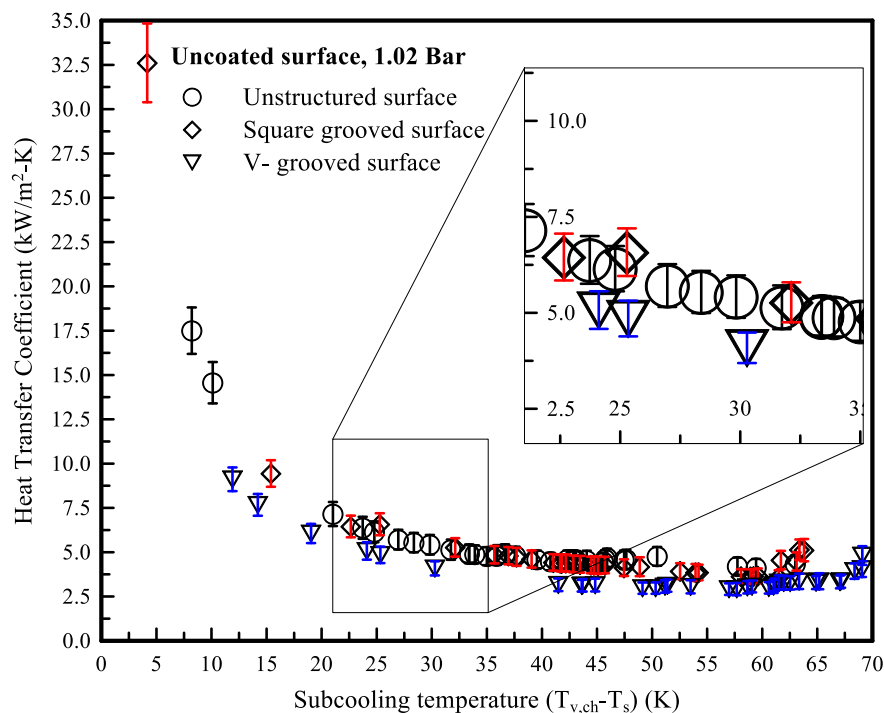


Figure 6-21: Comparison HTC of microstructured surfaces with unstructured surface

It is well known that the heat transfer coefficient for dropwise condensation is at least 10 times higher than filmwise condensation. Therefore, the surface area increase did not remarkably contribute to the intensification of heat transfer rate but it only supported the liquid accumulation and propagation. More investigations should be performed for finding the best geometrical dimensions of microstructures to improve heat transfer.

6.3 Condensation on Hydrophobic Surfaces

In this section, the effect of surface wetting (hydrophobic) on the condensation process is explained under different pressures of the vapor chamber. The manufacturing of the coating by using APTES SILANE liquid and the hydrophobic applications for different surface topographies are clarified in section 4.3. In addition, the droplet contact angle is measured experimentally at ambient condition (see section 4.5.1) over the hydrophobic surfaces and individually not during the condensation process. Then, the experimental results of the contact angle are shown in Figure 6-22 for all topographies before and after coating, with the measured droplet contact angle ranging in between $90^\circ < CA < 150^\circ$.

In addition, the effect of mass flow rate of cooling liquid and subcooling temperature on the condensation heat transfer mechanism for different surface topographies are shown from Figure 6-23 to Figure 6-34 as $p_{v, ch}$ is risen from 1.02 Bar to 1.25 Bar. Figure 6-35 through Figure 6-38 also show the comparison between the condensation heat flux versus HTC at a constant vapor pressure with different surface topographies.

In Figure 6-22, it can be seen that the average contact angle at each location from 1 to 5 (see Figure 4-14) was $93.2^\circ \pm 1.5^\circ$, $95.7^\circ \pm 6.9^\circ$ and $109^\circ \pm 5.1^\circ$ of the unstructured, V-grooved, and square grooved samples respectively. The discrepancies in CA before the surface treatment can be attributed to the finishing process caused by the manufacturing

procedure. The highest contact angle was found to be $117^\circ \pm 0.9^\circ$ at the location 1 of the square groove surface and the lowest contact angle was $88.6^\circ \pm 1.8^\circ$ at the location 4 of the unstructured surface because of the varying topography surface and roughness. Moreover, it can be seen that the average contact angle at each location increased after the surface coating (see Figure 6-22), and this led to the growth from $93.2^\circ \pm 1.5^\circ$ to $105.8^\circ \pm 0.8^\circ$. The discrepancies in CA among the measurement positions before the performed surface treatment can be related to the finishing caused by the machining procedure of the substrate. The variations in CA after the surface treatment might have been caused by the coating method, leading to a non-homogenously distributed hydrophobicity, while the lowest contact angle was measured at the location 4.

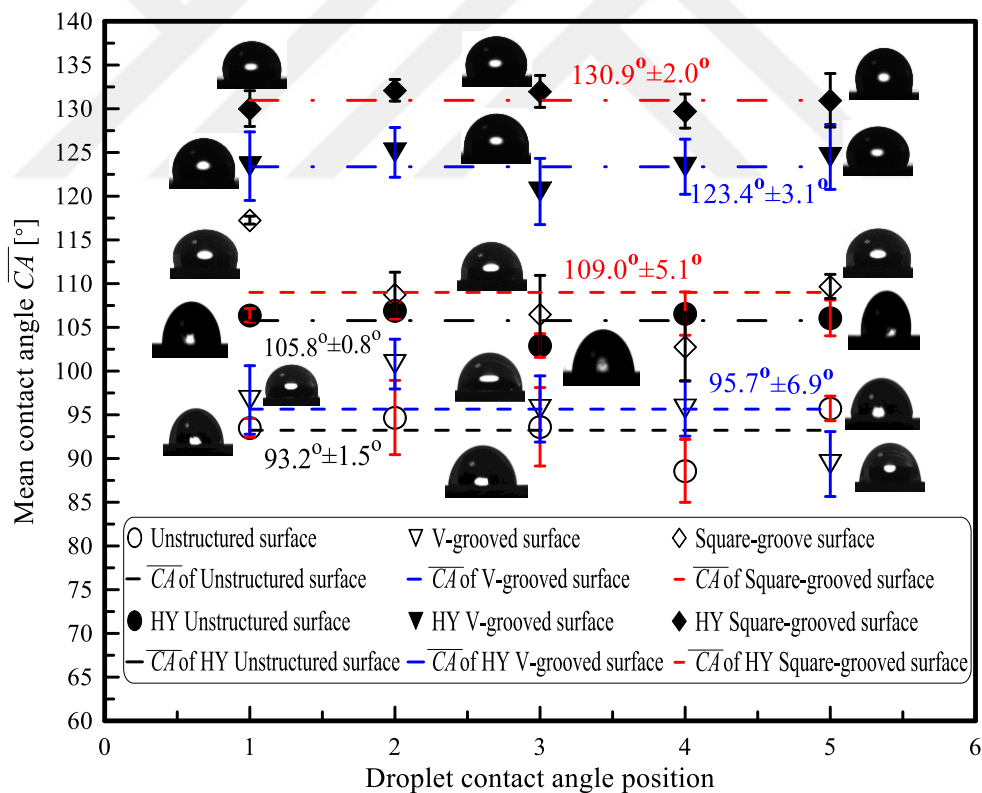


Figure 6-22: Average droplet contact angle at the hydrophobic condensing surface compared to the untreated surface

6.3.1 Unstructured Surfaces

In Figure 6-23, the surface temperature at varying \dot{M}_1 is presented for different pressures inside the vapor chamber. Experiments for both uncoated and coated surfaces are performed for a pressure range from 1.02 Bar to 1.25 Bar while the surface temperature decreased with increasing flow rate (\dot{M}_1). In the case of the hydrophobic surface, the surface temperatures were always larger than those observed with the untreated surface, while larger values of T_s could be achieved at higher pressures inside the vapor chamber. For higher pressures inside the vapor chamber, the surface temperature increases for comparable temperature differences due to the rise of the corresponding saturation temperature of vapor. However, at a low pressure (1.10 Bar), the coated surface temperature shows a sharp reduction starting at $\dot{M}_1 = 35.8$ g/s and follows the trend for the cases measured at $p_{v, ch} = 1.02$ Bar. At 1.20 Bar and 1.25 Bar, there is very small difference between the surface temperature values as it can be seen from the figure for the coated substrate at up to $\dot{M}_1 = 39.1$ g/s. At high mass flow rates, a difference in surface temperature is also observed between two pressures. However, the temperature differences at the uncoated surface are more distinctive at similar pressure levels.

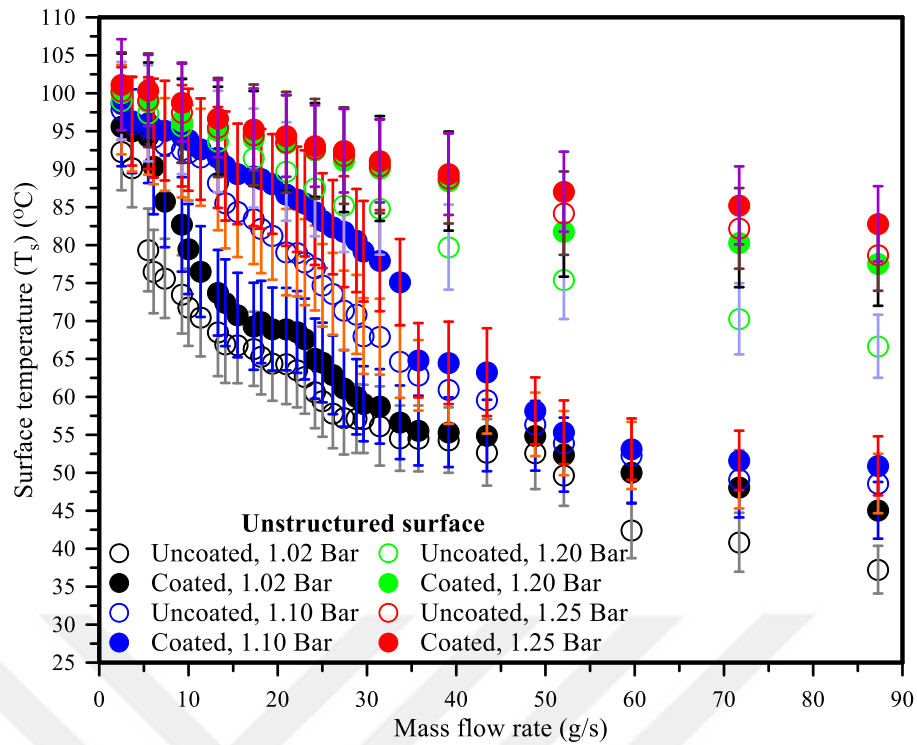


Figure 6-23: Surface temperature at various vapor pressures

Heat flux results are presented in Figure 6-24 for the uncoated and coated surfaces for a range of pressure values. In all cases, similar mass flow rate values were studied during the experiments. Therefore, heat flux values are calculated for the particular temperatures, which existed at the measurement locations. Because of that, some of the heat flux values do not correspond to similar wall subcooling. Generally, heat flux values increase with higher subcooling for the uncoated and coated surfaces. The coated surface shows larger heat fluxes at 1.02 Bar, 1.10 Bar, and 1.20 Bar at comparable wall subcooling similarly to the uncoated surface. At 1.25 Bar, the difference in heat flux reduces. Since larger CA at the treated copper surface has been measured, droplets appearing on the surface may not spread easily over the surface area. It is more likely to have a local growth and detachment from the initial spot. This probably contributes to the mitigation of the formation of a thermal resistance between solid and vapor. With

increasing pressure, the heat flux gradually increases more for both of the surfaces. The maximum heat flux was observed at about 436 kW/m² with increasing temperature difference from 6 K to 23 K at 1.25 Bar at the hydrophobic surface. This can be possibly explained by the surface-wetting phenomenon, which took place at the surface, since the quantity of droplets with small sizes increases due to larger numbers of active nucleation sites on the surface at an elevated pressure. As a result, the size of the effective area through which heat is transferred from the vapor to the wall surface increases [102]. Another key point is the gradient of the heat flux at the vapor pressures of 1.20 Bar and 1.25 Bar. It can be concluded that the heat flux is more prone to temperature differences than at lower pressures.

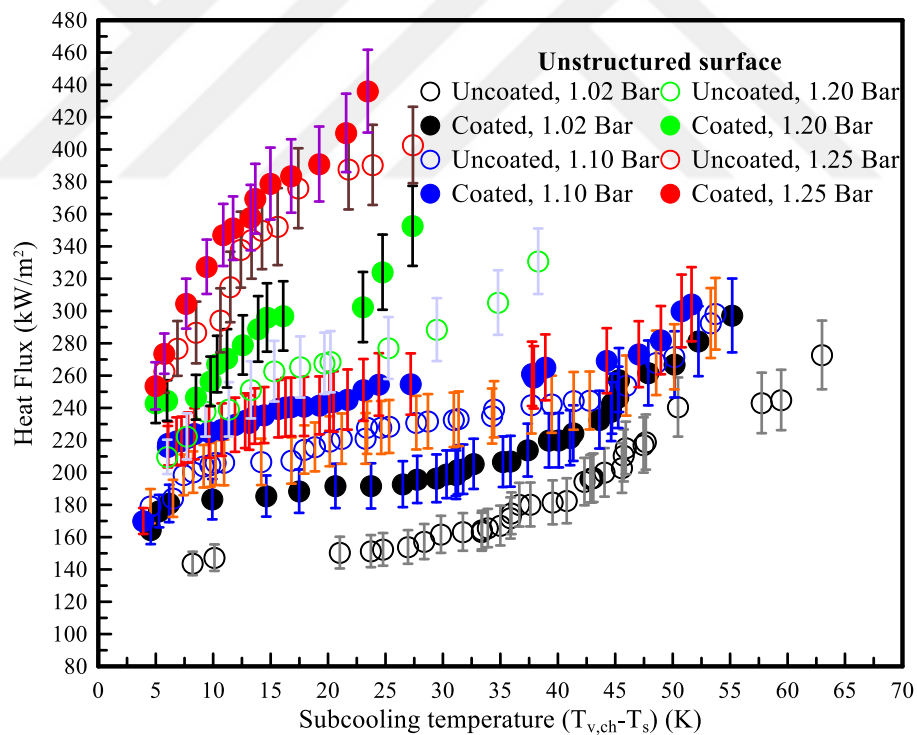


Figure 6-24: Effect of subcooling temperature difference over condensation heat flux at various vapor pressures

The dependency of the heat transfer coefficients obtained on the uncoated and coated surfaces on the subcooling temperature difference and vapor pressure is presented in Figure 6-25. For both surfaces and pressure levels, the HTC shows a decrease when the temperature difference increases. The experimental results produced at 1.02 Bar show that the largest HTC is obtained about 17.5 kW/m²-K at a wall subcooling of 8.2 K for the uncoated surface. For a comparable subcooling temperature difference (10 K), HTC for the coated surface resulted in 18.5 kW/m²-K, while a heat transfer coefficient was determined about 14.56 kW/m²-K for the uncoated surface. The maximum HTC for the coated surface could be reached at 4.6 K as approximately 36 kW/m²-K. Raising the operating pressure inside the vapor chamber led to a remarkable rise in the heat transfer coefficient for the coated surface. This effect can be probably traced back to the onset of droplet formation and their size and dynamics at the surface. At high pressures, the initiation of droplets occurs faster along with rapid growth and removal from the surface. The quick formation and motion of droplets leads to a reduction in the thermal resistance [102]. Hence, this precipitates an expansion of the local contact between the vapor and the subcooled wall causing heat transport augmentation [78].

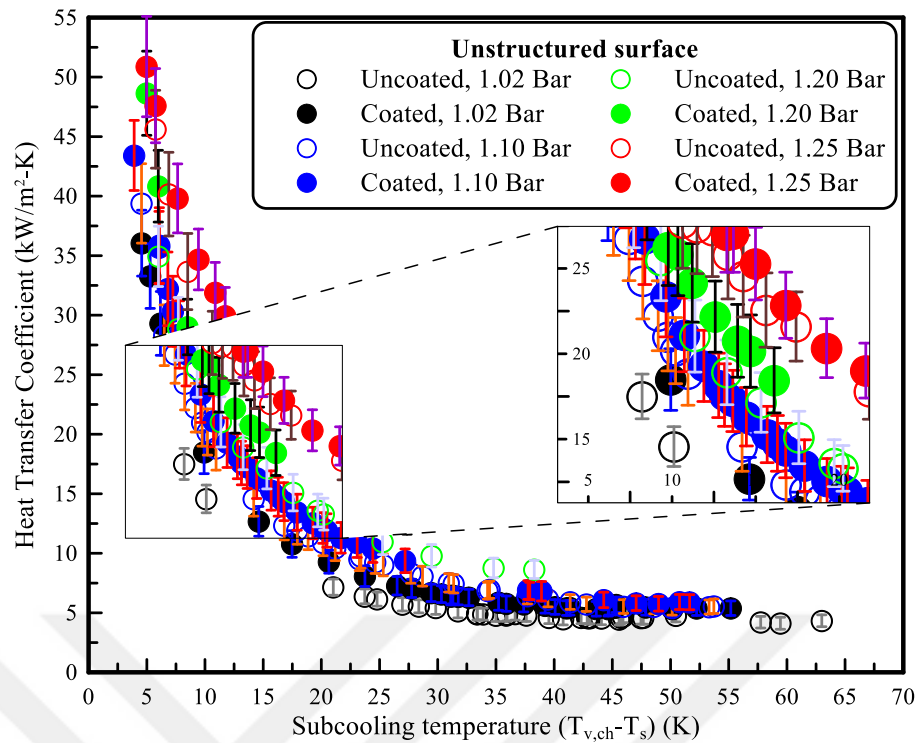


Figure 6-25: Measured Heat transfer coefficient versus subcooling temperature difference for different vapor pressures

Figure 6-26 illustrates the change of the heat transfer coefficient depending on heat flux with different vapor pressures. The heat transfer performance at the coated surface is stronger than the one at the uncoated surface for all pressure levels, while HTC is decreasing with higher heat flux. At a pressure of 1.02 Bar, the heat transfer coefficient for the untreated surface shows a constant trend beginning at approximately 160 kW/m². Similar behavior can be encountered for the hydrophobic sample where constancy for HTC starts at about 215.0 kW/m². For higher vapor pressures, the inception of the trend for constant HTC values migrates towards higher heat flux values. Furthermore, it is clearly seen that the coating can cause to higher heat transfer rates at comparable surface temperatures. The rise in vapor pressure results in a shift at HTCs towards larger heat fluxes while the slope decreases. The highest heat transfer coefficient was found to be about 51 kW/m²-K for the heat flux of 253.6 kW/m² when operating at 1.25 Bar.

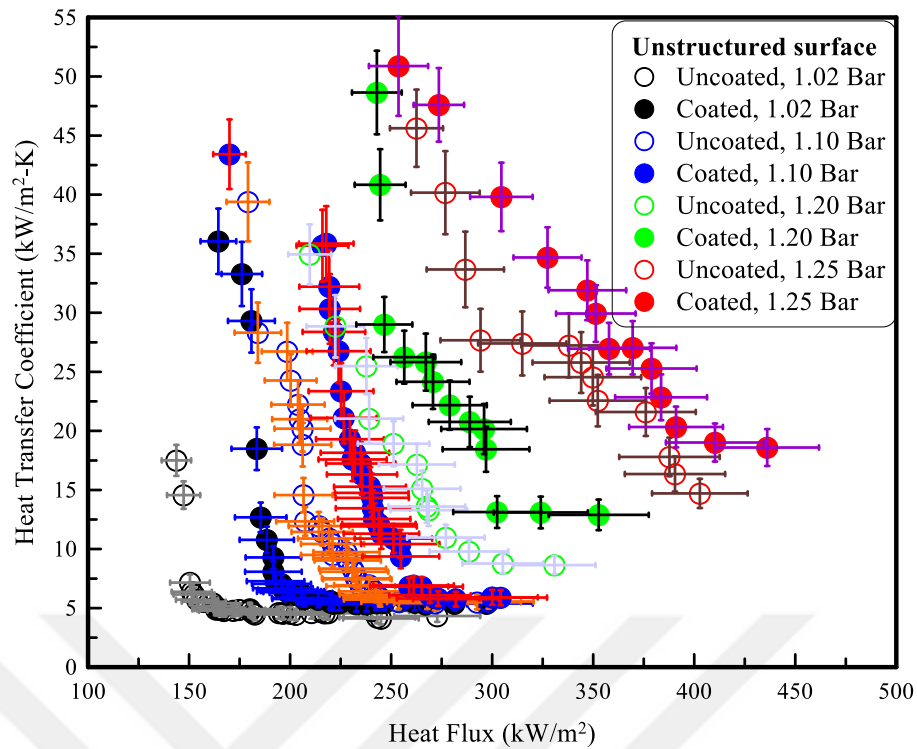


Figure 6-26: Heat transfer coefficient at various heat fluxes for different vapor pressures

6.3.2 Square-grooved Surface

The surface temperature at various mass flow rates of the cooling liquid \dot{M}_1 is illustrated for the measurements in which the micro-structured square grooved surface is studied with different pressures ranging from 1.02 Bar to 1.25 Bar as seen in Figure 6-27. Also, same experiments were conducted as in the case of the unstructured surface for different chemical treatments, vapor pressures and mass flow rates of the cooling liquid. The elevation in the mass flow rate of the cooling liquid from 4.5 g/s to 87.3 g/s caused a decrease in surface temperature due to the improved heat transfer rate between the copper fins of the heatsink and the cooling liquid for each vapor pressure inside the vapor chamber. It can be seen that the introduction of a new coating that improves the processes compared to the reference surface increases the surface temperature for each vapor chamber pressure since the exposed effective surface area to

the vapor is enlarged as the droplet contact angle increases (see Figure 6-22). The experimental results indicated that the relationship between the vapor pressure and the surface temperature is proportional due to the increase in saturation vapor temperature inside the vapor chamber. However, for both of the coated and uncoated surface at a low pressure of 1.10 Bar, the surface temperature showed a sharp reduction starting at \dot{M}_1 equal to 29.6 g/s and 33.7 g/s respectively, where it gradually decreased after $\dot{M}_1 > 35.7$ g/s. The same behavior can be observed for the unstructured surface while the smallest variation in the surface temperature is seen at the highest values of the vapor pressures of 1.20 Bar and 1.25 Bar. This is because of the lower convection heat transfer between the cooling liquid and the copper-block inside the liquid chamber at the mass flow rate of the cooling liquid lower than 31.4 g/s.

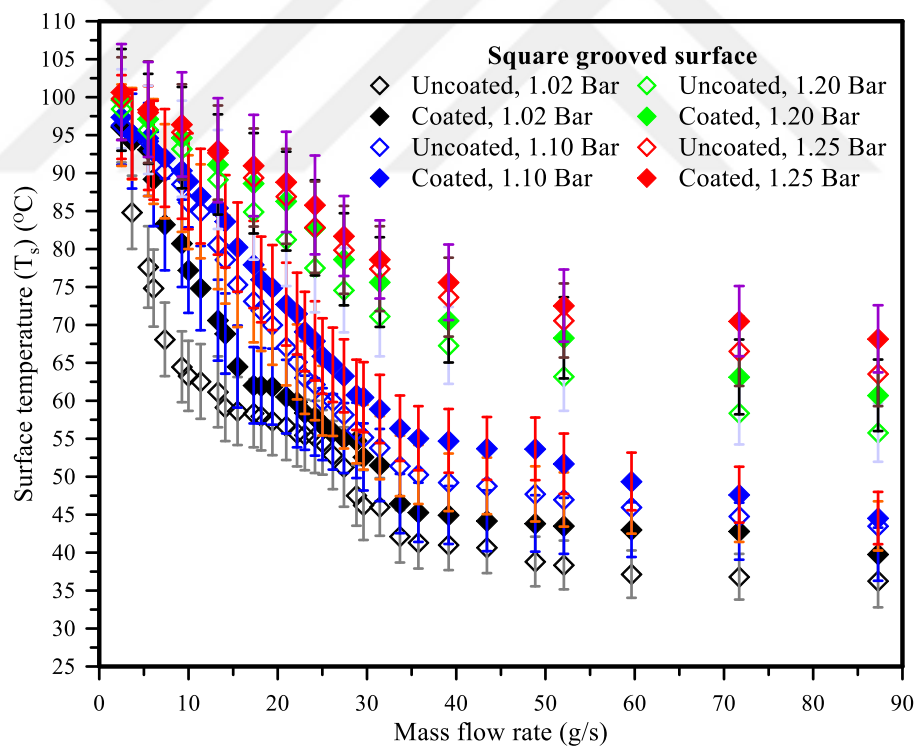


Figure 6-27: Variation of surface temperature at different vapor pressures

Variation of heat flux with the temperature difference between the vapor chamber and the condensation surface is presented in Figure 6-28 for the measurements of the micro-structured square grooved surface with a vapor pressure range from 1.02 Bar to 1.25 Bar. For large temperature differences, high heat fluxes were obtained for each coated and uncoated surface at different saturation vapor pressures. The experimental results illustrate similar behavior to the unstructured surface, where the heat flux increased by 42 % and 48.1 % at $\dot{M}_l > 17.31$ g/s for the uncoated and coated surface respectively at each $p_{v,ch}$ of the 1.02 Bar and 1.25 Bar. In addition, the heat fluxes of the hydrophobic surface increased by 2.6 % and 4 % when compared to the uncoated surface at the same vapor pressure, which were 1.02 Bar and 1.25 Bar respectively. Also, the figure shows that the heat flux values of the square groove were lower than the ones for the unstructured surface for each operating parameter with a larger droplet contact angle (see Figure 6-22). This could be explained by the film condensation occurring inside the groove, which increases the thermal resistance between the effective condensation surface and the vapor. At a high vapor pressure of 1.25 Bar, the maximum values of the heat flux are obtained as 378.5kW/m² and 292.3kW/m² by rising the subcooling temperature on the coated and uncoated surfaces respectively.

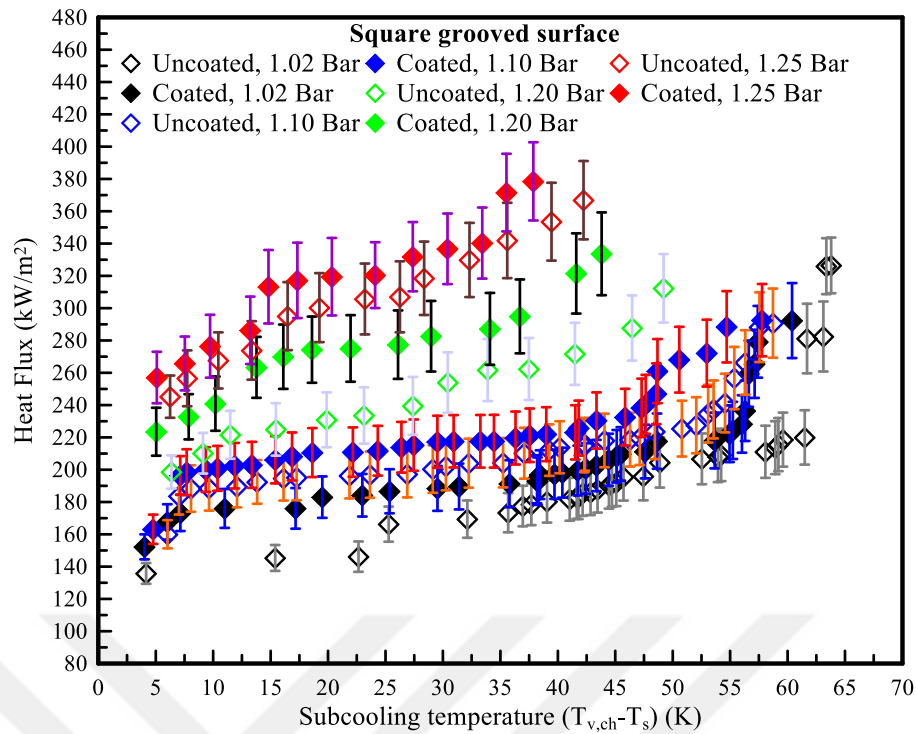


Figure 6-28: Heat flux versus subcooling temperature ($T_{v,ch}-T_s$) at various $p_{v,ch}$

The heat transfer coefficients and the subcooling temperature on the microstructured square groove surface with different wettability at vapor pressures range from 1.02 Bar to 1.25 Bar is presented in Figure 6-29. Since the operating pressure inside the vapor chamber and the cooling liquid temperature at the inlet of the liquid chamber were kept constant, an increase in the mass flow rate of the cooling liquid will also rise the subcooling temperature, and this leads to a decrease in the HTC. Accordingly, the experimental results showed that the HTC was increased by 11.3 % at 1.02 Bar and 2.5 % at 1.25 Bar for the uncoated and coated surfaces respectively. Also, as the operating vapor pressures increase from 1.02 Bar to 1.25 Bar, the HTC rises by 54.7% for the uncoated surface and 61.8% for the coated surface with an incremental temperature difference. In addition, at high operating vapor pressure of 1.25 Bar, the minimum and maximum values of the HTC for the coated surface were 10 kW/m²-K

and $50.5 \text{ kW/m}^2\text{-K}$ at $T_{v, \text{ch}} - T_s = 37.8 \text{ K}$ and 5.1 K , respectively. Furthermore, the HTC of micro-structured square groove surface was lower than the one for the unstructured surface due to the condensation types. During the condensation experiments, Drop-film wise condensation (DFWC) was observed on the square groove surface, while Drop-wise condensation (DWC) was noticed on the unstructured surface. In addition, the results demonstrated that the heat flux of DFWC for square groove is lower than the one for DWC over the unstructured surface (see Figure 6-28) with the rising subcooling temperature.

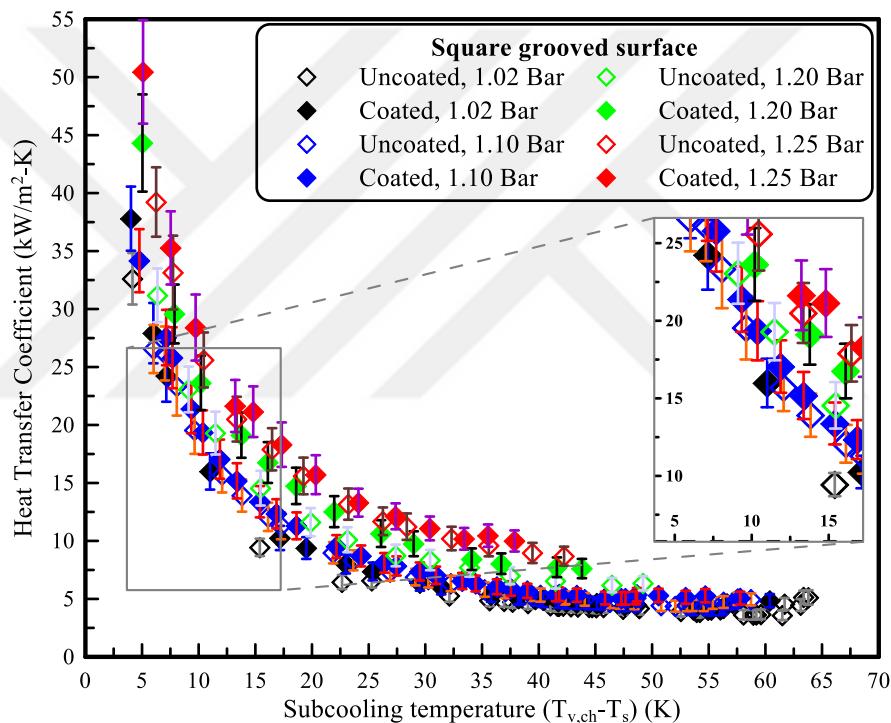


Figure 6-29: Variation of heat transfer coefficient with subcooling temperature difference at different vapor pressures

Figure 6-30 represents the change in heat transfer coefficient (HTC) with the heat flux over the uncoated and coated microstructured square grooved surface with different vapor pressures from 1.20 Bar to 1.25 Bar. The results showed that when the heat flux increases, the HTC decreases by 84.3 % for the untreated surface, while the HTC is

reduced by 87.2 % for the hydrophobic surface at constant $p_{v, ch}=1.02$ Bar due to the increasing subcooling temperature. While the largest value was observed in an operating vapor pressure of 1.25 Bar, the HTC was found to be decreasing by 77.8 % for the uncoated surface when the heat flux is ranging from 245.2 kW/m² to 366.9 kW/m². On the other hand, a 80.2% drop in HTC was seen for the coated surface when the heat flux was elevated from 257.1 kW/m² to 378.5 kW/m². In addition, for the uncoated and coated surfaces, the HTC decreases by 81.1% and 83.7 % with the increasing pressure level from 1.02 Bar to 1.25 Bar. The chemical treatment on the microstructured square grooved surface provided a significant enhancement by increasing the values of HTC and heat flux for all operating vapor pressures compared to the uncoated surface. On the other hand, the results of HTC and heat flux of square groove surface were found to be lower than the ones for unstructured surface (see Figure 6-26) due to the effect of the film condensation on the heat transfer parameters that led to increase the thermal resistance of liquid film condensation with the reduce of wall temperature.

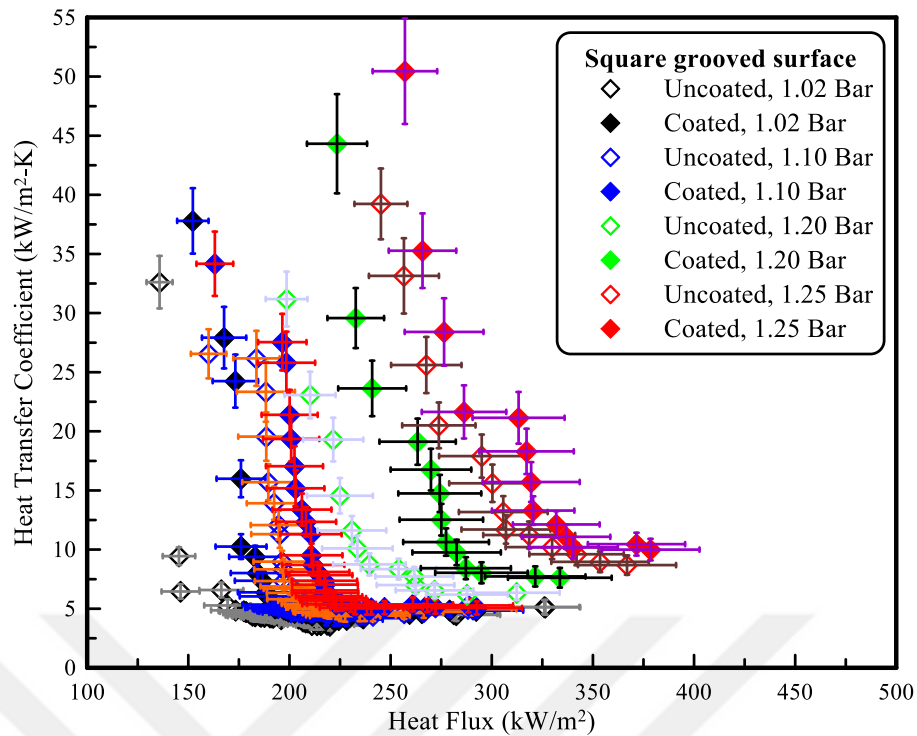


Figure 6-30: Variation of heat transfer coefficient with heat flux for different pressures

6.3.3 V- Grooved Surface

The variations of the surface temperature at various flow rates and vapor pressure for both the coated and uncoated microstructure V-groove surface are shown in Figure 6-31. The change in surface temperature has shown a similar trend over the unstructured and square groove surfaces since it decreases for all operating vapor pressures as the mass flow rate of cooling liquid is increased from 4 g/s to 87 g/s. Also, the condensation surface temperature rises as the vapor pressure is elevated from 1.02 Bar to 1.25 Bar due to the increasing vapor temperature inside the vapor chamber. At low and high pressures (1.02 Bar and 1.25 Bar), the experimental results showed that the surface temperature increases by 93.1 % and 78.3 % at $\dot{M}_l > 21$ g/s for each uncoated and coated surface. The surface temperature of the hydrophobic sample was higher than the uncoated one by 12 % and 2.4 % at $p_{v,ch} = 1.02$ Bar and 1.25 Bar.

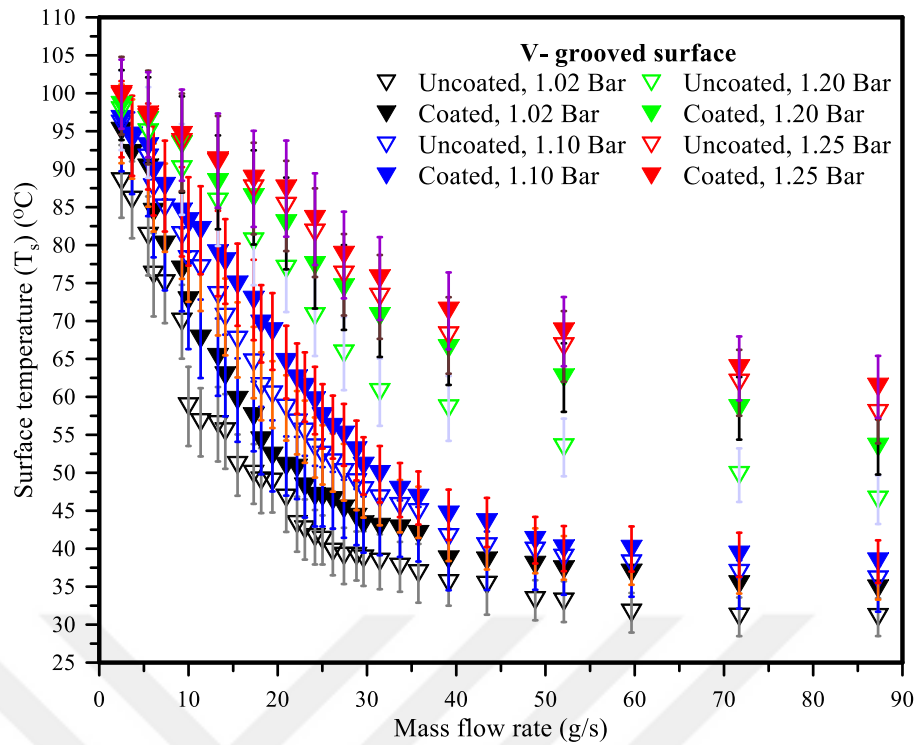


Figure 6-31: Surface temperature at the condensation surface at various mass flow rates

Figure 6-32 illustrates the relation between heat flux and the subcooling temperature on the V-groove surface during the condensation tests at the pressures ranging from 1.02 Bar to 1.25 Bar. The behavior of the heat flux versus $T_{v,ch}-T_s$ has been observed in the same trend when compared to other surfaces including square groove and unstructured one. The results showed that the heat flux increases from 109 to 333 kW/m² for the uncoated surface, while it rises from 230 to 320 kW/m² for the coated one at the same vapor pressure of 1.02 Bar. This is because the subcooling temperature of the coated surface is lower than the uncoated surface by approximately 30.4% and this can promote the dropwise condensation with the increased exposed surface area to the vapor. In addition, as the vapor pressure rises from 1.02 Bar to 1.25 Bar, the heat flux increases by 34.4% for uncoated surface and by 37.8 % for the coated surface with higher subcooling temperature. It can be related to the fast

condensation over the active surface as the vapor pressure is increased. The comparisons of the results between the uncoated and coated V-groove surfaces are obtained, and it has shown a considerable enhancement of heat flux by 11% at the vapor pressure of 1.02 Bar. Besides, the heat flux increased by 6% for coated V-groove surface compared to the uncoated surface at $p_{v, ch}=1.25$ Bar. As a result, the hydrophobic surface provides an enhancement in the heat transfer rate when the condensation surface area, surface temperature and heat flux are increased for each operating vapor pressure. Furthermore, the comparison of heat flux between the microstructured surfaces with different topographies is presented. The heat flux over the V-groove surface was lower than the one for the square groove surface for each operating vapor pressure. This is because of the growing liquid film thickness inside the groove, which led to the increasing condensation thermal resistance.

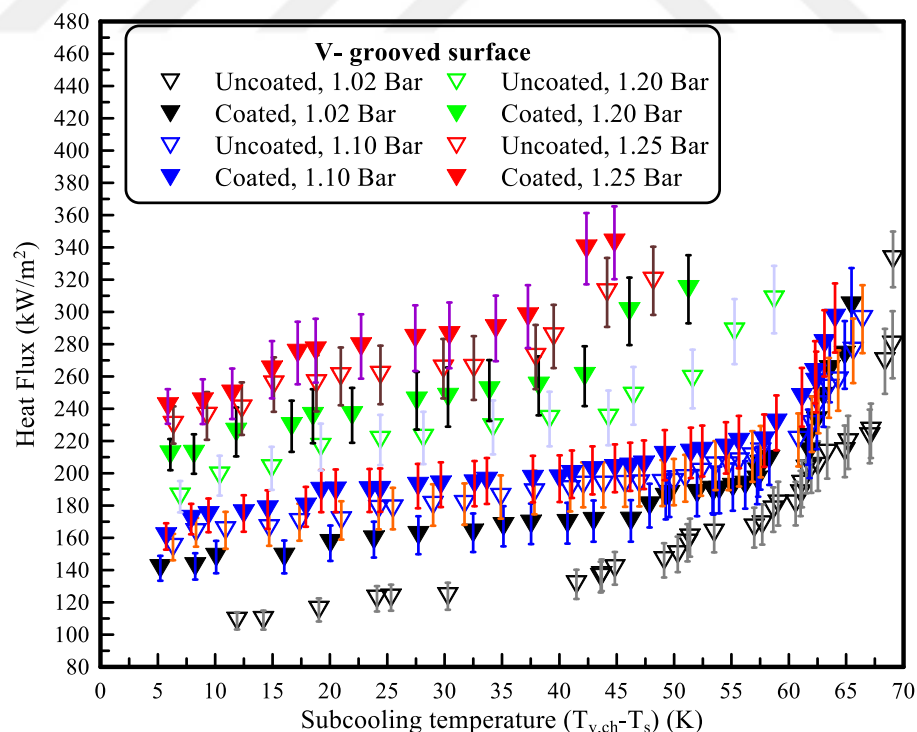


Figure 6-32: Variation of heat flux with the temperature difference at various $p_{v, ch}$

Figure 6-33 demonstrates the variation of HTC and subcooling temperature for uncoated and coated V-groove surface at vapor pressures ranging from 1.02 Bar to 1.25 Bar. The results indicated the lowest value of HTC as 7.7 kW/m² K, which was obtained for the coated surface at the subcooling temperature equal to 44.8 K and $p_{v, ch}=1.25$ Bar. Also, the similar results were found compared to the other surfaces as it was observed that heat transfer coefficient reduces, as the subcooling temperature rises for all operating vapor pressures. This could be related to the decreasing condensation surface temperature for coated and uncoated surface at a constant temperature of inlet cooling liquid in the back-side of heat sink. Experimental results of the hydrophobic surface demonstrated an increase in HTC by 2.4 % at 1.25 Bar and 12 % at 1.02 Bar compared to the uncoated surface. In addition, the figure illustrates the comparison of the HTC results at only minimum and maximum vapor pressures, and the enhancement in the condensation heat transfer coefficient is observed. As a result, it can be clearly seen that improvement in HTC is by 56.1% for the uncoated surface and 73.4% for the coated surface. Moreover, the heat transfer coefficient of V-groove surface is less than the other surfaces because of the same reason that was mentioned previously. This caused to a decrease in the condensation heat flux (see Figure 6-32).

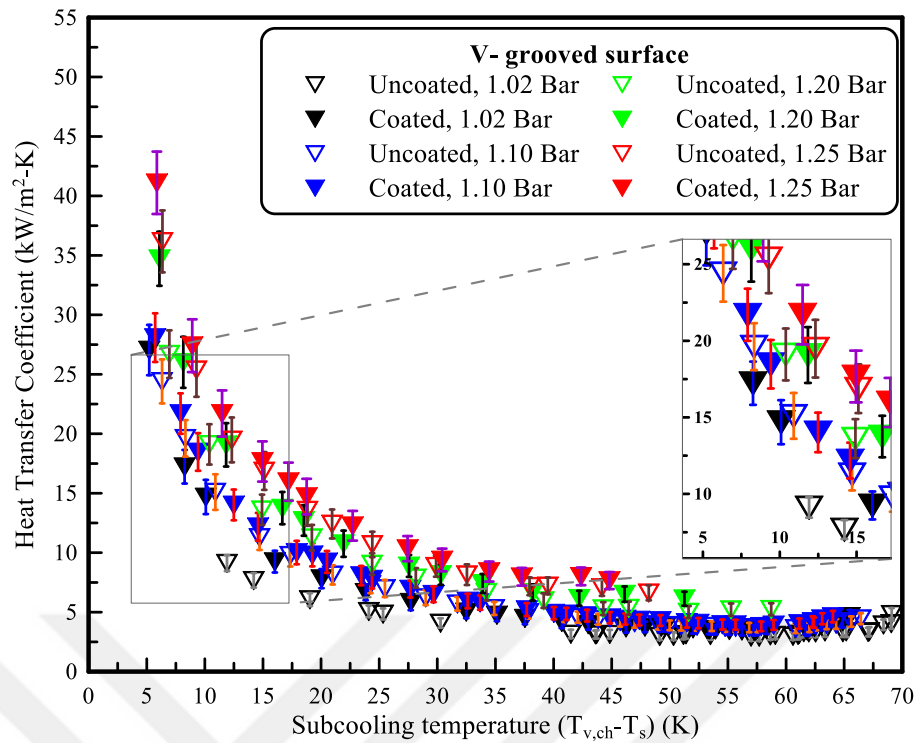


Figure 6-33: Variation of Heat transfer coefficient at different vapor pressures

The change of the heat transfer coefficient depending on the heat flux with different vapor pressures is presented in Figure 6-34. As the heat flux increases, the HTC decreases for all the operating vapor pressures. However, the heat transfer parameters such as the HTC and heat flux show an increasing trend when the level of the vapor pressure is raised from 1.02 Bar to 1.25 Bar for the uncoated and coated surfaces. For the uncoated surface, the results show that the HTC is reduced by 47.2% at 1.02 Bar and by 81.7% at 1.25 Bar with higher heat flux. For the coated surface, the heat transfer coefficient decreases by 82.8% and 81.4% at vapor pressure of 1.02 Bar and 1.25 Bar respectively. The experimental results for all operating parameters revealed that the lowest value of the HTC was 4.8 kW/(m²-K) at the heat flux value of 332.6 kW/m² for the uncoated surface when the vapor pressure is 1.02 Bar. On the other hand, the highest

value was found to be 41.1 kW/m²-K at 241.4 kW/m² for the hydrophobic surface at 1.25 Bar.

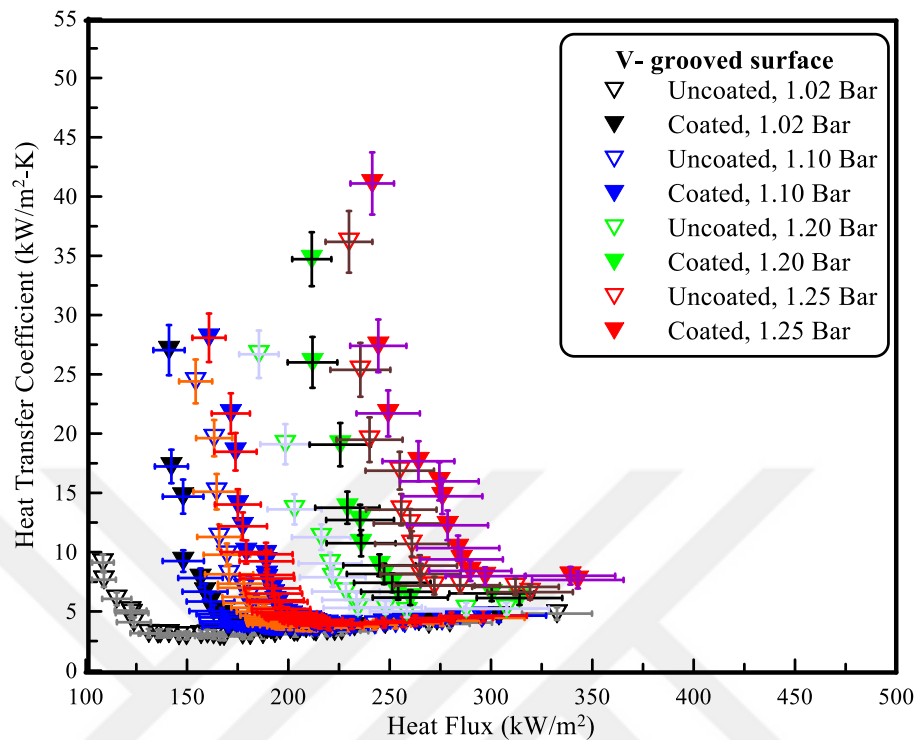


Figure 6-34: Variation of HTC with heat flux for different surfaces and vapor pressure

6.3.4 Comparison: Unstructured, Square-grooved and V-grooved Surfaces

The heat transfer coefficient vs. the heat flux for all the samples at constant vapor chamber pressure of 1.02 Bar is given in Figure 6-35. As the condensation heat flux rises, the HTC gets diminished for all the surface topographies due to the rising subcooling temperature and cooling liquid flow rate inside the liquid chamber. Moreover, the experimental results indicated that the HTC values were obtained less than 7.5 kW/m²-K at heat flux ranging from 200 kW/m² to 225 kW/m² for all surfaces due to the enhancement in the convective heat transfer when the fluid flow is accelerated over the surface fins inside the liquid chamber. In addition, the largest value of HTC value was observed for the coated and unstructured surface compared to the uncoated and/or unstructured surface for all samples. This is due to the filmwise

condensation happened on the microstructured surfaces, which was observed more dominantly compared to the unstructured one. This can increase the thermal resistance of the liquid film condensation as the surface temperature is reducing. The values of parameters for condensation heat transfer were determined for all experimental tests at the operating pressure of 1.02 Bar as $108.5 \leq \dot{q}_s \leq 297.2 \text{ kW/m}^2$ and $4.8 \leq \text{HTC} \leq 37.8 \text{ kW/m}^2\text{-K}$.

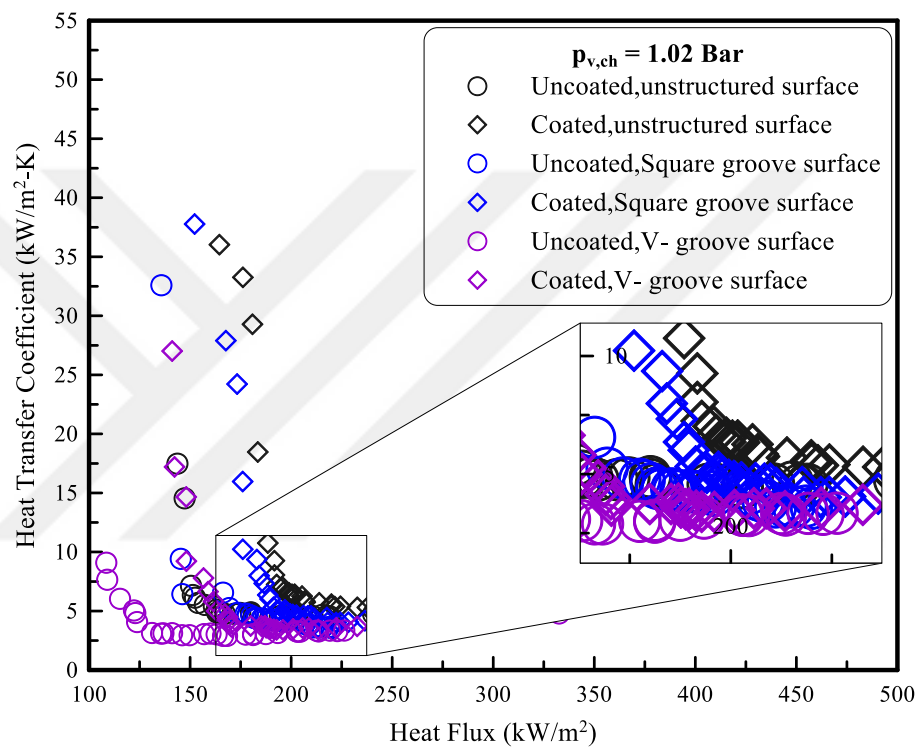


Figure 6-35: Variation of HTC with heat flux at 1.02 Bar

The variation of the heat flux with heat transfer coefficient at $p_{v,ch}=1.10$ Bar for various surface topographies is reported in Figure 6-36. Also, it can be seen that the results at vapor pressure 1.10 Bar showed the same trend compared to the results in Figure 6-35 for all the surfaces. In addition, the obtained range of data for the condensation heat transfer parameters can be summarized as $154.3 \leq \dot{q}_s \leq 304.2 \text{ kW/m}^2$ and $4.4 \leq \text{HTC} \leq 43.4 \text{ kW/m}^2\text{-K}$ at $p_{v,ch}=1.10$ Bar. Moreover, they were found to be higher

than the obtained results at 1.02 Bar. The enhancement of heat flux and HTC at 1.10 can be interpreted as that Bar due to accelerating the steam condensation speed on the effective surface led to the rise in the surface temperature with the reducing subcooling temperature. In addition, the comparison of the results between the coated and uncoated surfaces for all samples is explained in this figure at 1.10 Bar. Results showed an improvement of the heat flux and HTC by 6.6% and 37% respectively for the unstructured coated surface compared to the uncoated one. Further, the enhancement of the microstructured surface for the same heat transfer parameters were by 4.2% and 18.2% for the coated square groove; 3.2% and 17% for the coated V-groove surface compared to the untreated surface. Also, it can be observed that the HTC reduced with the increasing heat flux for all surfaces due to the elevated condensation subcooling temperature. That means the mounting of subcooling temperature is larger than the increments of condensation heat flux for each mass flow rates of cooling liquid during the condensation tests, which is governed by Newton's law of cooling. Despite the larger value of a droplet contact angle as $130.9^{\circ} \pm 2^{\circ}$ (see Figure 6-22) for the square groove surface after coating, the unstructured surface produced the biggest values of the heat transfer parameters such as HF and HTC compared to the other microstructure surfaces. This is due to befalling of the DWC phenomena on the unstructured surface and DFWC on the other surfaces, which led to increase the condensation surface area that exposed to the vapor.

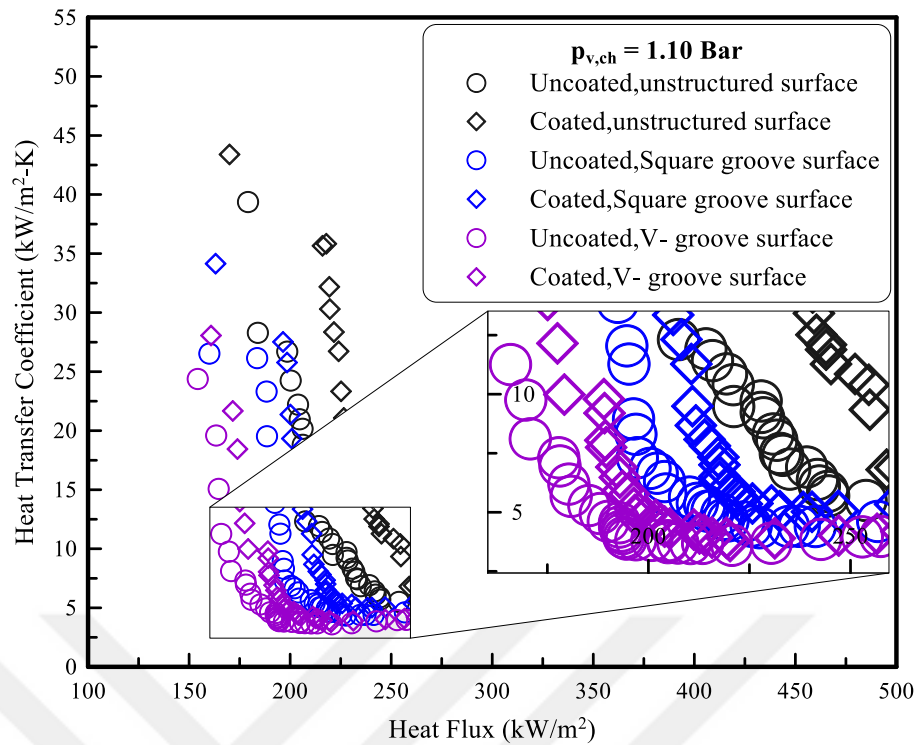


Figure 6-36: Heat transfer coefficient versus heat flux at 1.10 Bar

Figure 6-37 demonstrates the relationship between the heat transfer coefficient and the heat flux for all surfaces at a vapor pressure of 1.20 Bar. This figure clearly indicates that the HTC decreases as the heat flux rises for all surfaces with different wetting surfaces due to the increase in subcooling temperature. Also, it can be seen that the heat transfer parameters such as heat flux and HTC of the coated surface are larger than the uncoated surface for all the samples. This is due to the growing droplet contact angle and condensation surface area that led to the upsurge in the wall temperature. Also, the results illustrate that as the condensation heat flux rises up for each treated surfaces, the heat transfer coefficient is reduced by 73.5%, 82.8% and 82.4% for the unstructured, Square-groove and V-groove respectively because of the dropping surface temperature. The results revealed that the highest values of heat flux and HTC were 352.7 kW/m^2 and $48.6 \text{ kW/m}^2\text{-K}$ for the unstructured coated surface, while the lowest values of these heat transfer parameters for the uncoated V-groove were 185.5 kW/m^2 and

5.2 kW/m²-K. This is because of the existence of an additional thermal resistance in the liquid film condensation which reduces the droplets formation inside the grooves as the subcooling temperature is raised. Furthermore, the results indicated an enhancement in heat flux and HTC at $p_{v, ch}=1.2$ Bar for all surfaces compared with the same boundary conditions except the vapor pressure of 1.02 Bar and 1.10 Bar. This improvement heat transfer occurred due to the increased speed of steam condensation on the active surface in the front side of heat sink.

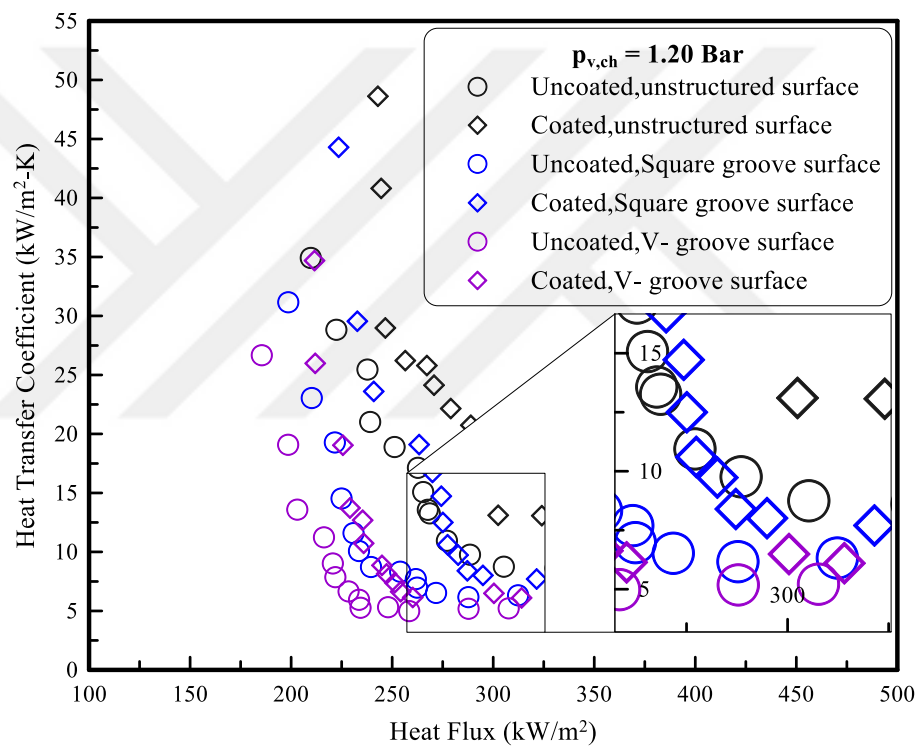


Figure 6-37: Variation of condensation heat transfer coefficient with heat fluxes at 1.20 Bar

The heat transfer coefficient and heat flux for all surface topographies at 1.25 Bar is illustrated in Figure 6-38. In general, the HTC reduces with a rise in the heat flux due to the increasing subcooling temperatures for all surfaces with different wettability. In addition, the results show the highest values of heat flux and HTC for the unstructured coated surface, while the lowest HF and HTC values existed at the uncoated V-groove

surface at the comparable value of a subcooling temperature. Therefore, it can be observed that the results of HTC and heat flux for all the surfaces at 1.25 Bar showed similar trends in Figure 6-36, Figure 6-37 and Figure 6-38. while, the biggest domain of heat transfer parameters are obtained at 1.25 Bar with the range of $230 \leq q_s \leq 436.1$ kW/m² and $6.6 \leq \text{HTC} \leq 51$ kW/m²-K for all the surfaces compared the other vapor pressures. Also, the experimental results showed the HTC of the coated surface was enhanced by 14.6%, 13.4% and 13.6% for the unstructured, square groove, and V-groove surfaces respectively compared to the uncoated ones. However, the enhancements of heat flux for the coated surface were by 4.7%, 3.9% and 6% for the unstructured, square groove and V-groove surface respectively compared to the untreated surfaces. Besides, the experimental results at 1.25 Bar resulted in a better improvement of condensation heat transfer parameters due to the increasing saturation temperature inside the vapor chamber with the rise in the condensation rate. Consequently, the lowest values of the heat transfer parameters such as heat flux and HTC for the untreated surfaces can be clearly seen. That is because of the decline in the droplet contact angle and the wall temperature with the rise in the subcooling temperature compared to the treated surfaces for all samples.

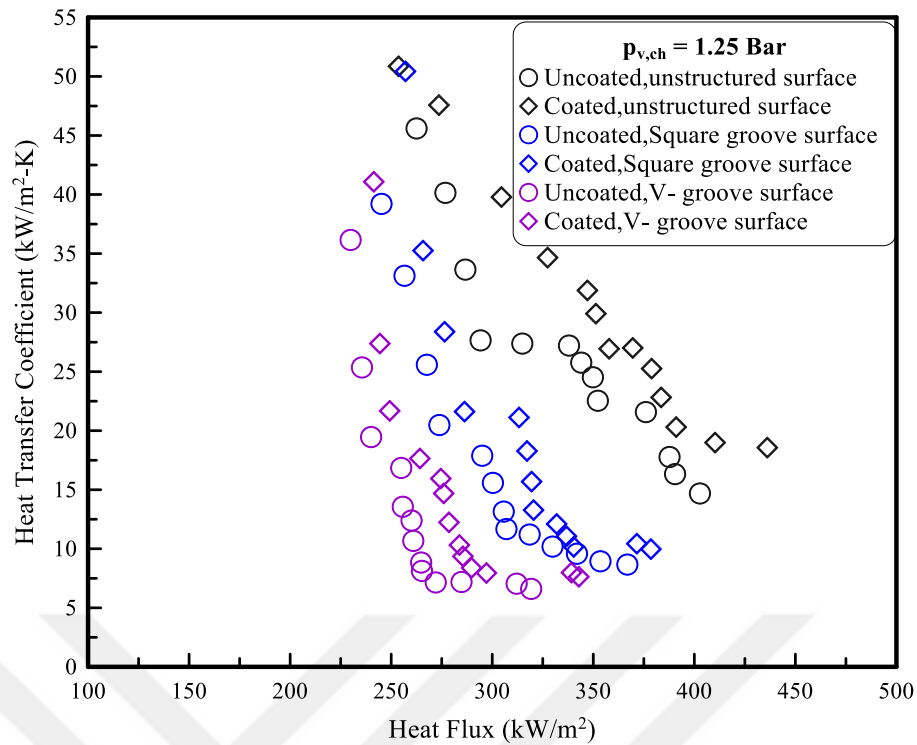


Figure 6-38: Variation of HTC with heat flux at 1.25 Bar

6.4 High-Speed Image Analysis

High-speed camera (Phantom v311) was used to record the hydrodynamic phenomena of DFW condensation on the active surface with different topographers which are unstructured, square groove and V-groove surfaces. The field of view of the camera had been adjusted to $10 \text{ mm} \times 20 \text{ mm}$ with a spatial resolution of 1024×768 pixels ($20 \mu\text{m}/\text{pixel}$). Fluid motion has been recorded at a frame rate of 800 Hz. The analysis of high-speed images is illustrated in three different cases. While, the first case was with untreated surfaces with different surface topographies at constant $p_{v, ch} = 1.02 \text{ Bar}$ (see Section 6.4.1), the second case was showed the untreated and treated unstructured surface with different operating vapor pressure from 1.02 Bar to 1.25 Bar (see Section 6.4.2). The final case was recording on different surface topographies and wetting surface at the minimum and maximum vapor pressure were 1.02 Bar and 1.25 Bar (see Section 6.4.3).

6.4.1 High-Speed Image Analysis for Untreated Surfaces

High-speed records (with a field of view of 10×20 mm) for the corresponding expected heat transfer coefficients and hydrodynamic phenomena of dropwise condensation at constant vapor pressure 1.02 Bar are shown in Figure 6-39. It can be seen that the dropwise condensation occurred on the unstructured copper block surface during the experiments made with a different in the Reynolds number. This can be due to a large temperature difference between vapor and surface temperature of the copper block, since the wall temperature reduces when the mass flow rate increases as shown in Figure 6-39. Over the unstructured uncoated surface for a Re number of 2025, images reveal that a large number of active nucleate sites appeared rather than the homogeneously distributed small droplets on the surface. Over a period, these droplets coalesce due to the reason that vapor condenses continuously and form larger droplets. Furthermore, the droplet condensation size of the untreated surface increases with the rising in Reynolds number. Thus, it leads to an increase in the exposed surface area to the vapor as the surface temperature is elevated. Next, the surface is again covered by droplets at the Re number of 3680 but the surface is not wetted homogeneously by droplets. This effect came more into account when higher Reynolds numbers were adjusted during the experiments. At the Reynolds number of 5960, large droplets formed and propagated downwards as a result of gravity force by leaving up smaller droplets over the surface. Thus, the surface is wiped away from the relatively large droplets and is exposed to the formation of new small droplets. The disposed area remains as a droplet-free stripe. This phenomenon occurred at the largest Re number of the liquid cooling (10920) while leading to inhomogeneous distribution of the droplets at the surface. At the microstructured square grooved and V- grooved surfaces at comparable operating conditions like the unstructured surface, the high-speed images

show the dropwise condensation occurred at the crests of the micro-structures. Accumulation of the droplets result in thin films formed inside the grooves by the means of capillary. The resulted liquid film then slides down by gravity concurrently covering whole area of the grooves. One can assume that this will lead to stemming the formation of new droplets, since the surface is not exposed to the vapour phase.

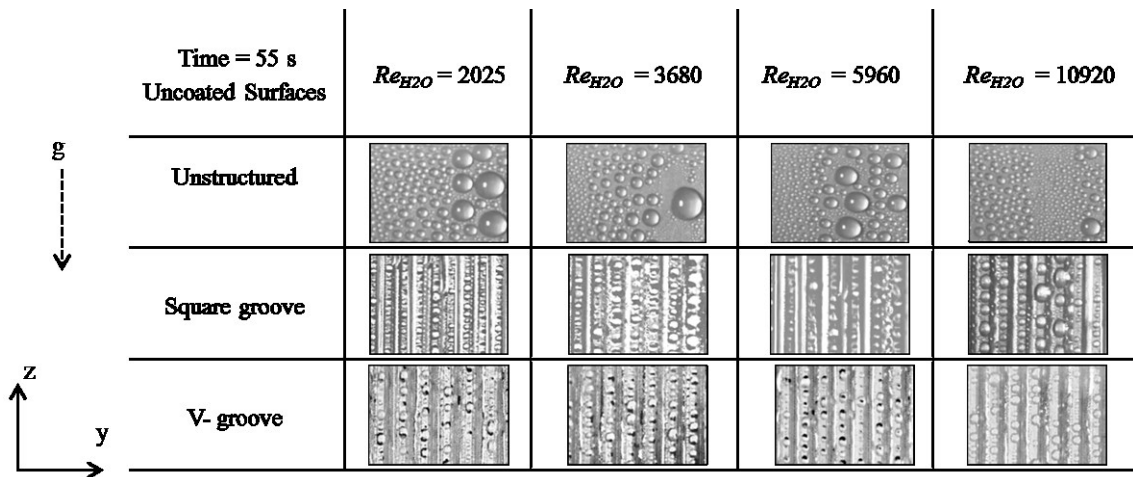


Figure 6-39: Surface wetting phenomena, dropwise condensation at untreated, unstructured and micro-structured surfaces

6.4.2 Image Analysis for Unstructured Surface with Different Wettability

High-speed camera images of the condensation process at the surfaces recorded for various vapor pressures and four different Reynolds numbers of cooling liquid that are presented in Figure 6-40. For the uncoated surface, the pictures reveal a formation of droplets with a rather circular shape for various Re numbers at 1.02 Bar. The surface exhibited small-sized droplets, which swell and become large-sized droplets through agglomeration. After they reached a certain size, they slid down once the gravitational force overcomes the adhesion force acting between the liquid and the subcooled wall. In contrast, the condensation process at the coated surface (1.02 Bar) shows large sizes of coalescing liquid along with a heterogeneous allocation character of droplets.

Furthermore, the droplet condensation size of the coated surface increases compared to the uncoated surface at the saturation vapor temperature. In addition, the droplet condensation size of the coated surface grows as the saturation temperature increases from 100.2 to 106 °C at the same Re number of the cooling liquid. Although the IPTES silane coating used in this study evoked a larger average contact angle at the surface (see Figure 6-22), the liquid droplets were not formed as hemispherical figures as with the condensation on the uncoated surface. Similar behavior has been found with larger pressures, contradicting the description of an increase in the number of small-sized droplets [102].

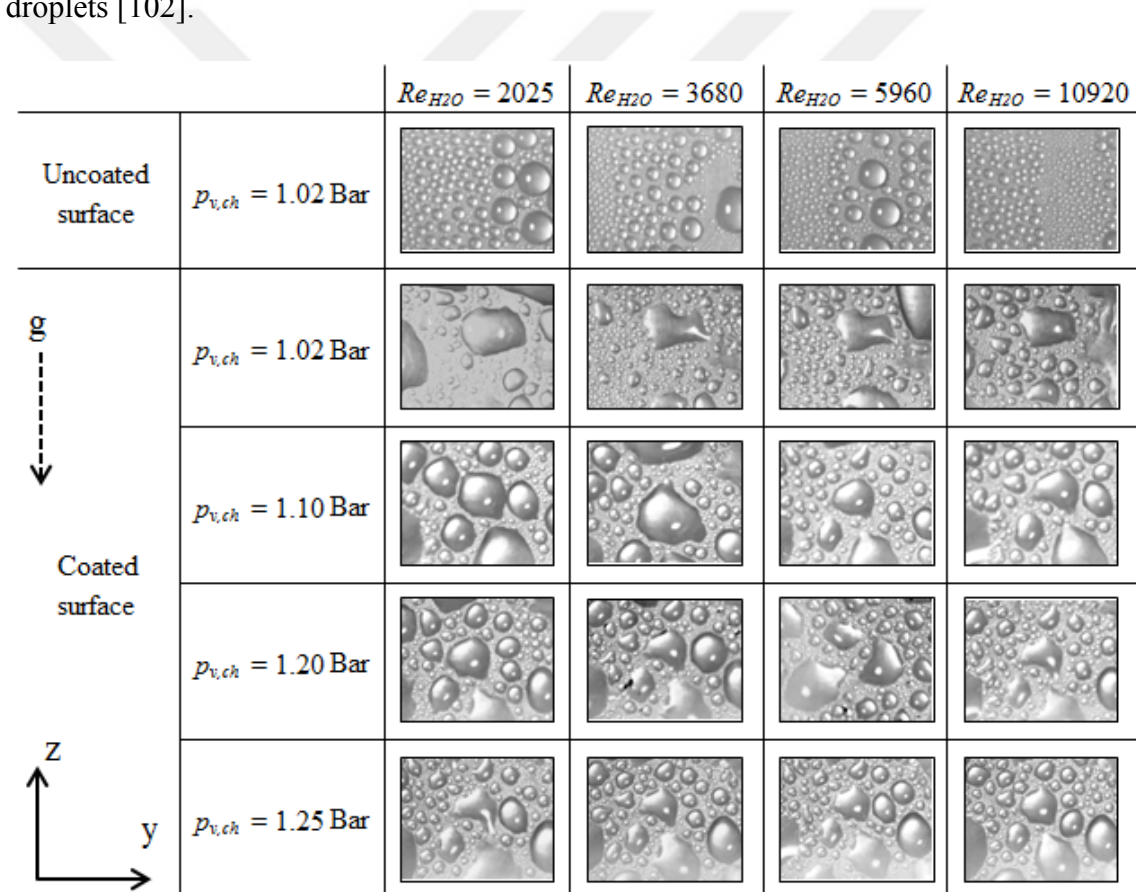


Figure 6-40: Surface wetting phenomena during condensation over uncoated and coated surfaces

6.4.3 High Speed Data Analysis with Different Wettability

High-speed camera videos and images obtained with a field of view of 10×20 mm for the different vapor pressures with increasing Reynolds numbers of cooling liquid that are shown in Figure 6-41. Also, the high-speed camera images reveal the occurring condensation at the crests of the micro-structures, wherein the grooves, the liquid is formed for all cases. For the untreated surface at 1.02 Bar pressure, the dropwise condensation phenomena can be observed clearly. While, a Re number is 2025, the images show a large number of active nucleate sites that appeared rather homogeneously distributed as small droplets on the surface. However, the inhomogeneous distribution of large droplets occurred due to gathering smaller droplets as a result of gravity when Re number equals to 10920 is observed for the unstructured surfaces. This is mainly because of the overcoming adhesion force between the condensation liquid and the subcooled active surface. Moreover, at the lowest vapor pressure and for the untreated microstructure surfaces, the droplets at the crests grow and accumulate by capillary forces inside the micro-grooves to a thin liquid film. Then the film is driven by gravity downwards concurrently covering the whole area of the grooves. When more liquid is collected in the grooves, the larger droplets are formed propagating along the path of the microstructures and collecting smaller droplets. Subsequently, it can be assumed that this will lead to reduce the number of new droplets, as the contact between the surface and the vapor is diminished. The second test of the condensation process at the coated surface with different vapor pressures shows larger sizes of the liquid droplet with a variable distribution of droplets. The hydrophobic surface is created by using IPTES silane coating which gives higher droplet contact angle for all coated surfaces compared to the untreated surfaces (see Figure 4-7 in sections 4.3.2 and 4.3.3). However, the images show the shapes of liquid

droplets on the treated surface at high vapor pressure are different compared the untreated surface at low vapor pressure for all topographies. for more explaining, the images exhibit the drops formation during the condensation test on the treated surface not as hemispherical shapes compared the case of untreated surfaces. In addition, for all unstructured and microstructured surfaces, the droplet condensation size of the coated surface grows as the vapor pressure increases from 1.02 Bar to 1.25 Bar while the Re number of the cooling liquid kept constant. This enhances the condensation heat transfer coefficient by increasing the exposed surface area to the vapor inside the vapor chamber as the surface temperature is raised. According to the captured images, the same behavior has been observed for all surfaces after coating [102].

Surfaces types		$Re_{H_2O} = 2025$	$Re_{H_2O} = 3680$	$Re_{H_2O} = 5960$	$Re_{H_2O} = 10920$
Uncoated $p_{v,ch} = 1.02 \text{ Bar}$	Unstructured				
	Square groove				
	V-groove				
Coated $p_{v,ch} = 1.02 \text{ Bar}$	Unstructured				
	Square groove				
	V-groove				
Coated $p_{v,ch} = 1.25 \text{ Bar}$	Unstructured				
	Square groove				
	V-groove				

Figure 6-41: Surface wetting phenomena during condensation at the uncoated and coated surfaces

6.5 Comparison with Literature and Developed Correlation

The validation of current experimental results is performed for the chemically treated and untreated unstructured surfaces at the different operating vapor pressures.

Therefore, the comparison of current results such as heat flux and heat transfer coefficients are achieved with heat transfer values that were reported in literature (see Figure 6-42 and Figure 6-43). Also, the experimental results are analyzed for all surface topographies before coating at $p_{v, ch}=1.02$ Bar. To improve the accuracy of current experimental results, they have been compared with the current analytical results and correlation formulas for each surface (see Figure 6-44 through Figure 6-55). The comparison method with analytical calculations and correlation equations are explained clearly in Figure 5-3 section 5.3.1.

6.5.1 Unstructured Surface

Experimental heat transfer results are compared with experimental values found in other papers (see Figure 6-42). Heat flux findings in this work for both uncoated and coated surfaces for 1.02 Bar are lower than the heat flux values reported in the work of Huang and Leu and Ma et al. [51], [103]. This might be due to the fact that there may be still some non-condensable gases present in the working fluid. Air might have been trapped inside the condensation section and partially vapor line. As reported in [104], the influence of non-condensable gases can be very strong in condensation processes and a concentration of about 1 % air can result in approximately 50 % heat flux reduction, which in this case is rather identifiable. High-speed images shown in (Figure 6-40, section 6.4.2) display a quite distinct formation of droplets for both uncoated and coated surfaces. This wetting behavior has been even detected for wall subcooling values over 10 K. In contrast to the characteristic mode of FWC reported by some researchers, one can conclude that this disagreeing behavior would strengthen the argument for the presence of non-condensable gases in the condensation section of the test system. For comparably small $T_{v, ch} - T_s < 25$ K, the experimentally obtained HTC values

($p_{v,ch} = 1.10 \text{ Bar}, 1.20 \text{ Bar}, 1.25 \text{ Bar}$) show an agreement with those reported in [51], [103] determined at DWC regime. For identical temperatures, the wetting phenomena at the coated surface is represented by droplets with different sizes and in some collection areas of small liquid particles non-circular clusters were identified (see Figure 6-40 in section 6.4.2).

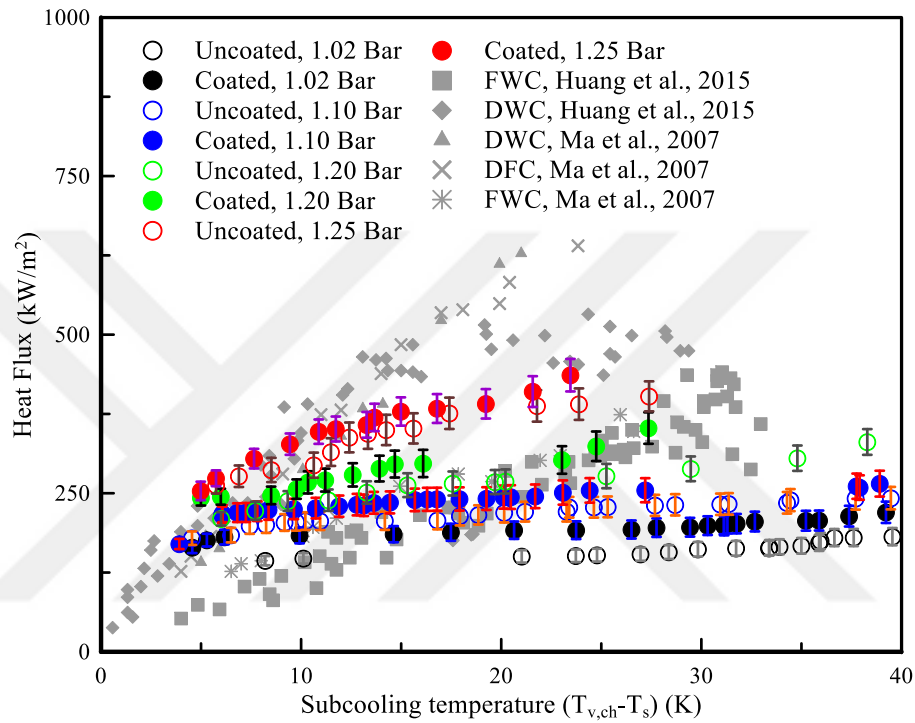


Figure 6-42: Effect of subcooling temperature over heat flux at different pressures

The HTC results of different saturation pressures of vapor that were compared with [51], [103] are illustrated in Figure 6-43. At 1.02 Bar and a wall subcooling temperature of 20 K, the heat transfer performance at both uncoated and coated substrates was weaker than the heat transfer rates presented in the literature at FWC mode. For the subcooling of 20 K, HTC values (1.02 Bar and 1.10 Bar) were found to be similar to the values determined by Huang et al. and Ma et al. at FWC regime. For much lower driving temperature differences, the heat transfer coefficients are found to be high,

concurring with HTC values for DFWC mode given in [51], [103]. By adjusting the pressure to a larger value, heat transfer coefficient shifted towards the DWC regime. However, with increasing thermal driving force, one can witness that heat transfer coefficient decreases more on the region where FWC mode has been reported in the literature.

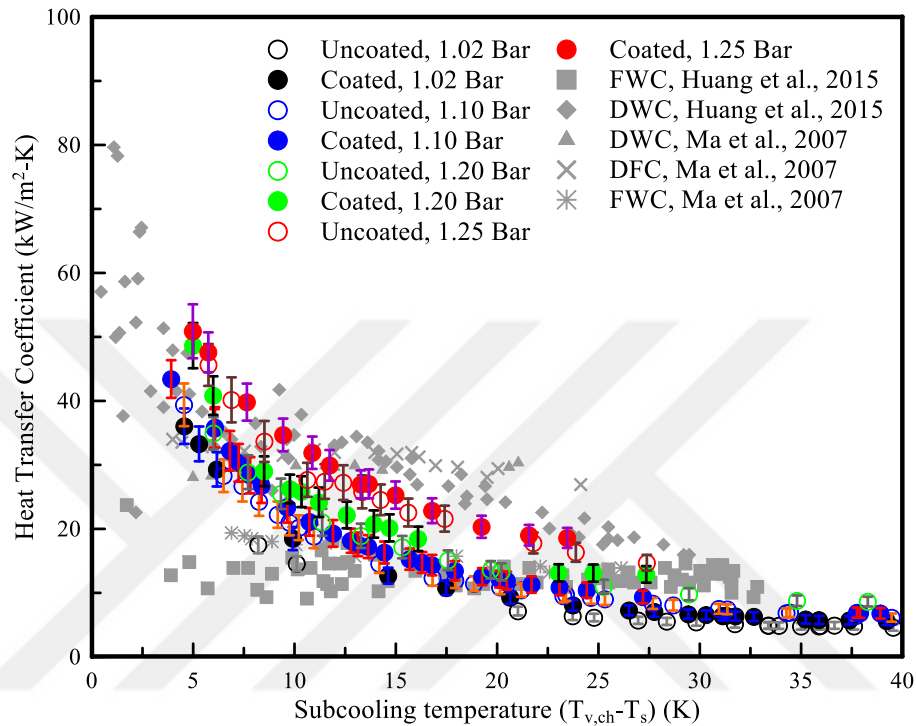


Figure 6-43: Variation of condensation heat transfer coefficients with subcooling temperature at various pressures

The change in the condensation heat flux with the increasing temperature difference between the vapor saturation and the surface temperature of the unstructured condensation surface is illustrated in Figure 6-44. The experimental results indicate that the heat flux rises with the increase in the temperature difference as the surface temperature is lowered from 92°C to 37°C because of the elevated mass flow rate of the cooling liquid from 4 g/s to 87 g/s at the back-side of the copper block. Furthermore, the current analytical results of the condensation heat flux show an identical behavior compared to the experimental result with the largest variation of 21.5 %. Finally, the

validations of experimental results were achieved by using the second analytical approach and two correlations. Accordingly, the results using the correlations suggested in Ma et al. [52] provided a closer agreement with the experimental results obtained in this study. The maximum error compared to the other correlations is achieved about 1.2 %.

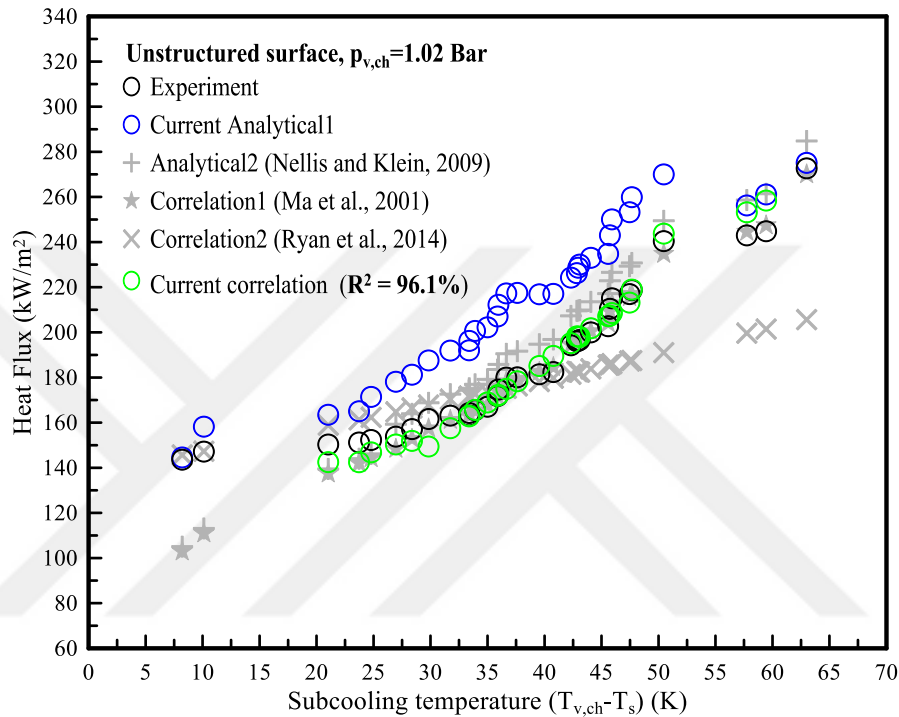


Figure 6-44: Variation of heat flux with subcooling temperature difference ($T_{v, ch} - T_s$)

As displayed in Figure 6-45, the condensation heat transfer coefficient drops as the temperature difference increases in case of the unstructured surface. The higher mass flow rate of cooling liquid will cause a greater temperature difference and lower heat transfer coefficient between the surface and vapor at a constant saturation vapor pressure and inlet cooling liquid temperature. Moreover, the analytical results show a similar trend to the experimental results where the maximum and minimum error percentages in the HTC are 21.7% and 0.7% respectively. To validate the experimental results, the second analytical method and two correlations are used as Nellis and Klein

[62], Ryan et al. [87], Ma et al. [52]. All the correlation results of the HTC follow the same trend in the experimental and analytical results, which shows that the heat transfer coefficient is decreased as the temperature difference becomes greater. The correlation results of the HTC are at approximately the same maximum error percentage (8%) when compared with the Nellis and Klein [62] and Ryan et al. [87] studies. However, a lower error percentage (1.4%) was attained in the comparison made with the results from Ma et al. [52] correlation.

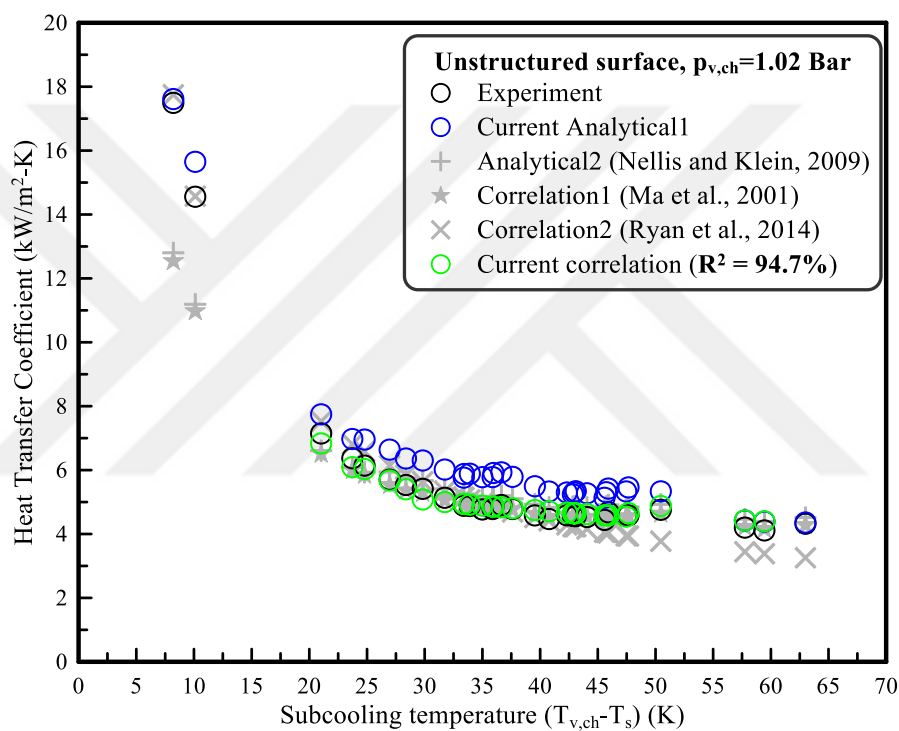


Figure 6-45: Effect of subcooling temperature over heat transfer coefficient

The impact of the temperature variation on the condensation Nu number is displayed in Figure 6-46 for all the analytical and experimental calculations of the unstructured surface. It can be observed that Nu number is inversely proportional with the temperature difference because of the proportional relationship between the heat transfer coefficients (see Figure 6-45). Thus, Nu number also decreases in the current analytical result as the temperature difference becomes greater. The current analytical

results of Nu have been demonstrated to have the highest error percentage of 22.4% compared to the experimental results. As a comparison of the correlations and the experimental results, the maximum and minimum variations are found to be 8% and 1.8% for Nellis and Klein [62] and Ma et al. [52] correlations respectively.

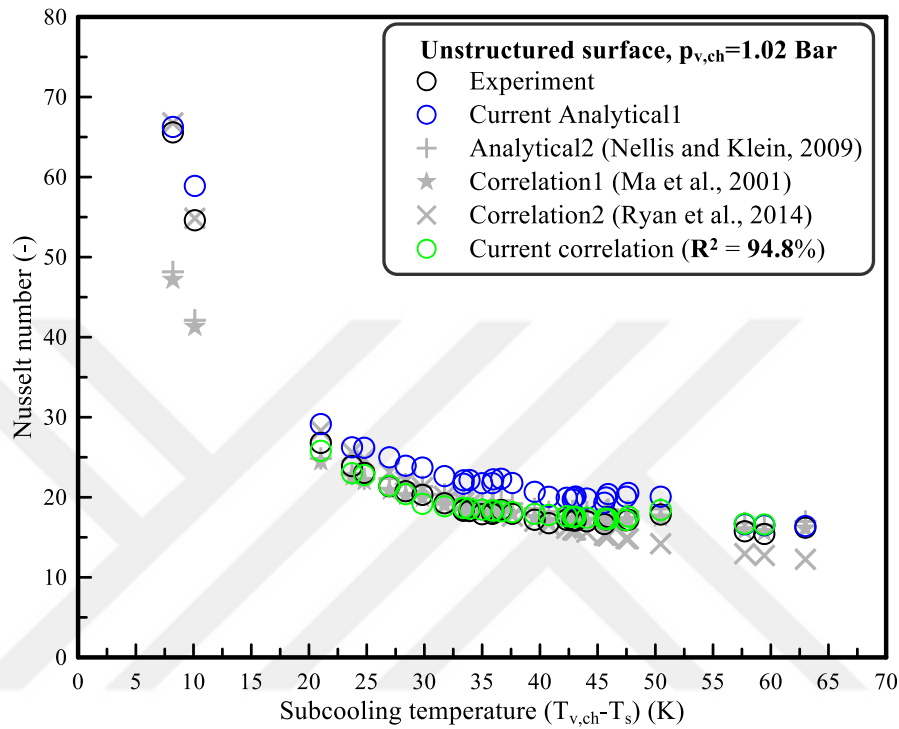


Figure 6-46: Variation of Nu number with temperature difference

In Figure 6-47 the comparison between the analytical and experimental results for the heat flux and heat transfer coefficient is presented. The agreement between the comparison results is fair for both heat flux and HTC parameters within about 25% deviation. One of the possible reasons for the deviation may be attributed to the combined impact of the assumption made in the theoretical model and the inaccuracies in the measurements. Also, Ma et al. [52] correlation provided a good agreement compared to the experimental results for condensation heat transfer parameters. The biggest deviations for heat flux and heat transfer coefficient were by 1.2 % and 1.4 % respectively compared to the other correlations.

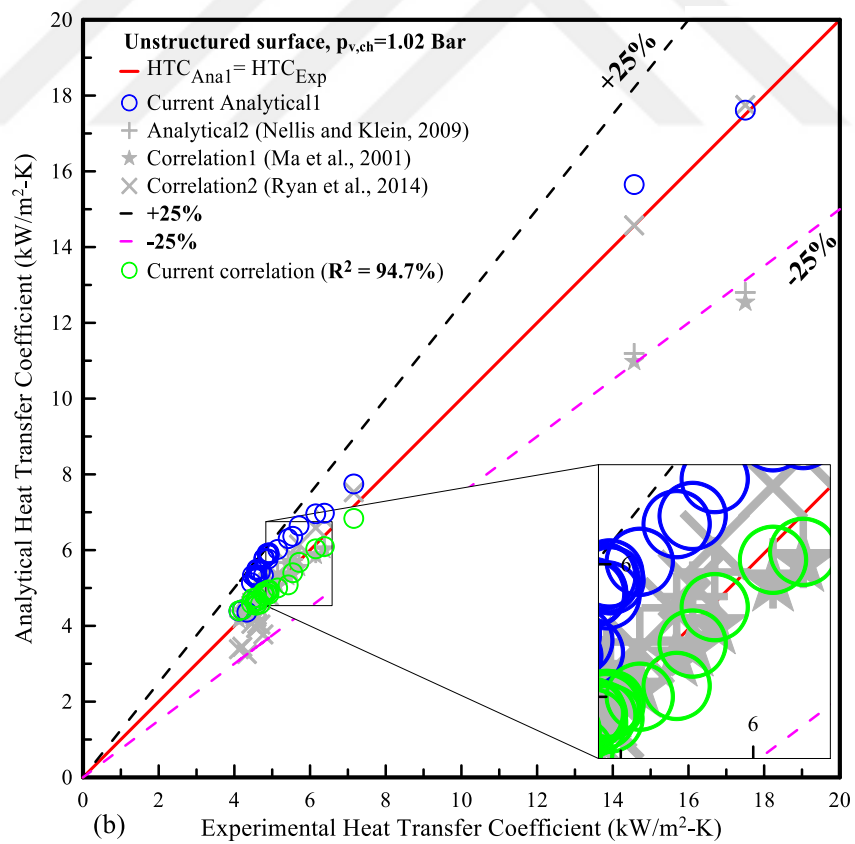
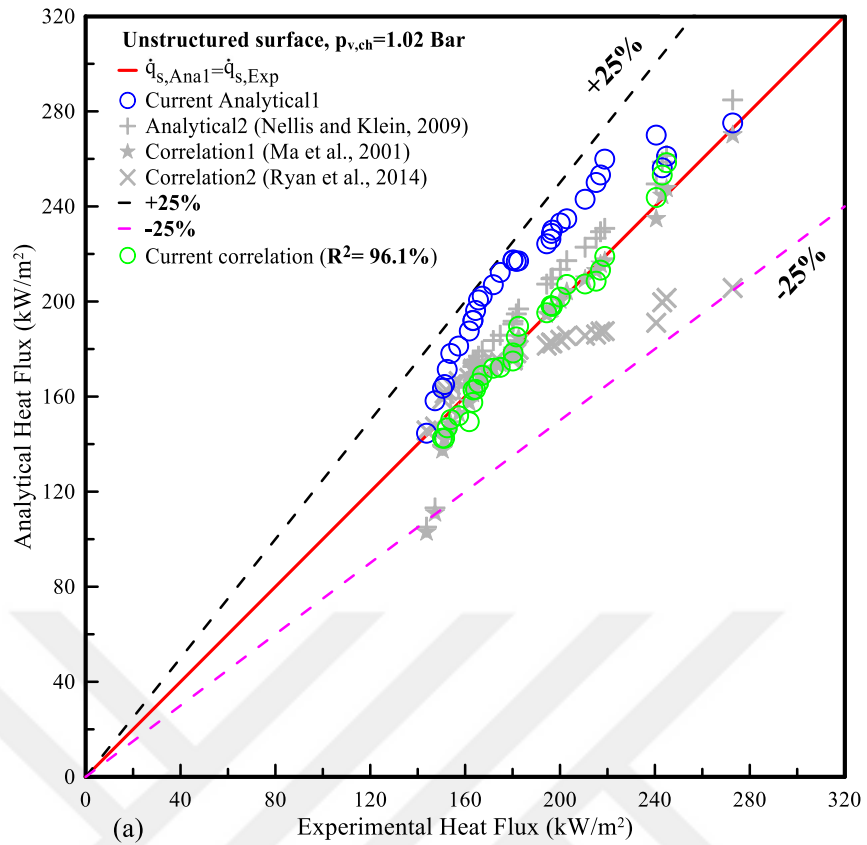


Figure 6-47: Comparison of the experimental results with analytical results of the unstructured surface, a) heat flux and b) heat transfer coefficient

6.5.2 Square-grooved Surface

The heat flux and the temperature difference between the vapor chamber and the condensation surface is presented in Figure 6-48 for the measurements of the micro-structured square grooved surface. The experimental results illustrate that the heat flux increases from 135.8 kW/m² to 326.5 kW/m² due to the fall in surface temperature from 98.4 to 36.3°C as the mass flow rate of the cooling liquid is elevated. In addition, the analytical calculation is in line with the results for the heat flux versus the temperature difference while the maximum variation is encountered as 11.56% compared with the experimental data. The experimental results of condensation heat flux are validated with two correlations. The correlation of Ma et al. [52] offered a good agreement with the highest error percentage of 5.4% compared to the experimental results while Ryan et al. [87] correlation showed the biggest variations of 9.75% at the subcooling temperature lower than 45 K.

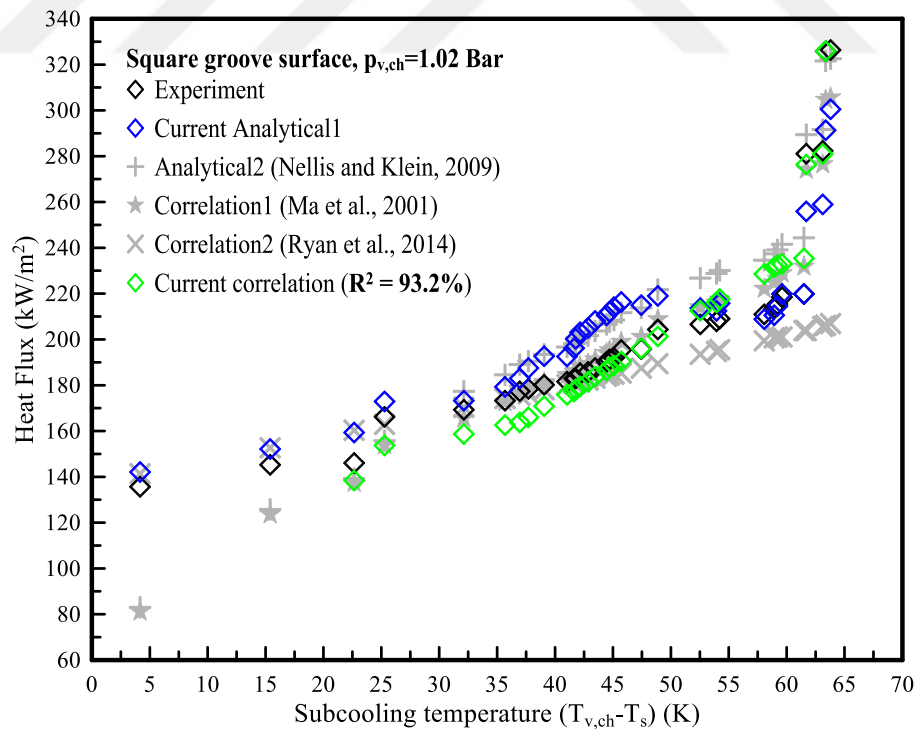


Figure 6-48: Heat flux versus subcooling temperature difference of square groove surface

Figure 6-49 shows heat transfer coefficients HTC at various temperature differences. For a larger temperature difference such as $\Delta T=63.8$ K, a lower heat transfer coefficient $HTC=5117.7$ W/m²-K is obtained. Since the vapor and the inlet temperature of the cooling liquid were kept constant, an increase in mass flow rate of the cooling liquid will cause the larger temperature differences between the surface and the vapor. The experimental and analytical results of HTC are predicting a similar behavior with the maximum error percentage of 11.63%. In addition, the maximum error percentage of experimental HTC results according to the Nellis and Klein [62], Ryan et al. [87] and Ma et al. [52] are 11.43%, 9.75%, and 5.5% respectively.

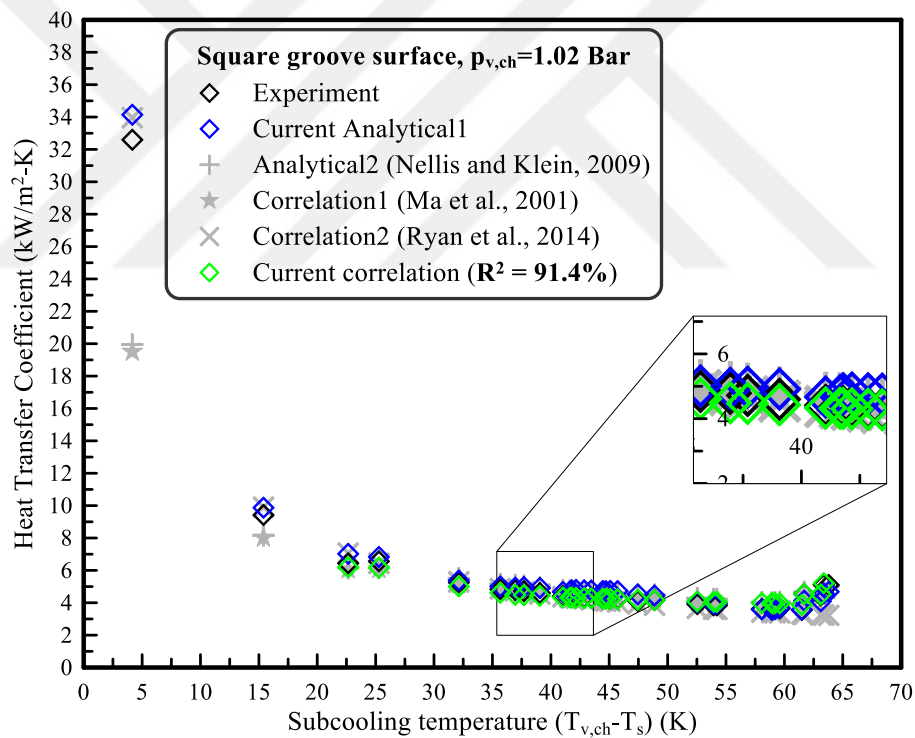


Figure 6-49: Heat transfer coefficient versus Subcooling temperature difference of square groove surface

Since the rise in the mass flow rate of the cooling liquid will enlarge the temperature difference between the surface and the vapor (see Figure 6-50), Nusselt number of the

condensation will be lowered as a result (see Eq.5-23). The difference in Nu numbers becomes more visible when the temperature range of 6 K – 65 K is closely observed. Nu numbers for all tests are reduced as the temperature difference of the vapor and condensation surface rises up due to the proportional relation of HTC (see Figure 6-49). As a comparison between the experimental and analytical results, the highest Nu number was obtained (37.2) at the lower temperature differences than 15 K, while the rest of Nu numbers calculated lower than 30 occurred at the range of a temperature difference from 27 K to 65 K. Then, the results suggest that analytically found Nu number is higher than the experimentally obtained Nu number by 12% due to the influence of the heat loss during the condensation tests. In addition, Nellis and Klein [62] and Ma et al. [52] correlations gave a good agreement compared to the experimental results of Nu number, in which the highest variations are 11.8% and 5.8% respectively for each correlation [62] and [52].

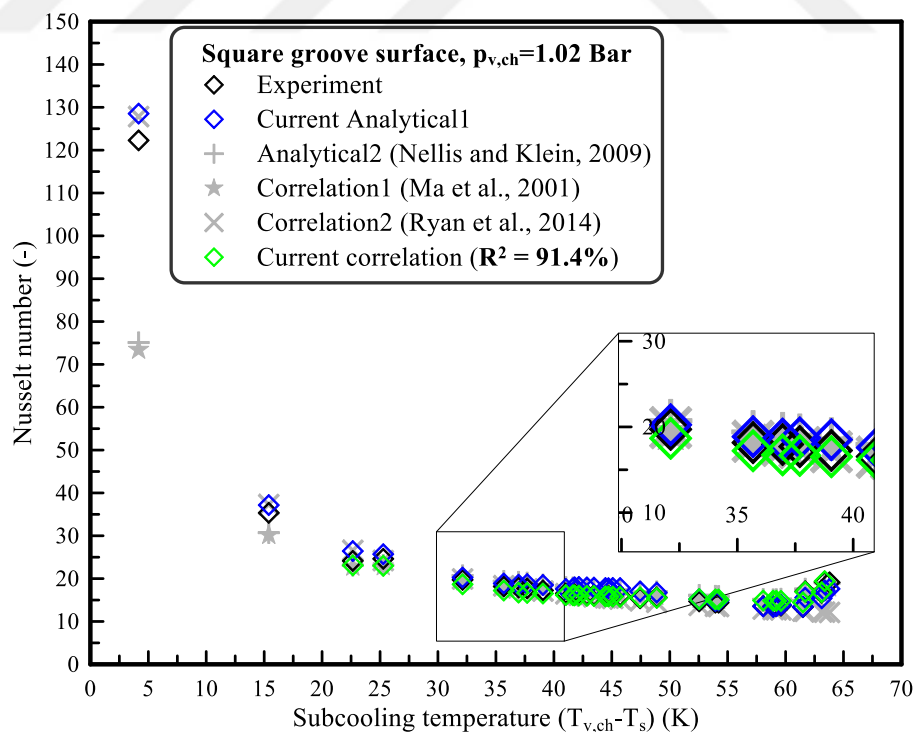


Figure 6-50: Nu number versus subcooling temperature difference of square groove surface

The comparison between the analytical and experimental results of heat flux and heat transfer coefficient for a square groove surface is illustrated in Figure 6-51 (a) and (b) respectively. The analytical results indicate a good match with the present experimental data for each heat transfer parameter such as heat flux and HTC. In addition, the deviation between the analytical and experimental results of heat flux and HTC are 11.56% and 11.63%, respectively. This agreement clearly verifies the reliability of the analytical model for the condensation heat transfer on micro-structured surfaces and the accuracy of the experimental measurement. Moreover, the average deviation of the experimental values from the correlation results in the condensation heat transfer parameters yield a similar outcome for heat flux and HTC. For example, the maximum deviation percentage of heat flux and HTC for Nellis and Klein [62] is 11.2% and 11.4%, while the minimum deviation of Ma et al [52] is 5.4 %, and 5.5% respectively.

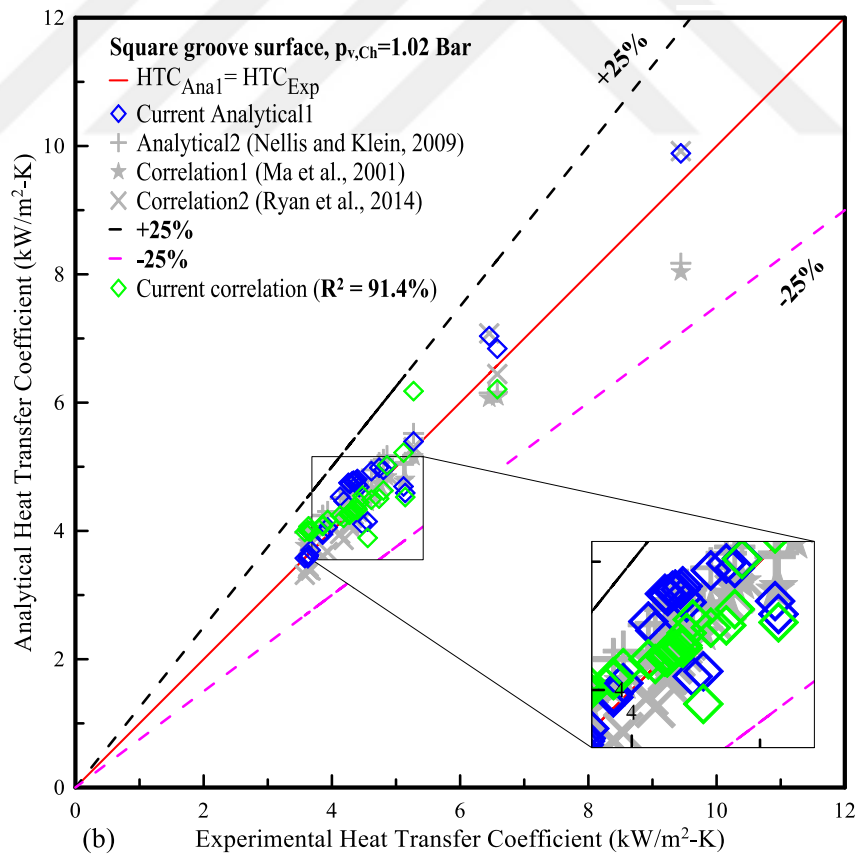
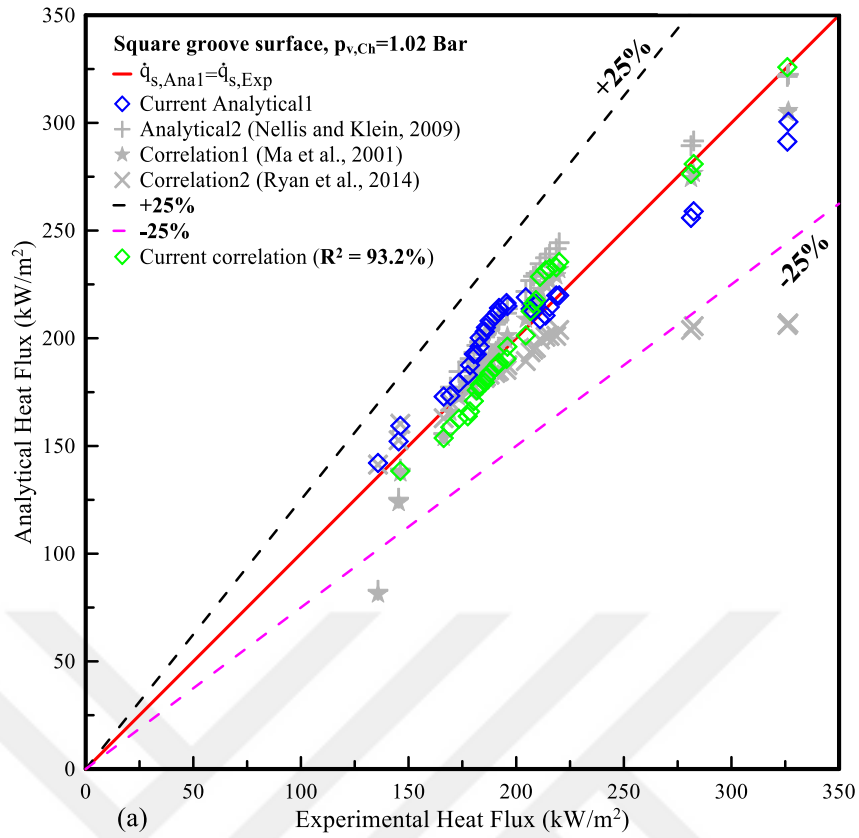


Figure 6-51: Comparison of experimental results with analytical results of square groove surface, a) heat flux and b) heat transfer coefficient

6.5.3 V- Grooved Surface

Behavior of the heat flux at different temperature differences of the vapor chamber and the condensation surface is illustrated in Figure 6-52 for the measurements of the micro-structured V-grooved surface. It was thought that the high heat fluxes would arise as the temperature difference increases. Then, the experimental results also demonstrated that the elevation in the heat flux from 109 to 333 kW/m² was because of the drop in the surface temperature while the mass flow rate of the cooling liquid increased at a constant saturation pressure. Also, analytical results confirm the findings in the experimental data as the maximum error percentage of 22.7% is acquired for the heat flux versus the differing temperature results. Finally, the experimental results are confirmed by utilizing various correlations, in which Ma et al [52] and current correlation Eq.5-30 shows proximity with the maximum error percentage of 13.3% and 10.5% respectively.

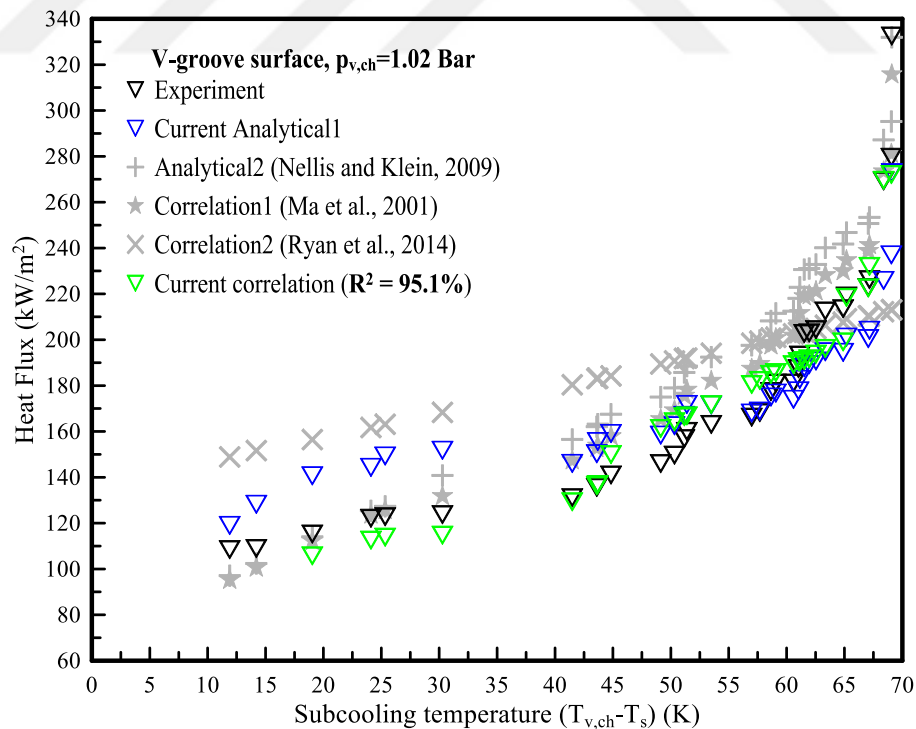


Figure 6-52: Heat flux versus subcooling temperature difference of V-grooved

The heat transfer coefficients, HTC at varying temperatures are represented in Figure 6-53. Because the vapor pressure and the inlet temperature of the cooling liquid were kept constant, increasing the mass flow rate of the cooling liquid resulted in bigger temperature variations between the surface and the vapor. The experimental results show that the HTC for all tests is lowered with the increase in the temperature variation of the vapor and condensation surface. In the case of the micro-structured V-groove surface, the highest heat transfer coefficient was acquired at temperature differences lower than 15 K at a constant saturation pressure of 1.02 Bar. Meanwhile, it can be seen that the lowest values of HTC are obtained during the condensation tests on V-groove surface at subcooling temperature greater than 30 K. This is due to the decreasing condensation rate with more film-wise condensation phenomena that happened inside the surface grooves. Thus, the experimental and analytical results of the HTC could predict the similar behavior with the maximum error percentage of 22.7%. Moreover, the correlations are used for the validation of the experimental results and the maximum error percentage of the HTC for Nellis and Klein [62], Ryan et al [87], Ma et al [52] and Eq.5-31 are 19.9%, 38.8%, 13.2%, and 11.5 % respectively.

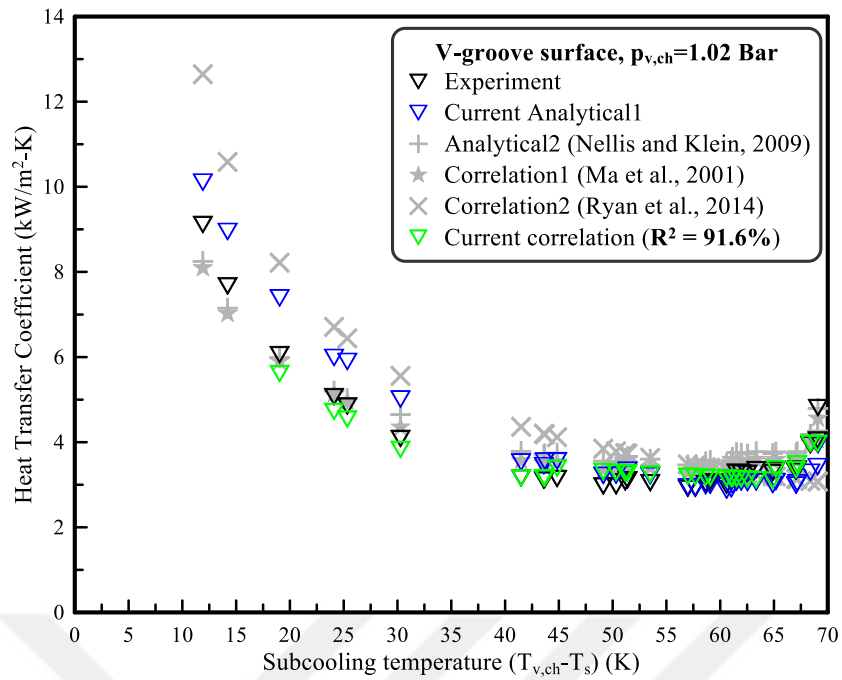


Figure 6-53: Effect of subcooling temperature over Heat transfer coefficient of the V-groove surface

The Nusselt number at varying temperature differences of the micro-structured V-groove surface is given in Figure 6-54. The experimental results similarly demonstrate that the Nu reduces as the temperature difference between the vapor chamber and condensation surface increases. This is because Nu number represents the enhancement of condensation heat transfer rate, as it is defined as the heat transfer ratio of convection to the conduction. Therefore, a similar trend can be observed in the change of Nu number and HTC with respect to the subcooling temperature (see Figure 6-53). Comparing the experimental and analytical results, the highest Nu number was achieved at temperature differences lower than 30K, while all the calculation results of the Nu lower than 20 are obtained at the range of temperature difference from 40 K to 70 K. The results show that the analytically calculated Nusselt number is higher than the experimentally found Nu number by 23.1% because of the neglected heat losses during the theoretical calculations. Also, the correlation equations Ma (2001) and Eq. 5-32 are

in a good match when compared to the experimental results with the maximum error percentages of the Nu as 13.5% and 12.5% respectively.

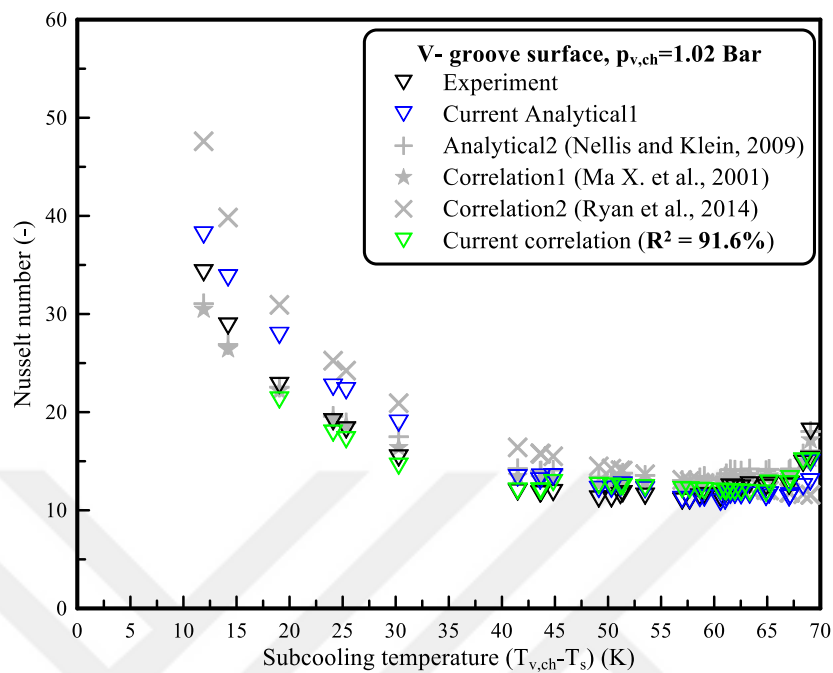


Figure 6-54: Nu number versus temperature difference of V- groove surface

The comparison between the analytical and experimental results of heat flux and heat transfer coefficient for the V-groove surface is depicted in Figure 6-55 (a) and (b) respectively. The analytical results yielded a good agreement with the current experimental data for each heat transfer parameter such as the heat flux and HTC. Also, the deviation between the analytical and experimental results of the heat flux and HTC is 25%. This can prove the dependability of the current analytical calculations on the V-groove surface and the correctness of the experimental measurement for the condensation heat transfer mechanism. Moreover, the average deviation between the experimental and correlation results acquired a good agreement for both heat flux and HTC. For instance, the maximum deviation percentage of the heat flux and HTC for Nellis and Klein [62] is 20%, while the minimum deviations for each correlated equation of Ma et al [52] and Eqs.5-30 and 5-31 are 13% , 10.5% and 11.5% respectively.

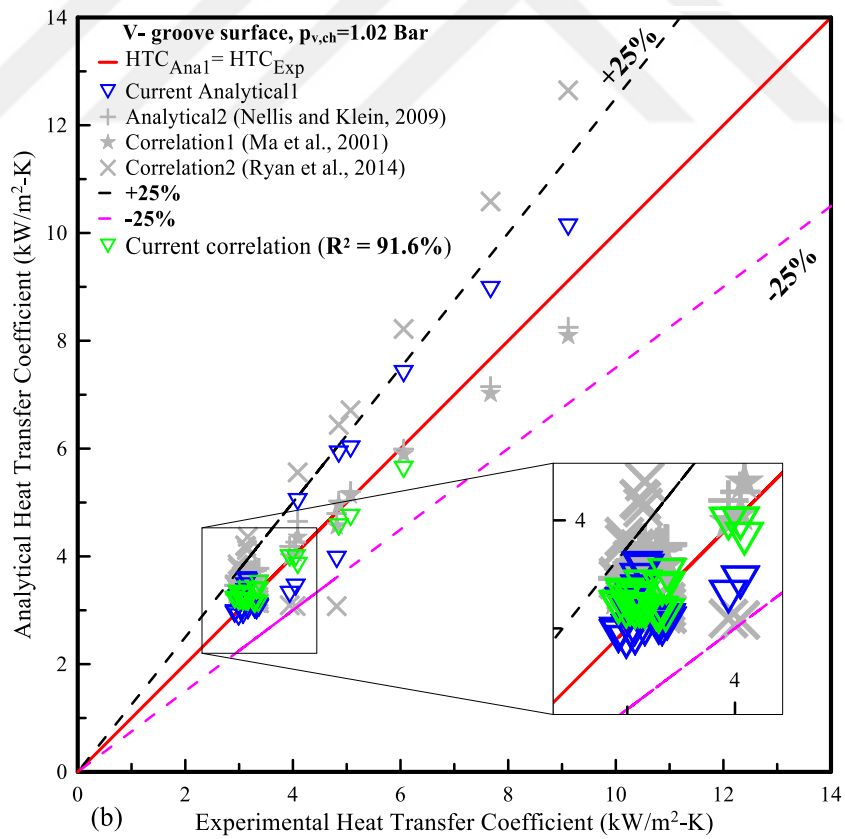
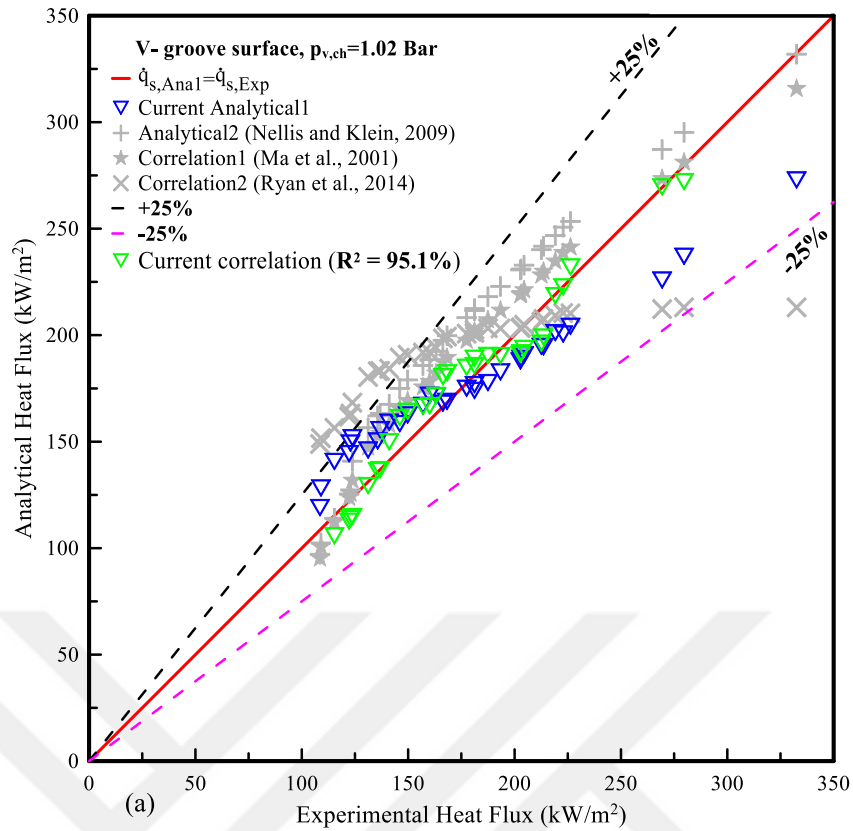


Figure 6-55: The experimental results versus the analytical results over V- groove surface, a) heat flux and b) heat transfer coefficient

CHAPTER VII

SUMMARY AND FUTURE WORK

7.1 Summary and Conclusions

In the present study, a significant bottleneck for heat pipes, low performing condenser, has been studied. By manipulating surfaces condensation convective heat transfer has been studied. New procedures were applied successfully to produce unique surfaces in the condenser part of a heat pipe with different topographies (square and V grooves) and surface wetting (hydrophobicity) at an operating vapor pressure. Experimental and numerical studies were conducted on developing the condensation phenomena on copper substrates. Two substrates were used in the experiments, as a reference substrate and a modified substrate. The latter was prepared by means of a dip-coating in a perfluoro silane mixture and Ultra ever dry to obtain large contact angles for liquid water droplets at the surface. Concurrent with heat transfer measurements, the condensation process was monitored with a high-speed camera at particular subcooling temperatures. The results were compared with the experimental data published in the literature and with correlation formulas. Accordingly, the following conclusions can be deduced that:

In the first task, thermal management of the cooling system was studied through experimental and theoretical investigations on a heat-pipe-embedded printed circuit board and it was compared with a commercial heat pipe as a reference point.

- 1- The conventional heat pipe was tested for different inclination angles (-90° , -45° , 0° , 45° and 90°) and also validated with a previous study from the literature.
- 2- The optimal temperature distribution and thermal resistances of the embedded heat pipe were studied with experimental, theoretical and numerical models individually.

- 3- The heat pipe was embedded inside two plates (plastic and aluminum) with known thermal conductivities. The results showed that the difference between the minimum and maximum temperatures on the surface decreased abruptly compared to the non-embedded board due to the effective heat spreading with a low spreading resistance.
- 4- Thermal resistances of a plain PCB made up of polymer or aluminum were compared in each case with the conventional cooling method and 50% reduction in the overall resistance was observed.

Experimental and analytical studies were conducted to investigate the influence of micro-nano-textured uncoated and super-hydrophobic surfaces on the liquid wetting phenomena as explained in the second task. Three different test specimens with unstructured, square-grooved and V-grooved surface topography were deployed in the condenser part of the heat pipe. In order to obtain super-hydrophobic surface, samples were coated with a commercially available liquid mixture by applying the dip-coating method.

- 1- The contact angle measurements were evaluated based on many parameters such as number of droplets per measurement position, number of coating layers, immersion/pull velocity and heat treatment process.
- 2- The results reveal that the contact angles could be increased up to 103.8 % for all surfaces while large immersion/pull speeds lead to a reduction in the rate of contact angle increase by 8.7%.
- 3- Super-hydrophobic behavior could be observed after coating the samples with three layers where the largest value of contact angle was found to be $162.3^{\circ} \pm 0.9^{\circ}$. However, a further increase of the layer number did not result in larger contact angles. In addition, the effect of heat treatment on contact angle was also observed at

a constant temperature (95°C) for different durations (1, 2 and 3 hours) and the results were compared with the contact angles measured at 25°C. It was concluded that the difference between the results was negligible.

- 4- Experimental results were validated with analytical calculations which include a classical thermodynamic model and the capillary Laplace equation. Hereby, the experimental uncertainty was estimated about 10 %.
- 5- Experimental results of droplet contact angle were illustrated to increase by 34.5% and 52.5% for the square-grooved and V-grooved surfaces compared to the uncoated one. However, a larger average contact angle was measured on the coated square-grooved surface than the V-grooved surface by 4.6 %.
- 6- The maximum Cassie-Baxter contact angle and maximum surface energy of the microstructure V-groove surface were found to be 157.5° and -1.24×10^{-8} J respectively by using the Gibbs surface energy model. On the other hand, a micro-structured square-grooved surface led to a higher Wenzel contact angle (118°) and surface energy (-5.76×10^{-7} J) when compared to the other surfaces.
- 7- Finally, analytical results of Gibbs surface energy model and droplet contact angle for all proposed surfaces are also validated with Anderson (2013).

Further investigations were performed in order to determine the effect of different surface properties such as modification of liquid-wall contact angle on the wettability of the surface and hence on the heat transfer during condensation at 1.02 Bar.

- 1- The driving force for heat transfer in this case is the drop in temperature of wall where main heat transfer mechanism is governed by dropwise condensation and it can be identified by high-speed images.

- 2- Although the topographical modification of surface should have evoked higher heat transfer coefficients compared to the unstructured surface, the grooves over the surface were covered by thin liquid films and heat transfer coefficients were slightly affected.
- 3- The rates of heat transfer from uncoated and coated surfaces were compared by using UED. The experimentally found HTC and heat flux over the coated surfaces was found to be lower than the uncoated surfaces. This could be attributed to the coating process and the resistance to the temperature gradient during condensation tests.
- 4- The hydrophobic surface by using the perfluoro silane as a second method of coating and this resulted in an increase of contact angle, heat transfer coefficient, and heat flux by 14 %, 25 % and 28 % respectively.
- 5- High-speed camera provided certain images that visualize the wetting process of the surface during DFWC. While the shape of droplets forming over the uncoated surface was circular, the droplets on the coated surface were asymmetric.
- 6- Through the comparison of experimental results with data published in other scientists, it was revealed that the experimentally obtained HTCs and heat fluxes for similar pressure conditions are lower than those of the other studies.
- 7- Although DFWC mode was observed in high-speed videos, the expected enhancement in heat transfer did not materialize significantly. The major reason was the presence of non-condensable gases leading to an increase of the thermal resistance at the interfacial boundary where vapor and solid interact.

In the following task, experimental and analytical studies focused on investigating the impact of various topographic surfaces on the drop-film wise condensation (DFWC) at a constant vapor pressure of 1.02 Bar.

- 1- A correlation was proposed to evaluate the heat flux, heat transfer coefficient, and the Nusselt number as a function of surface temperature and subcooling temperature.
- 2- An experimental setup was established and the results were validated by the analytical studies. Based on the comparisons made among various correlations, the maximum error percentage was found to be lower than 15% for each sample.
- 3- Experimental results showed that the heat transfer coefficient of the unstructured surface was higher than the ones for V-groove and square groove surfaces by 30% and 7.2%. This was related to the significant enhancement in the condensation surface area and droplet contact angle by approximately 50% and 14% respectively compared to the unstructured surface.
- 4- The comparison between the experimental and the current analytical results indicated that the maximum variations in HF for each unstructured, square groove and V-groove surface were 21.50%, 11.56% and 22.70%, while they were 21.7%, 11.63% and 22.7% respectively in HTC.
- 5- The comparison between the experimental and current analytical results of HF and HTC was conducted and the maximum deviation in all samples was determined as 25%.
- 6- Lastly, the current correlation gave an acceptable agreement compared with the experimental results (R^2 greater than 91 %).

In the final task, the condensation phenomena on the hydrophobic surface was studied using perfluoro silane mixture at different topographies and various operation vapor pressures from 1.02 Bar to 1.25 Bar.

- 1- The hydrophobic square groove surface provided a good enhancement in the droplet contact angle by 6.1% and 23.7% compared to the other surfaces, V-groove and

unstructured respectively. This is due to the increased resistance during the motion of a droplet inside the groove and between the coating particles.

- 2- The highest enhancement in the droplet contact angle was 29% for the V-groove surface when compared to the other coated surfaces. This is related to the accumulating coating particles inside the grooves. The reason was the presence of coating particles inside the micro-grooves that could decrease the surface energy and raise the surface resistance against the droplet. This would prevent the droplet from sitting on the surface crests for a long time.
- 3- At the operating vapor pressure of 1.25 Bar and subcooling temperature of 7.4 K, the experimental results of hydrophobic unstructured surface showed improvement in HF by 3% and 12%, while in HTC by 35% and 73.7% compared to the square groove and V-groove surfaces respectively.
- 4- High-speed camera images illustrated that the condensation phenomena on the effective surfaces occurred in two types, DWC and DFWC modes. It was also determined for all surfaces that the shape of droplets forming on the uncoated surface was circular with a small droplet size while the droplets on the coated surface were asymmetric with a large droplet size at a different operating pressure.

7.2 Recommendations for Future Work

This thesis provides a fundamental understanding of the condensation phenomena realized on an active surface with different topographies and the impact of the hydrophobic surface on the rate of condensation heat transfer in a range of operating vapor pressures from 1.02 Bar to 1.25 Bar. The understanding gained from this thesis work can be used to develop a condenser part of any thermal system, and to improve the cooling efficiency, increase the amount of heat dissipation, and reduce the size. In

addition to summary of the insights provided by experiments, models and analytical calculations, an outline of future directions are demonstrated in this chapter.

Although the outcomes of this work indicated that the micro-nano-structured surfaces characteristics influence on the condensation heat transfer rate, several characteristics and parameters should still be considered in the investigation of condensation phenomena. This work can be further expanded to investigate several other characteristics on the condensation processes, which are essential to indicate the condensation type that happened on the active condensation surface inside the vapor chamber. Therefore, a brief list of suggestions can be considered in any future investigation. The condensation process on the active surface produces some oxidation, fouling, etc, that led to increase of thermal resistance of film liquid condensation and to decrease the rate of condensation heat transfer. Thereby, the active condensation surface needs to be cleaned by using alcohol to prevent any oxidation in the future. In addition, as the vapor pressure rising, the speed of the drops condensation increases on the wall surface. Therefore, the investigation on the vapor flow characteristic on the DWC needs to be expanded by considering the effect of rising the vapor pressure more than 2.0 Bar. A smart approach is applied for controlling the condensation phenomena at active surface by using LabVIEW, that achieved by varying operation conditions. The operating conditions that examined in this study were different surface wetting by using ultra-ever dry and perfluoro silane, surface topographies (unstructured and microstructured square groove and V-groove), and the operating vapor pressure from 1.02 to 1.25 Bar.

The current study explains that we can improve the condensation heat transfer rate and thermal performance of heat pipe systems by optimizing the surface coating with different topographies. The samples models and experiments results show that the

proposed innovative surface coating idea is suitable for both wetting and thermal performance in the condenser part of the heat pipe. Then, new approaches and ideas which may broaden the current research more on the condensation thermal enhancements. A brief list of suggestions for future work can be given as the following;

- Condensation process has shown as the most appropriate cooling mechanism for the problem in the current work for heat pipe by using the working fluid is deionized water. While the dielectric liquid coolants can provide on-demand more condensation at different thermos-physical properties such as Fc-72, HFE-7100, HFE7200, etc.; more can be given as listed below, since dielectric liquid can be the main importance in the condensation heat transfer mechanism.
 - New possible dielectric coolants can be experimentally investigated according to the required performances. After system level characterization, it can also be used for condensation phenomena of high-performance thermal cooling systems.
 - The candidate vapor condensation can be studied with varying operating conditions to meet the thermal performance expectations of other systems. However, it can be coupled with condensation heat transfer rate expectations too by controlling some other parameters such as surface wetting, surface topographies, and vapor pressure, etc.
- The condensation approaches were achieved by performing different tasks for thermal performance of heat pipe, characteristics of surface wetting, and experimental tests of condensation phenomena with variable surface topographies at 1.02 Bar, condensation tests with various operating vapor pressures and finally, the analytical calculations of the condensation process on the vertical plate for each samples.

- Increasing the convective heat transfer rate on the back-side of the heatsink by applying another working fluid with different freezing temperature such as dielectric fluid, refrigerants, etc.
- Increasing the convective heat transfer coefficient between the copper fins and cooling liquid by utilizing other types of heatsink as pin-fins, cross cut fins, perforated fins, etc.
- A novel liquid can be used by mixing two or three dielectric liquids to produce a new steam with different physical properties, which operated as steam during the condensation tests. Thereby, the main parameters of condensation will be achieved such as heat flux and HTC are determined by using the novel liquid.
- Some part of the current work focuses on the coating technology to enhance the condensation heat transfer rate by making the hydrophobic surface for every surface topography. Although, the effect of each idea has been successfully explained, much effort can be given on purely coating experiments.
 - The proposed surface coating in the current work can be enlarged with varying thicknesses as a new factor that affected of the condensation heat transfer mechanism.
 - In the current work, Ultra ever dry coating used to create the super-hydrophobic surface on all samples. The results showed a good enhancement of droplet contact angle larger than 160° , but this type of coating is failed during the condensation experiments. This is due to lower thermal resistance of the UED versus temperature gradient between the cooler side and the hot side of the copper block. Then, the suggestion could be finding another coating type to make a super-hydrophobic surface with high thermal resistance to the temperature gradient.

- The microstructured square groove and V-grooved surfaces that are chosen for this study, different surface topographies of the condensation active surface such as a pyramid, triangle, rectangular, semicircle, pin structures, etc. and would be nice to compare with similar coating techniques to see the effectiveness of the proposed coating ideas for different applications.



REFERENCES

- [1] D. Pounds and R. W. Bonner, "High heat flux heat pipes embedded in metal core printed circuit boards for LED thermal management," *Thermomechanical Phenom. Electron. Syst. -Proceedings Intersoc. Conf.*, pp. 267–271, 2014.
- [2] C. Choi and M. Kim, "Wettability Effects on Heat Transfer, Two Phase Flow, Phase Change and Numerical Modeling," in *Book, ch.14*, ISBN 978-953-307-584-6, 2010, p. 311–341, DOI: 10.5772/19512.
- [3] W. Feng, "Making a Case for Efficient Supercomputing," *ACM Queue*, vol. 1, no. 7, pp. 54–64, 2003.
- [4] Y. R. Mahulkar and C. M. Sedani, "Analysis Of Miniature Loop Heat Pipe," vol. 3, no. 10, pp. 77–83, 2014.
- [5] O. Environments, "Loop Heat Pipe (LHP) Modeling and Development by Utilizing Coherent Porous Silicon (CPS) Wicks," *Ind. Eng.*, p. 23, 2003.
- [6] H. Dubbel, "Two Phae Flow Heat Transfer Devices, Heat Pipe Science And Technology," in *Berlin: Springer,c1994, edited by Beitz, W.; chapter 1*, 1994, pp. 1–31.
- [7] C. J. Oshman, "Development , Fabrication , and Experimental Study of Flat Polymer Micro Heat Pipes," Ph.d. thesis of Mechanical Engineering, University of Colorado at Boulder, pp 1-162, 2012.
- [8] X. Luo, T. Cheng, W. Xiong, Z. Gan, and S. Liu, "Thermal analysis of an 80W light-emitting diode street lamp," *Optoelectron. IET*, vol. 1, no. 5, pp. 191–196, 2007.
- [9] D. R. Nuttall, R. Shuttleworth, and G. Routledge, "Design of a LED street lighting system," *4th IET Int. Conf. Power Electron. Mach. Drives. PEMD*, pp.

- 436–440, 2008.
- [10] S. H. Moon, G. Hwang, S. C. Ko, and Y. T. Kim, “Experimental study on the thermal performance of micro-heat pipe with cross-section of polygon,” *Microelectron. Reliab.*, vol. 44, no. 2, pp. 315–321, 2004.
- [11] S. Küçük, “A Comparative Investigation Of Heat Transfer Capacity Limits Of Heat Pipes,” M.Sc. Thesis of Mechanical Engineering, Middle East Technical University, pp 1-100, 2007.
- [12] J. Weyant, S. Garner, M. Johnson, and M. Occhionero, “Heat pipe embedded AlSiC plates for high conductivity - Low CTE heat spreaders,” *12th IEEE Intersoc. Conf. Therm. Thermomechanical Phenom. Electron. Syst.*, pp. 1–6, 2010.
- [13] C. K. Loh, E. Harris, and D. J. Chou, “Comparative study of heat pipes performances in different orientations,” *Semicond. Therm. Meas. Manag. IEEE Twenty First Annu. IEEE Symp.*, 2005.
- [14] S. Pulipaka, “The Effect of Surface Wettability on Heterogeneous Condensation,” M.SC. thesis, Jawaharlal Nehru Technological University, Hyderabad, India, 2008.
- [15] L. Duta, A. C. Popescu, I. Zgura, N. Preda, and I. N. Mihailescu, “Wettability of Nanostructured Surfaces,” in *Wetting and Wettability*, no. chapter 8, 2015, p. 207–252, DOI: 10.5772/60808.
- [16] D. M. Anderson, “Theoretical and Experimental Investigation of Condensation on Amphiphilic Nanostructured Surfaces,” Georgia Institute of Technology, Thesis of Master Science in Mechanical Engineering, 2013.
- [17] R. N. Wenzel, “Resistance of solid surfaces to wetting by water,” *J. Ind. Eng. Chem. (Washington, D. C.)*, vol. 28, no. 8, p. 988–994, DOI:

- 10.1021/ie50320a024, 1936.
- [18] L. Gao and T. J. McCarthy, "How Wenzel and Cassie were wrong," *Langmuir*, vol. 23, no. 7, p. 3762–3765, DOI: 10.1021/la062634a, 2007.
- [19] M. Nosonovsky, "On the Range of Applicability of the Wenzel and Cassie Equations," *Langmuir*, vol. 23, p. 9919–9920, DOI: 10.1021/la701324m, 2007.
- [20] S. Frank, E. Noem, V. Doris, and B. Hans-Jurgen, "How Water Advances on Superhydrophobic Surfaces," *Phys. Rev. Lett.*, vol. 116, no. 9, pp. 2–7, 2016.
- [21] J. X. H. Wong and H. Z. Yu, "Preparation of transparent superhydrophobic glass slides: Demonstration of surface chemistry characteristics," *J. Chem. Educ.*, vol. 90, no. 9, pp. 1203–1206, 2013.
- [22] S. Launay, V. Sartre, and J. Bonjour, "Parametric analysis of loop heat pipe operation: a literature review," *Int. J. Therm. Sci.*, vol. 46, no. 7, pp. 621–636, 2007.
- [23] A. A. Orlov, K. A. Goncharov, E. Y. Kotliarov, and T. A. Tyklina, "The loop heat pipe experiment on board the 'GRANAT' spacecraft," *27th ICES, Noordwijk, Netherlands*, pp. 341–353, 1997.
- [24] C. L. Baker, W. B. Bienert, and A. S. Ducao, "Loop Heat Pipe flight experiment," *AIP Conf. Proc.*, vol. 420, no. 1, pp. 511–513, 1998.
- [25] K. Cheung, T. Hoang, J. Ku, and T. Kaya, "Thermal Performance and Operational Characteristics of Loop Heat Pipe (NRL LHP)," *Int. Conf. Environ. Syst. Danvers, (SAE Pap. 981813)*, no. 724, p. 10, 1998.
- [26] D. Douglas, J. Ku, and T. Kaya, "AIAA 99-0473 Testing of the Geoscience Laser Altimeter System (GLAS) Prototype Loop Heat Pipe," *Tarik Kaya NRC Resident Research Associate 37th AIAA Aerospace Sciences Meeting and Exhibit*, *Sci. York*, 1999.

- [27] M. Amidieu, T. Tjiptahardja, S. Van Oost, B. Mullender, G. Bekaert, and J. Mauduyt, "STENTOR CPL: Ground Test and Modelling Results," *Int. Conf. Environ. Syst. Toulouse, (SAE Pap. 2000-01-2454)*, no. 724, pp. 1–9, 2000.
- [28] Y. F. Maydanik, "Loop heat pipes," *Appl. Therm. Eng.*, vol. 25, no. 5–6, pp. 635–657, 2005.
- [29] O. Uçar and Y. Erbil, "Droplet condensation on polymer surfaces: A review," *Turkish J. Chem.*, vol. 37, no. 4, pp. 643–674, 2013.
- [30] H. Jo, D. I. Yu, H. Noh, H. S. Park, and M. H. Kim, "Boiling on spatially controlled heterogeneous surfaces: Wettability patterns on microstructures," *Appl. Phys. Lett.*, vol. 106, no. 18, p. 181602, 2015.
- [31] N. R. Chiou, C. Lu, J. Guan, L. J. Lee, and A. J. Epstein, "Growth and alignment of polyaniline nanofibres with superhydrophobic, superhydrophilic and other properties," *Nat. Nanotechnol.*, vol. 2, no. 6, pp. 354–357, 2007.
- [32] Y. Li, J. Zhang, S. Zhu, H. Dong, F. Jia, Z. Wang, Z. Sun, L. Zhang, Y. Li, H. Li, W. Xu, and B. Yang, "Biomimetic surfaces for high-performance optics," *Adv. Mater.*, vol. 21, no. 46, pp. 4731–4734, 2009.
- [33] R. Chen, M. Lu, V. Srinivasan, Z. Wang, H. Hee, and A. Majumdar, "Nanowires for enhanced boiling heat transfer," *Nano Lett.*, vol. 9, pp. 548–553, 2009.
- [34] P. C. Stephan and C. A. Busse, "Analysis of the heat transfer coefficient of grooved heat pipe evaporator walls," *Int. J. Heat Mass Transf.*, vol. 35, no. 2, pp. 383–391, 1992.
- [35] L. Zhai, M. C. Berg, F. Ç. Cebeci, Y. Kim, J. M. Milwid, M. F. Rubner, and R. E. Cohen, "Patterned superhydrophobic surfaces: Toward a synthetic mimic of the namib desert beetle," *Nano Lett.*, vol. 6, no. 6, pp. 1213–1217, 2006.
- [36] C. H. Choi and C. J. Kim, "Large slip of aqueous liquid flow over a

- nanoengineered superhydrophobic surface,” *Phys. Rev. Lett.*, vol. 96, no. 6, pp. 1–4, 2006.
- [37] D. Del Col, R. Parin, A. Bisetto, S. Bortolin, and A. Martucci, “Film condensation of steam flowing on a hydrophobic surface,” *Int. J. Heat Mass Transf.*, vol. 107, pp. 307–318, 2017.
- [38] C. H. Chen, Q. Cai, C. Tsai, C. L. Chen, G. Xiong, Y. Yu, and Z. Ren, “Dropwise condensation on superhydrophobic surfaces with two-tier roughness,” *Appl. Phys. Lett.*, vol. 90, no. 17, pp. 23–25, 2007.
- [39] Y. Zhong, A. M. Jacobi, and J. G. Georgiadis, “Condensation and Wetting Behavior on Surfaces With Micro-Structures : Super-Hydrophobic and Super-Hydrophilic,” *Int. Refrig. Air Cond. Conf. Purdue Univ.*, pp. R100, 1–8, 2006.
- [40] A. M. Macner, S. Daniel, and P. H. Steen, “Condensation on surface energy gradient shifts drop size distribution toward small drops,” *Langmuir*, vol. 30, no. 7, pp. 1788–1798, 2014.
- [41] C. S. Sharma, J. Combe, M. Giger, T. Emmerich, and D. Poulikakos, “Growth Rates and Spontaneous Navigation of Condensate Droplets Through Randomly Structured Textures,” *ACS Nano*, vol. 11, no. 2, pp. 1673–1682, 2017.
- [42] X. Chen, J. Wu, R. Ma, M. Hua, N. Koratkar, S. Yao, and Z. Wang, “Nanograssed micropyrarnidal architectures for continuous dropwise condensation,” *Adv. Funct. Mater.*, vol. 21, no. 24, pp. 4617–4623, 2011.
- [43] N. Miljkovic and E. N. Wang, “Condensation heat transfer on superhydrophobic surfaces,” *MRS Bull.*, vol. 38, no. 5, pp. 397–406, 2013.
- [44] H. S. Wang and J. W. Rose, “Theory of heat transfer during condensation in microchannels,” *Int. J. Heat Mass Transf.*, vol. 54, no. 11–12, pp. 2525–2534, 2011.

- [45] R. Seemann, M. Brinkmann, E. J. Kramer, F. F. Lange, and R. Lipowsky, "Wetting morphologies at microstructured surfaces," *Proc. Natl. Acad. Sci.*, vol. 102, no. 6, pp. 1848–1852, 2005.
- [46] R. W. Bonner, "Dropwise condensation in vapor chambers," *IEEE26th IEEE SEMI-THERM Symp.*, pp. 224–227, 2010.
- [47] A. w. Neumann, A. h. Abdelmessih, and A. Hameed, "The role of contact angles and contact angle hysteresis in dropwise condensation heat transfer," *Int. J. Heat Mass Transf.*, vol. 21, no. 1, pp. 947–953, 1978.
- [48] B. Richard W, "Dropwise Condensation on Surfaces With Graded Hydrophobicity," *Proc. ASME - Heat Transf. Summer Conf. July 19-23, San Fr. Calif. USA*, pp. 1–5, 2009.
- [49] Q. Baojin, Z. Li, X. Hong, and S. Yan, "Experimental study on condensation heat transfer of steam on vertical titanium plates with different surface energies," *Exp. Therm. Fluid Sci.*, vol. 35, no. 1, pp. 211–218, 2011.
- [50] R. Enright, N. Dou, N. Miljkovic, Y. Nam, and E. N. Wang, "Condensation On Superhydrophobic Copper Oxide Nanostructures," in *Proceedings of the ASME 2012 3rd Micro/Nanoscale Heat & Mass Transfer International Conference, Atlanta, Georgia, USA, March 3-6, 2012*, no. 1, pp. 1–7.
- [51] D.-J. Huang and T.-S. Leu, "Condensation heat transfer enhancement by surface modification on a monolithic copper heat sink," *Appl. Therm. Eng.*, vol. 75, pp. 908–917, 2015.
- [52] X. Ma, B. Tao, J. Chen, D. Xu, and J. Lin, "Dropwise condensation heat transfer of steam on a polytetrafluoroethylene film," *J. Therm. Sci.*, vol. 10, no. 3, pp. 247–253, 2001.
- [53] J. J. Shu, "Laminar Film Condensation Heat Transfer on a Vertical, Non-

- Isothermal, Semi-Infinite Plate,” *Arab. J. Sci. Eng.*, vol. 37, no. 6, pp. 1711–1721, 2012.
- [54] H. W. Hu and G. H. Tang, “Theoretical investigation of stable dropwise condensation heat transfer on a horizontal tube,” *Appl. Therm. Eng.*, vol. 62, no. 2, pp. 671–679, 2014.
- [55] M. A. Fayazbakhsh and M. Bahrami, “Analytical Modeling of Mist Condensation by Natural Convection over Inclined Flat Surfaces,” in *ASME 2013 Summer Heat Transfer Conference*, 2013, pp. 1–7.
- [56] S. Herminghaus, M. Brinkmann, and R. Seemann, “Wetting and Dewetting of Complex Surface Geometries,” *Annu. Rev. Mater. Res.*, vol. 38, no. 1, pp. 101–121, 2008.
- [57] M. Budakli, T. K. Salem, and M. Arik, “Experimental investigation on heat transfer and surface wetting phenomena during vapor condensation on nano textured surfaces,” in *10th International Conference on Boiling and Condensation Heat Transfer 12th-15th March 2018 in Nagasaki, Japan* www.icbcht2018.org, 2018, no. March, pp. 2–3.
- [58] I. Viorel, *Study of condensation phenomena on flat surfaces*, no. March. 2016, pp. 1–33.
- [59] A. Cavalli, “Wetting on micro-structured surfaces: modelling and optimization,” Ph.D. Thesis-Technical University of Denmark (DTU) Department, 2013.
- [60] T. P. Garvin, “Fabrication, characterization, and wettability analysis of a microstructured hybrid hydrophobic/hydrophilic surface,” MSc thesis- University of Illinois at Urbana-Champaign, 2012.
- [61] Y. Zheng, C. H. Chen, H. Pearlman, M. Flannery, and R. W. Bonner III, “Effect of porous coating on condensation heat transfer,” *9th Int. Conf. Boil. Condens.*

- Heat Transf.*, no. February 2016, 2015.
- [62] G. Nellis and S. Klein, "Heat Transfer," in *Coulson and Richardson's Chemical Engineering*, USA: Gregory & Sanford, 2009, pp. 3–264.
- [63] R. R. Kumar, M. Narasimha, and K. Sridhar, "Heat Transfer Enhancement in Heat Pipe Using TiO₂ Nanofluid with N-Butanol," *Sci. Technol.*, vol. 3, no. 4, pp. 105–111, 2013.
- [64] H. Lee, *Thermal Design Heat Sinks , Thermoelectrics , Heat Pipes , Compact Heat Exchangers , and Solar Cells*. Hoboken, New Jersey: John Wiley & Sons, Inc., 2011.
- [65] D.A. Reay and P.A. Kew, *Heat Pipes: Theory, design and application*, Fifth Edit. Whitley Bay, UK, 2006.
- [66] G.P. Peterson, *An Introduction to Heat Pipes: Modeling, Testing, and Applications*, 1st Editio. United States: John Wiley and Sons Ltd, 1994.
- [67] G. P. P. and D. W. B.R. Babin, "Steady-State Modeling and Testing of a Micro Heat Pipe," *J HEAT TRANS-T ASME*, vol. 112, no. August, pp. 595–601, 1990.
- [68] Bahman Zohuri, *Heat Pipe: Design and Technology*, Taylor & F. New York-USA, 2011.
- [69] A. Faghri, *Heat Pipe Science and Technology*. Washington, DC: Taylor and Francis, 1995.
- [70] Y. A. Çengel and A. J. Ghajar, *Heat and Mass Transfer fundamental and applications*, Fourth Edi., no. chapter 9. The McGraw-Hill Companies, 2011.
- [71] T. K. Salem, F. S. Khosroshahi, M. Arık, O. Hamdan, and M. Budakli, "Numerical and experimental analysis of a heat pipe embedded printed circuit board for solid state lighting applications," *Exp. Heat Transf.*, pp. 1–13, 2017.
- [72] G. S. Hwang, M. Kaviany, W. G. Anderson, and J. Zuo, "Modulated wick heat

- pipe,” *Int. J. Heat Mass Transf.*, vol. 50, no. 7–8, pp. 1420–1434, 2007.
- [73] I. Advanced Thermal Solutions, “Collection of Technical Articles on Heat Pipes and their Roles in the Thermal Management of Electronics,” in *ATS Engineering eBook*, 2013, pp. 1–18.
- [74] Y. Kawahara, M. Mochizuki, and Y. Saito, “One-millimeter Heat Pipe and Application to Cooling Module for Electronic Devices,” 2011.
- [75] T. Salem, M. Budakl, and M. Arik, “An experimental and analytical study on the influence of superhydrophobic micro-textured surfaces on liquid wetting phenomena,” *Colloids Surfaces A Physicochem. Eng. Asp.*, vol. 555, no. June, pp. 191–200, 2018.
- [76] H. J. Jeong, D. K. Kim, S. B. Lee, S. H. Kwon, and K. Kadono, “Preparation of water-repellent glass by sol-gel process using perfluoroalkylsilane and tetraethoxysilane,” *J. Colloid Interface Sci.*, vol. 235, no. 1, pp. 130–134, 2001.
- [77] B. Mahltig and H. Böttcher, “Modified silica sol coatings for water-repellent textiles,” *J. Sol-Gel Sci. Technol.*, vol. 27, no. 1, pp. 43–52, 2003.
- [78] G. Gu, Z. Zhang, and H. Dang, “Hydrophobic inorganic-organic thin films with a low coefficient of friction,” *Mater. Res. Bull.*, vol. 39, no. 7–8, pp. 1037–1044, 2004.
- [79] K. Badri, W. Sien, M. Shahrom, L. Hao, N. Baderuliksani, and N. Rabbi, “Ftir Spectroscopy Analysis Of The Prepolymerization Of Palm-Based Polyurethane,” *Solid State Sci. Technol.*, vol. 18, no. 2, pp. 1–8, 2010.
- [80] “Ultra-Ever Dry Specifications,” *Datasheet*, 2014. [Online]. Available: <http://www.spillcontainment.com/media/2320/ultra-ever-dry-spec-sheet-12-14-16>.
- [81] Y. Yuan and T. R. Lee, “Contact Angle and Wetting Properties,” in *Surface*

- science techniques, ch.1*, 2013, p. 3–34, DOI 10.1007/978-3-642-34243-1_1.
- [82] R. J. Moffat, “Describing the uncertainties in experimental results,” *Exp. Therm. Fluid Sci.*, vol. 1, no. 1, pp. 3–17, 1988.
- [83] M. BUDAKLI, T. SALEM, and M. ARIK, “Effect Of Micro-Structured Surfaces On Heat Transfer And Surface Wetting Phenomenon During Vapour Condensation,” in *21th National Conference of Heat Science and Technology (ULIBTK'17)*, 2017, pp. 991–1002.
- [84] Attension TN 7, “Influence of surface roughness on contact angle and wettability,” *www.attension.com*, pp. 1–3, 1936.
- [85] B. D. Cassie and S. Baxter, “Wettability Of Porous Surfaces,” *Trans. Faraday Soc.*, vol. 40, no. 5, pp. 546–551, 1944.
- [86] R. M. do Nascimento, A. E. Martinelli, and A. J. A. Buschinelli, “Review article: recent advances in metal-ceramic brazing,” *Cerâmica*, vol. 49, no. 312, pp. 178–198, 2003.
- [87] R. Enright, N. Miljkovic, J. L. Alvarado, K. Kim, and J. W. Rose, “Dropwise condensation on micro-and nanostructured surfaces,” *Nanoscale Microscale Thermophys. Eng.*, vol. 18, no. 3, pp. 223–250, 2014.
- [88] H. Lee, *Thermal Design: Heat Sinks, Thermoelectrics, Heat Pipes, Compact Heat Exchangers, and Solar Cells*. 2010.
- [89] A. Yunus and Cengel, *heat Transfer, A practical approach*, SECOND EDI. 2000.
- [90] C. Long, N. Sayma, D. Free, and T. At, *Heat Transfer - Exercises*. Publishing in APS, 2010.
- [91] J. Mahmoudi and J. Vaarno, *Copper Heat Sink Design A Practical Application of Mathematical Modelling*, vol. SIMS, no. 2. 2003, pp. 1–40.
- [92] F. P. Incropera, D. P. DeWitt, T. L. Bergman, and A. S. Lavine, “Fundamentals

- of Heat and Mass Transfer.” SIXTH EDITION, p. 997, 2007.
- [93] Y. A. Çengel, *Heat and Mass Transfer*, Seven Edit. The McGraw-Hill Companies: ,ch.13, pp.673, 2011.
- [94] W. Rohsenow, J. Hartnett, and Y. Cho, *Handbook of heat transfer*, Third., vol. 18, no. 10. MCGRAW-HILL New, 1975.
- [95] S. Kline and F. McClintock, “Describing uncertainties in single - sample experiments,” *Mech. Eng.*, vol. 75, no. 1, pp. 3–8, 1953.
- [96] J. H. Kim and T. W. Simon, “Journal Of Heat Transfer Policy On Reporting Uncertainties In Experimental Measurements And Results,” *J. Heat Transf.*, vol. 115, no. 1, pp. 5–6, 1993.
- [97] R. J. Moffat, “Using Uncertainty Analysis in the Planning of an Experiment,” *J. Fluids Eng.*, vol. 107, no. 2, pp. 173–178, 1985.
- [98] J. P. Holman, *Heat Transfer*, Tenth Edit. McGraw-Hill Series in Mechanical Engineering, 2012.
- [99] R. S. Figliola and D. E. Beasley, *Theory and Design for Mechanical Measurements*, Fifth Edit. John Wiley & Sons, Inc., 2011.
- [100] H. W. Coleman and W. G. J. Steele, “Experimentation, errors, and uncertainty,” in *Experimentation, Validation, and Uncertainty Third Edition*, Third Edit., John Wiley & Sons, Inc. ISBN: 978-0-470-16888-2, 2009, pp. 1–27.
- [101] I. N. Shishkova, A. P. Kryukov, and V. Y. Levashov, “Solution Of Evaporation And Condensation Problems Based On The Conjugate Approach,” in *Proceedings of the 2nd MIGRATE Workshop*, 2017, pp. 1–2.
- [102] R. Wen, Z. Lan, B. Peng, W. Xu, and X. Ma, “Droplet dynamics and heat transfer for dropwise condensation at lower and ultra-lower pressure,” *Appl. Therm. Eng.*, vol. 88, pp. 265–273, 2015.

- [103] X.-H. Ma, X.-D. Zhou, Z. Lan, T.-Y. Song, and J. Ji, “Experimental Investigation of Enhancement of Dropwise Condensation Heat Transfer of Steam-Air Mixture: Falling Droplet Effect,” *J. Enhanc. Heat Transf.*, vol. 14, no. 4, pp. 295–305, 2007.
- [104] X. H. Ma, X. D. Zhou, Z. Lan, Y. M. LI, and Y. Zhang, “Condensation heat transfer enhancement in the presence of non-condensable gas using the interfacial effect of dropwise condensation,” *Int. J. Heat Mass Transf.*, vol. 51, no. 7–8, pp. 1728–1737, 2008.
- [105] Crystran LTD, *The Design of Pressure Windows*, no. September. 2013, pp. 307650–307651.
- [106] M. T. Scholar, M. Engineering, and B. V. C. E. College, “Analysis of Hyoid Structured And Perforated Pinfin Heat Sink In Inline And Staggered Flow,” *IJSEAT*, vol. 2, no. 4, pp. 125–130, 2014.
- [107] T. O. O. Important and N. O. T. To, “v-Series Cameras Throughput :,” pp. 2–5, 2013.
- [108] “Phantom v311,” pp. 1–10.
- [109] A. T. Measurement, F. F. Rates, and M. F. Wheel, “FLIR Silver SC5200-USB.”
- [110] T. Bank and E. Syracuse, “JUMO MIDAS S05 OEM Pressure Transmitter – Universal,” pp. 1–11.
- [111] M. Flowrate, “VARIABLE AREA ROTAMETERS With 65 mm and 150 mm Scales.” pp. B29–B30.
- [112] H. Electronic Sensor GmbH, “Resistance-thermometers (Pt 100) of DIN EN 60751,” no. Pt 100, pp. 1–2, 2011.
- [113] C. En-, “Technical data,” vol. 181, no. 716, pp. 6–8, 2006.
- [114] K. B.- Umwälzthermostat, K. Leistungsstarke, and M. Ag, “Hubre-Ministat 125,”

2014. [Online]. Available: www.huber-online.com.
- [115] F. Tek, “Mini Float Level Switch.” www.fine-tek.com, Germany, pp. 1–27, 2015.
- [116] S. Guide, “Keysight Technologies Power Products – October 2015 A guide to power product solutions to match your test and measurement needs,” no. October, 2015.
- [117] S. Dc and P. Supply, “Agilent Technologies System DC Power Supply.”
- [118] P. Supplies, “Agilent N8700 Series System DC Power Supplies Basic System DC,” pp. 1–12.
- [119] S. Guide, “Agilent E3633A and E3634A DC Power Supplies DC Power Supplies,” 2014.
- [120] S. Guide, “Keysight 34970A/34972A Data Acquisition/Switch Unit.”
- [121] T. Overview, “Keysight 34970A Data Acquisition / Switch Unit Family.”
- [122] C. V. Collett and A. D. Hope, *Engineering Measurements*, Second Edi. Singapore: ELBS., 1983.

APPENDIX A

A.1 Literature Summary

Table A-1: The summary table of literatures review

No	Authors	Contains	Link with current thesis
1.	Pulipaka [14]	<ul style="list-style-type: none"> ▪ Non-uniform condenser surface ▪ Hydrophilic & hydrophobic effect ▪ Droplet growth rate & condensation 	<ul style="list-style-type: none"> - Surface geometry - Wetting surface - Condensation
2.	Duta et al. [15]	<ul style="list-style-type: none"> ▪ nanostructured surface & wettability ▪ Young, Cassie, and Wenzel models ▪ Coating by ZnO, SiO₂, TiO₂ and DLC. ▪ hydrophobic surface 	<ul style="list-style-type: none"> - Nanotextured - Wettability - Hydrophobic surface
3.	Jo et al. [30]	<ul style="list-style-type: none"> ▪ Nucleate boiling heat transfer. ▪ Heterogeneous wetting ▪ Microstructures hydrophilic surface. ▪ Two coating method -SiO₂ and SAM 	<ul style="list-style-type: none"> - Treated surface. - - Micro/Nanostructures - Wetting surface
4.	DelCol et al.[37]	<ul style="list-style-type: none"> ▪ FWC and DWC ▪ Untreated and Treated surface ▪ surface wetting characteristics ▪ Condensation experiments at 1 Bar 	<ul style="list-style-type: none"> - DFWC at 1.02 Bar - Unstructured copper surface.
5.	Chen et al.[42]	<ul style="list-style-type: none"> ▪ FWC(hydrophilic) ▪ DWC (hydrophobic) ▪ Condensation experiments at 3.44 Bar ▪ Untreated flat copper surface 	<ul style="list-style-type: none"> - Flat surface - Pv,ch=1.02-1.25 Bar - qualities (> 0.9) - Untreated surface
6.	Miljkovic et al.[43]	<ul style="list-style-type: none"> ▪ FWC (hydrophilic) ▪ DWC (hydrophobic) ▪ JC(superhydrophobic) ▪ Droplet morphology 	<ul style="list-style-type: none"> - DFWC - Hysdrophobic and Superhydrophobic - Droplet contact angle
7.	Neumann et al.[47]	<ul style="list-style-type: none"> ▪ Dropwise condensation. ▪ Condenser coating (hydrophobic). ▪ HTC and Hysteresis contact angle. 	<ul style="list-style-type: none"> - Hydrophobic surface - HTC - Condensation - Contact angle
8.	Ryan et al.[50]	<ul style="list-style-type: none"> ▪ Nanostructured copper surface ▪ Superhydrophobic condensation ▪ SAM method and DWC on the hydrophobic nanostructured surface ▪ Condensation experimental at 1.5 Bar 	<ul style="list-style-type: none"> - Micro/nano-structured - Superhydrophobic - DFWC at 1.02 Bar
9.	Huang and Leu [51]	<ul style="list-style-type: none"> ▪ Condensation ▪ Wenzel wetting mode ▪ Superhydrophobic copper surface. 	<ul style="list-style-type: none"> - Microstructured surface - Dionized Water - Wenzel and Cassie–Baxter modes

APPENDIX B

B.1 *Optical Window Optimization*

The optical window is critical in this case for the visualization purposes. While, there are many factors that could affect the design of glass window such as pressure load, transmissivity, manufacturing and cost, the major factors must be considered for having the best design of optical windows. First, the thickness of glass is taken into account to hold the pressure load inside the vapor chamber without any failure. Second, the transmissivity of optical glass should be high enough to get a good image of dropwise condensation the test surface by using infrared and high-speed cameras [105]. For this purposes, the optical glass material type CaF_2 has been chosen which is suitable for utilizing in several applications such as infrared camera and high-speed camera. Also, the specifications of CaF_2 optical glass are determined by considering two parameters which are the wavelength ranging from 150 nm to 10000 nm and the glass thickness between 2 mm and 100 mm as seen in **Table B-1**. In addition, the analytical calculations are performed to determine the suitable wall thickness of optical glass by using EES program. These calculations are run with different pressures loads from 9 Bar to 15 Bar as an input data to determine the optimum glass thicknesses as 6.5 mm and 8.5 mm as shown in **Table B-2**. In this study, the glass thickness has been chosen as 5 mm because the vapor pressure inside the vapor chamber did not exceed more than 1.3 Bar. This is due to the operational conditions of the boiler during the condensation. There are two methods for designing the optical glass which is affected much by the way of fixing method of the glass window. These methods can be analyzed by observing the maximum stress applied on the center (unclamped) or edge (clamped) of the glass plate as seen in Figure B-1.

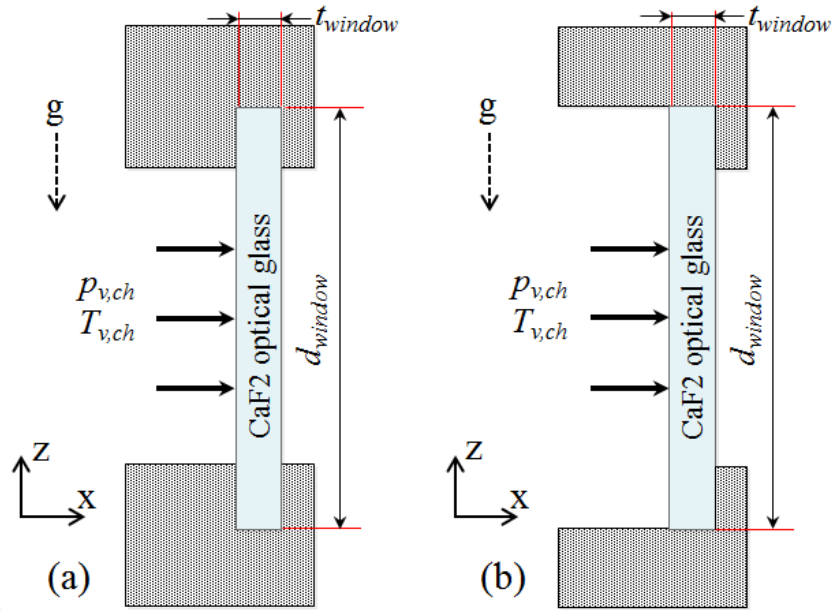


Figure B-1: Shows the schematic diagram of a circular optical window with two types design are (a) Clamped, σ_{\max} at edge and (a) Unclamped, σ_{\max} at center

In this case, the clamped circular glass design has been chosen where the maximum pressure is applied at each edge of the glass window. The maximum tensile stress σ_{\max} when there is uniform loading on the glass window can be calculated by [105]:

$$\sigma_{\max} = \frac{(Kc d_{\text{window}}^2 p_{v,\text{ch}})}{(4 t_{\text{window}}^2)} = \frac{Fa}{SF} \quad (\text{B-1})$$

The rectangular glass window thickness (t_{Window}) is solved by:

$$t_{\text{Window}} = d_{\text{window}} \sqrt{SF Kc/2} \sqrt{(p_{v,\text{ch}}/Fa)} \quad (\text{B-2})$$

where $SF=4$, $Kc=0.75$, the thickness of glass window becomes:

$$t_{\text{Window}} = 0.866 d_{\text{window}} \sqrt{(p_{v,\text{ch}}/Fa)} \quad (\text{B-3})$$

Table B-1: The optical glass transmission

Glass types	Glass thickness mm	Wave length nm	Max. transmission
Calcium Fluoride (CaF ₂)	2	(200-7000)	94%
		11789	10%

Table B-2: The optical glass thickness calculation by EES program

P _{v,ch}	d _{window}	E _{window}	t _{window}
[Pa]×10 ⁵	[mm]	[Pa]×10 ⁷	[mm]
8.92	50	4	6.5
15.54	50	4	8.5

B.2 Heatsink Design

Heat sink is a passive device that is used for dissipating the undesired heat from any system. The removal of this unwanted heat can be realized by fins with different shapes and geometries. The use of fins in a heat sink system enhances the heat transfer rate because of the increased surface area. Today, heat sinks are used in many applications as a solution part of thermal management of usually electronic devices and systems. The fundamental design of a heat sink is based on many parameters such as the amount of unwanted heat, required size, geometry, material type, fins type, and manufacturing method etc. Also, the operating principle of a heat sink is performed by considering the type of heat transfer such as conduction and/or convection heat transfer. In this study, the heat sink type was chosen during the condensation tests as a longitudinal heatsink composed of copper material. [106]. The analytical calculations have been made to determine the best design; thus, a parallel plate-fin heat sink was found to absorb the excessive heat flux greater than 100 W/cm². In addition, the

analytical calculations are based on many equations that were clearly already explained in section 5.3.2 to find the optimum design of the heat sink. Finally, the specifications of the heat sink model are illustrated in Table B-3 and also the schematic diagram of heat sink is shown in section 5.4 (see Figure 5-6).

Table B-3: The heatsink specification

Heat sink	specification
Type	longitudinal
Material	Copper
Fin length (L_{fin})	45 mm
Fin thickness (t_{fin})	1 mm
Fin space (S_{opt})	1 mm
Fins number (n_f)	11
Height of heat sink base (t_{base})	19.5 mm
Width of heat sink base (W_{base})	20 mm
Length of heat sink base (L_{base})	30 mm

B.3 Measurement Technique and Instrumentation

To have accurate results for all tasks; heat pipe, wettability phenomena on different topography surfaces and condensation on the vertical plates are investigated carefully. There are many techniques are used for analyzing the experimental results for all tasks such as Ansys-Icepak, EES program, IR techniques and visualization by using HSC individually. Besides, the experiments' tests of dropwise condensation were conducted at 33 measurements points with the different operating vapor pressure and all tests were repeated three times to check the results accuracy. Also, the experimental results are validated by using different tools such as analytical calculation by using the EES

program, numerical simulation by using Icepack program, comparing the results with other authors and Nusselt condensation correlations.

Two experimental setups were used in this thesis. First, a heat pipe setup consists of cylindrical and embedded heat pipe, low power supply and data acquisition with K-type thermocouple. Second, the condensation setup, in which a number of measurement devices are used such as low and high power supply, data acquisition, Huber chiller, pressure transmitter, Pt-100 thermocouple, omega rotameter and sensor liquid level. All specifications of measurement devices and tools are shown in Table B-4. A number of tools for different facilities are used to record the hydrodynamic phenomena during the condensation process, temperature measurement on each position in the experimental setup especially at heatsink base for calculating the condensation surface temperature, heat flux, heat transfer coefficient, and the droplet contact angle measurement with different topography surface, wetting surfaces (hydrophobic and super-hydrophobic surfaces), the temperature distribution on the heat pipe surface by using IR camera. All these facilities are illustrated in the following sections.

High speed camera- The condensation phenomena on the microstructure surface can be visualized in two ways: the first way is an experiment in which the working fluid interface will move through the microstructure surface which was operated with different electrical power inputs. The second way is visualizing the meniscus of droplet contact angle on the microstructure condenser surface. The visualization experiment will be done by a high-speed camera (see Figure B-2), which is placed vertically on the object with two optic light sources. The optical light sources with high intensity illuminators was also used to light the microstructure condenser surface and the liquid vapor that condense on the surface, but the light source position was distinguished experimentally to get the best visualization result. This visualization practically is

capturing images of the liquid meniscus and liquid contact angle. The field of view of the camera had been adjusted to $10\text{ mm} \times 20\text{ mm}$ with a spatial resolution of 1024×768 pixels ($20\text{ }\mu\text{m}/\text{pixel}$). Moreover, the fluid motion has been recorded at a frame rate of 800 Hz (see Table B-4)[107]-[108].

Also, the droplet contact angle can be measured by a protractor or analytically by using capillary Laplace equation Eq. 5-10, but experimentally by using a tensiometer type (KSV Attention Theta Lite Optic Contact Angle) with the similar liquid adopted in the experiments (deionized water). The high-speed camera of the tensiometer was used to record sessile droplets on the surface within the FOV ($5\text{ mm} \times 10\text{ mm}$) with a spatial resolution of 512×512 pixels ($10\text{ }\mu\text{m}/\text{pixel}$) and a frame rate of 60 Hz.



Figure B-2: High-speed camera with lamps lights during the condensation test

Infrared Thermal Camera (IR) - In this case, IR camera is used to record the infrared radiation emitted from the evaporator surface of embedded heat pipe shown in

Figure B-3. The camera is placed about 40 cm above the evaporator section, looking directly down and focused on the top surface of the liquid as evaporation process is happening. The camera is a Thermo-vision SC-5200 (FLIR Systems) with a spectral sensitivity range from 3 to 5 μm in wavelength. The working temperature range of IR camera is $-20\text{ }^{\circ}\text{C}$ to $1200\text{ }^{\circ}\text{C}$ and the temperature sensitivity is $0.05\text{ }^{\circ}\text{C}$ (see Table B-4)[109]. The aim of the IR camera use is to find the average surface temperature in the evaporator section of the heat pipe and also to validate the experimental results of the heat pipe.

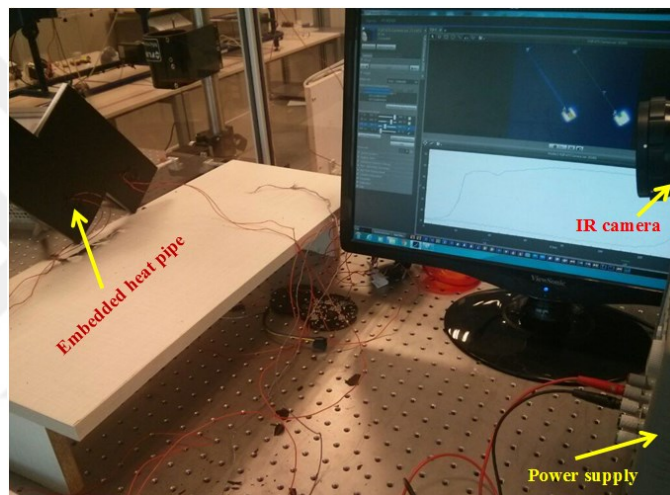


Figure B-3: IR camera during the embedded heat pipe test

Pressure measurements - The OEM transmitter (MPS500) is working by using charger type 24 VDC - 1 ampere and all device specification is written in Table B-4 [110]. The absolute pressure is measured at boiler and vapor chamber parts of the condensation setup. Repeatability, accuracy and turndown ration are very important while we question the correctness of the information and the quality of a transmitter. Then, the correlation formula was done as a function of the output value from 4 to 20 mA at the pressure range 0 to 6 Bar (see Figure B-4). Consequently, the results showed at 12mA in the controller or screen, while the absolute pressure is 6 Bar.

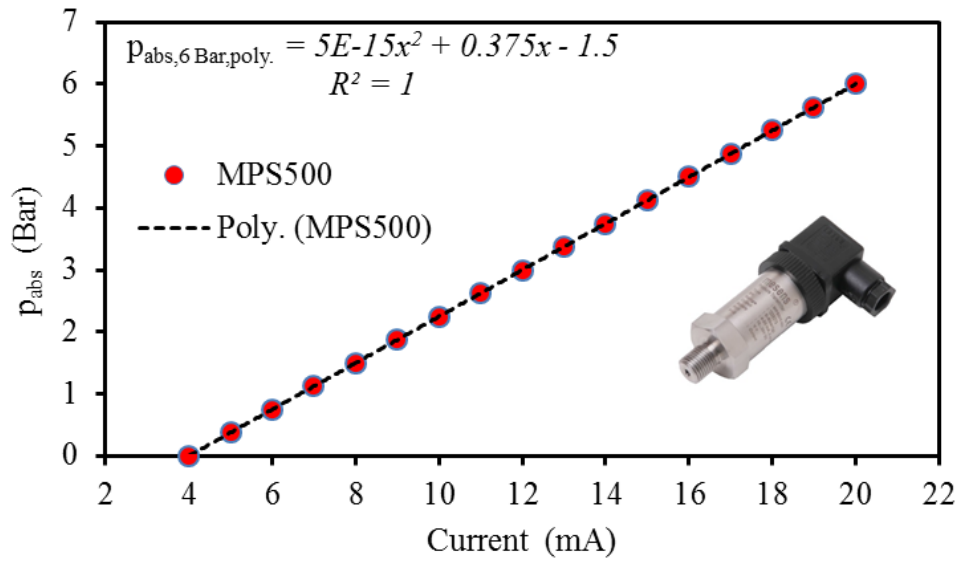


Figure B-4: The correlation test of pressure transmitter

Rotameter - OMEGAR precision variable area rotameters can measure flows of air, water, and gases, with up to $\pm 5\%$ of full scale accuracy and 0.25% of full scale repeatability. These units feature an easy-to-read millimeter scale and are supplied with correlation charts for water (see Figure B-5). Correlation data for other gases are also available. The scale is fused on the metering tube in 1 mm increments, which enables the user to read the flow rate with the highest accuracy. In the calibration data sheet, the maximum scale of rotameter was 65mm but we used two rotameter, because of the maximum speed of chiller pump is 3300 rpm that reaches to 130 mm on rotameter scale. The specification of the rotameter is also presented in Table B-4. In addition, the maximum operating pressure is 13.8 Bar at temperatures up to 121°C. Also, the minimum flow rate at the rated accuracy is 10% of the maximum flow rate. All connections are 1/8" female NPT threaded [111].

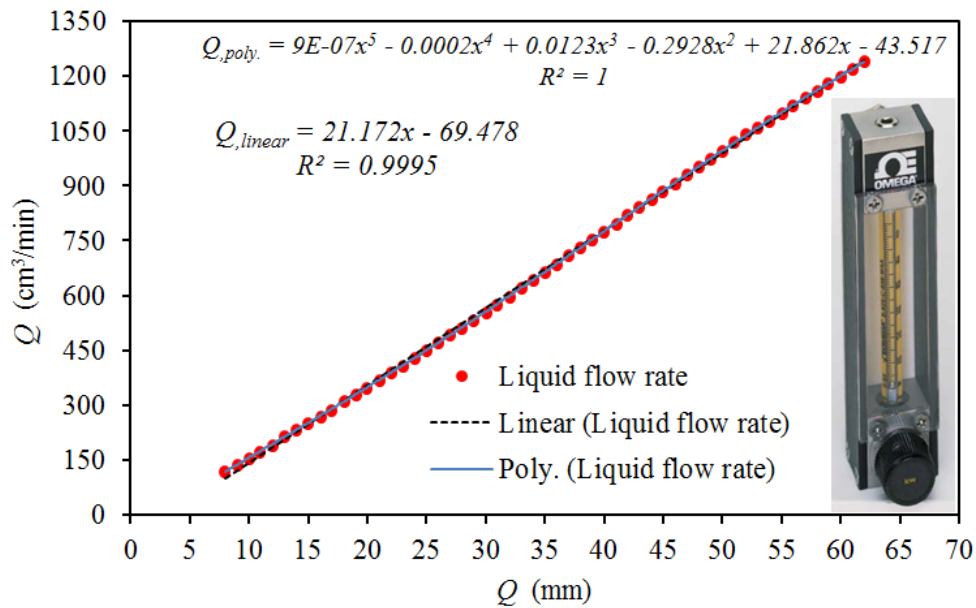


Figure B-5: Correlation for the rotameter

Temperature measurements - Pt-100 thermocouple is easy to use in processing field and flow operation. There are some characteristics of Pt-100 such as fast response, small and inexpensive and can be embedded into an object and high measuring precision. Also, some of the wire features of Pt-100 can be written as thermos-stability, insulated, fire retardant, corrosion-resisting, aging resistance and electrostatic prevention. Mineral insulated metallic sheathed cable consists from Nickle and Copper materials which are dominated-connecting wires in the magnesium-oxide solidly embedded. The correlation tests are done two times by using 11 thermocouples (Pt-100 type) compared with reference thermocouple type Pt-100 of the Huber chiller (see Figure B-6). Figure B-7 shows the temperature sensor in 4-wire circuit that built from ceramics or glass and with the connecting wires of the metallic sheathed cable, and the correlation equation of the boiler temperature relate to the reference temperature of chiller set point. The protection tube and the metallic sheathed cable are from stainless-steel as well as Inconel and laser-welds together. The sheet-diameter is 1 mm is used for

measuring the temperature of 11 point in the condensation setup. Also, there is some specification of the thermocouple Pt-100 is represented in Table B-4 [112]-[113].

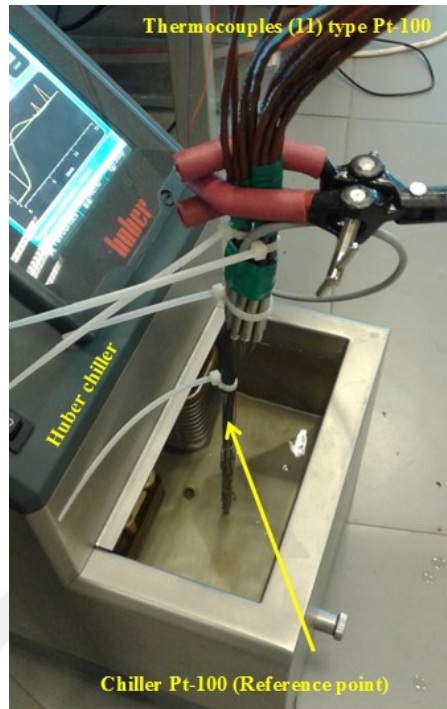


Figure B-6: Calibration test for thermocouples

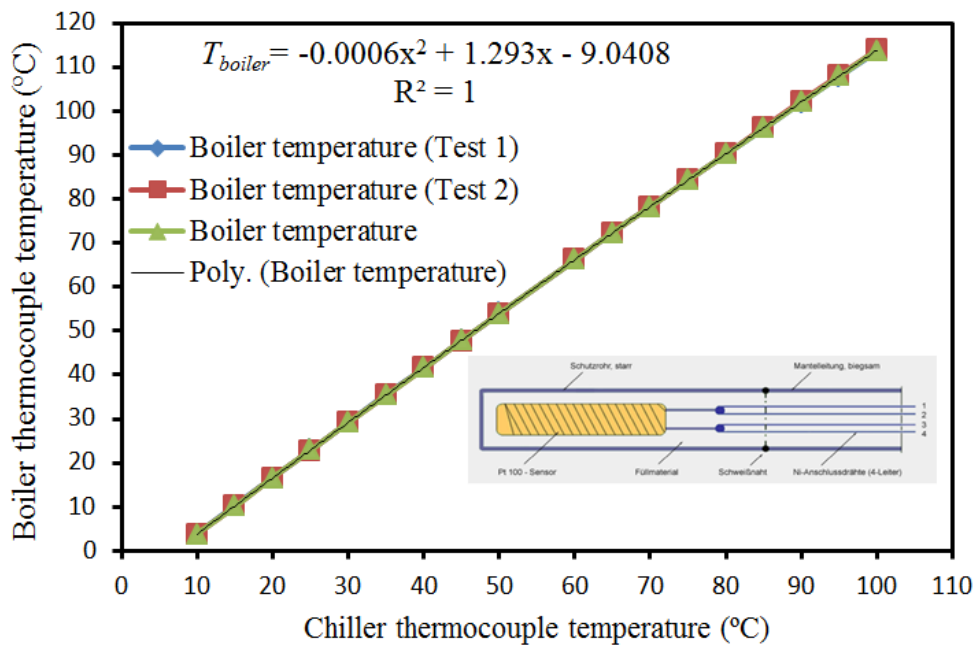


Figure B-7: Show the correlation equation of boiler thermocouple related to the chiller set point temperature

Huber Ministat 125 - is the smallest cooling circulator chiller in the world. Also, a Huber chiller is the main part of the refrigeration system by using R290. Their dimensions of the chiller are $178 \times 80 \times 120$ mm to take the smallest space. The chiller components are like the refrigeration system components including a compressor, condenser, evaporator, refrigerant pipes, coolant expansion reservoir, pumps and so on. The water inside the chiller tank is cooled or heated related to the process type and pumped via a hydraulic circuit to re-circulate the process equipment. Then, the chiller is used to remove heat from the copper heat sink fins inside the liquid chamber by forced convection. Next, it is used to control the main operating parameters at the liquid chamber entrance of the condensation setup, such as water set point temperature from 5 to 95 °C and the liquid flow rate from 4 to 87 g/s. Figure B-8 shows the correlation formula of the chiller is calculated to measure the rotameter flow rate (mm) related to chiller pump speed (rpm). The specification of the chiller is explained in Table B-4 [114].

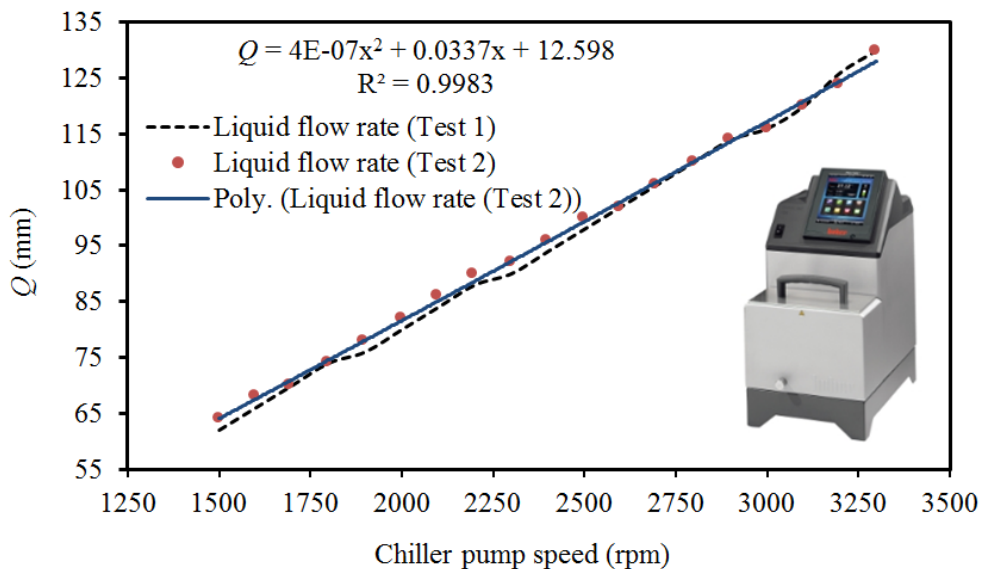


Figure B-8: Show the correlation equation of chiller flow rate in mm vs chiller pump speed in rpm

Water level sensor - the level sensor type (FDMH60C) is a very necessary device to know the liquid level inside the boiler tank. The circuit diagram consists of relay connection, red led and the water level sensor (see Figure B-9). The relay connection is used to convert the current amber from 1000 mA to 100 mA. Then, the light of red led used to know the suitable water level inside the boiler tank and protect the heater. Next, when the red led is turn on automatically that means the water level isn't enough for the condensation test, as a result, the boiler tank needs to fill by water. The level sensor specification is very important to know for working limitations of the device (see Table B-4) [115].

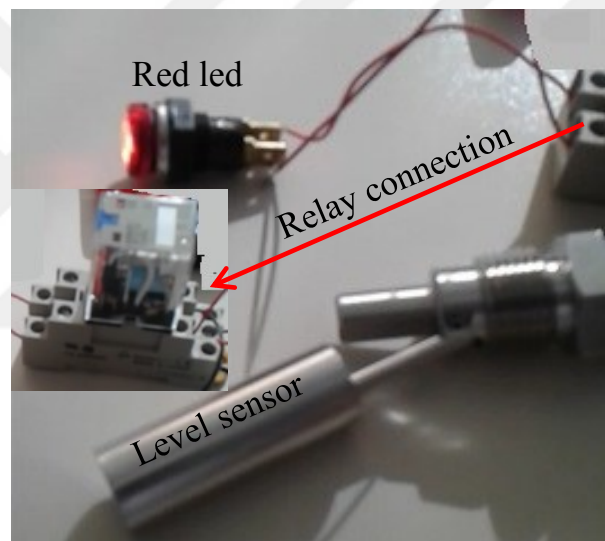


Figure B-9: Show the circuit diagram components of the water level sensor

Table B-4: The specification of all measurement devices

No	Measurement devices	Power supply	Analog in/ out	Specification	Ref.
1.	Keysight N5750A high power supply	150V,5A, 750 W AC Input: 100 –240V; 50/60Hz	Accuracy 75 mV+5 mA 150 mV+15 mA Output no: 1	T _{amb} : 0 - 40 °C Efficiency: 76 – 87 % Universal input, 100/200 V, 0.5A/5A GPIB, LAN, USB	[116] , [117] , [118]

2.	Agilent E3634A low power supply	Power: 200 W V_{max} : 25-50 V I_{max} : 4-7 A	Output no: 1 Output range:- Low: 25V/7A High: 50V/4A	Accuracy: 0.05%+10 mV 0.2 %+10 mA Resulation: 3 mV $Power_{in,max}$: 700 W	[116] , [119]
3.	Agilent 34972A-DAQ	Port 1, 2: V_{in} : 0.8- 2.0V V_{out} : 0.8- 2.4V I_{out} : -400 - 1mA $V_{in Max}$: < 42V	Analog output 16-bit, 20 channels $I_{o,max}$: 10-16mA A_I/A_O : 100 mV- 10 V	Thermocouple Types: B, E, J, K, N, R, S, T LAN: Local Area Network USB: Universal Serial Bus RS-232:Interface Connector	[120] , [121]
4.	OEM Pressure Transmitter – Universal	Connections Type 401006/000-495-405-502-20-61	Output (405) I_{A_O} : 4-20 mA, 2-wire	$P_{relative}$: 1-100 Bar P_{abs} < 25 Bar $T_{amb,error}$: -20 to 85 °C Connections: 502 (G1/4)	[110]
5.	Resistance - thermometer of DIN EN 60751	Pt-100	Analog output 0-10 V/10 mA 0-20, 4-20 mA, and load 500 Ω	In 2-, 3- or in 4-wires The sheat-diameters of 1, 1.5, 2, 3 and 4 mm T_{range} : -200-600 °C	[112] , [113]
6.	Infrared camera SC5200	Power 12 VDC	Analog Video output: RS 170-60 Hz 14 bit Digital	Shutter speed = 10 μ s to 10ms Resolution= 320 \times 256 $Distance_{avg}$ = 14 \pm 2 cm T_{op} = -15-3000 °C	[109]
7.	High-speed camera	Power: 12 VDC, 1.5 A	Phantom V311 Target distance 70 \pm 1.75 mm	1280 \times 720 @3250 fps 128 \times 8 @500'000 fps Shutter speed 1/10 ⁶ s	[107] , [108]
8.	Omega Rotameter	FL-1356-S 01b20231551	Liquid-water	119-1240 ccm (ml/min) Pressure drop=1.7 Bar	[111]
9.	Huber chiller	Thermostat: Order-No.: 2014.0006.01	Cooling power: T_{range} 0, 25-150 °C 2000 and 3000 W	Max. delivery: 27l/min, 1620 l/hr $p_{max,delivery}$ = 0.7 Bar	[114]

10.	Liquid level sensor	FD MH50/56C Connection =1/2 inch	Material: SUS316 Voltage Max.: 240 AC/200 VDC	Capacity Max.: 50 W Max. Pressure: 5 Bar T_{range} : -20 to 120 °C	[115]
11.	Resistance heater	Material: nickel alloy	V=12 - 38 V A=0.5 - 8 A R = 5.98 Ω /m	Diameter=0.3 mm Length=3 m	Mv
12.	Ceramic insulators		Diameter=0.3 mm	Used for insulating the heater element	Mv

The experimental setup of condensation phenomena with all measurement technique and instrumentation are presented in Figure B-10.

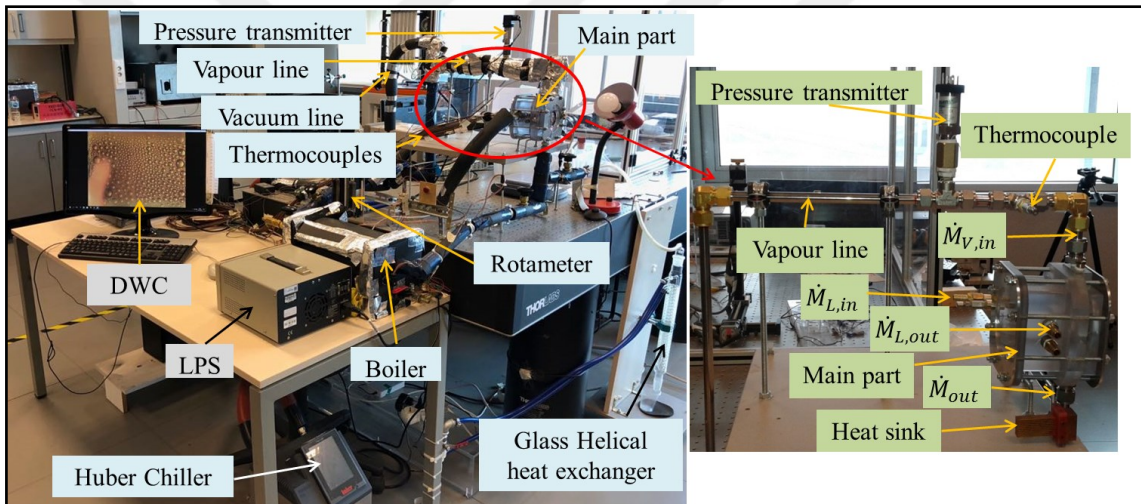


Figure B-10: Shows the photograph of condensation experimental setup with all measurement tools

APPENDIX C

ANALYSIS OF THE EXPERIMENTAL UNCERTAINTY

C.1 *Analysis of Uncertainty for independent Parameters*

While, there may be a number of sources for errors, the main error sources are divided into three groups as the errors from calibration, data collection and data reduction. Moreover, each of these groups has many sources of the errors elements individually such as the data provided by the manufacturer of any equipment or tool in use in the tests and different information system as in the list of specifications like, linearity, accuracy, drifts, slowdown and repetition.

Independent parameters (such as temperature, dimensions, etc.) have been found the bias error (B) and precision limit (P_x) by using the collect root-sum-squares (RSS) method:

The bias error is calculated from [99]:

$$B = \pm [(0.5 \text{ Resolution})^2 + (\text{Accuracy})^2]^{0.5} \quad (\text{C-1})$$

The average value of scale or average of measurement is calculated from:

$$\bar{x} = \frac{1}{n} \sum_{i=1}^n x_i \quad (\text{C-2})$$

The standard deviations (σ) of the sample distribution can be calculated as:

$$\sigma_x = \left[\frac{1}{n-1} \sum_{i=1}^n (x_i - \bar{x})^2 \right]^{0.5} \quad (\text{C-3})$$

The mean standard deviations ($\sigma_{\bar{x}}$) for the sample was deduced by using the following relation:

$$\sigma_{\bar{x}} = \sigma_x / \sqrt{n} \quad (C-4)$$

The overall precision error limits can be calculated by using the student-t distribution at 95 % confidence interval with the (n-1) degrees of freedom that is written as:

$$P_x = t_{(n-1), 95\%} \times \sigma_{\bar{x}} \quad (C-5)$$

To integrate between the elemental errors to obtain their 95 % for confidence uncertainty (U_x), has been using the following formulas to evaluate the absolute uncertainty by:

$$U_x = \pm [B^2 + P_x^2]^{0.5} \quad (C-6)$$

The relative uncertainty (in percentage) is calculated from:

$$RU\% = \frac{U_x}{x} \% = \pm \left(\frac{U_x}{x} \right) \times 100 \quad (C-7)$$

In all Equations starting from C-2 to C-7 the x is used as any independent parameters.

C.2 Uncertainty Estimation of Thermocouples

Calibration helps to estimate the uncertainty in a certain piece of equipment employed. Errors from the calibration contain those errors elemental which enter in the system of measurement through its calibration. Errors of calibration can enter from three sources that are (i) the process of calibration (ii) the system or device which used in calibration, and the reference or standard value employed in the calibration. In addition to that, the calibration fitting curve is determined by developing the mathematical relation as a correlation equation between the input and output results for any independent parameters [99].

The uncertainty in reference thermocouple Pt-100 is defined as:

$$U_{Temp} = \pm \left[(U_{Std})^2 + (U_{Fitting-curve})^2 \right]^{0.5} \quad (C-8)$$

where U_{Temp} , U_{Std} and $U_{Fitting-curve}$ are the uncertainties of reference thermocouple type Pt-100, standard instrument used in the calibration and the fitting of curve error,

respectively. Uncertainty from the bias is calculated by using Eq.5-35, and the instruments' errors are shown in Table C-1.

Table C-1: The instrument error of measurements devices

	Accuracy	Resolution
DAQ	$\pm 0.014 \text{ }^\circ\text{C}$	0.1 $^\circ\text{C}$
Pt-100	$\pm 0.5 \text{ }^\circ\text{C}$	0.1 $^\circ\text{C}$
Pc-E73 (assumption)	$\pm 0.015 \text{ }^\circ\text{C}$	0.1 $^\circ\text{C}$
Rotameter (FL-A356)	$\pm 0.25 \text{ g/s}$	0.5 g/s

The reference thermocouple type Pt-100 is fixed with all thermocouples (11 T-types) inside the water tank of the chiller (Huber Ministat-125) see Figure B-8. The average temperature and mean standard deviation for 13 readings starting from 5 to 95 $^\circ\text{C}$ of each thermocouple are determined from Eqs. C-2 to C-5. Then, the overall precision error in the temperature measurement, P_T is determined by using Eq.C-5 and the final standard uncertainty is determined by Eqs.C-5 and C-1.

The reference thermocouple type Pt-100 was immersed inside deionized water. After that, water is heated by using Huber chiller with different set point ranges from 5 $^\circ\text{C}$ to 95 $^\circ\text{C}$ again to reach the under boiling point and then record the values by using Data acquisition and LabVIEW program for which sample calculations are shown in Table C-2 [122]. Thus, the uncertainty in the reference thermocouples is same or near to the uncertainty correlated with the fitting curve procedure between the reference Pt-100 reading and standard points. However, the uncertainty of fitting curve is calculated by using the average standard deviation according to Eq. C-4 [99]:

$$U_{\text{Fitting-curve}} = \sigma_{\bar{x}} \times t_{(n-1),95\%} \quad (\text{C-9})$$

where: $B_{\text{Fitting-curve}} = 0$.

Table C-2: The uncertainty calculation procedure for curving-fitting temperature

No	T_{Std} Referance thermocouple Pt-100 (°C)	T_{Exp} , After calibration (°C)	(Deviation) ² = $T_{Std}-T_{Exp}$ (°C)
1	4.91	4.56	0.35
2	9.98	10.01	-0.03
3	20.05	19.99	0.06
4	30.11	29.95	0.16
5	40.08	39.89	0.19
6	50.1	49.90	0.20
7	60.07	59.87	0.20
8	70.08	70.02	0.06
9	74.95	75.07	-0.12
10	80.08	79.85	0.23
11	85.05	85.00	0.05
12	90.04	90.04	0.00
13	95.07	95.32	-0.25
Freedom degree		(n-1)	12
Average (\bar{x})		Eq. C-2	0.085
Mean standard deviation ($\sigma_{\bar{x}}$)		Eq. C-4	0.044
Student distribution factor		$t_{(n-1),95\%}$	2.180
$P_{Fitting-curve}$		Eq. C-5	0.097

According to Eq. C-8 the absolute overall uncertainty for temperature for all eleven points in the experimental setup can be seen in **Figure 4-16**. Also, relative uncertainty (in percentage) can be obtained by using Eq.C-7. Finally, the absolute and relative overall uncertainties for all temperature points are calculated with same method.

LIST OF PUBLICATIONS

List of papers and conference contributions as shown below:

No	Title	Journal name	Status	Date
1	Numerical and experimental analysis of a heat pipe-embedded printed circuit board for solid state lighting applications	Experimental Heat Transfer https://doi.org/10.1080/08916152.2017.1397818	Published	2017
2	Effect of micro-structured surfaces on heat transfer and surface wetting phenomenon during vapour condensation	21th National Conference of Heat Science and Technology (ULIBTK'17)	Published	2017
3	Experimental investigation on heat transfer and surface wetting phenomena during vapor condensation on nano textured surfaces	10th International Conference on Boiling and Condensation Heat Transfer www.icbcht2018.org	Published	2018
4	An experimental and analytical study on the influence of superhydrophobic micro-textured surfaces on liquid wetting phenomena	Colloids and Surfaces A 555 (2018) 191–200 https://doi.org/10.1016/j.colsurfa.2018.06.084	Published	2018
5	Impact of functional nanofluid coolant on radiator performance	ASME - Journal of Thermal Science and Engineering Applications	Submitted	2018
6	Effect of Polymer Coating on Vapor Condensation Heat Transfer	ASME - Journal of Heat Transfer	Submitted	2018

7	Energy and exergy analyses of a refrigeration cycle	International Journal of Air-Conditioning and Refrigeration	Submitted	2018
8	Role of micro-structured surfaces in condensation I: experimental procedure and heat transfer analysis		In progress	
9	Role of micro-structured surfaces in condensation II: heat transfer results and discussion		In progress	
10	An experimental study of hydrophobic micro-structured surfaces during vapor condensation under different pressure conditions		In progress	
11	Wettability and Heat Transfer Performance of Chemically Structured Nano Surfaces During Pool Boiling		In progress	

BIBLIOGRAPHY



Dr. Thamer Khalif Salem

Research Areas

Cooling technologies in electronics (Heat pipe), heat transfer on micro-structured surfaces, CFD analysis and experimental studies for two Phase Forced Convection of condensation process.

PhD

Özyeğin University 2018.

Graduate

University of Technology
Baghdad, Iraq, 2003.

Undergraduate

College of Military Engineering,
Baghdad, Iraq, 1996.

M.Sc. Thamer Khalif Salem received his B.Sc. degree in mechanical engineering from the College of Military Engineering, Baghdad, Iraq. In July 1996, he graduated first in the graduating class with a Bachelor of Science degree in Mechanical engineering department.

His M.Sc. degree in Mechanical Engineering / Refrigeration and air-conditioning from the University of Technology, Baghdad, Iraq, in 2003 with the master grade was (83.921). In 2004 he joined Tikrit University in Salahuddin, Iraq, and worked as an instructor there until 2012. During that time, he gave several courses such as Thermodynamics, Air-conditioning, and programming in FORTRAN. Currently, he is a Ph.D. student in the Mechanical Engineering Department of Özyeğin University, Istanbul, Turkey. His research interest contains Electronic cooling system, Heat pipe, microstructure surface, Condensation and Refrigeration cycles.

At the end of his study, 2 Journals and 2 Conferences were published, 3 Journals submissions, 4 papers under review with my supervisor. Also, I designed a new experimental setup for studying the effect of surface wetting on the critical heat flux during the pool boiling process.